
Silica nanoparticles and their interaction with cells: a multidisciplinary approach

Inauguraldissertation

zur

Erlangung der Würde eines Doktors der Philosophie

vorgelegt der

Philosophisch-Naturwissenschaftlichen Fakultät

der Universität Basel

von

Hélène Emilie Kettiger

aus Liestal (BL)

Basel, 2014

Genehmigt von der Philosophisch-Naturwissenschaftlichen Fakultät auf
Antrag von

Prof. Dr. Jörg Huwyler

Prof. Dr. Barbara Rothen-Rutishauser

Basel, den 11.11.2014

Prof. Dr. Jörg Schibler
Dekan

Originaldokument gespeichert auf dem Dokumentenserver der Universität Basel
edoc.unibas.ch



Dieses Werk ist unter dem Vertrag „Creative Commons Namensnennung-Keine kommerzielle Nutzung-Keine Bearbeitung 3.0 Schweiz“ (CC BY-NC-ND 3.0 CH) lizenziert.

Die vollständige Lizenz kann unter
creativecommons.org/licenses/by-nc-nd/3.0/ch/
eingesehen werden.

Für meine Liebsten

*I have loved the stars too fondly
to be fearful of the night.*

(Sarah Williams- The Old Astronomer to His Pupil)

Table of contents

Acknowledgements	iii
Abbreviations	v
Summary	1
1 Introduction	3
1.1 Definition and application	3
1.2 Nanoparticles as drug delivery systems- history and application	4
1.3 Safety of nanoparticles: the need of a new toxicological science?	6
1.4 Mode of nanotoxicity	7
1.4.1 General mode of nanotoxicity	7
1.4.2 Mode of toxicity for silica nanoparticles	9
1.5 Choice of material	9
1.6 Synthesis methods for silica nanoparticles- the sol-gel route	10
1.6.1 Non-porous silica nanoparticles	10
1.6.2 Mesoporous silica nanoparticles	10
1.6.3 Removal of the template	11
1.6.4 Alteration of the surface	12
1.7 Physico-chemical characterization	12
1.7.1 Size and morphology- dry state	12
1.7.2 Size- dispersive state	13
1.7.3 Surface measurements	13
1.7.4 Other parameters	14
1.8 <i>In vitro</i> systems and cell-based assays	15
1.8.1 Cell type	15
1.8.2 Dosimetry	15
1.8.3 Viability	16
1.8.4 Oxidative stress	17
1.8.5 Genotoxicity and inflammation	17
1.8.6 Hemolysis	18
2 Aim of the thesis	19

3	Published and submitted results	23
3.1	Engineered nanomaterial uptake and disposition	23
3.2	Safety of silica nanoparticles	39
3.3	Hemolysis of silica nanoparticles: a mechanistic approach	69
3.4	Polymersomes containing quantum dots	85
3.5	Multiparametric sensor approach for drug-induced toxicity	99
3.6	P2X7 receptors and cellular stress	113
4	Discussion	137
4.1	The importance of characterized material	137
4.2	Experimental considerations	138
4.2.1	Choice of assay	138
4.2.2	Cell lines and cell density	138
4.2.3	Plasma proteins	139
4.2.4	Interference	140
4.2.5	Mechanistic studies	141
4.3	Translation of knowledge to small molecule toxicity	142
5	Conclusion and Outlook	143
6	Appendix	147
6.1	Bibliography	147
6.2	Curriculum vitae	159

Acknowledgements

Ich möchte mich an erster Stelle ganz herzlich bei meinem Betreuer und Doktorvater Jörg Huwyler bedanken. Es war eine grossartige Erfahrung mit Dir zu arbeiten, und ich bedanke mich für Dein Vertrauen und deinen unermüdlichen Optimismus. Arigato.

Bei Barbara Rothen-Rutishauser bedanke ich mich für die spontane und unkomplizierte Zusage fürs Korreferat.

Ebenfalls bedanke ich mich beim Team der pharmazeutischen Technologie der Universität Basel, speziell bei ehemaligen Mitgliedern wie Pascal Detampel und Le-Ha Dieu, sowie auch bei aktuellen Teammitglieder, wie Dominik Witzigmann, Philipp Grossen und Stefan Siegrist. Bei euch bedanke ich mich für die lustigen Stunden, die spannenden Diskussionen und die aufbauenden Worte. Nicht unterkriegen lassen. Wegen euch weiss ich, dass das keine blosses Floskel ist. Danke für eure Unterstützung! Ein grosses Danke geht auch an meine Masterstudentin Laura Schiesser, die mir bei der Datengenerierung eine grosse Hilfe war. Es war abwechslungsreich und interessant, mit dir zu arbeiten!

Ein spezielles Dankeschön geht an Maxim Puchkov, Gabriela Québatte und Tanja Stirnimann. Ich bedanke mich bei euch für die vielen haarsträubenden Diskussionen (wissenschaftliche und andere), die lustigen Abende, die abenteuerlichen Ausflüge und die abwechslungsreichen Unternehmungen.

Diese Arbeit wäre ohne die grossartige Unterstützung verschiedener Collaborators nicht in diesem Mass zustande gekommen. An erster Stelle bedanke ich mich bei der EMPA St. Gallen, bei Cordula Hirsch, Angela Schipanski und Peter Wick. Ein grosses Danke geht nach Turku, Finnland, an Didem Sen Karaman und Jessica Rosenholm. Durch euch konnte ich erst richtig in die Partikelsynthese eintauchen. Ich bedanke mich auch herzlich bei Dr. Barbara Perrone von Bruker, Fällanden, die bei den NMR Messungen eine grosse Hilfe war.

Für die finanzielle Unterstützung bedanke ich mich beim Swiss Centre for Applied Human Toxicology und bei der Freiwilligen Akademischen Gesellschaft Basel.

Meiner Familie und meinen Freunden möchte ich für die grossartige Unterstützung während dieser Zeit danken.

Mein grösster Dank geht an Beatrice Gehri, die mich in all meinen Entscheidungen unterstützt hat und mir stets beistand, wenn ich den Wald vor lauter Bäumen nicht mehr gesehen habe.

Abbreviations

AFM atomic force microscopy

DCFH-DA dichloro-dihydro-fluorescein diacetate

DDS drug delivery system

DLS dynamic light scattering

HepG2 Liver hepatocellular cells (human)

ITC isothermal titration calorimetry

MTT 3-(4,5-dimethylthiazol-2-yl)-2,5-diphenyltetrazolium bromide

NADH nicotinamide adenine dinucleotide

NADPH nicotinamide adenine dinucleotide 2'-phosphate

PI propidium iodide

PS phosphatidyl serine

RBC Red blood cells

ROS reactive oxidative stress

SEM scanning electron microscopy

SNPs silica nanoparticles

ssNMR solid state nuclear magnetic resonance

TEM transmission electron microscopy

THP-1 leukemic monocytes (human)

List of Figures

1.1	Definition of nanomaterials.	4
1.2	Interactions of nanoparticles with their environment	8
1.3	The growth of silica nanoparticles	11
1.4	Dosimetry in <i>in vitro</i> systems.	15
2.1	Pillars of nanotoxicology	19
4.1	Viability decrease is cell-number dependent	139
4.2	Interferences of nanoparticles with reporters.	140

Summary

Silica nanoparticles are increasingly used as drug delivery systems and for biomedical imaging. Therapeutic and diagnostic agents can be incorporated into the silica matrix to improve the stability and solubility of hydrophobic drugs in biological systems. However, the safety of silica nanoparticles as drug carriers remains controversial. To date, no validated and accepted nanospecific tests exist to predict the potentially harmful impact of these materials on the human body. The mechanism proposed for hemolysis of unmodified silica nanoparticles is based on the electrostatic interaction between the silanol surface groups and the quaternary ammonium in the choline head group of the phospholipids. However, a detailed understanding of this process is missing.

In this thesis, different silica nanoparticles were synthesized, characterized, and tested in two cell lines regarding viability and oxidative stress. Hemolysis was assessed using red blood cells. Furthermore, the hemolytic mechanism of a chosen silica nanoparticle type was investigated in depth using a biophysical chemistry approach. We used the dye-leakage assay, isothermal titration calorimetry, solid state nuclear magnetic resonance, and flow cytometry to elucidate this mechanism.

Our results revealed that silica nanoparticles with a porous surface and negative surface charge had the strongest impact on viability in a concentration dependent manner. This is in contrast to non-porous silica nanoparticles. None of the studied particles caused oxidative stress in either cell lines. Particles with a negative surface charge induced hemolysis. The mechanism responsible for the hemolysis for silica nanoparticles had no electrostatic component. The nuclear magnetic resonance data revealed no interaction with the choline group. However, nuclear magnetic resonance data suggested the presence of faster tumbling species.

Our toxicological and mechanistic studies showed potential hazards of spherical amorphous silica nanoparticles. Physico-chemical properties mediating toxicity in living cells were identified. We propose that our standardized silica nanoparticles may serve as a readily available reference material for nanotoxicological investigations. Mechanistic data did not support an electrostatic interaction as postulated in the literature, but rather a strong adsorption process that may lead to hemolysis. Furthermore, the presence of faster tumbling species suggested the formation of smaller lipid bilayer structures upon silica nanoparticles exposure. Flow cytometry data revealed that their size is about 100 nm. It remains to be proven if the bilayer wraps around the hemolytic silica nanoparticles, if an exclusive formation of smaller species without wrapping is present, or both of the aforementioned.

Chapter 1

Introduction

1.1 Definition and application

"Nano" stems from the greek word *nannos* and means "dwarf". One nanometer is defined as 10^{-9} m. Hence, nanotechnology is interested in very small objects and has been widely known and used throughout history. For example, in ancient Egypt and China colloidal gold had already been introduced to medicine. Later on, nano-sized gold and silver were used to embellish glass. In the Middle Ages, church windows were colored with nanomaterials. But it was not until 1875, that M. Faraday was able to synthesize gold nanoparticles intentionally by the reduction of gold chloride [1]. Colloidal sciences were born at that time. Later, nanotechnology had emerged from the colloidal sciences by the famous lecture of Richard Feynman in 1959 ("There is plenty of room at the bottom") [2]. With the invention of various microscopic techniques such as the scanning tunnel microscope or the atomic force microscopy (AFM), objects at the nanoscale could be observed in real time [1].

Amongst others, terms like nanomaterials, nanorods, and nanoparticles are frequently used as synonyms. However, it is important to discriminate between several terms that contain the prefix "nano". Each of these terms is defined by its dimensions, as depicted in Figure 1.1. Common to all nano-related terms is the size-dependent definition that spans from 1 nm to 100 nm, as defined by the OECD, ISO, and DIN [3]. A nanomaterial is defined by its inner or outer dimensions, with either of them in the range of 1-100 nm. This definition also includes microscaled particles with pores in the nanorange. A nano-object is confined by its outer dimensions only. Nano-objects can furthermore be divided into three sub-classes, starting with one dimension (nanoplates), two dimensions (nanofibers) and three dimensions in the nanoscale (nanoparticles).

This cut-off of the upper size limit (100 nm) is not scientifically justified. It is assumed, that so called quantum effects start at this size for some materials [4]. For example gold nanoparticles change their excitation and emission spectra due to their size [5]. This feature is not present in gold particles that exceed a critical size above 100nm. Another example is that inert material such as titanium becomes explosive at the nano-size range [6]. However, some scientists postulated that these special nano-effect occurs below 30 nm [7]. Otherwise, nanoparticles up to 300 nm or even 500 nm are interacting with biological systems and can be endocytosed by cells. This is a feature that microparticles hardly possess. Among toxicologists and pharmacologists it is commonly

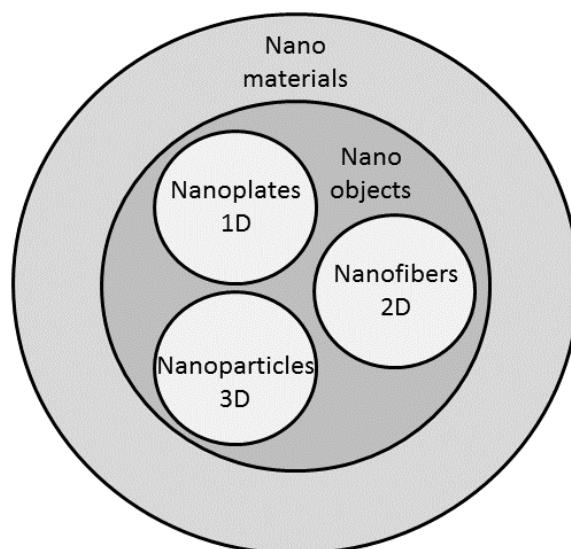


Figure 1.1: Definition of nanomaterials. "D" stands for dimension; 1D is nanoscaled in the x-dimension; 2D in x and y dimensions and 3D in x, y, and z-dimension.

known that particles below 250 nm can distribute throughout the human body and are therefore referred as nanoparticles. In this size range we also find most of the drug delivery systems drug delivery system (DDS). Therefore, federal institutions like the Food and Drug Administration further extended the upper boundary of nanoparticles up to 1000 nm, if the particle exhibits distinct properties from the bulk (physical, chemical, biological). Throughout this thesis, the term nanoparticles will be used up to 500 nm.

Today, nanoparticles are used in our daily life. Amongst various applications, they are used in consumer products, nanomedicine, and in the environment [1]. In consumer products they function as food additives to aid flowing (Aerosil[®]), or they can be found in the cosmetic sector as antioxidants or blockers of ultra violet light. For example, titanium dioxide is used in sunscreen and is proposed as an alternative to chemical sunscreen. Apart from this, they are found in solar cells, where the use of quantum dots enhances the efficiency compared to conventional solar cells [8].

1.2 Nanoparticles as drug delivery systems- history and application

In the 1970s, nanoparticles were first proposed to be used as DDS. Research started with lipid bilayer particles (liposomes) as organic carriers and to date, nanoformulated drugs such as liposomal encapsulated doxorubicin (Doxil[®]) have been marketed successfully. After Doxil[®] was launched to the market, various lipid formulations followed and were mainly used for treating

1.2. NANOPARTICLES AS DRUG DELIVERY SYSTEMS- HISTORY AND APPLICATION

cancer [9]. One of the non-liposomal nanodrug on the market is Abraxane[®], where the hydrophobic drug paclitaxel is coupled to albumin. Only recently, inorganic nanoparticles like porous silica were proposed as DDS [10]. Silica nanoparticles consist of silicium dioxide and is the same material used to make glass. Compared to liposomes, porous silica has the advantage of a high specific surface area and can therefore guest a considerable amount of drug. Additionally, core-shell silica nanoparticles (SNPs) are emerging: in 2005 they were proposed to use as imaging agents [11]. The excellent photostability of encapsulated dyes into the silica matrix and their subsequent accumulation in a tumor makes them an attractive alternative for imaging. These so-called CU (Cornell University) Dots are currently tested in clinical trials [12].

Most of the marketed drugs are small molecules (molecular weight up to 500 Da). Depending on their route of entry to the human body, they are distributed according to their chemical properties i.e. molecular weight, electron donors, electron acceptors, and logP (water-octanol partition coefficient). [13]. Small molecules can also bind throughout the body to non-specific targets and hence cause adverse drug reactions, or are even cytotoxic for healthy cells [14]. In contrary to free drugs, drugs encapsulated into nanoparticulate delivery systems can minimize this effect.

Kettiger at al. discuss obstacles which DDS must overcome in order to exert a pharmacological effect [15]. The size of a nanocarrier is crucial to ensure successful pharmacological efficacy. The carrier should be large enough (around 100-200 nm) to ensure sufficient drug loading. However, it should not exceed a certain size, because otherwise it will be recognized by macrophages [15]. Once injected into the blood stream, the DDS comes into contact with cells and proteins. These proteins will start to adsorb immediately to the nanoparticle. If so-called opsonins (proteins that render foreign material "visible" to macrophages) bind to the DDS, premature clearing from the circulation due to macrophage uptake reduces drug efficacy. Hence, stealth properties need to be introduced to a carrier to render them invisible for opsonins.

When a DDS is distributed via blood stream, accumulation on the target side (mostly tumors) is crucial. This is mainly achieved by passive diffusion out of a leaky vasculature in the tumor region. Accumulation in diseased cells is enhanced by decorating the carrier system with a targeting moiety to specifically get incorporated by diseased cells. Ideally, healthy cells do not recognize the targeting moiety. Furthermore, targeted drug delivery reduces multiple drug resistance [16]. Unfortunately, only some fractions of the injected dose are reaching the tumor, so off-target effects are mainly expected in the clearing organs as liver and spleen. Hence, the carrier itself should be essentially non-toxic and be degraded safely.

1.3 Safety of nanoparticles: the need of a new toxicological science?

Toxicology is the science of measuring adverse effects of chemicals to living organisms including human, animals, and the environment [17]. Paracelsus' famous sentence "*Alle Dinge sind Gift, und nichts ist ohne Gift; allein die Dosis macht, dass ein Ding kein Gift sei*" is often mentioned to illustrate a well-known dose-response curve for small molecules. Nanotoxicology however is, compared to small molecules toxicology, a relatively new domain in toxicology and has emerged years after the boom of nanotechnology. At this time point, numerous new and unregulated nanoparticles have already been introduced to the market. Nanoparticles have properties which are helpful for consumers and industrial applications. However, the same properties that render them unique compared to the bulk material give rise to a certain biological reactivity. Until now, many tests have been proposed to determine the safety of nanoparticles. However, no clear statement is possible. Moreover, standard methods for testing the safety of nanoparticles are missing [18]

While a lot is known about bulk and small molecule safety, only little is known about safety in the transitional range. In the 1970s a lot of effort was put in understanding the health impact of so-called ultra fine particles, i.e. particles below 100 nm in size. The focus was put on the health impact of airborne particles. One of the most prominent findings of this research was the relation between inhaled asbestos and chronic lung inflammation with subsequent tumors in the lung [19]. The ability of nanoparticles to interact with biological systems in an adverse way was recognized in the 1990s [1].

Since then, a lot of effort has been put in establishing safety margins, always with the asbestos sample in mind. Human epidemiological data are available on airborne ultra fine particles. However, there is still a knowledge gap regarding the interaction between living organisms and nanoparticles. With the ability to be taken up by living cells and crossing barriers, such particles are rendered as bioactive. Their appearance may change dramatically with their changing environment (i.e. a native nanoparticles compared to a protein-coated particle may already exert different toxicological profiles *in vitro*).

Table 1.1 shows the difference between three groups, namely small molecules, nanoparticles, and microparticles. Compared to small molecule toxicity, where relatively well characterized structure-activity-relationship exists, it is still difficult to determine, what renders nanoparticles cytotoxic. As listed in table 1.1, various physico-chemical properties could mediate cytotoxicity. However, it is difficult to conclude from bulk material toxicity to nanotoxicity, although a recent review questions nanotoxicity [20]. Nevertheless, several *in vivo* studies are suggesting to pay special attention, not only to inhaled nanoparticles, but also to DDS or particles used for imaging. Additionally, the research was mainly focused on airborne particles in the last years. In contrary to airborne particles, DDS and particles for imaging are directly injected into the blood stream.

1.4. MODE OF NANOTOXICITY

< 1nm	100nm	> 1000nm
Diffusion, Brownian motion	Sedimentation and diffusion	Sedimentation
Log P, molecular weight, hydrophilicity	size, shape, surface modification, surface area, crystallinity	size, shape, surface modification, surface area, crystallinity
Passive (membrane) or active (transporters)	active (phago-endocytotic processes)	negligible

Table 1.1: Main differences between small molecules, nanoparticles, and microparticles. The difference between the three species lies in size, force of movement, chemical or physico-chemical properties, and uptake into cells.

Hence, safety assessment is faced with different questions and needs other approaches.

1.4 Mode of nanotoxicity

1.4.1 General mode of nanotoxicity

Nanoparticles have various physico-chemical properties and may hence exert different toxicological profiles related to these properties (depicted in Figure 1.2). One of the most studied impacts on nanotoxicity is its size. A smaller nanoparticle is generally considered more cytotoxic compared to their larger counterpart. This has been shown for a variety of materials including gold nanoparticles [21], silver nanoparticles [22], and quantum dots [23], just to mention a few. The enhanced toxicity by smaller nanoparticles can be explained as follows. With a decrease in size an exponential increase in surface area is the consequence. This leads to a higher curvature and therefore an increased reactivity of the atoms on the particle surface. These high-energy surfaces can initiate or catalyze reactions, such as unfolding of proteins or generation of reactive oxidative stress (ROS) (Figure 1.2). The second feature is the solubility enhancement of a nanosized material. For particles with a toxic core material like quantum dots (some of them consist of cadmium) the release of toxic ions from the particle mediates a viability decrease. This mechanism is also responsible for copper nano particles toxicity [24]. For silver nanoparticles, which also release ions and cause cytotoxicity, it is still under debate, if the toxicity is mediated by the size, the ionic

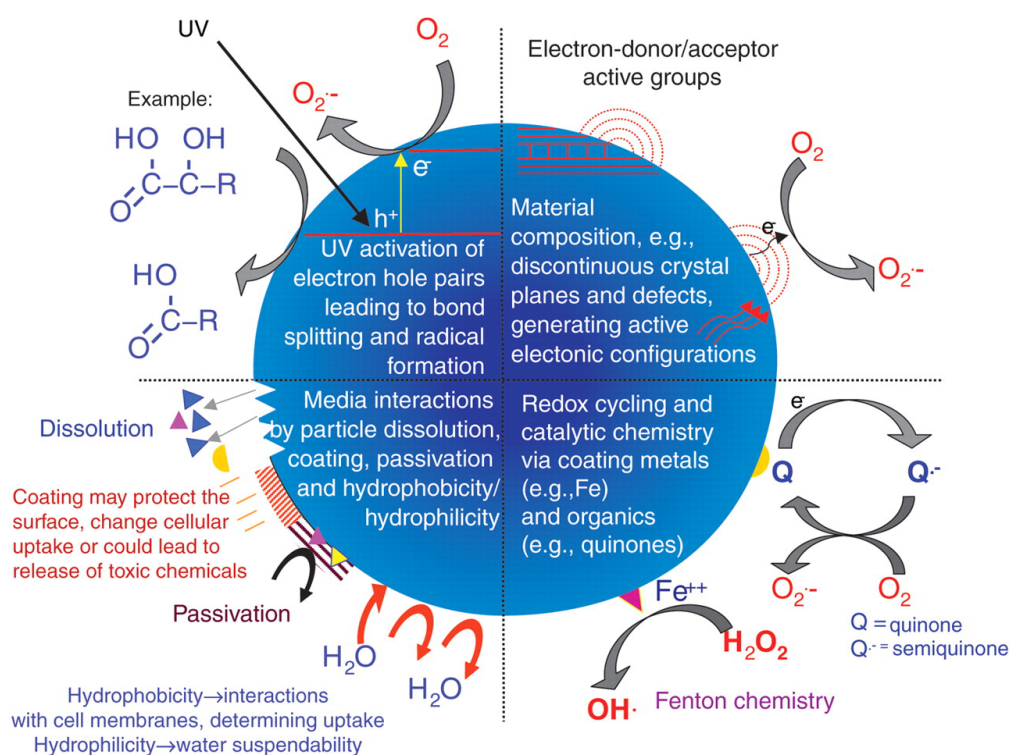


Figure 1.2: Interactions of nanoparticles with their environment. Catalyzing reactions, redox-cycling, particle dissolution, and generation of reactive oxidative species can result in cytotoxicity. Figure reproduced from [4].

constitution or both [25].

The surface groups influence the hydrophilicity or hydrophobicity, where hydrophobic surfaces tend to agglomerate and interact strongly with the cellular membrane. This can lead to membrane distortion or passive uptake [26]. If the surface is modified with functional groups, it changes the appearance of the particle. The charge density on the surface of a nanoparticle can also impact the toxicity. If the charge density on the surface is too high, this leads to cytotoxicity. This phenomenon of high charge density is well known from transfection reagents like poly-ethylene imine, which carry a large amount of positive charges [27]. To render a surface non-toxic, the surface can be modified by a non-toxic polymer like poly-ethylene glycol [15].

Beside these factors, shape and crystallinity play an important role in nanoparticle-mediated toxicity. Well-known examples for shape-mediated cytotoxicity are mainly high aspect ratio particles like asbestos or carbon nanotubes [28]. The tubes are causing oxidative stress, which is mediated by the tubes themselves or by impurities from the synthesis. This leads to ultimate cell death. Crystallinity is a key factor for the toxicity of quartz (crystalline silica), which causes silicosis. Here, a chronic inflammation is provoked by the crystals [29]. Titanium nanoparticles may present

two different crystalline forms, anatase and rutile, where anatase generates ROS and rutile does not [30].

1.4.2 Mode of toxicity for silica nanoparticles

The first studies on toxic effects of silica based material focused on crystalline silica in occupational inhalation exposure [29]. The particles were in the size range of 500 nm up to 10 μm . The consequences of inhaled crystalline silica is silicosis, a progressive fibrotic lung disease [29]. However, the mechanism is not well understood at a cellular level. It was described, that an inflammation process is initiated, when organisms are exposed to crystalline silica [31]. The generation of ROS is also well documented [32]. ROS can lead to DNA damage or oxidative membrane damage. It was shown that particle surface reactivity and the particle for (shape, size) are potentially hazardous factors to induce crystalline silica toxicity.

Due to the high abundance of amorphous nanosilica in consumer products, toxicological research shifted towards smaller non-crystalline SNPs. Although many factors are known to mediate cytotoxicity like size or different shapes, it is not yet clear, which parameter is predominantly responsible for a viability decrease SNPs [18]. Different studies have shown that a viability decrease could be observed in a concentration dependent manner [33–35]. Smaller sizes have a stronger influence on the viability decrease, as described earlier. A plethora of studies is available, which mainly show that amorphous silica at smaller sizes is able to induce oxidative stress, where in turn oxidative DNA damage is observed. However, the vast amount of studies is difficult to compare, since particle syntheses differ (or particles were provided by an external supplier) and only one cell line was used [18]. Mesoporous SNPs (i.e. SNPs with pores in their matrix) were mainly tested with regard to their hemolytic properties. They showed mainly to be non-hemolytic, regardless of their size, surface groups, and dosage [33,36]. Furthermore, certain cell lines are less susceptible of getting damaged in the presence of SNPs than others [18]. Zhang et al. have shown in a study how the synthesis influences the cytotoxicity of different amorphous SNPs [37].

1.5 Choice of material

In pharmaceutical technology, silica has gained a lot of interest in solid dosage form processing, since it is used as a flowing agent (Aerosil[®]). SNPs were proposed as imaging tools, when labeled with a fluorophore [38]. Recently, also mesoporous SNPs have been proposed to use as i.v. DDS [10]. Since one of the nano-mediated toxic mechanisms is the dissolution of the core material and a subsequently high concentration of metal ions (like cadmium or silver), a core material was chosen of which the degradation products were inherently non-toxic. In contrast to other oxide nanoparticles, SNPs do not release toxic ions which in turn lead to locally high concentration and therefore kill the cells. The degradation products of silica have been described to be essentially

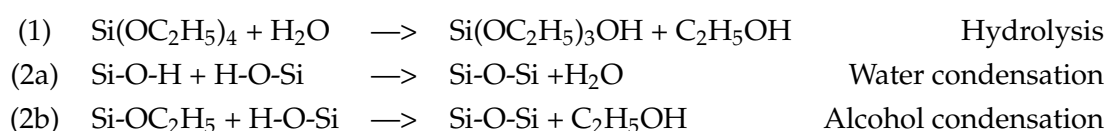
non-toxic [39]. Additionally, the synthesis is well studied and allows changing one specific parameter at the time by only slightly changing the synthesis protocol. Furthermore, the desired material should have already application and the potential to serve as a future DDS.

Silica exhibits all these features and was hence chosen as a reference material for further nanotoxicological experiments.

1.6 Synthesis methods for silica nanoparticles- the sol-gel route

1.6.1 Non-porous silica nanoparticles

The process of forming SNPs with the sol-gel route involves three steps. The reaction is displayed below. In a first instance, a metal alkoxide such as tetraethylorthosilicate (TEOS) is hydrolyzed to silanol monomers (SiOH_4), as shown in step 1a. This process is catalyzed by the presence of either an acid like HCl or a base like NH_3 . The next step in the reaction is the water condensation of the silanol monomers. .



Step 2a represents the condensation between silanol groups. This condensation results in siloxane bridges. Step 2b shows the formation of siloxane bonds from ethoxy groups and silanols. The resultant siloxanes are the same, except the byproduct is either water (2a) or ethanol (2b). These siloxane bridges are forming cyclic structures and then primary particles, as depicted in Figure 1.3. Depending on the chosen catalyst, different gels are formed. Under acidic conditions, the hydrolysis is faster than the condensation step ($1a \gg 2a$), and a lot of smaller particles are formed which then agglomerate into a 3D gel-network, as depicted in Figure 1.3. If a base is used as catalyst, the hydrolysis is much slower than the condensation step ($1a \ll 2a$). In contrast to the acid-catalyzed reaction, the particles grow in size and decrease in number, since small (soluble) particles dissolve and precipitate on larger, less soluble particles. The particle growth is called Ostwald ripening. The first systematic study, where the influence of all reactants and the temperature was investigated was published in 1968 by Stöber et al. [41]. With the now termed "Stöber" synthesis, it was possible to obtain spherical SNPs with size ranges from 50 nm to 2 μm .

1.6.2 Mesoporous silica nanoparticles

It was in 1991, when scientists from the Mobil Oil Research first synthesized mesoporous material with the aid of supramolecular surfactant aggregates as templates for mesopores (pore size 2-50

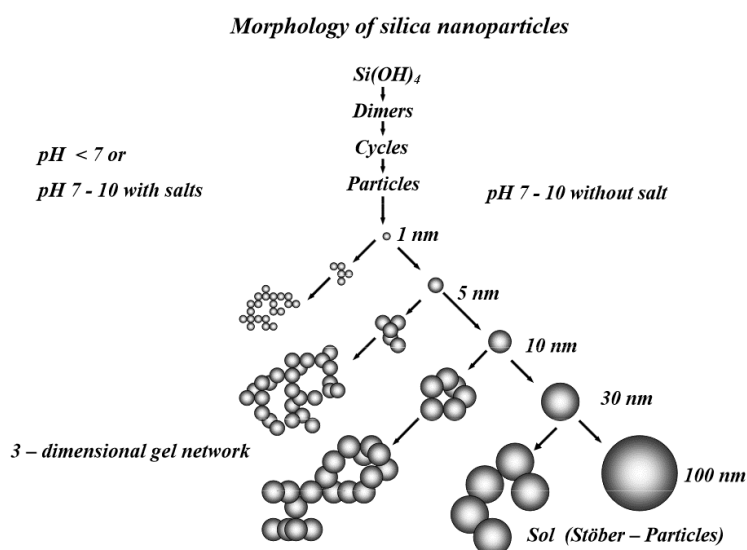


Figure 1.3: Silica nanoparticles can be grown by the sol-gel process. Depending on the reaction conditions, they grow to aggregated gels (acid-catalysis) or to monodisperse silica nanoparticles (base-catalysis). Figure reproduced from [40].

nm [42]). When mesopores are introduced to the silica nanoparticles (SNPs), the specific surface area dramatically increases up to $1000 \text{ m}^2/\text{g}$ (Comparison to non-porous particles: $30\text{-}200 \text{ m}^2/\text{g}$). Mesoporous SNPs synthesis need mainly four components: Like for the synthesis of non-porous SNPs, a silica precursor is needed, a catalyst, solvents, and surfactant to form the pores. Surfactants self-assemble into a wide range of three dimensional ordered structures and act as templates for the mesopores. Depending on the ratio of water, organic phase and surfactant, the surfactant forms different supramolecular structures as micelles, linear tubes, hexagonal tubes, or others. For mesoporous SNPs, cylindrical micelles or hexagonal tubes are the most studied ones. Around these surfactant templates, the silica matrix is grown as described in chapter 1.6.1. The surfactant template needs to be removed carefully [43]. This is important, since most of these surfactants are highly cytotoxic [44].

1.6.3 Removal of the template

There are two common processes for template removal [45]. The first one is calcination, where the synthesized particles are heated up to $800 \text{ }^\circ\text{C}$ in order to burn the surfactant. However, with this treatment the particle surface is altered, as the surface silanols are contracted and form siloxane bonds [37]. Furthermore, the contraction of the silica network may lead to a decrease in pore size. With heat treatment, the SNPs additionally become more hydrophobic [29].

Another possibility to remove the surfactant from the pores is solvent extraction. The extraction procedure is strongly depending on the chosen synthesis route: where for acidic synthesis routes,

water at a certain temperature (70 °C) is already sufficient in template removal, the basic synthesis route needs ion exchange to remove the template completely [46]. Normally, this is done by refluxing the particles in acidic ethanol solution. Another method like extraction with ammonium nitrate during multiple washing steps can remove the template successfully as well [47]. Whatever method is used for surfactant removal, it is crucial to check for traces in the particles. Even small amounts can influence the toxicological profile of the mesoporous SNPs. Normally, this is checked by infrared spectroscopy or thermogravimetric analysis.

1.6.4 Alteration of the surface

When SNPs are synthesized as described above, they exhibit several different surface groups, mostly silanols (Si-OH) or siloxanes (Si-O-Si). The amount of silanols and siloxanes is related to the thermal history of the particle [48]. The native silica surface can be modified with different silica precursors either by co-condensation or post-grafting. Co-condensation is a one pot approach, where the functional group as a silane precursor is added during the particle growth. The precursor is equally incorporated into the silica matrix. Opposite to this, the post-grafting approach uses plain SNPs which were previously synthesized. Then, the desired surface group is grafted onto the bare silica surface as a additional layer. Hence, this is a two-step synthesis.

1.7 Physico-chemical characterization

Characterization of nanoparticles prior to cytotoxicity testing is crucial [3]. Unlike small molecules, where characterization is normally confined to chemical composition and purity, nanoparticles require more extensive identification [49]. Several reviews published within the last years suggest to characterize size and size distribution in biological relevant medium, specific surface area, morphology, solubility, and surface charge [3, 50, 51]. This characterization ensures a better comparability amongst results. Even if particles were obtained from a supplier, the specifications should be double checked. Data given by manufacturers may differ from what researchers have measured [52].

1.7.1 Size and morphology- dry state

Size and size distribution are the utmost important parameters to be characterized, since the quantum effects of nanoparticles sets in at different sizes, as described earlier. A plethora of methods are available for size determination, however, each of the methods is limited by its principles. The most common techniques for size determination in dry state include microscopy like transmission electron microscopy (TEM), scanning electron microscopy (SEM), and AFM [1]. The advantage of microscopic approaches is that more than one parameter can be measured at the same time: Besides size and size distribution, shape can also be directly determined. More sophisticated

1.7. PHYSICO-CHEMICAL CHARACTERIZATION

microscopes are equipped with energy-dispersive X-ray spectroscopy and can inform about the elemental composition. Some researchers also use microscopy to get information about the state of agglomeration; however, due to the drying process, the particles may contract, which results in an artifact [53]. Sound results for size measurements are time-consuming, because a sufficient number of particles per frame are required for statistical analysis. Furthermore, attention needs to be paid to the true identity of nanoparticles in a TEM sample. This is especially demanding, if nanoparticles are observed inside cells using TEM [54].

1.7.2 Size- dispersive state

To measure the hydrodynamic size, light scattering methods are used, where the most common is dynamic light scattering (DLS) or in more diluted form static light scattering. DLS measures the fluctuations of the scattering intensity in a time dependent manner. These scattering patterns is obtained by the Brownian motion. Usually, the diameter given by DLS is bigger than the one measured with for example TEM. DLS also measures agglomeration in different solvents, or at various salt concentrations, and biological fluids [55]. The main drawback of DLS is that the data is normally intensity-weighted. This means, that bigger particles scatter more light which results in a stronger signal (10^6), so that few bigger particles in the suspension skew the results towards bigger diameters. In this case, the volume distribution could be used, which does still overestimate the bigger particles, but only by 10^3 . It should always be noted if the size is measured by intensity distribution or by volume distribution. The size distribution is given by the polydispersity index (PDI) in DLS. The higher this number, the more polydisperse is a suspension. Newer techniques include nanoparticle tracking and analysis, and field flow fractionation with induced couple plasma mass spectrometry (ICP-MS).

1.7.3 Surface measurements

It is important to know the surface area of a nanoparticle because it represents the area that comes in contact either with proteins in the cell culture medium or the cell membrane. Also the inner, i.e. accessible pores may play a role in cytotoxicity, because they can guest solutes and nutrients from the cell culture medium [56]. The method of choice to measure the specific surface area is the nitrogen gas adsorption, since it measures simultaneously the specific surface area, the pore volume, and the pore size distribution. The adsorption and desorption of nitrogen molecules on the surface of particles is measured. When the layer of gas is formed, the desorption starts and the amount of desorbed nitrogen is measured upon vaporization. This method allows also to measure mesopores.

The forms of these mesopores can also differ, i.e. cylindrical tubes or hexagonal tubes. The method of choice to determine the pore ordering is X-ray diffraction (XRD). XRD is used to measure the

structure of a material with repeating structure elements at the angstrom level. Mesoporous material diffract in the low angle range and their arranging can be measured with small angle X-ray scattering.

The zeta potential gives information about the surface charge, although it is not directly the surface charge that is measured. When a particle is dispersed, ions in the dispersant will immediately adsorb firmly to the particle surface by electrostatic interaction or Van-der-Waals interactions. The type of interaction depends on both, the particle's surface and the solutes in the dispersant. This firm layer is the so-called Stern layer. The next layer consists of less strongly adsorbed ions. Together, these layers are termed electric double layer. When the particle is now moving, according to an applied electric field, this double layer is moving along with it. The border between this layer and the surrounding dispersant is called shear plane. The potential at the surface of the shear plane is the zeta potential.

The main application of the zeta potential is an indication for colloidal stability via electrostatic repulsion. The larger the value is, the more stable is the suspension. A value of ± 30 mV is generally considered as stable. The zeta potential is strongly depending on the surrounding medium. Higher salt concentrations are "neutralizing" the surface charges and may lower colloidal stability based on electrostatic repulsion. Furthermore, pH plays an important role. Hence, a zeta potential without its quoted pH and electrolyte concentration is meaningless.

1.7.4 Other parameters

The most common physico-chemical properties can be characterized by the methods described above. However, other characteristics like the elemental composition of a nanoparticle can be measured by different techniques with mass spectrometry (MS). In combination with TEM, energy-dispersive X-ray spectroscopy can measure the composition of the same probe as used for dry state size measurements.

For soluble nanoparticles, the rate of dissolution can be measured in either *in vitro* or in a model fluid, like the simulated body fluid [57]. Solubility can be determined by measuring the solubilized species in the supernatant of the particles, which is normally done by ICP-MS. Additionally, colorimetric products that complex the dissolved species can also give insight into the dissolution kinetics [58]. X-ray scattering and small angle x-ray scattering are used to determine the crystalline or amorphous structure of nanoparticles [1, 43].

1.8 *In vitro* systems and cell-based assays

1.8.1 Cell type

The underlying mechanism of cellular uptake is a key factor in understanding the biological fate of nanoparticles. The uptake route can impact the intracellular fate of a particle. Mostly, nanoparticles are endocytosed via the clathrin dependent uptake (for details see chapter 3.1). However, it is difficult to categorize uptake and intracellular fate according to the physico-chemical properties of a nanoparticle. Results in the literature are disparate, and the great variety of materials studied, the different cell lines used, and other factors hamper to draw an straight forward conclusion [18]. Since the uptake and subsequent adverse effects of nanoparticles can vary from cell line to cell line, one should consider including more than one cell line for nanotoxicological studies. Hence, it is suggested to use one phagocytic and one non-phagocytic cell line.

1.8.2 Dosimetry

The dose in nanotoxicological studies is most often expressed by mass per volume, i.e. $\mu\text{g}/\text{ml}$. Other metrics include mass per unit surface area of the culture dish ($\mu\text{g}/\text{cm}^2$), since it is more comparable. However, the dose administered is not necessarily the dose that reaches the cells. The particles that have reached the cells are not necessarily taken up by the cells, as depicted in Figure 1.4. This figure explains, that only fractions of the administered dose may reach the

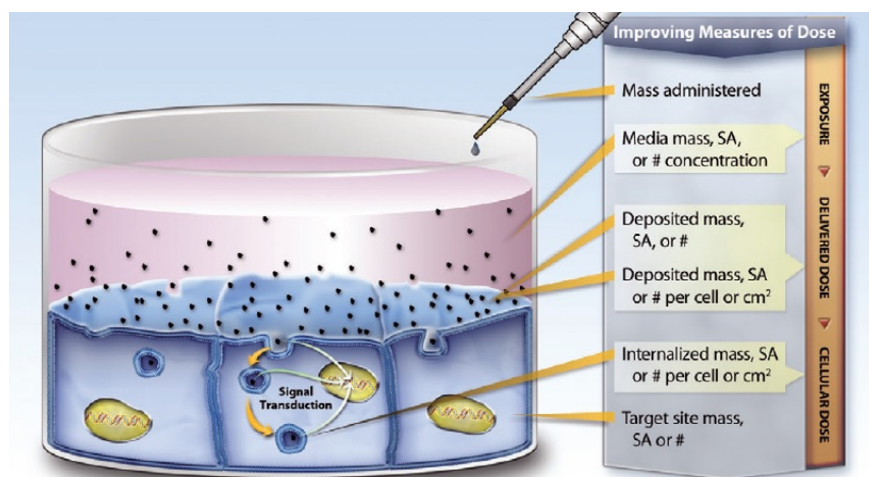


Figure 1.4: Dosimetry in *in vitro* systems. The mass administered may differ from the mass that is endocytosed by cells. From exposure to delivered dose to cellular dose, the mass administered is affected by medium volume, medium and particle density, and time. Figure reproduced from [59].

cells. Depending on the mass, the density of the medium, and the density of the nanoparticles, the number of particles reaching the cell surface may vary dramatically. Once in contact with

the cellular membrane, the surface groups determine the rate of uptake into the cell (with surface groups, hydrophilicity/hydrophobicity is included). Particles can agglomerate due to plasma proteins and are thus no longer available for uptake (for uptake into the cells, see review in section 3.1). Nevertheless, agglomerates can still interact with the cell surface and disturb the lipid bilayer. Teeguarden et al. thus suggested to first measure the portion of nanoparticles taken up by the cell, and, if not applicable, use their model to estimate how many of the administered particles will adsorb to the plasma membrane and be then internalized [59,60]. However, the majority of nanotoxicological studies are administering a dose as mass/volume. This dose can also easily be converted into other doses as particles exposed per cell surface, particles surface exposed per number of cells and others.

1.8.3 Viability

When cytotoxicity is measured, the most frequently investigated element is the viability [61]. The viability of cell is defined by its ability to live and to develop. There are several *in vitro* assays measuring cell viability, the most common ones use tetrazolium salts. These compounds are metabolically reduced to formazans, followed by a change in color. The product can be detected by UV/Vis spectroscopy.

A frequently used viability assay is the 3-(4,5-dimethylthiazol-2-yl)-2,5-diphenyltetrazolium bromide (MTT) [62]. This assay bases on the principle that a yellowish substrate is transformed by viable cells into water insoluble violet formazan crystals. This intracellular reaction is achieved by enzymes of the endoplasmatic reticulum. It uses reduced pyridine nucleotides like nicotinamide adenine dinucleotide (NADH) and nicotinamide adenine dinucleotide 2'-phosphate (NADPH), the latter to a smaller extent. Since the violet formazan crystals are water insoluble, an additional solution step is required prior to absorption measurement. Recently, newer variants of the MTT reagent have come to the market, where this dissolving step is not necessary anymore. However, they are reacting in the extracellular space and involve other mechanisms compared to the MTT [63].

Other viability assays include lactate dehydrogenase (LDH), an enzyme that is released into the cell culture medium upon membrane leakiness [64]. This assay measures necrosis. A possibility to distinguish the mechanism of cell death (apoptosis versus necrosis) is the annexin V/propidium iodide (PI) assay [65]. Annexin V is a protein that detects phosphatidyl serine (PS) on the membrane. PS in healthy cells is only present on the inner leaflet of the plasma membrane and therefore not accessible to annexin V [66]. In the presence of calcium, fluorescently labeled annexin V binds to PS and can be detected. The annexin A5 protein binds to apoptotic cells in a calcium-dependent manner using PS-containing membrane surfaces that are usually present only on the inner leaflet of the membrane. PI, a dye which intercalates with the DNA needs to be used in parallel. Due to

the necrotic process, the plasma membrane leaks and annexin V can bind to the PS in the inner leaflet, resulting in apoptosis. Hence, PI needs to be used in parallel, because it exclusively stains necrotic cells.

1.8.4 Oxidative stress

ROS include oxygen ions, superoxide anion, hydroxyl radicals, and peroxygens. They are present in the cell as side products of the aerobic metabolism [67]. However, the overproduction of ROS is directly linked with oxidative stress inside the cell. Above a certain threshold, the antioxidant defense of the cell cannot compete any longer, and the resulting imbalance induces oxidative damage in the cells [68].

Oxidative species are highly reactive due to the presence of an unpaired electron. A variety of oxidative species have different reactivity with the hydroxyl radical being the most reactive one, followed by the superoxide anion radical and hydrogen peroxide. These intermediates exist for different times, with hydrogen peroxide as a rather stable molecule compared to the other ones [69]. Among the most common oxidative stress assay is the dichloro-dihydro-fluorescein diacetate (DCFH-DA) assay. The non-polar DCFH-DA passively enters the cell where it first gets deacetylated by intracellular esterases to 2',7'-dichlorofluorescein (DCFH) and later on oxidized by reactive species to the fluorescent 2',7'-dichlorofluorescein (DCF). DCF can be measured spectroscopically [68]. However, the terms oxidative stress, ROS and reactive nitrogen species (RNS) are often not specified. Moreover, assays may claim to measure "total" ROS, but a majority of them is in fact not measuring the superoxide anion [68]. The proposed mechanism to cause adverse effects in presence of nanoparticles is oxidative stress [70–72].

1.8.5 Genotoxicity and inflammation

Inflammatory processes can be detected via enzyme-linked immunosorbent assays (ELISA). These markers are specifically detected in the supernatant of the cells by antibodies [73]. Among the most common markers tested with nanoparticles are the chemokine interleukin-8 (IL-8) followed by TNF- α , and IL-6 [74]. When testing nanoparticles with regard to their inflammatory potential, it is crucial to test, if the nanoparticles are endotoxin-free. Here, the *Limulus* amoebocyte lysate (LAL) test is frequently used to detect endotoxins [75]. An alternative for the LAL assay is the macrophage activation test [76].

Nanoparticles can enter the nucleus of a cell via pores or by penetrating the nucleus membrane. Hence, they can interact with the DNA and may exert adverse effects there. Genotoxicity of nanoparticles is frequently tested by the following assays: comet assay [77], the micronucleus assay, the chromosome aberrations test [78], and the bacterial reverse mutation assay (AMES) [74].

In the comet assay cells are embedded in agarose on a microscope slide. Then, they are treated with detergent and high salt to "isolate" the DNA. If DNA breaks are present, relaxed loops of the DNA are extending during electrophoresis. The resulting comet-tail can be visualized by fluorescence microscopy. The intensity of the tail is indicative for breaks in the DNA [74].

1.8.6 Hemolysis

Red blood cells (RBC) are important cells in our body since they deliver oxygen to organs and cells. RBC do not possess a nucleus when mature and also lack organelles resulting in more space to increase the capacity of oxygen transportation [79]. Hence, they also do not possess an endocytotic uptake machinery, which renders them attractive to study unspecific (i.e. non-energy dependent) uptake or membrane interaction. The majority of the plasma membrane (outer leaflet) of RBC consists of phosphatidylcholine, sphingomyelin, and cholesterol. Hemolysis is characterized as the rupture of RBC. Thereby, the erythrocytes release their contents to the surrounding fluid. The resulting loss of erythrocytes leads to anemia, which is associated with more serious blood conditions [80]. *In vitro* hemolysis is assessed by exposing erythrocytes to the nanoparticles. After an incubation time, undamaged cells are separated by centrifugation from the supernatant. Oxyhemoglobin present in the supernatant can be detected spectroscopically.

Chapter 2

Aim of the thesis

As described in the introduction, three main factors are important in nanotoxicology, as depicted in Figure 2.1. Chemistry, physico-chemical properties and biological systems are in constant interplay with each other in nanotoxicology. The titles in the dotted boxes below the three key points represent the publications in the corresponding section written during this thesis. Chem-

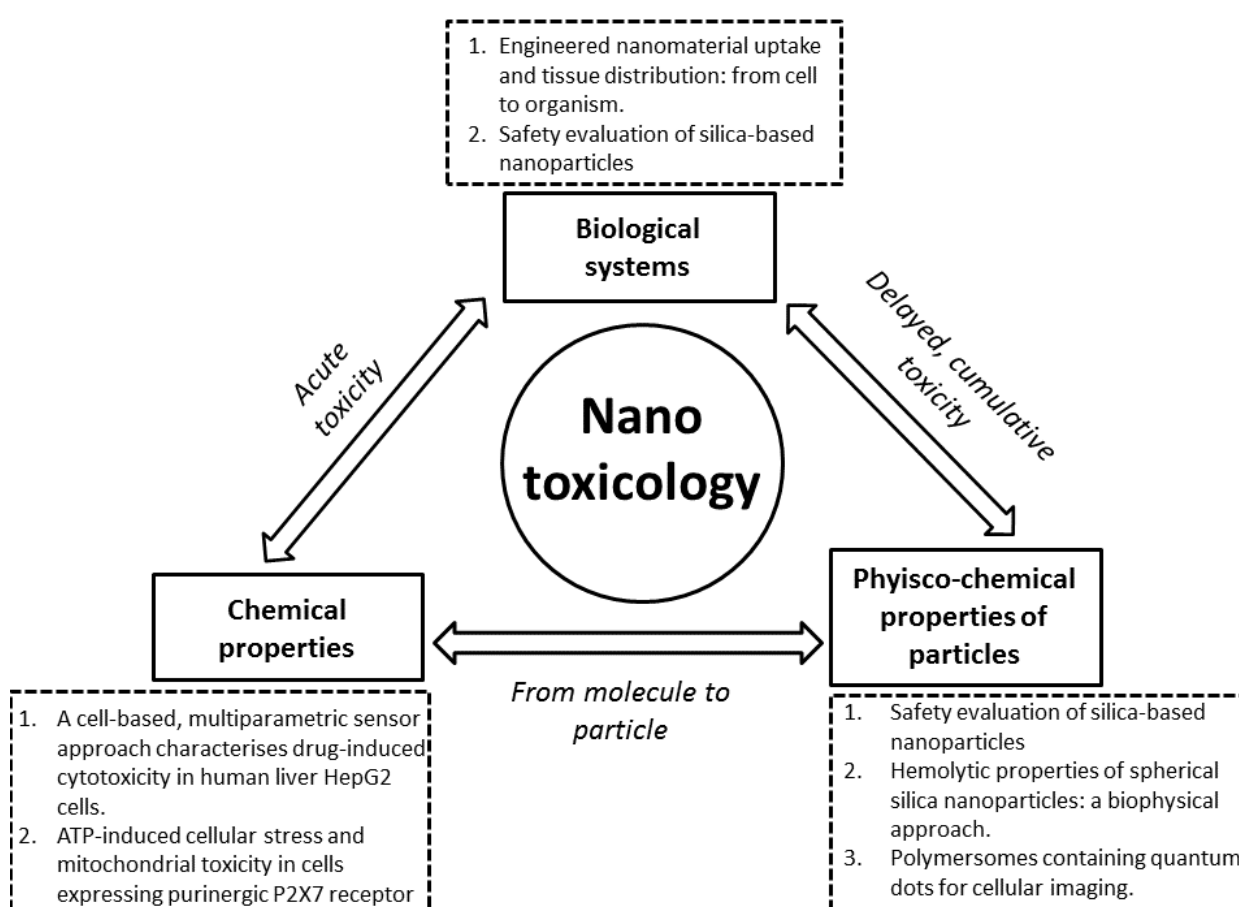


Figure 2.1: Pillars of nanotoxicology. Three main components were studied during this thesis, namely chemicals that mitigate acute toxicity and can be transformed into nanoparticles, which lead to a delayed and cumulative toxicity. Here, the physico-chemical properties were studied and connected to the interaction with biological systems. The dashed boxes name the publications in the respective fields.

ical properties are important if the particle solubility is high. As described earlier, released ions from nanoparticles can mitigate toxicity. In this thesis, the knowledge from nanotoxicology was transferred in joint-projects with small-molecules toxicologists. Physico-chemical properties of particles play the key role when studying the interaction of nanoparticles with the environment. In one publication, the physico-chemical properties were connected with the outcome of three cytotoxicity assays. The hemolytic potential of some SNPs were investigated in more depth and drafted as a manuscript. In a third publication, a new DDS was tested with respect to its cytotoxicity.

The chosen biological system plays a key role in nanotoxicology. Different cell lines are capable of taking up nanoparticles via various uptake mechanisms. Depending on the cell line, the extent of uptake is also connected to size and surface charge. A review was written and addressed the questions of nanoparticulate uptake into the cell and *in vivo* biodistribution. The arrows in Figure 2.1 show the connection between the three pillars.

Up to date, nanotoxicological studies suffer from proper material characterization, essential interference controls for common cytotoxicity assays, and mechanistic approaches to explain the mode of toxicity. This thesis hence addresses the following points:

- *Synthesis of silica nanoparticles.* The in-house synthesis has the main advantage that all chemicals used during the synthesis are known and their removal can be monitored. The surfactant was removed by extraction in order to maintain the silanols on the surface. The SNPs were further modified to create different sizes (80 nm and 250 nm), specific surface areas (<100 m²/g and >1000 m²/g), and different surface charges (negatively charged, neutrally charged, and positively charged). Throughout this thesis, co-condensation was employed to alter the surface of the SNPs.
- *Physico-chemical characterization.* The synthesized SNPs were characterized regarding their size, specific surface area, porosity, surface charge, and residues from the synthesis. The colloidal stability and redispersibility were studied in different biological relevant media.
- *Cell-based assays.* The SNPs were tested regarding their viability and oxidative stress. Nanoparticles can interfere with cytotoxicity assays in three different ways. For each assay, these interferences were tested carefully to avoid over- or underestimation of the results. Both tests were performed in a phagocytic cell line and a non-phagocytic cell line to reflect cell-specific differences. Furthermore, the hemolytic potential of the SNPs was assessed.
- *Mechanistic approach.* With different biophysical methods such as isothermal titration calorimetry (ITC) or solid state nuclear magnetic resonance, the underlying mechanism of hemolytic

SNPs was investigated in depth.

- *Transferring knowledge.* Knowledge gained from cell-based assays with nanoparticles was used to further test safety of small molecules in different projects.

Chapter 3

Published and submitted results

3.1 Engineered nanomaterial uptake and disposition

Engineered nanomaterial uptake and tissue distribution: from cell to organism

Helene Kettiger¹, Angela Schipanski², Peter Wick², Jörg Huwyler¹

¹ Department of Pharmaceutical Sciences, University of Basel, Switzerland

² Empa Swiss Federal Laboratory for Materials Science and Technology, Laborarotry for Materials-Biologiccy Interaction, St. Gallen, Switzerland.

Contribution H.Kettiger: author of review

International Journal of Nanomedicine 2013;8:3255-3269.

Engineered nanomaterial uptake and tissue distribution: from cell to organism

Helene Kettiger^{1,*}
Angela Schipanski^{2,*}
Peter Wick²
Jörg Huwyler¹

¹Department of Pharmaceutical Sciences, Division of Pharmaceutical Technology, University of Basel, Basel, Switzerland; ²Empa, Swiss Federal Laboratories for Materials Science and Technology, Laboratory for Materials-Biology Interactions, St Gallen, Switzerland

*These authors contributed equally to this work

Abstract: Improved understanding of interactions between nanoparticles and biological systems is needed to develop safety standards and to design new generations of nanomaterials. This article reviews the molecular mechanisms of cellular uptake of engineered nanoparticles, their intracellular fate, and their distribution within an organism. We have reviewed the available literature on the uptake and disposition of engineered nanoparticles. Special emphasis was placed on the analysis of experimental systems and their limitations with respect to their usefulness to predict the in vivo situation. The available literature confirms the need to study particle characteristics in an environment that simulates the situation encountered in biological systems. Phenomena such as protein binding and opsonization are of prime importance since they may have a strong impact on cellular internalization, biodistribution, and immunogenicity of nanoparticles in vitro and in vivo. Extrapolation from in vitro results to the in vivo situation in the whole organism remains a challenge. However, improved understanding of physicochemical properties of engineered nanoparticles and their influence on biological systems facilitates the design of nanomaterials that are safe, well tolerated, and suitable for diagnostic or therapeutic use in humans.

Keywords: biodistribution, cellular transport, cellular uptake, endocytosis, engineered nanomaterials, nanosafety

Introduction

Engineered nanomaterials (ENMs) are defined as materials composed of particles in an unbound state, or as an aggregate or agglomerate with one or more external dimensions in the size range from 1 nm to 100 nm.¹ Since active cellular uptake and tissue translocation of ENMs have been described for particles larger than 100 nm,^{2,3} we included literature reports on ENMs up to a size of 300 nm. There are many examples of clinical uses of ENMs. The majority of ENMs used as therapeutics on the market and in late clinical studies have diameters above 100 nm.⁴ Small particles with a size of less than 2 nm show passive uptake into erythrocytes.²⁷ However, uptake mechanisms of such very small particles will not be discussed in this review. Due to their small size, ENMs have unique properties (ie, optical, thermal, catalytic, and biological) compared to larger particles.^{5,6} During the last two decades, ENMs with tailored physicochemical properties have emerged in different fields of our daily life. They are used for a variety of applications, such as color pigments, solar cells, and waste water treatment. Furthermore, ENMs are found in consumer products that may be in contact with the human organism, eg, food packaging, shampoos, sunscreens, and toothpastes. Thus, regulatory agencies are faced with new materials for which no

Correspondence: Jörg Huwyler
Department of Pharmaceutical Sciences,
Division of Pharmaceutical Technology,
University of Basel, Klingelbergstrasse 50,
4056 Basel, Switzerland
Tel +41 61 267 1513
Fax +41 61 267 1516
Email joerg.huwyler@unibas.ch

submit your manuscript | www.dovepress.com

Dovepress

<http://dx.doi.org/10.2147/IJN.S49770>

International Journal of Nanomedicine 2013:8 3255–3269

3255



© 2013 Kettiger et al. This work is published by Dove Medical Press Ltd, and licensed under Creative Commons Attribution – Non Commercial (unported, v3.0) License. The full terms of the License are available at <http://creativecommons.org/licenses/by-nc/3.0/>. Non-commercial uses of the work are permitted without any further permission from Dove Medical Press Ltd, provided the work is properly attributed. Permissions beyond the scope of the License are administered by Dove Medical Press Ltd. Information on how to request permission may be found at: <http://www.dovepress.com/permissions.php>

3.1. ENGINEERED NANOMATERIAL UPTAKE AND DISPOSITION

nano-specific safety standards have been established. Moreover, products containing ENMs are often not declared since formal requirements are lacking.⁵ The ingredients of ENMs tend to be listed as chemicals or micronized substances, and information about the ENMs' content in the product may be missing. Little is known on how ENMs interact with the environment, including animals and human beings.⁷ When used in a physiological environment, ENMs are faced with biological fluids, phospholipid membranes, clearing mechanisms, and harsh intracellular conditions. Due to their distinct physicochemical properties, ENMs interact in a different way with living cells as compared to dissolved molecules. It is a challenge to predict the mechanism of uptake in relation to one specific physicochemical property. Figure 1 highlights the differences between ENMs and small molecules with regard to their physical and chemical properties, cellular uptake mechanisms, intracellular fate, and toxic effects.

Small molecules are defined as compounds with a molecular weight of less than 1,000 Da. It is generally believed that lipophilic molecules below this threshold are able to penetrate cell membranes by passive diffusion. They have the potential to be taken up actively as well as passively

by cells and to overcome cellular barriers within the body including the blood–brain barrier.^{8,9} In contrast, ENMs and macromolecules are mostly unable to diffuse passively into a living cell. They are colloiddally dispersed and therefore require an active transport process for their uptake by target cells.^{10,11} Furthermore, ENMs are characterized by a high surface area to volume ratio as well as different geometries and surface characteristics. Particles of the same material can differ in shape, size, and porosity; whereas a molecule is a well-defined system.¹² The state of dispersion and the variable size and shape of ENMs induces different uptake mechanisms for the same material.

The present review focuses on interactions of ENMs with biological systems on a cellular level (ie, mechanisms of cellular uptake and intracellular accumulation) and on the level of the whole organism (ie, circulation, distribution, and elimination). These interactions are a function of the intrinsic physicochemical properties of ENMs. An additional factor is protein binding. Protein adsorption onto the surface of an ENM leads to the formation of a protein corona and changes properties such as size or surface charge dramatically.^{13–15} We reviewed published experimental procedures since the

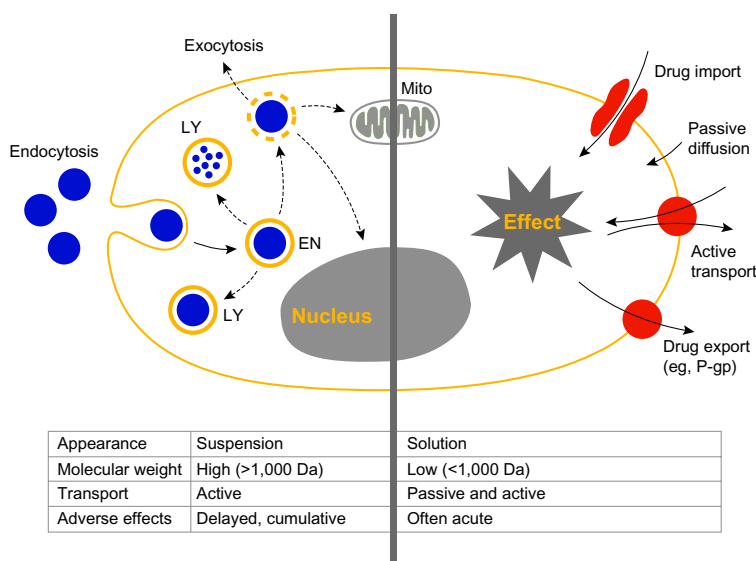


Figure 1 Interactions of cells with small molecules and nanoparticles.

Notes: Schematic representation of a eukaryotic cell and its interaction with nanoparticles (left part of picture) and small molecules (right part of picture). Interactions with nanoparticles are preceded by active cellular uptake leading to intracellular accumulation. Acute effects induced by small molecules are a consequence of both active and passive cell membrane permeation. Endocytosis leads to uptake of particles into endosomes (EN) and lysosomes (LY), followed by lysosomal degradation. Endosomal escape may lead to accumulation of particles in the cytoplasm or within mitochondria (Mito).

Abbreviations: EN, endosomes; LY, lysosomes; Mito, mitochondria; P-gp, P-glycoprotein.

handling of ENMs is often a challenge, leading to statistical variability and artifacts.

General considerations

The state of dispersion of ENMs depends on their surface properties and the medium composition. Uptake studies should be performed with nonagglomerated ENMs. Agglomeration occurs by material interaction (ie, association of ENMs into clusters) or material-protein interaction. The resulting agglomerates sediment according to Stoke's law. The rate of agglomeration should be studied prior to in vitro uptake studies in the correspondent medium, for example, with dynamic light scattering (DLS). However, when complex biological media are involved (as in vivo), DLS is unsuited for studying agglomeration kinetics since blood components may interfere, fluorescence single particle-tracking (fSPT) may be an alternative method to be used under these conditions.¹⁶

Since the majority of ENM uptake studies use fluorescence as a tracking signal, it is crucial to minimize dye leakage from the ENM.¹⁰ Approaches to test dye leakage are centrifugation, sodiumdodecyl sulfate polyacrylamide gel electrophoresis (PAGE), or fluorescence correlation spectroscopy (FCS).¹⁷⁻¹⁹ Special care should be taken when choosing an appropriate dye since lipophilic dyes may partition from the particulate structure into the lipid membranes of the cell. To circumvent dye leakage, intrinsic fluorescence of nanoparticles is an attractive alternative, as has been described for gold.^{20,21}

To study the entry route of a specific ENM, physical and pharmacological blockers may be used. All methods used to induce a physical or pharmacological block of uptake pathways have certain limitations. Most pharmacological inhibitors are not specific and may influence alternative internalization routes and the actin cytoskeleton.²² Pharmacological inhibitors interfere with vital cell functions and are therefore intrinsically toxic. Experiments have to be designed to prevent toxic effects, such as the complete disruption of all actin-dependent processes by actin-interfering agents. Moreover, compensatory routes of uptake may be activated in target cells upon inhibition of specific transport pathways. Finally, it should be taken into account that different cell lines have different uptake strategies. This impedes extrapolation of experimental results from one cell line to another. A recent review by Iversen et al summarizes the pharmacological blocking strategies and highlights the pitfalls of these reagents.²³ It should be mentioned that

genetically modified cells offer an interesting alternative to pharmacological intervention.²⁴

The influence of plasma protein binding on opsonization

The properties of ENMs have the potential to modulate biological interactions between particles and target cells by different molecular mechanisms.^{6,25} Adsorption of biomolecules to surfaces influences the interactions at the nano-bio interface.²⁶⁻²⁸ In this way, bound proteins and biomolecules form a dynamic protein corona shaping the biological identity of the ENM. The composition of the protein corona varies over time due to continuous protein association and dissociation.^{29,30} Surface properties of ENMs will influence the composition of the protein corona. Hydrophobic ENMs easily adsorb proteins whereas hydrophilic ones are less prone to protein binding.³¹ Therefore, hydrophobic ENMs agglomerate readily and interact with other hydrophobic residues of proteins or peptides (eg, blood or membrane proteins), thus promoting internalization.³⁰ Equally, positively charged ENMs adsorb different sets of proteins on their surface than negatively charged ones, elucidating distinct cellular interactions.³² This influences the mode of cell entry, biodistribution, and biocompatibility of ENMs. Interestingly, ENMs with identical chemical composition but different size may attract different proteins, thereby giving rise to different biological identities.³³ An ENM in blood will have a different biological identity than the same ENM in body fluid and is therefore processed differently. The protein corona, in turn, modifies certain properties of the original ENM, such as surface charge and size. For example, highly positively charged nanoparticles with a positive zeta-potential may change their apparent charge to negative in cell-culture medium.³⁴ These factors should be carefully considered when using ENMs as drug delivery devices, as the targeting ability of functionalized ENMs may be shielded by adsorbed proteins.³⁵

Cellular uptake of nanoparticles

The phospholipid membrane of cells regulates the transport of molecules into the cells, thereby representing a universal barrier protecting fragile intracellular structures from extracellular materials (Figure 2). To enter the cell, polar or charged biomolecules, such as amino acids, nucleosides, or glucose, require active transport systems involving proteins or ion channels. Many macromolecules are actively taken up by cells via endocytosis, which is a vesicular transport mechanism.^{36,37} Because ENMs may exist in the size range

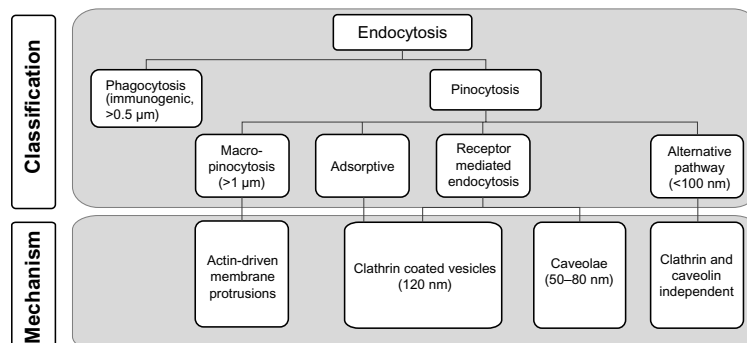


Figure 2 Known pathways of cellular uptake of nanoparticles.

Notes: Uptake of nanoparticles by eukaryotic cells is an active process. Endocytotic pathways include phagocytosis, and pinocytosis.

of proteins, eg, the hydrodynamic radius of an IgG antibody is close to 5 nm,³⁸ they are able to interact with the cellular machinery in a similar way to macromolecules.^{10,25,26} Experimental studies revealed that most ENMs are actively incorporated into the cell via different endocytic pathways (Figure 2) comprising phagocytosis (“cell-eating”) and pinocytosis (“cell-drinking”). The latter pathway can be divided into clathrin-mediated endocytosis (CME), caveolae-mediated endocytosis (CvME), and alternative routes.^{39,40} The resulting transport vesicles differ with respect to the composition of the protein coat of the engulfed vesicle, size of the detached vesicle, and fate of the ingested cargo. ENMs have the potential to access cells by all entry portals depending on their size, shape, chemical composition, and surface modification. As stated above, it remains a challenge to correlate a given ENM property with an uptake route. In the following, we discuss the main cellular entry routes (ie, phagocytosis and pinocytosis) to establish a tentative link between nanoscale characteristics of ENMs and specific mechanisms of cellular uptake.

Phagocytosis

Phagocytosis is performed predominantly by specialized cells of the immune system (ie, macrophages, monocytes, neutrophils, and dendritic cells), to remove particles larger than 500 nm from the organism, mainly through the mode of a receptor-mediated process (Figure 2).^{41,42} Particles are recognized by small proteins (opsonins) including immunoglobulins type G or M, complement fragments (C3, C5), or blood serum proteins such as fibronectin and laminin.⁴³ This process promotes the specific binding of protein-coated particles to internalizing receptors on the cell plasma

membrane, ie, Fc receptors of the immunoglobulin superfamily or complement receptors.⁴¹ Other receptors involved in the uptake of ENMs are the mannose/fucose receptor^{44,45} as well as the scavenger receptor,⁴⁶ where the involvement of the latter one may depend on the cell line used. The receptor-ligand interaction triggers a signal cascade in the target cell resulting in actin assembly and formation of a cell surface extension that zippers around the particle, engulfing it in an intracellular vesicle with a diameter of approximately 0.5 to 1 μm.⁴² These vesicles, or phagosomes, mature by several fission and fusion events with late endosomes and lysosomes, resulting in the formation of phagolysosomes. Internalized particles are subsequently degraded, and the receptors are cycled back to the cell surface. The rate of these successive events depends greatly on the ingested particle and typically lasts from 30 minutes to several hours.⁴⁷ Although phagocytosis is generally thought to be involved in the uptake of larger particles, ie, particles sized >500 nm, recent reports document the phagocytic uptake of considerably smaller particles.^{48–50} The phagocytic uptake route seems to be rather unspecific since it depends on opsonization. ENMs taken up as agglomerate tend to be less easily degraded by the host as they can be detected in macrophages for several months, thus bearing a risk of long-term toxicity.^{51,52}

Pinocytosis

Small particles ranging from a few nanometers to several hundred nanometers are generally taken up by pinocytosis (ie, fluid-phase uptake) occurring in almost all cell types (Figure 2). There are four modes of pinocytosis, ie, macropinocytosis, adsorptive and receptor-mediated endocytosis, and alternative routes of uptake.³⁶ With macropinocytosis, large

amounts of external fluid are taken up nonspecifically. ENMs located near the plasma membrane are thereby coincidentally internalized. During adsorptive pinocytosis, ENMs interact in a nonspecific manner with generic complementary binding sites on the cell surface. In contrast to macropinocytosis and adsorptive pinocytosis, RME is highly specific since it depends on the interaction between a ligand (eg, insulin or transferrin) and its complementary receptor on the surface of a target cell. RME is mediated predominantly either via the clathrin pathway or the caveolin pathway, depending on the specific nanoparticle-receptor interaction.^{23,53} Thus, several distinct pinocytic entry portals exist, depending on the type of interaction with the plasma membrane, size of incorporated vesicles, and type of proteins involved, eg, clathrin, caveolin, or receptors.³⁶ Thereby, the size of endocytic vesicles of approximately 60 nm (caveolae) and 120 nm (clathrin-coated vesicles) imposes limitations with respect to the maximum size of ENMs entering these pathways. Different mechanisms of pinocytic uptake into cells are discussed in more detail below.

Macropinocytosis

During macropinocytosis, ENMs with a size of $>1 \mu\text{m}$ are taken up nonspecifically. This process is stimulated, for example, by growth factors interacting with receptor tyrosine kinases.⁵⁴ Activation of the signaling cascade results in the formation of actin-driven circular membrane protrusions that collapse onto the membrane and fuse with it. This generates uncoated endocytic vesicles with a size of $1 \mu\text{m}$. These macropinosomes are of irregular shape and are handled by the endosomal/lysosomal route.³⁶ Macropinocytosis contributes to the internalization of larger ENMs, albeit in a rather unspecific manner and often in conjunction with other entry mechanism.^{11,55} The capacity of this uptake pathway for ENMs is very high, suggesting a possibility for pharmaceutical delivery.⁵⁶

Clathrin-mediated endocytosis

CME is considered to be the “classical” and best characterized route of cellular entry.³⁷ In polarized cells such as endothelial or epithelial cells, transport is initialized at the apical membrane domain.^{36,57} ENMs with a size of 120–150 nm are internalized within clathrin-coated vesicles entering the endosomal/lysosomal trafficking route.^{58,59} The upper size limit reported for particles entering the cell via this pathway is 200 nm.⁵⁵ CME is either adsorptive¹⁴ or receptor-mediated.⁶⁰ Cationic particles or proteins bind nonspecifically to the negatively charged cell surface.^{61–63}

This triggers adsorptive CME. In contrast, the receptor-mediated process is highly selective and specific. Receptor ligands being internalized by this pathway include low-density lipoprotein (LDL), transferrin, growth factors, and insulin.¹⁴

Caveolin-mediated endocytosis

CvME is the most prominent clathrin-independent uptake mechanism. This pathway is most pronounced in endothelial cells on the basolateral side, where it is an important uptake route for ENMs.^{36,64} The caveola is a small, flask-like structure, with a diameter of about 50–80 nm that is coated with caveolin-1.⁶⁵ These vesicles invaginate with the help of dynamin from hydrophobic membrane domains, which are rich in cholesterol and glycosphingolipids.⁶⁶ Caveolae are stable plasma membrane-associated structures.^{67,68} However, they can be induced to bud off by interaction with pathogens such as SV40 virus,⁶⁹ cholera toxin subunit B, or Shiga toxin.⁷⁰ With respect to ENMs, small particles seem to be transported more efficiently. For example, uptake of nanoparticles of 20 and 40 nm in size was demonstrated to be 5–10 times faster than that of nanoparticles sized 100 nm.^{64,71} Larger particles ($>500 \text{ nm}$) appear to be taken up only in exceptional cases.⁵⁵ However, it is possible that ENM associating with the membrane may cover enough surface and colocalize by chance with certain markers like the caveolar marker. This does not mean that the uptake is actively dependent on caveolae.

The intracellular trafficking routes of caveolae are discussed controversially. While nonacidic, nondigestive pathways are favored, an additional link between caveolae and lysosomal routes for degradation cannot be excluded.^{65,70,72} In addition, the so-called caveosomes (previously supposed to represent a special type of caveolar endosome) were shown to be an artifact created by overexpression of caveolin or caveolin mutants.⁷³ Pathogens escape from normal degradation in lysosomes and are directly transported to the Golgi and/or endoplasmic reticulum.⁷⁴ Thus, pathogens and ENMs can bypass lysosomal degradation.⁷⁵

Alternative routes of uptake

More recently, several endocytic routes that do not fit into the categories described above have emerged. Many of them are clathrin- and caveolin-independent. These routes depend on specific regulation by proteins such as Ras homolog family member A, ADP-ribosylation factor 6, or the cell division control protein 42 homolog, Cdc42.^{37,68} Although these mechanisms are still poorly understood, available data

suggest that particles larger than 100 nm are internalized via these routes.⁶⁶

Characteristics of ENMs influencing cellular uptake

The size of ENMs is not the only criterion that predicts the mechanism of ENM uptake. Nonetheless, trends based on particle size exist and are summarized in Figure 2. Nanoparticles with a diameter of 50 nm are more efficiently internalized by cells than smaller (about 15–30 nm) or larger (about 70–240 nm) particles.^{58,76} Nanoparticles with a diameter of 30–50 nm efficiently recruit and interact with membrane receptors and are subsequently taken up by receptor-mediated endocytosis.⁷⁷

Besides size, ENM shape is an important factor. Spherical ENMs are taken up much faster and more efficiently than rod-shaped ENMs, presumably due to the longer membrane wrapping time required for the longer rod-shaped particles.^{78,79} This notion is supported by *in vivo* experiments in rodents, where intravenous (IV)-injected elongated polymer micelles (filomicelles) remained in the circulation 10 times longer than spherical ENMs.⁸⁰ However, controversial findings were obtained using different materials. For example, Gratton et al⁷¹ investigated hydrogel particle uptake into HeLa cells. The highest internalization rate was found for particles with an aspect ratio of three. ENMs seemed to use all internalization routes simultaneously.⁷² Recent findings suggest that silica rods with an aspect ratio of 2.1 to 2.5 are taken up to a higher extent into HeLa cells than their spherical counterparts. In addition, uptake of rods with higher aspect ratios was marginal.⁸¹ Tissue macrophages struggle to incorporate long and rigid fibers into phagosomes, thereby releasing harmful oxygen radicals and hydrolytic enzymes, causing chronic inflammation.⁸² Similarly, the needle-like structure of carbon nanotubes may penetrate biological membranes, inflicting mechanical damage. These controversial results suggest that additional factors promote cellular uptake besides ENM size and shape.

Surface functionalities (eg, surface charge and functional groups) mediate interactions between ENMs and the cell surface. Positively charged particles interact strongly with the slightly anionic plasma membrane. They are taken up more readily⁸³ or may disrupt plasma membrane integrity.⁸⁴ Positively charged ENMs are taken up via adsorptive mediated pinocytosis, whereas negatively charged ENMs use alternative uptake routes.⁸⁵ Nonionic particles tend not to interact with the cell membrane, as demonstrated for the polymer polyethylene glycol (PEG).⁸⁶ Nanoparticles can be

functionalized with a plethora of ligands such as antibodies, peptides, or sugars. Their density, spatial distribution, and molecular weight plays an important role in determining the fate of ENMs in biological systems.⁸⁷ In addition, the chain length of chemical linkers like PEG, which are used to attach ligands to the surface of nanoparticles, may affect delivery to target cells.⁸⁸

Finally, specific cell types may interact with identical ENMs differently.^{23,89} It has been shown, for example, that macropinocytosis or phagocytosis is absent in brain capillary endothelial cells.⁸ Red blood cells are known to be incapable of endocytosis. Furthermore, recent studies revealed an influence of the cell cycle phase on the cell's capacity to take up ENMs.⁹⁰

Intracellular fate and endosomal escape

Once ENMs have been taken up by target cells, they are directed to the endosomal/lysosomal pathway in most instances. The intracellular vesicles either gradually mature (acidify) to late endosomes through multiple fission and fusion events, or they are recycled back to the cellular surface as trafficking endosomes (Figure 1).⁹¹ ENMs entrapped in late endosomes are likely to proceed to lysosomes where they are degraded. These compartments harbor proteases, hydrolases, and other enzymes promoting ENM degradation.⁹² However, some ENMs (in particular positively charged, basic nanoparticles) are capable of escaping the endosome. This phenomenon has previously been described as the “proton sponge effect”.^{25,93} Osmotic swelling of the organelles leads to their rupture, as shown in the case of polyethylene imine.^{93,94} To implement drug delivery strategies, endosomal/lysosomal escape can be induced actively. pH-sensitive fusogenic liposomes, for example, contain synthetic sterols and phospholipids, which undergo phase transition upon protonation at low pH. This results in the conversion of the hexagonal to lamellar structure of the liposomal membrane, thus disrupting the endosomal/lysosomal membrane.^{95–97} Similar effects can be induced using pH-sensitive fusogenic peptides (eg, amphiphilic peptides with repetitive GALA sequences) in combination with cationic liposomes.⁹⁸ Other ENMs (eg, certain types of carbon nanotubes) penetrate the vesicle (or cell) membrane directly and enter the cytosol.⁹⁹ Once in the cytosol, ENMs may induce the production of reactive oxygen species and inflict oxidative stress.¹⁰⁰ In addition, potentially toxic interactions with other cellular organelles, such as mitochondria and the cell nucleus, may occur.² Effects that may be harmful for a healthy cell are

desired in tumor cells, where an endosomal escape is needed to deliver a specific nanoparticulate drug to its intracellular compartment of action.

Methods to determine nanoparticle uptake

Widely used methods to study cellular uptake of ENMs are flow cytometry and microscopy. While flow cytometry allows for an efficient, fast, and quantitative assessment of particle uptake, microscopy provides qualitative insight into the subcellular localization of particles by analyzing small sample volumes. Flow cytometry as a quantitative approach to measure uptake cannot distinguish between externally attached and fully internalized ENM. Interaction with the cell surface can be studied experimentally if cellular uptake is inhibited. For example, endocytotic pathways can be blocked using pharmacological inhibitors.^{22,101} Alternatively, cells can be incubated at lowered temperatures to interrupt endocytic processing of particles. Temperatures around 20°C prevent progression of particles from early to late endosomes.¹⁰² Further temperature lowering to 4°C, for example, blocks all energy-dependent processes.¹⁰³ Consequently, signals from fluorescent ENMs located at the surface of cells or within specific intracellular vesicles or organelles can, for example, be detected quantitatively by flow cytometry or qualitatively by confocal scanning laser microscopy.^{104,105} Intracellular localization of particles can be further confirmed using the quenching agent, trypan blue. This dye quenches signals from fluorescent dyes such as fluorescein isothiocyanate. Since trypan blue does not penetrate the membrane, only extracellular signals of free or surface-bound dye molecules are quenched.¹⁰⁶

Another quantitative approach is induced coupled plasma mass spectroscopy (ICP-MS). ICP-MS is a powerful tool for intracellular quantification of electron-dense materials and is a sensitive (ie, nanogram range) method for detecting elements with the exception of H, C, O, N, F, S, and inert gases. Due to this limitation, “soft” nanoparticles, such as liposomes, polymers, or dendrimers, are not detected. Additionally, ICP-MS is not able to distinguish between dissolved ions and nanoparticles. However, loading nanoparticles with a heavy metal may make the use of ICP-MS possible in such cases, as long as the physicochemical properties of the particles are not changed by the loading procedure.¹⁰⁷

Alternatively, confocal microscopy provides information on the three-dimensional structure of objects. Fluorescence colocalization studies give insight into intracellular trafficking after fixation of cells or by live-cell imaging. The latter

technique relies on highly photostable fluorophores but avoids artifacts introduced by fixation reagents such as paraformaldehyde.¹⁰⁸ Subcellular fractionation can give additional insight into partitioning of ENMs inside the cell. Transmission electron microscopy is used to confirm subcellular particle localization with high resolution. This method allows quantitative assessments, but the procedure is time-consuming.^{109,110}

It is advisable to use transmission electron microscopy in combination with energy-dispersive X-ray spectroscopy (EDX) to confirm the presence of nanoparticles.¹¹¹ Brandenberger et al studied intracellular particle distribution using quantum dots as reference material.¹¹² In this study, EDX was used to confirm the identity of quantum dots based on X-ray emission spectra of the elements Cd and S. This method seems to be particularly useful for identifying very small (5–10 nm) particles.¹¹³

The biological fate of ENMs

In previous sections, we discussed interactions of ENMs with biological systems on a cellular level. This section focuses on *in vivo* kinetic properties of ENMs, addressing processes related to circulation, distribution, degradation, and excretion. There are different routes of administration including pulmonary,¹¹⁴ dermal,^{115,116} oral,^{117,118} and IV routes.¹¹⁹ However, this review will focus only on the IV route in healthy subjects. Figure 3 illustrates technical hurdles, challenges, and the different steps taken by ENMs before and during interaction with the living organism.

Circulation of ENMs

The state of dispersion in both the injected solution and the blood stream has to be defined, since agglomerates or precipitated material in the syringe may lead to dose variability (Figure 3A). Advanced pharmaceutical technologies are needed to stabilize nanosuspensions during storage and administration.¹²⁰ Size is an important parameter regarding circulation and distribution within the organism. In the blood stream, agglomerates may cause embolism with a potentially fatal outcome. Agglomerated particles have a tendency to accumulate after IV administration within the lung since venous blood is directed from the right heart ventricle to this organ. *In vivo* studies in the rat using polystyrene particles demonstrated passive accumulation in the lung for particles with a size exceeding a threshold of 10 μm.¹²¹ Thus, findings of lung targeting of ENMs may be indicative of “accidental” trapping of agglomerates.¹²² As mentioned above, phagocytosis of ENMs is an additional

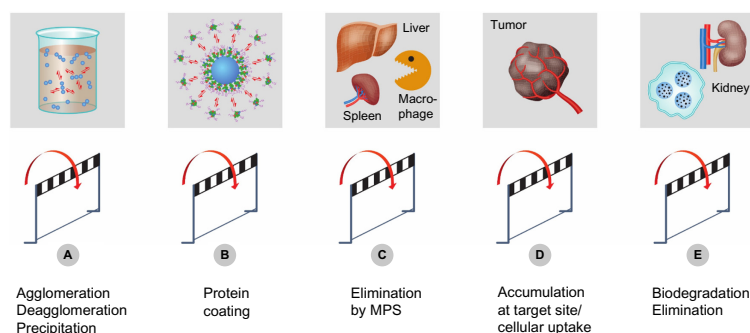


Figure 3 Experimental challenges and hurdles.

Notes: Specific physicochemical properties of ENMs may lead to technical challenges and artifacts in experimental systems. Particle agglomeration (A) reduces dosing accuracy or may lead to embolism after IV injection. Plasma-protein binding and opsonization of nanoparticles (B) may trigger a humoral immune response. Interaction of nanoparticles with cells of the MPS leads to accelerated plasma clearance (C). Accumulation of particles at a defined target site (D) might be impeded by their premature degradation and elimination (E).

Abbreviations: ENMs, engineered nanomaterials; IV, intravenous; MPS, mononuclear phagocytic system.

factor limiting prolonged circulation of particles bigger than $0.5\ \mu\text{m}$ (Figure 2). On the other hand, small ENMs ($<5\ \text{nm}$ to $10\ \text{nm}$) are cleared by kidney glomerular filtration.^{123,124}

Opsonization and immunologic responses

When injected into the blood stream, foreign materials encounter different blood constituents such as red blood cells, white blood cells, platelets, and a variety of proteins. ENMs are known to interact with both proteins²⁶ and cells.¹²⁵ Protein binding and opsonization are processes that change the surface properties of ENMs (Figure 3B). ENMs used for imaging or as a drug delivery system should be assessed with regard to their potential to cause hemolysis, thrombocyte aggregation, and complement activation.^{47,126} Hemolysis has been described for rigid materials such as silica nanoparticles¹²⁷ or for soft nanoparticles such as liposomes.¹²⁸ Due to protein binding, these measurements should be done in presence of plasma proteins.¹²⁹

Protein coating of an ENM is a highly dynamic process, starting immediately upon IV injection.¹³⁰ The resulting protein corona is complex and varies depending on the size,¹³ hydrophobicity/surface charge,³⁰ and shape¹³¹ of the particles. In the first instance, readily available proteins such as albumin are adsorbed onto the ENM surface, but may be replaced by other proteins (eg, lipoproteins or opsonins) over time, depending on the surface structure of the ENMs. Prediction of the extent of protein binding to ENM remains a challenge. Recent findings indicate that uncharged ENMs are opsonized more slowly than charged ENMs. The size of ENMs influences the binding of opsonins to spherical particles. Due to the higher curvature, smaller ENMs ($<20\ \text{nm}$) will attract

fewer opsonins than bigger ENMs ($>200\ \text{nm}$). This explains why agglomerates are cleared by the mononuclear phagocytic system (MPS) more easily. The same is true for hydrophobic ENMs.¹³² Recent studies revealed a strong shape dependency in relation with MPS recognition. Duan and Li¹³³ stated that an ellipsoidal ENM can be attacked by a macrophage in two different ways: when the macrophage attaches to the pointed end, the ENM will be internalized; however, when it attaches on the flat surface of the ellipsoid, it just spreads on the ENM and prolongs its circulation. This observation is in agreement with the findings of Arnida et al who found that gold nanorods were less recognized by the MPS compared to their spherical counterparts.¹³⁴

The question arises as to how ENMs can be designed to specifically adsorb certain proteins or avoid their adsorption. The best known strategy to diminish protein adsorption is by masking the particle surface with PEG. This hydrophilic, biocompatible, and nontoxic polymer is used to minimize interactions of macromolecules, eg, cytokines¹³⁵ and nanoparticles, ie, liposomal carriers¹⁰¹ with phagocytic cells of the immune system. The protective properties of PEG as a function of PEG chain length and PEG surface density were reviewed by Li and Huang.¹³⁶ Nevertheless, PEG is not able to fully prevent protein adsorption or opsonization. For example, for $5\ \text{nm}$ gold nanoparticles, the protective effect of PEG diminishes within hours.¹³⁷ In addition, PEG may elicit an immunological response resulting in an accelerated blood clearance of ENMs. It has been observed that repeatedly injected PEGylated liposomal formulations are markedly less efficacious, probably because of anti-PEG antibody formation.¹³⁸ As an alternative to PEGylation, ENMs can be

coated with amino acids such as lysine or cysteine. Such a mixed-charge monolayer-coating prevented protein adsorption in fetal bovine serum to 5 nm gold nanoparticles.¹³⁹ In summary, a hydrophilic coating (eg, PEG) and a neutral charge (expressed as the zeta potential in the correspondent medium) can minimize particle recognition by the immune system. Targeting strategies are often implemented using PEG-coated ENMs with surface ligands (such as folic acid, cell adhesion molecules, or transferrin⁴²) in order to enhance cellular uptake into target tissues and to avoid exposure of healthy cells. By this approach, it is crucial to maintain the stealth properties of the PEG, despite the bound ligands, to avoid interactions with cells of the immune system.¹⁰¹

Distribution

ENMs are distributed throughout the body via the blood stream and extravasate this transport system according to their size. Extravasation of ENMs is restricted to specific tissues since the presence of tight junctions prevents ENMs larger than 2 nm to leave the circulation.¹⁴⁰ The fenestrations of blood vessels vary from organ to organ and can have different ranges in different species.¹⁴⁰ Moreover, the state of disease is changing the fenestration size,¹⁴¹ with typical size for tumors ranging from 200–780 nm in mice.¹⁴² ENMs with sizes ranging from 150–300 nm are mainly found in the liver and spleen, whereas smaller counterparts extravasate into the bone marrow. ENMs are cleared from the circulation in different organs. As depicted in Figure 3C, they are often trapped in the liver and spleen as these organs host the largest concentration of tissue resident macrophages (ie, MPS cells such as hepatic Kupffer cells). Glomerular filtration eliminates ENMs with a hydrodynamic diameter of <5 nm to 10 nm. Nonetheless, the relationship between the physicochemical properties and pharmacokinetic behavior of ENMs is poorly understood. Interpretation of experimental data is difficult since a plethora of different materials, excipients, and animal species are used. However, trends were identified for selected materials such as gold nanoparticles of different sizes and surface characteristics.^{143,144} Increased liver accumulation was found for particles with a size of ≥ 5 nm as compared to particles with a size of 1.4 nm. Particle size-dependent accumulation was found in no other organ than the liver. However, elevated levels of charged (positive and negative) gold nanoparticles were found in the spleen. In another study, PEG-coated gold nanoparticles with a size of 20–80 nm were investigated.¹⁴⁵ The length of the PEG chains was 2,000–5,000 Da. PEGylated gold nanoparticles were not recognized by macrophages. The PEG-5,000 coated

gold particles with a size of 20 nm accumulated in solid tumors of experimental animals to an extent of 6.5% of the injected dose. Most of the remaining particles accumulated in other organs, mainly liver and spleen. Xie et al investigated the influence of the size of silica nanoparticles on their biodistribution.¹⁴⁶ After 30 days, they found silica particles trapped in the lungs, liver, and spleen and observed signs of liver injury. Compared to small silica particles (20 nm), larger particles (80 nm) were cleared faster from the body. A recent study investigated the difference in biodistribution of solid silica nanoparticles, mesoporous silica nanoparticles, and rod-shaped silica nanoparticles.¹⁴⁷ All particle types had a positively charged surface and showed extensive distribution to liver and spleen. Thus, most particles were recognized and eliminated by phagocytic macrophages. Porous particles with an aspect ratio of eight preferentially accumulated in the lung, whereas the nonporous particles were less prevalent in the lung. Amine modified silica nanoparticles reduced the affinity to lungs and kidneys. Silica nanoparticles were degraded and excreted via the hepatobiliary and renal routes. It has been reported that elongated fibers such as filomicelles⁸⁰ or gold nanorods¹³⁴ display a longer circulation time since they are able to align with the blood flow. Compared to their spherical counterparts, rods are less preferentially taken up by macrophages, which reduce accumulation in MPS organs like the liver and spleen. Furthermore, gold nanorods had a higher accumulation in tumor tissue compared to spherical gold nanoparticles.¹³⁴

ENMs can be designed in a way to promote or avoid interactions with specific tissues or organs. The topic of active drug targeting was recently reviewed by Moghimi et al.¹⁴⁸ With such targeting strategies, ENMs can be designed and used for diagnostic imaging purposes or to deliver drugs to diseased tissues such as solid tumors (Figure 3D). The passive accumulation in the tumor is due to the enhanced permeability and retention effect, which is present in some tumors and dictates the maximum size for ENMs to extravasate into tumor tissue. This phenomenon is discussed in more detail by Jain.¹⁴⁹

Degradation and excretion

The term “metabolism” as defined in classical pharmacokinetics is not suitable for ENMs. In this section, the term “degradation” will be used instead to collectively cover multiple processes such as erosion, deagglomeration, disintegration, dissolution, or chemical degradation of particles. Available excretion and degradation studies solely included single administration of ENMs at a certain concentration.

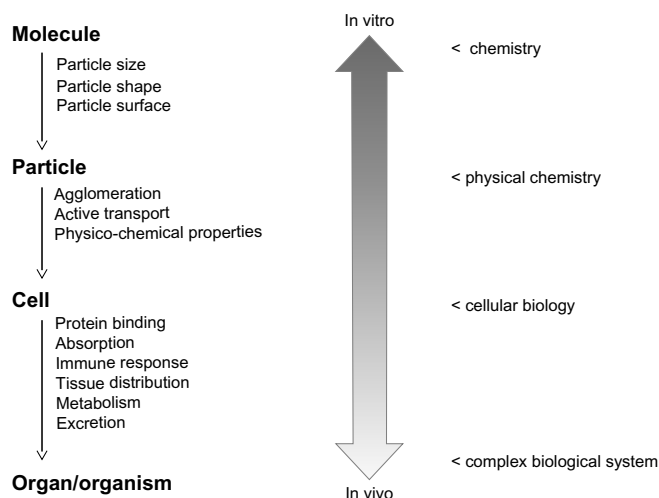


Figure 4 Extrapolation from in vitro data to the in vivo situation.

Notes: In vitro experimental systems can be used to characterize nanoparticles with respect to their chemical composition and physicochemical properties. Cell-culture-based experimental systems can be used to study molecular mechanisms of cellular uptake and intracellular processing of particles. However, additional information is needed to address questions related to the in vivo behavior of nanomaterials and their interaction with complex biological systems. In particular, the prediction of pharmacokinetic parameters remains a challenge.

Accumulation effects after multiple dosing and bioaccumulation have only been studied in zebra fish.¹⁵⁰ Chemical reactivity and composition of the shell and core materials play an important role in degradation. ENMs known to “safely” degrade are porous silica nanoparticles²⁰ and iron oxide particles.¹⁵¹ Degradation of silica nanoparticles leads to the formation of silicic acid, which is excreted via feces and urine.¹⁵² Due to the high specific surface area of the mesoporous material, hydrolysis of the silica network is a fast process.¹⁵³ Metal oxides including iron oxides are transformed by metallothionein that is abundantly expressed in liver and kidney.¹⁵⁴ Levy et al used two different methods to trace biodegradation of super paramagnetic iron oxide nanoparticles (SPIONs).¹⁵⁵ Upon degradation, these iron species lose their paramagnetic behavior and are transformed to ferritin. Thus, intact particles can be identified and traced due to their magnetic properties. However, degradation is a slow process. After two months, paramagnetic iron was still present in macrophages. Over prolonged time, the storage form of iron (ie, nonparamagnetic species) was more prevalent. The authors hypothesized that degradation of SPIONs took place in the acidic lysosomal compartment. It remains to be elucidated if these mechanisms of degradation might apply to other nanomaterials including other metal oxide materials with poor solubility. ENMs, like polymeric particles, have been shown to

degrade by hydrolysis or enzymatic digestion in vitro.¹⁵⁶ Similar effects were observed in vivo.¹⁵⁷

Materials with poor solubility may remain in the organism over several weeks to months. When considering the use of a specific ENM as a drug delivery tool, its biodegradation and excretion pathways have to be known. Upon multiple dosing, ENMs may accumulate in MPS organs and cause severe damage. For example, Ye et al have studied long-term effects of quantum dots containing Cd-Se in rhesus monkeys.¹⁵⁸ In vivo, acute toxicity of these nanoparticles was very low. However, chemical analysis after 90 days revealed that more than 90% of the injected Cd dose remained in the animals’ organs. In view of the limited availability of data, much more work needs to be done in the field of nanosafety.

Conclusion

ENMs have emerged in different fields of our daily life. However, their interaction with biological systems and their biological fate remain incompletely understood. It is therefore important to elucidate molecular mechanisms involved in cellular binding, uptake, and processing of ENMs. This knowledge is needed to design novel pharmaceutical applications for ENMs such as, for example, drug delivery and drug targeting strategies. By the same token, optimized ENM design may help to avoid unwanted interactions and toxicity, thereby making human use of novel materials possible.

The interaction of ENMs with complex biological systems, such as the human body, is still poorly understood. In vitro characterization of ENMs may help to obtain a mechanistic insight into their behavior in a biological environment (Figure 4). This includes information on chemical properties and reactivity as well as particle dynamics in biological fluids. Studies have shown that protein binding may alter the properties of ENM surfaces influencing cellular binding and uptake. Interactions with the immune system depend on ENM size, geometry, and surface charge. However, this information cannot be easily extrapolated to any given cell line or even to another ENM with the same surface properties but different core materials. We propose to combine in vitro systems with ex vivo models such as lung models,¹⁵⁹ cell coculture systems, chicken egg models harboring xenografted tumors,⁵⁰ and placenta models.³ These tools will be instrumental when designing nanomaterials with favorable pharmacokinetic properties and low intrinsic toxicity.¹⁶⁰ In any case, ENMs should be designed to be biocompatible and biodegradable to prevent their accumulation in the human body and limit their long-term toxic effects upon chronic exposure. Combining this knowledge about ENMs with smart drug delivery and drug targeting strategies will lead to innovative diagnostic and therapeutic applications.

Acknowledgments

The present work was supported by grants from the “Freie Akademische Gesellschaft (FAG) Basel” and the Swiss Centre for Applied Human Toxicology (SCAHT). We thank Dr Silvia Rogers for editorial assistance.

Disclosure

The authors report no conflicts of interest in this work.

References

- Bleeker EA, de Jong WH, Geertsma RE, et al. Considerations on the EU definition of a nanomaterial: science to support policy making. *Regul Toxicol Pharmacol*. 2013;65(1):119–125.
- Rothén-Rutishauser B, Mühlfeld C, Blank F, Musso C, Gehr P. Translocation of particles and inflammatory responses after exposure to fine particles and nanoparticles in an epithelial airway model. *Part Fibre Toxicol*. 2007;4:9.
- Wick P, Malek A, Manser P, et al. Barrier capacity of human placenta for nanosized materials. *Environ Health Perspect*. 2010;118(3):432–436.
- Chang HI, Yeh M-K. Clinical development of liposome-based drugs: formulation, characterization, and therapeutic efficacy. *Int J Nanomedicine*. 2012;7:49–60.
- Kessler R. Engineered nanoparticles in consumer products: understanding a new ingredient. *Environ Health Perspect*. 2011;119(3):a120–a125.
- Oberdörster G, Maynard A, Donaldson K, et al. Principles for characterizing the potential human health effects from exposure to nanomaterials: elements of a screening strategy. *Part Fibre Toxicol*. 2005;2:8.
- Som C, Wick P, Krug H, Nowack B. Environmental and health effects of nanomaterials in nanotextiles and façade coatings. *Environ Int*. 2011;37(6):1131–1142.
- Pardridge WM. Transport of small molecules through the blood-brain barrier: biology and methodology. *Adv Drug Deliv Rev*. 1995;15(1–3):5–36.
- Pardridge WM. Drug transport across the blood-brain barrier. *J Cereb Blood Flow Metab*. 2012;32(11):1959–1972.
- Salvati A, Aberg C, dos Santos T, et al. Experimental and theoretical comparison of intracellular import of polymeric nanoparticles and small molecules: toward models of uptake kinetics. *Nanomedicine*. 2011;7(6):818–826.
- Shapero K, Fenaroli F, Lynch I, Cottell DC, Salvati A, Dawson KA. Time and space resolved uptake study of silica nanoparticles by human cells. *Mol Biosyst*. 2011;7(2):371–378.
- Krug HF, Wick P. Nanotoxicology: an interdisciplinary challenge. *Angew Chem Int Ed Engl*. 2011;50(6):1260–1278.
- Jansch M, Stumpf P, Graf C, Rühl E, Müller RH. Adsorption kinetics of plasma proteins on ultrasmall superparamagnetic iron oxide (USPIO) nanoparticles. *Int J Pharm*. 2012;428(1–2):125–133.
- Lesniak A, Campbell A, Monopoli MP, Lynch I, Salvati A, Dawson KA. Serum heat inactivation affects protein corona composition and nanoparticle uptake. *Biomaterials*. 2010;31(36):9511–9518.
- Monopoli MP, Aberg C, Salvati A, Dawson KA. Biomolecular coronas provide the biological identity of nanosized materials. *Nat Nanotechnol*. 2012;7(12):779–786.
- Filipe V, Poole R, Kutscher M, Forier K, Braeckmans K, Jiskoot W. Fluorescence single particle tracking for the characterization of submicron protein aggregates in biological fluids and complex formulations. *Pharm Res*. 2011;28(5):1112–1120.
- Magde D, Elson E, Webb WW. Thermodynamic Fluctuations in a Reacting System – Measurement by Fluorescence Correlation Spectroscopy. *Phys Rev Lett*. 1972;29(11):705–708.
- Onaca O, Hughes DW, Balasubramanian V, Grzelakowski M, Meier W, Palivan CG. SOD antioxidant nanoreactors: influence of block copolymer composition on the nanoreactor efficiency. *Macromol Biosci*. 2010;10(5):531–538.
- Ow H, Larson DR, Srivastava M, Baird BA, Webb WW, Wiesner U. Bright and stable core-shell fluorescent silica nanoparticles. *Nano Lett*. 2004;5(1):113–117.
- He X, Nie H, Wang K, Tan W, Wu X, Zhang P. In vivo study of biodistribution and urinary excretion of surface-modified silica nanoparticles. *Anal Chem*. 2008;80(24):9597–9603.
- Lemelle A, Veksler B, Kozhevnikov IS, Akchurin GG, Piletsky SA, Meglinski I. Application of gold nanoparticles as contrast agents in confocal laser scanning microscopy. *Laser Phys Lett*. 2009;6(1):71–75.
- Ivanov AI. Pharmacological inhibition of endocytic pathways: is it specific enough to be useful? *Methods Mol Biol*. 2008;440:15–33.
- Iversen TG, Skotland T, Sandvig K. Endocytosis and intracellular transport of nanoparticles: Present knowledge and need for future studies. *Nano Today*. 2011;6(2):176–185.
- Smith PJ, Giroud M, Wiggins HL, et al. Cellular entry of nanoparticles via serum sensitive clathrin-mediated endocytosis, and plasma membrane permeabilization. *Int J Nanomedicine*. 2012;7:2045–2055.
- Nel AE, Mädler L, Velegol D, et al. Understanding biophysicochemical interactions at the nano-bio interface. *Nat Mater*. 2009;8(7):543–557.
- Aggarwal P, Hall JB, McLeland CB, Dobrovolskaia MA, McNeil SE. Nanoparticle interaction with plasma proteins as it relates to particle biodistribution, biocompatibility and therapeutic efficacy. *Adv Drug Deliv Rev*. 2009;61(6):428–437.
- Wang T, Bai J, Jiang X, Nienhaus GU. Cellular uptake of nanoparticles by membrane penetration: a study combining confocal microscopy with FTIR spectroelectrochemistry. *ACS Nano*. 2012;6(2):1251–1259.
- Prapainop K, Witter DP, Wentworth P Jr. A chemical approach for cell-specific targeting of nanomaterials: small-molecule-initiated misfolding of nanoparticle corona proteins. *J Am Chem Soc*. 2012;134(9):4100–4103.

3.1. ENGINEERED NANOMATERIAL UPTAKE AND DISPOSITION

29. Darabi Sahneh F, Scoglio C, Riviere J. Dynamics of nanoparticle-protein corona complex formation: analytical results from population balance equations. *PLoS ONE*. 2013;8(5):e64690.
30. Cedervall T, Lynch I, Lindman S, et al. Understanding the nanoparticle-protein corona using methods to quantify exchange rates and affinities of proteins for nanoparticles. *Proc Natl Acad Sci U S A*. 2007;104(7):2050–2055.
31. Esmaeili F, Ghahremani MH, Esmaeili B, Khoshayand MR, Atyabi F, Dinarvand R. PLGA nanoparticles of different surface properties: preparation and evaluation of their body distribution. *Int J Pharm*. 2008;349(1–2):249–255.
32. Fleischer CC, Payne CK. Nanoparticle surface charge mediates the cellular receptors used by protein-nanoparticle complexes. *J Phys Chem B*. 2012;116(30):8901–8907.
33. Zhang H, Burnum KE, Luna ML, et al. Quantitative proteomics analysis of adsorbed plasma proteins classifies nanoparticles with different surface properties and size. *Proteomics*. 2011;11(23):4569–4577.
34. Limbach LK, Wick P, Manser P, Grass RN, Bruinink A, Stark WJ. Exposure of engineered nanoparticles to human lung epithelial cells: influence of chemical composition and catalytic activity on oxidative stress. *Environ Sci Technol*. 2007;41(11):4158–4163.
35. Salvati A, Pitek AS, Monopoli MP, et al. Transferrin-functionalized nanoparticles lose their targeting capabilities when a biomolecule corona adsorbs on the surface. *Nat Nanotechnol*. 2013;8(2):137–143.
36. Conner SD, Schmid SL. Regulated portals of entry into the cell. *Nature*. 2003;422(6927):37–44.
37. Kumari S, Mg S, Mayor S. Endocytosis unplugged: multiple ways to enter the cell. *Cell Res*. 2010;20(3):256–275.
38. Jössang T, Feder J, Rosenqvist E. Photon correlation spectroscopy of human IgG. *J Protein Chem*. 1988;7(2):165–171.
39. Lühmann T, Rimann M, Bittermann AG, Hall H. Cellular uptake and intracellular pathways of PLL-g-PEG-DNA nanoparticles. *Bioconjug Chem*. 2008;19(9):1907–1916.
40. Mailänder V, Landfester K. Interaction of nanoparticles with cells. *Biomacromolecules*. 2009;10(9):2379–2400.
41. Aderem A, Underhill DM. Mechanisms of phagocytosis in macrophages. *Annu Rev Immunol*. 1999;17:593–623.
42. Hillaireau H, Couvreur P. Nanocarriers' entry into the cell: relevance to drug delivery. *Cell Mol Life Sci*. 2009;66(17):2873–2896.
43. Owens DE 3rd, Peppas NA. Opsonization, biodistribution, and pharmacokinetics of polymeric nanoparticles. *Int J Pharm*. 2006;307(1):93–102.
44. Irache JM, Salman HH, Gamazo C, Espuelas S. Mannose-targeted systems for the delivery of therapeutics. *Expert Opin Drug Deliv*. 2008;5(6):703–724.
45. Patel PC, Giljohann DA, Daniel WL, Zheng D, Prigodich AE, Mirkin CA. Scavenger receptors mediate cellular uptake of polyvalent oligonucleotide-functionalized gold nanoparticles. *Bioconjug Chem*. 2010;21(12):2250–2256.
46. Wang H, Wu L, Reinhard BM. Scavenger receptor mediated endocytosis of silver nanoparticles into J774A.1 macrophages is heterogeneous. *ACS Nano*. 2012;6(8):7122–7132.
47. Dobrovolskaia MA, McNeil SE. Immunological properties of engineered nanomaterials. *Nat Nanotechnol*. 2007;2(8):469–478.
48. França A, Aggarwal P, Barsov EV, Kozlov SV, Dobrovolskaia MA, González-Fernández Á. Macrophage scavenger receptor A mediates the uptake of gold colloids by macrophages in vitro. *Nanomedicine (Lond)*. 2011;6(7):1175–1188.
49. Krpetić Z, Porta F, Caneva E, Dal Santo V, Scari G. Phagocytosis of biocompatible gold nanoparticles. *Langmuir*. 2010;26(18):14799–14805.
50. Lunov O, Syrovets T, Loos C, et al. Differential uptake of functionalized polystyrene nanoparticles by human macrophages and a monocytic cell line. *ACS Nano*. 2011;5(3):1657–1669.
51. Wang X, Xia T, Ntim SA, et al. Dispersal state of multiwalled carbon nanotubes elicits profibrogenic cellular responses that correlate with fibrogenesis biomarkers and fibrosis in the murine lung. *ACS Nano*. 2011;5(12):9772–9787.
52. Zhu MT, Feng WY, Wang Y, et al. Particokinetics and extrapulmonary translocation of intratracheally instilled ferric oxide nanoparticles in rats and the potential health risk assessment. *Toxicol Sci*. 2009;107(2):342–351.
53. Vercauteren D, Rejman J, Martens TF, Demeester J, De Smedt SC, Braeckmans K. On the cellular processing of non-viral nanomedicines for nucleic acid delivery: mechanisms and methods. *J Control Release*. 2012;161(2):566–581.
54. Mercer J, Helenius A. Virus entry by macropinocytosis. *Nat Cell Biol*. 2009;11(5):510–520.
55. Rejman J, Oberle V, Zuhorn IS, Hoekstra D. Size-dependent internalization of particles via the pathways of clathrin- and caveolae-mediated endocytosis. *Biochem J*. 2004;377(Pt 1):159–169.
56. Rima W, Sancey L, Aloy M-T, et al. Internalization pathways into cancer cells of gadolinium-based radiosensitizing nanoparticles. *Biomaterials*. 2013;34(1):181–195.
57. Sandvig K, Pust S, Skotland T, van Deurs B. Clathrin-independent endocytosis: mechanisms and function. *Curr Opin Cell Biol*. 2011;23(4):413–420.
58. Chithrani BD, Ghazani AA, Chan WCW. Determining the size and shape dependence of gold nanoparticle uptake into mammalian cells. *Nano Lett*. 2006;6(4):662–668.
59. Harush-Frenkel O, Rozentur E, Benita S, Altschuler Y. Surface charge of nanoparticles determines their endocytic and transcytotic pathway in polarized MDCK cells. *Biomacromolecules*. 2008;9(2):435–443.
60. Bickel U, Yoshikawa T, Pardridge WM. Delivery of peptides and proteins through the blood-brain barrier. *Adv Drug Deliv Rev*. 2001;46(1–3):247–279.
61. Herve F, Ghinea N, Scherrmann J-M. CNS delivery via adsorptive transcytosis. *AAPS J*. 2008;10(3):455–472.
62. Predescu SA, Predescu DN, Malik AB. Molecular determinants of endothelial transcytosis and their role in endothelial permeability. *Am J Physiol Lung Cell Mol Physiol*. 2007;293(4):L823–L842.
63. Thomsen LB, Lichota J, Eskehave TN, et al. Brain delivery systems via mechanism independent of receptor-mediated endocytosis and adsorptive-mediated endocytosis. *Curr Pharm Biotechnol*. 2012;13(12):2349–2354.
64. Wang Z, Tiruppathi C, Minshall RD, Malik AB. Size and dynamics of caveolae studied using nanoparticles in living endothelial cells. *ACS Nano*. 2009;3(12):4110–4116.
65. Parton RG, Simons K. The multiple faces of caveolae. *Nat Rev Mol Cell Biol*. 2007;8(3):185–194.
66. Mayor S, Pagano RE. Pathways of clathrin-independent endocytosis. *Nat Rev Mol Cell Biol*. 2007;8(8):603–612.
67. Hommelgaard AM, Roepstorff K, Vilhardt F, Torgersen ML, Sandvig K, van Deurs B. Caveolae: stable membrane domains with a potential for internalization. *Traffic*. 2005;6(9):720–724.
68. Howes MT, Kirkham M, Riches J, et al. Clathrin-independent carriers form a high capacity endocytic sorting system at the leading edge of migrating cells. *J Cell Biol*. 2010;190(4):675–691.
69. Pelkmans L, Püntener D, Helenius A. Local actin polymerization and dynamin recruitment in SV40-induced internalization of caveolae. *Science*. 2002;296(5567):535–539.
70. Hayer A, Stoerber M, Ritz D, Engel S, Meyer HH, Helenius A. Caveolin-1 is ubiquitinated and targeted to intraluminal vesicles in endolysosomes for degradation. *J Cell Biol*. 2010;191(3):615–629.
71. Gratton SE, Ropp PA, Pohlhaus PD, et al. The effect of particle design on cellular internalization pathways. *Proc Natl Acad Sci U S A*. 2008;105(33):11613–11618.
72. Pelkmans L, Bürli T, Zerial M, Helenius A. Caveolin-stabilized membrane domains as multifunctional transport and sorting devices in endocytic membrane traffic. *Cell*. 2004;118(6):767–780.
73. Parton RG, Howes MT. Revisiting caveolin trafficking: the end of the caveosome. *J Cell Biol*. 2010;191(3):439–441.
74. Bengali Z, Rea JC, Shea LD. Gene expression and internalization following vector adsorption to immobilized proteins: dependence on protein identity and density. *J Gene Med*. 2007;9(8):668–678.

75. Rejman J, Conese M, Hoekstra D. Gene transfer by means of lipopolyplexes: role of clathrin and caveolae-mediated endocytosis. *J Liposome Res*. 2006;16(3):237–247.
76. Lu F, Wu SH, Hung Y, Mou CY. Size effect on cell uptake in well-suspended, uniform mesoporous silica nanoparticles. *Small*. 2009;5(12):1408–1413.
77. Albanese A, Tang PS, Chan WC. The effect of nanoparticle size, shape, and surface chemistry on biological systems. *Annu Rev Biomed Eng*. 2012;14:1–16.
78. Champion JA, Katare YK, Mitragotri S. Particle shape: a new design parameter for micro- and nanoscale drug delivery carriers. *J Control Release*. 2007;121(1–2):3–9.
79. Ferrari M. Nanogometry: beyond drug delivery. *Nat Nanotechnol*. 2008;3(3):131–132.
80. Geng Y, Dalhaimer P, Cai S, et al. Shape effects of filaments versus spherical particles in flow and drug delivery. *Nat Nanotechnol*. 2007;2(4):249–255.
81. Meng H, Yang S, Li Z, et al. Aspect ratio determines the quantity of mesoporous silica nanoparticle uptake by a small GTPase-dependent macropinocytosis mechanism. *ACS Nano*. 2011;5(6):4434–4447.
82. Donaldson K, Murphy FA, Duffin R, Poland CA. Asbestos, carbon nanotubes and the pleural mesothelium: a review of the hypothesis regarding the role of long fibre retention in the parietal pleura, inflammation and mesothelioma. *Part Fibre Toxicol*. 2010;7:5.
83. Qiu Y, Liu Y, Wang L, et al. Surface chemistry and aspect ratio mediated cellular uptake of Au nanorods. *Biomaterials*. 2010;31(30):7606–7619.
84. Lovrić J, Bazzi HS, Cuie Y, Fortin GRA, Winnik FM, Maysinger D. Differences in subcellular distribution and toxicity of green and red emitting CdTe quantum dots. *J Mol Med*. 2005;83(5):377–385.
85. Dausend J, Musyanovych A, Dass M, et al. Uptake mechanism of oppositely charged fluorescent nanoparticles in HeLa cells. *Macromol Biosci*. 2008;8(12):1135–1143.
86. Woodle MC, Lasic DD. Sterically stabilized liposomes. *Biochim Biophys Acta*. 1992;1113(2):171–199.
87. Elsbahy M, Wooley KL. Design of polymeric nanoparticles for biomedical delivery applications. *Chem Soc Rev*. 2012;41(7):2545–2561.
88. Cruz LJ, Tacken PJ, Fokkink R, Figdor CG. The influence of PEG chain length and targeting moiety on antibody-mediated delivery of nanoparticle vaccines to human dendritic cells. *Biomaterials*. 2011;32(28):6791–6803.
89. Dos Santos T, Varela J, Lynch I, Salvati A, Dawson KA. Quantitative assessment of the comparative nanoparticle-uptake efficiency of a range of cell lines. *Small*. 2011;7(23):3341–3349.
90. Kim JA, Åberg C, Salvati A, Dawson KA. Role of cell cycle on the cellular uptake and dilution of nanoparticles in a cell population. *Nat Nanotechnol*. 2012;7(1):62–68.
91. Saftig P, Klumperman J. Lysosome biogenesis and lysosomal membrane proteins: trafficking meets function. *Nat Rev Mol Cell Biol*. 2009;10(9):623–635.
92. Fischer HC, Hauck TS, Gómez-Aristizábal A, Chan WC. Exploring primary liver macrophages for studying quantum dot interactions with biological systems. *Adv Mater*. 2010;22(23):2520–2524.
93. Boussif O, Zanta MA, Behr JP. Optimized galenics improve in vitro gene transfer with cationic molecules up to 1000-fold. *Gene Ther*. 1996;3(12):1074–1080.
94. Moore NM, Sheppard CL, Barbour TR, Sakiyama-Elbert SE. The effect of endosomal escape peptides on in vitro gene delivery of polyethylene glycol-based vehicles. *J Gene Med*. 2008;10(10):1134–1149.
95. Caracciolo G, Caminiti R, Digman MA, Gratton E, Sanchez S. Efficient escape from endosomes determines the superior efficiency of multicomponent lipopolyplexes. *J Phys Chem B*. 2009;113(15):4995–4997.
96. Chu CJ, Dijkstra J, Lai MZ, Hong K, Szoka FC. Efficiency of cytoplasmic delivery by pH-sensitive liposomes to cells in culture. *Pharm Res*. 1990;7(8):824–834.
97. Zuhorn IS, Bakowsky U, Polushkin E, et al. Nonbilayer phase of lipoplex-membrane mixture determines endosomal escape of genetic cargo and transfection efficiency. *Mol Ther*. 2005;11(5):801–810.
98. Kobayashi S, Nakase I, Kawabata N, et al. Cytosolic targeting of macromolecules using a pH-dependent fusogenic peptide in combination with cationic liposomes. *Bioconjug Chem*. 2009;20(5):953–959.
99. Mu Q, Broughton DL, Yan B. Endosomal Leakage and Nuclear Translocation of Multiwalled Carbon Nanotubes: Developing a Model for Cell Uptake. *Nano Lett*. 2009;9(12):4370–4375.
100. AshaRani PV, Low Kah Mun G, Hande MP, Valiyaveetil S. Cytotoxicity and genotoxicity of silver nanoparticles in human cells. *ACS Nano*. 2009;3(2):279–290.
101. Huwyler J, Drewe J, Krähenbühl S. Tumor targeting using liposomal antineoplastic drugs. *Int J Nanomedicine*. 2008;3(1):21–29.
102. Punnonen EL, Ryhänen K, Marjomäki VS. At reduced temperature, endocytic membrane traffic is blocked in multivesicular carrier endosomes in rat cardiac myocytes. *Eur J Cell Biol*. 1998;75(4):344–352.
103. Ogris M, Wagner E, Steinlein P. A versatile assay to study cellular uptake of gene transfer complexes by flow cytometry. *Biochim Biophys Acta*. 2000;1474(2):237–243.
104. Leclerc L, Boudard D, Pourchez J, et al. Quantification of micro-sized fluorescent particles phagocytosis to a better knowledge of toxicity mechanisms. *Inhal Toxicol*. 2010;22(13):1091–1100.
105. Yang H, Lou C, Xu M, Wu C, Miyoshi H, Liu Y. Investigation of folate-conjugated fluorescent silica nanoparticles for targeting delivery to folate receptor-positive tumors and their internalization mechanism. *Int J Nanomedicine*. 2011;6:2023–2032.
106. Nuutila J, Lilius E-M. Flow cytometric quantitative determination of ingestion by phagocytes needs the distinguishing of overlapping populations of binding and ingesting cells. *Cytometry A*. 2005;65(2):93–102.
107. Drescher D, Giesen C, Traub H, Panne U, Kneipp J, Jakubowski N. Quantitative imaging of gold and silver nanoparticles in single eukaryotic cells by laser ablation ICP-MS. *Anal Chem*. 2012;84(22):9684–9688.
108. Bacallao R, Sohrab S, Phillips C. Guiding Principles of Specimen Preservation for Confocal Fluorescence Microscopy. In: Pawley JB, editor. *Handbook of Biological Confocal Microscopy*. 3rd ed. Madison, WI: Springer Science+Business Media; 2006:368–380.
109. Elsaesser A, Barnes CA, McKerr G, et al. Quantification of nanoparticle uptake by cells using an unbiased sampling method and electron microscopy. *Nanomedicine (Lond)*. 2011;6(7):1189–1198.
110. Mühlfeld C, Mayhew TM, Gehr P, Rothen-Rutishauser B. A novel quantitative method for analyzing the distributions of nanoparticles between different tissue and intracellular compartments. *J Aerosol Med*. 2007;20(4):395–407.
111. Schmutz HR, Detampel P, Bühler T, Büttler A, Gygax B, Huwyler J. In vitro assessment of the formation of ceftriaxone-calcium precipitates in human plasma. *J Pharm Sci*. 2011;100(6):2300–2310.
112. Brandenberger C, Clift MJD, Vanhecke D, et al. Intracellular imaging of nanoparticles: is it an elemental mistake to believe what you see? *Part Fibre Toxicol*. 2010;7:15.
113. Mühlfeld C, Brandenberger C. Uptake of nanoparticles by cells: do you know their number? *Nanomedicine (Lond)*. 2011;6(7):1149–1151; author reply 1153–1154.
114. Choi HS, Ashitate Y, Lee JH, et al. Rapid Translocation of Nanoparticles from the Lung Airspaces to the Body. *Nat Biotechnol*. 2010;28(12):1300–1303.
115. Shim J, Seok Kang H, Park WS, Han SH, Kim J, Chang IS. Transdermal delivery of mixnoxidil with block copolymer nanoparticles. *J Control Release*. 2004;97(3):477–484.
116. Aggarwal N, Goindi S. Preparation and in vivo evaluation of solid lipid nanoparticles of griseofulvin for dermal use. *J Biomed Nanotechnol*. 2013;9(4):564–576.
117. Des Rieux A, Fievez V, Garinot M, Schneider YJ, Préat V. Nanoparticles as potential oral delivery systems of proteins and vaccines: a mechanistic approach. *J Control Release*. 2006;116(1):1–27.
118. Xu Q, Zhang N, Qin W, Liu J, Jia Z, Liu H. Preparation, in vitro and in vivo evaluation of budesonide loaded core/shell nanofibers as oral colonic drug delivery system. *J Nanosci Nanotechnol*. 2013;13(1):149–156.

3.1. ENGINEERED NANOMATERIAL UPTAKE AND DISPOSITION

119. Mager DE, Mody V, Xu C, et al. Physiologically based pharmacokinetic model for composite nanodevices: effect of charge and size on in vivo disposition. *Pharm Res*. 2012;29(9):2534–2542.
120. Petri-Fink A, Steitz B, Finka A, Salaklang J, Hofmann H. Effect of cell media on polymer coated superparamagnetic iron oxide nanoparticles (SPIONs): colloidal stability, cytotoxicity, and cellular uptake studies. *Eur J Pharm Biopharm*. 2008;68(1):129–137.
121. Kutscher HL, Chao P, Deshmukh M, et al. Threshold size for optimal passive pulmonary targeting and retention of rigid microparticles in rats. *J Control Release*. 2010;143(1):31–37.
122. Aneja MK, Geiger JP, Himmel A, Rudolph C. Targeted gene delivery to the lung. *Expert Opin Drug Deliv*. 2009;6(6):567–583.
123. Choi HS, Liu W, Misra P, et al. Renal clearance of quantum dots. *Nat Biotechnol*. 2007;25(10):1165–1170.
124. Maeda H. The enhanced permeability and retention (EPR) effect in tumor vasculature: the key role of tumor-selective macromolecular drug targeting. *Adv Enzyme Regul*. 2001;41:189–207.
125. Shah NB, Vercehlotti GM, White JG, Fegan A, Wagner CR, Bischof JC. Blood-Nanoparticle Interactions and in Vivo Biodistribution: Impact of Surface PEG and Ligand Properties. *Mol Pharm*. Epub July 23, 2012.
126. Dobrovol'skaia MA, Clogston JD, Neun BW, Hall JB, Patri AK, McNeil SE. Method for analysis of nanoparticle hemolytic properties in vitro. *Nano Lett*. 2008;8(8):2180–2187.
127. Yu T, Malugin A, Ghandehari H. Impact of silica nanoparticle design on cellular toxicity and hemolytic activity. *ACS Nano*. 2011;5(7):5717–5728.
128. Quirion F, St-Pierre S. Reduction of the in vitro hemolytic activity of soybean lecithin liposomes by treatment with a block copolymer. *Biophys Chem*. 1991;40(2):129–134.
129. Paula AJ, Martinez DST, Araujo Júnior RT, Souza Filho AG, Alves OL. Suppression of the hemolytic effect of mesoporous silica nanoparticles after protein corona interaction: independence of the surface microchemical environment. *J Braz Chem Soc*. 2012;23(10):1807–1814.
130. Lynch I, Dawson KA. Protein-nanoparticle interactions. *Nano Today*. 2008;3(1–2):40–47.
131. Gasser M, Rothen-Rutishauser B, Krug HF, et al. The adsorption of biomolecules to multi-walled carbon nanotubes is influenced by both pulmonary surfactant lipids and surface chemistry. *J Nanobiotechnology*. 2010;8:31.
132. Gessner A, Waicz R, Lieske A, Paulke BR, Mäder K, Müller R. Nanoparticles with decreasing surface hydrophobicities: influence on plasma protein adsorption. *Int J Pharm*. 2000;196(2):245–249.
133. Duan X, Li Y. Physicochemical characteristics of nanoparticles affect circulation, biodistribution, cellular internalization, and trafficking. *Small*. 2013;9(9–10):1521–1532.
134. Arnida, Janát-Amsbury MM, Ray A, Peterson CM, Ghandehari H. Geometry and surface characteristics of gold nanoparticles influence their biodistribution and uptake by macrophages. *Eur J Pharm Biopharm*. 2011;77(3):417–423.
135. Bailon P, Palleroni A, Schaffer CA, et al. Rational design of a potent, long-lasting form of interferon: a 40 kDa branched polyethylene glycol-conjugated interferon α -2a for the treatment of hepatitis C. *Bioconjug Chem*. 2001;12(2):195–202.
136. Li SD, Huang L. Stealth nanoparticles: high density but sheddable PEG is a key for tumor targeting. *J Control Release*. 2010;145(3):178–181.
137. Lipka J, Semmler-Behnke M, Sperling RA, et al. Biodistribution of PEG-modified gold nanoparticles following intratracheal instillation and intravenous injection. *Biomaterials*. 2010;31(25):6574–6581.
138. Ishihara T, Takeda M, Sakamoto H, et al. Accelerated blood clearance phenomenon upon repeated injection of PEG-modified PLA-nanoparticles. *Pharm Res*. 2009;26(10):2270–2279.
139. Murthy AK, Stover RJ, Hardin WG, et al. Charged gold nanoparticles with essentially zero serum protein adsorption in undiluted fetal bovine serum. *J Am Chem Soc*. 2013;135(21):7799–7802.
140. Garnett MC, Kallinteri P. Nanomedicines and nanotoxicology: some physiological principles. *Occup Med (Lond)*. 2006;56(5):307–311.
141. Svistounov D, Warren A, McNerney GP, et al. The Relationship between fenestrations, sieve plates and rafts in liver sinusoidal endothelial cells. *PLoS ONE*. 2012;7(9):e46134.
142. Gaumet M, Vargas A, Gurny R, Delie F. Nanoparticles for drug delivery: The need for precision in reporting particle size parameters. *Eur J Pharm Biopharm*. 2008;69(1):1–9.
143. Liu X, Huang N, Li H, Jin Q, Ji J. Surface and size effects on cell interaction of gold nanoparticles with both phagocytic and non-phagocytic cells. *Langmuir*. 2013;29(29):9138–9148.
144. Hirn S, Semmler-Behnke M, Schleh C, et al. Particle size-dependent and surface charge-dependent biodistribution of gold nanoparticles after intravenous administration. *Eur J Pharm Biopharm*. 2011;77(3):407–416.
145. Zhang G, Yang Z, Lu W, et al. Influence of anchoring ligands and particle size on the colloidal stability and in vivo biodistribution of polyethylene glycol-coated gold nanoparticles in tumor-xenografted mice. *Biomaterials*. 2009;30(10):1928–1936.
146. Xie G, Sun J, Zhong G, Shi L, Zhang D. Biodistribution and toxicity of intravenously administered silica nanoparticles in mice. *Arch Toxicol*. 2010;84(3):183–190.
147. Huang X, Li L, Liu T, et al. The shape effect of mesoporous silica nanoparticles on biodistribution, clearance, and biocompatibility in vivo. *ACS Nano*. 2011;5(7):5390–5399.
148. Moghimi SM, Hunter AC, Andresen TL. Factors controlling nanoparticle pharmacokinetics: an integrated analysis and perspective. *Annu Rev Pharmacol Toxicol*. 2012;52:481–503.
149. Jain RK. Normalizing tumor microenvironment to treat cancer: bench to bedside to biomarkers. *J Clin Oncol*. 2013;31(17):2205–2218.
150. Wang J, Zhu X, Zhang X, et al. Disruption of zebrafish (*Danio rerio*) reproduction upon chronic exposure to TiO₂ nanoparticles. *Chemosphere*. 2011;83(4):461–467.
151. Mahmoudi M, Hofmann H, Rothen-Rutishauser B, Petri-Fink A. Assessing the in vitro and in vivo toxicity of superparamagnetic iron oxide nanoparticles. *Chem Rev*. 2012;112(4):2323–2338.
152. Park JH, Gu L, von Maltzahn G, Ruoslahti E, Bhatia SN, Sailor MJ. Biodegradable luminescent porous silicon nanoparticles for in vivo applications. *Nat Mater*. 2009;8(4):331–336.
153. Chen K, Zhang J, Gu H. Dissolution from inside: a unique degradation behaviour of core-shell magnetic mesoporous silica nanoparticles and the effect of polyethyleneimine coating. *J Mater Chem*. 2012;22(41):22005–22012.
154. Coyle P, Philcox JC, Carey LC, Rofe AM. Metallothionein: the multipurpose protein. *Cell Mol Life Sci*. 2002;59(4):627–647.
155. Levy M, Luciani N, Alloyeau D, et al. Long term in vivo biotransformation of iron oxide nanoparticles. *Biomaterials*. 2011;32(16):3988–3999.
156. Akagi T, Higashi M, Kaneko T, Kida T, Akashi M. Hydrolytic and enzymatic degradation of nanoparticles based on amphiphilic poly(γ -glutamic acid)-graft-L-phenylalanine copolymers. *Biomacromolecules*. 2006;7(1):297–303.
157. Park K, Kim JH, Nam YS, et al. Effect of polymer molecular weight on the tumor targeting characteristics of self-assembled glycol chitosan nanoparticles. *J Control Release*. 2007;122(3):305–314.
158. Ye L, Yong KT, Liu L, et al. A pilot study in non-human primates shows no adverse response to intravenous injection of quantum dots. *Nat Nanotechnol*. 2012;7(7):453–458.
159. Wilkinson K, Ekstrand-Hammarström B, Ahlinder L, et al. Visualization of custom-tailored iron oxide nanoparticles chemistry, uptake, and toxicity. *Nanoscale*. 2012;4(23):7383–7393.
160. Som C, Nowack B, Krug HF, Wick P. Toward the Development of Decision Supporting Tools That Can Be Used for Safe Production and Use of Nanomaterials. *Acc Chem Res*. Epub October 31, 2012.

International Journal of Nanomedicine

Dovepress

Publish your work in this journal

The International Journal of Nanomedicine is an international, peer-reviewed journal focusing on the application of nanotechnology in diagnostics, therapeutics, and drug delivery systems throughout the biomedical field. This journal is indexed on PubMed Central, MedLine, CAS, SciSearch®, Current Contents®/Clinical Medicine,

Journal Citation Reports/Science Edition, EMBase, Scopus and the Elsevier Bibliographic databases. The manuscript management system is completely online and includes a very quick and fair peer-review system, which is all easy to use. Visit <http://www.dovepress.com/testimonials.php> to read real quotes from published authors.

Submit your manuscript here: <http://www.dovepress.com/international-journal-of-nanomedicine-journal>

3.2 Safety of silica nanoparticles

Safety evaluation of silica-based nanoparticles

Helene Kettiger¹, Didem Sen Karaman², Laura Schiesser¹, Jessica M. Rosenholm², Jörg Huwyler¹

¹ Department of Pharmaceutical Sciences, University of Basel, Switzerland

² Laboratory of Physical Chemistry, Åbo Akademi University, Porthansgatan 3-5, FI-20500 Turku, Finland

Contribution H.Kettiger: author, experimental part (synthesis, biological assays)

Submitted to Nanotoxicology *reformatted for thesis layout*

ORIGINAL ARTICLE

Safety evaluation of silica-based nanoparticles

Helene Kettiger¹, Didem Sen Karaman², Laura Schiesser¹, Jessica M. Rosenholm², and Jörg Huwyler¹

¹Department of Pharmaceutical Sciences, Division of Pharmaceutical Technology, University of Basel, Basel, Switzerland;

²Laboratory of Physical Chemistry, Åbo Akademi University, Porthansgatan 3-5, FI-20500 Turku, Finland

Running title: Safety of silica nanoparticles

Author for correspondence:

Prof. Dr. Jörg Huwyler

University of Basel

Department of Pharmaceutical Sciences

Division of Pharmaceutical Technology

Klingelbergstrasse 50

4056 Basel, Switzerland

Tel +41 61 267 1513; Fax +41 61 267 1516; Email joerg.huwyler@unibas.ch

Keywords: Cell viability, oxidative stress, hemolysis, uptake, toxicity

Abstract

Purpose: Silica nanoparticles (SNPs) are increasingly used as drug delivery systems (DDS) and for biomedical imaging. Therapeutic and diagnostic agents can be incorporated into the silica matrix to improve the stability and dissolution of drug substances in biological systems. However, the safety of SNPs as drug carriers remains controversial. To date, no validated and accepted nano-specific tests exist to predict the potentially harmful impact of these materials on the human body.

Methods: We systematically synthesized 12 different types of SNPs with varying size, surface topology (porous vs non-porous), and surface modifications. We characterized these particles in terms of dry state and hydrodynamic diameter, specific surface area, and net surface charge (zeta potential). For cellular studies, we exposed non-phagocytic (HepG2) cells, phagocytic (THP-1) cells, and erythrocytes to SNPs. Cellular uptake and stability of fluorescently labeled SNPs were analyzed by confocal microscopy and flow cytometry.

Results: SNPs with a porous surface and negative net surface charge had the strongest impact on cell viability. This is in contrast to non-porous SNPs. None of the studied particles induced oxidative stress in either cell lines. Particles with a negative surface charge induced hemolysis in a concentration-dependent manner.

Conclusions: Our study revealed potential hazards of spherical amorphous SNPs. Physico-chemical properties mediating toxicity in living cells were identified. We propose that our standardized SNPs may serve as a readily available reference material for nanotoxicological investigations.

Introduction

During the past years, interest in the use of silica nanoparticles (SNPs) has increased. Such nanoparticles have been traditionally used as filler, desiccant, thickener for liquid dosage forms, or anticaking agent in powders. An example of such materials is fumed or pyrogenic silica which was introduced in 1942 under the brand name of Aerosil®. Recently, amorphous SNPs were proposed to be used as drug delivery systems (DDS) (Rosenholm et al., 2009; Wu et al., 2011) or imaging probes (Ow et al., 2004). Hence, humans are increasingly exposed to SNPs.

For DDS, different routes of administration have been proposed, namely oral intake as a suspension or tablet (Ensign et al., 2012), transdermal delivery (Escobar-Chavez et al., 2012), or inhalation (Bailey and Berkland, 2009). In all cases, the DDS has to cross cellular barriers, such as the inner surface of the gastrointestinal tract, before reaching its target. When administered intravenously, the nanoscaled DDS is distributed throughout the body, thus raising the question whether these materials are safe and well tolerated in humans (Kettiger et al., 2013; Wu et al., 2011). Nanoparticles can enter the cell via various energy-dependent routes and are able to penetrate the nucleus (dos Santos et al., 2011; Tao et al., 2009). Tight cell layers, such as the blood-brain barrier, can be crossed by small-sized SNPs *in vivo* (Barandeh et al., 2012).

Several *in vitro* toxicity studies have been carried out to assess the toxicity of different nanoparticles. Frequently used endpoints include cell viability, membrane leakage, generation of reactive oxygen species (ROS), and genotoxicity (Kroll et al., 2011). It is generally assumed that smaller nanoparticles are more toxic than bigger particles (Sohaebuddin et al., 2010). Shape and crystalline state additionally affect the toxicity profile. Frequently cited examples are “the fiber paradigm” for carbon nanotubes (Donaldson et al., 2010) or silicosis for crystalline silica (Byrne and Baugh, 2008). The large specific surface area may enhance solubility and release of metal ions, as was described for copper oxide or silver nanoparticles (Nel et al., 2006). Additionally, plasma proteins, nutrients, or growth factors can adsorb to this surface and lead to an indirect loss of cell viability (Casey et al., 2008).

3.2. SAFETY OF SILICA NANOPARTICLES

For SNPs, there are different synthetic routes available. Sol-gel synthesis results in exposed silanol groups on the particle surface, whereas fumed silica is characterized by the presence of siloxane groups on the surface (Figure 1). It is commonly believed that silanols remain intact when the SNPs are dried under vacuum at ambient temperature. Siloxane formation on the particle's surface is observed under vacuum at temperatures above 100 °C (Zhuravlev, 2000). The synthesis route influences biological outcomes like oxidative stress generation and hemolysis. This may partially explain the heterogeneous data available on SNPs toxicity (Zhang et al., 2012). Furthermore, results may vary among different cell lines and experimental conditions depending on the presence or absence of serum. Serum addition resulted in lower toxic potential of nanoparticles (Ge et al., 2011).

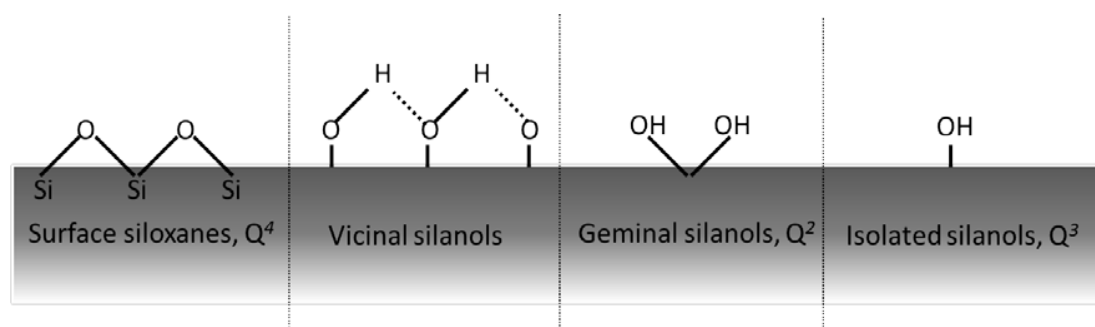


Figure 1: Schematic representation of an amorphous silica surface.

Suppliers of commercially available SNPs do not necessarily disclose their protocols for the synthesis of nanoparticles. Consequently, information on surface properties of commercial nanoparticles is hardly available. This is a major concern since the strategy used for the synthesis and preparation of nanoparticles can also influence their surface properties and hence their interaction with cells. Additionally, it has been reported that particle information provided by a commercial supplier should always be double-checked (Sayes et al., 2007).

The aim of this study was to avoid this uncertainty by using in house synthesized SNPs. Hence, we have synthesized 12 types of SNPs and altered their physico-chemical properties step by step. The SNPs vary in their size, surface charge, and porosity. We related the physico-chemical properties of different SNPs with the outcome of cytotoxicity, generation of oxidative stress, and hemolysis. In contrast to commercial SNPs,

our particles have a known thermal history and were characterized carefully. Furthermore, special controls for each assay were added to avoid over- or underestimation of the results.

Materials and methods

Materials

Absolute ethanol (EtOH), tetraethylorthosilicate (TEOS, 98%), (3-aminopropyl)triethoxysilane (APTES), thiazolyl blue tetrazolium bromide (MTT), fluorescein isothiocyanate isomer 1, 2',7'-dichlorofluorescein diacetate (FITC), hexadecyltrimethylammonium bromide (CTAB), ethylene glycol (EG), dichloro-dihydro-fluorescein diacetate (DCFH-DA), and phorbol 12-myristate 13-acetate (PMA) were purchased from Sigma-Aldrich (Buchs, Switzerland). Ammonium hydroxide solution (30 wt. %) was obtained from Roth (Arlesheim, Switzerland).

Synthesis of non-porous silica nanoparticles

In accordance with Stöber et al., we prepared non-porous SNPs of two different sizes (non-porous small SNPs (SS) and non-porous big SNPs (SB)) (Stoeber et al., 1968). In brief, reaction solution for the small SNPs had a molar composition of 1 TEOS: 0.087 NH₃: 64.3 EtOH: 27.8 H₂O and for the big ones 1 TEOS: 0.35 NH₃: 64.3 EtOH: 27.8 H₂O. Alteration of net surface charge was carried out by direct incorporation of amine groups by co-condensation of an aminosilane ((3-aminopropyl)triethoxysilane, APTES) by altering the amount of APTES relative to TEOS (2.5 mol %, 5 mol %, 10 mol %). This resulted in SNPs with a negative (-), a neutral (0), and a positive (+) surface charge. The mixture was stirred under ambient conditions for 3 h (SS) and 4 h (SB). The SNPs were collected by centrifugation, washed three times with EtOH, and dried overnight in a vacuum oven at ambient temperature.

Fluorescent particles (SB(-)) were needed for cellular uptake studies. Fluorescent dye was introduced into the synthesis as described elsewhere (Karaman et al., 2012). Briefly, an excess of FITC was added to pre-conjugate with APTES in ethanol solution and was stirred for 2 h under argon. This mixture was then introduced into the synthesis of the SB(-) as described above.

Synthesis of mesoporous silica nanoparticles

Mesoporous SNPs were synthesized as described above, albeit with certain modifications (Karaman et al., 2012). In brief, an ethanol basic aqueous reaction solution was prepared and structure directing agent CTAB was added. Subsequently, TEOS was added as silica source. Briefly, the prepared reaction solution

contained the reagents with the molar composition 1 TEOS: 0.12 CTAB: 946 H₂O:73 EtOH: 0.32 NaOH. After mixing the reagents, the reaction mixture was stirred overnight at room temperature. In order to modify particle surfaces to obtain different net surface charges, APTES was introduced as above. For these synthesis solutions, molar composition was 1 TEOS: 0.04 APTES: 0.12 CTAB: 946 H₂O:73 EtOH: 0.32 NaOH and 1 TEOS: 0.1 APTES: 0.12 CTAB: 946 H₂O:73 EtOH: 0.32 NaOH. For mesoporous small SNPs (MS), a modified synthesis protocol was used (Gu et al., 2007). The synthesis solution for MS consisted of a molar ratio of 1 TEOS: 0.45 CTAB: 12.9 NH₃:1392 H₂O:74.7 EG. The synthesis solution was subjected to vigorous stirring for 2 h at 50 °C, and then kept under static conditions at 50 °C overnight. In the same manner as for MB, APTES was added to the reaction mixture to obtain different net surface charges of SNPs. The resulting particles were collected by centrifugation and washed at least three times with 50 mL extraction solution (ethanol ammonium nitrate solution) to completely remove the CTAB template (Han et al., 2011). FITC was introduced into the synthesis of MB(-) as described above.

Suspension stability of silica nanoparticles

For size determination of the SNPs, we used two approaches. Dynamic light scattering (DLS) was used to measure the hydrodynamic diameter of SNPs in suspensions in two solutions, namely 10 mM HEPES (pH 7.2) and cell medium. The polydispersity index (PDI) indicated the size distribution. Secondly, we measured the dry diameter of all SNPs by transmission electron microscopy (TEM). With TEM, we were additionally able to assess the porosity of the SNPs. The TEM samples were previously negative-stained and then observed under a Philips CM100, operating in the bright field mode at 80 kV. In order to confirm the success of surface charge altering by incorporating APTES, ζ - potential measurements were performed in ethanol. Additionally, ζ - potential measurements were carried out in 10 mM HEPES buffer and cell medium to mimic the SNPs behavior as suspension in cell experiments. The amount of APTES incorporated was determined by thermo-gravimetric analysis (TGA), as seen in supplementary information (Figure S1). The structural parameters related to the surface of SNPs (i.e. specific surface area) were determined by nitrogen sorption measurements (ASAP 2020; Micromeritics Instrument Corp., Norcross, GA, USA) using the Brunauer-Emmet-Teller (BET) method.

3.2. SAFETY OF SILICA NANOPARTICLES

Cell culture

Dulbecco's modified Eagle medium (DMEM) was supplemented with 1x HEPES buffer, 10% FCS, 1% penicillin-streptomycin (P/S), and 1% non-essential amino acids (denoted as cell medium). All products used for medium preparation were purchased from Sigma-Aldrich, except FCS that was obtained from Amimed (Bioconcept, Switzerland). HepG2 cells were kindly provided by Prof. Dr. Dietrich von Schweinitz (University Hospital Basel, Switzerland) and were maintained in DMEM comp. THP-1 cells (ATCC, TIB-202) were maintained in Roswell Park Memorial Institute (RPMI) medium supplemented with 10% FCS, 1% P/S, 10 mM HEPES, 1% sodium pyruvate, and 0.05 mM mercaptoethanol. Freshly drawn sheep blood from the slaughterhouse Basel was collected in Vacutainer® tubes coated with potassium ethylenediaminetetraacetic acid (K₂EDTA) and was used within 4 h after collection.

Viability

HepG2 cells were seeded at a density of 1.5×10^4 cells per well in a 96-well plate and allowed to attach for 24 h at 37 °C. THP-1 cells were seeded at a density of 4×10^4 cells and were differentiated by 100 nM PMA over 72 h. The SNPs suspensions were prepared by ultrasonication for 30 min in 10 mM HEPES at 2.5 mg/mL. Then, the stocks were diluted with cell medium at different concentrations (10, 50, 100, and 250 µg/mL) and added to the cells. After exposure of cells for 24 h, 48 h, and 72 h, the medium was removed, 100 µL of MTT solution (0.5 mg/mL) was added to each well, and the cells were incubated for another 2 h at 37° C. The resulting formazan crystals were solubilized with 100 µL of acidified isopropyl alcohol and 20 µL of 3% SDS (Seeland et al., 2013). The absorption was read at a wavelength of 560 nm, and unspecific signals at 670 nm were subtracted (Spectramax M2 plate reader, Molecular Devices, Sunnyvale, CA). Cytotoxicity was expressed as the percentage of cell viability, where untreated cells were set to be 100% viable. A commercially available kit with a water-soluble formazan salt (CellTiter 96® AQueous One Solution Cell Proliferation Assay, MTS) was obtained from Promega (Dübendorf, Switzerland) and used according to the manufacturer's instructions.

Oxidative stress

Induction of oxidative stress was determined using DCFH-DA. HepG2 cells were seeded at a density of 5×10^4 cells per well in a black 96-well plate with a clear bottom and were allowed to attach for 24 h. THP-1

cells were seeded and differentiated as described above, using black plates with clear bottom. Phenol red free cell culture medium was used. Prior to exposing SNPs, cell medium was removed and 50 μM of DCFH-DA in protein-free medium was added to each well for 1 h. After washing the cells twice with phosphate-buffered saline (PBS), the particle suspensions in cell medium (10, 50, 100, and 250 $\mu\text{g}/\text{mL}$) were added to the cells. Fluorescence signals were measured through the bottom of the cell culture plates at an excitation wavelength of 485 nm and an emission wavelength of 528 nm (Spectramax M2 plate reader) after 1 h, 4 h, and 24 h of exposure. A commercially available total ROS detection kit (Enzo, Lausen, Switzerland) was used according to the manufacturer's instructions.

Hemolysis

Hemolysis was tested as previously described (Yu et al., 2011). Briefly, a 4 mL sample of blood was mixed with 8 mL PBS. The red blood cells (RBCs) were collected by centrifugation at 4500 rpm for 5 min and washed five times with sterile PBS. Purified RBCs were diluted in 40 mL PBS. Then, 0.2 mL of RBCs was mixed with 0.8 mL of SNP suspensions. Two concentrations (25 $\mu\text{g}/\text{mL}$ and 250 $\mu\text{g}/\text{mL}$) were tested for each particle type. The RBC-SNP suspensions were left at room temperature for 4 h. After centrifugation, absorbance of the supernatant was measured at 577 nm (oxyhemoglobin). Unspecific signals at 655 nm were subtracted. The results are given as the percentage of hemolysis compared to a positive control (MilliQ water).

Interference of nanoparticles with test systems

For each assay, optical, catalytic, and adsorptive interference was tested. Optical and catalytic interference were tested as described elsewhere (Kroll et al., 2012). Catalytic interference of the DCFH-DA assay was assessed by prior de-acetylation of the reporter as described in the literature (Kroll et al., 2012; Napierska et al., 2012). Adsorptive interference was tested by incubating the SNPs with the reporter and subsequent centrifugation. Then, optical density or fluorescence of the supernatant was measured to determine the fraction of bound reporter to the particles.

3.2. SAFETY OF SILICA NANOPARTICLES

Uptake and degradation of silica nanoparticles

Representative uptake into HepG2 and THP-1 cells was determined for two fluorescently labeled SNP types, namely the non-porous SB(-) and the mesoporous MB(-). We chose MB(-) due to the results in the MTT, and the SB(-) as a “non-toxic” control with the same physico-chemical characteristics except the porosity. Cells were cultured at 50% confluence on poly-d-lysine-coated glass slides and left for attachment for 24 h. Then, SNPs were incubated at 50 µg/mL, and uptake was determined after 1 h, 8 h, and 24 h. The nuclei were stained with Hoechst 33342 for 5 min at the end of the uptake experiment. Actin staining was performed after cell fixation with rhodamine phalloidin. The samples were embedded in Prolong Gold antifade agent (Gibco) and sealed with nail polisher. After 24 h, uptake was qualitatively visualized with confocal microscopy (Olympus FV-1000, Tokyo, Japan) using a 60x PlanApo N oil immersion objective. The images were further processed by GIMP 2.8 software (GNU image manipulation program). For live-cell imaging, we proceeded in the same way; the cells were maintained in the chamber with 5% CO₂ and at 37° C for 2 h to monitor the disintegration of the SNPs. Additionally, we determined the amount of free silicon with the blue silicomolybdic acid assay as reported earlier (Coradin et al., 2004). For quantitative uptake, we measured the green fluorescence shift relative to the control (non-treated cells) in a time-dependent manner (FACS Canto II). For each experiment, 10,000 viable cells were counted. To quench extracellular fluorescence, cell suspensions were diluted with one volume of 0.4% trypan blue in buffer (Vranic et al., 2013).

Statistical analysis

Each experiment was performed in triplicate and repeated three times (MTT, DCFH-DA, and hemolysis). Statistical significance was determined by using one-way analysis of variance (ANOVA), followed by Tukey's post-hoc test. Differences were considered significant at $p < 0.05$.

Results

Characterization of silica nanoparticles

Systematic material characterization of SNPs is crucial (Krug and Wick, 2011). We therefore decided to synthesize and characterize silica particles used in the present study in our laboratory and not to rely on commercially available nanomaterials. In this study, the sol-gel method was used to prepare SNPs with different characteristics.

Table 1: Physico-chemical properties of SNPs. Particle size was determined by transmission electron microscopy (TEM) and dynamic light scattering (DLS) in HEPES buffer in presence or absence of 10% serum. The different types of SNPs used in the present study are named as follows: First prefix “S” = non-porous, “M” = mesoporous. Second prefix “S” = small particle size and “B” = big particle size. “-” = negative ζ -potential in 10 mM HEPES buffer. “0” = net neutral ζ -potential in 10 mM HEPES. “+” = positive ζ -potential. PDI: polydispersity index determined by DLS. BET: Brunauer Emmett Teller (as determined by nitrogen sorption). nd: not determined.

Name	Size (nm)			Surface	
	TEM	HEPES (PDI)	10% serum (PDI)	ζ -potential (mV)	BET (m ² /g)
SS(-)	105	135.6 (0.12)	160.9 (0.017)	-18	35
SS(0)	110	506.8 (0.25)	164.5 (0.19)	-7	nd
SS(+)	100	166.5 (0.14)	194.6 (0.20)	21	nd
SB(-)	250	369 (0.08)	327.6 (0.30)	-23	18
SB(0)	230	399 (0.06)	411.1 (0.25)	8	nd
SB(+)	235	359.7 (0.13)	226.2 (0.16)	23	nd
MS(-)	80	196.6 (0.16)	243.2 (0.21)	-24	1380
MS(0)	85	agglomerate	agglomerate	-3	nd

3.2. SAFETY OF SILICA NANOPARTICLES

MS(+)	80	1400 (0.41)	270.9 (0.19)	22	nd
MB(-)	200	287.1 (0.1)	301.4 (0.28)	-29	1223
MB(0)	220	1780.6 (0.22)	337.6 (0.28)	-11	nd
MB(+)	250	433 (0.09)	484.4 (0.38)	32	nd

Table 1 provides an overview of the physico-chemical characteristics and indicates the abbreviations for each SNP type. There, the first letter represents solid (S) or mesoporous (M) SNP, the second one denoted the size (S for small and B for big), while the value in brackets represented the zeta potential in 10 mM HEPES. For example, MB(-) stands for mesoporous, big, negatively charged SNPs. We have chosen a size of 100 nm for the small SNPs and about 250 nm for the big SNPs, since these sizes are common for drug delivery systems. Particle size distribution of the SNP suspensions was evaluated by hydrodynamic size measurements in cell medium. According to the results obtained, colloidal particle suspensions with low poly-dispersity index values were obtained for all non-porous SNPs (SS and SB series) and the mesoporous large SNPs (MB) series, whereas no measurable hydrodynamic diameter results were obtained for the MS suspensions. For instance, the MS(0) sample with net neutral surface charge value both in HEPES buffer and cell medium resulted in agglomeration and subsequent sedimentation of the particles, which prevented DLS measurements. Figure 2 shows the dry-state diameter of representative SNPs and gives insight into the porous structure by TEM. The specific surface area measurements additionally revealed the porous structure of the mesoporous series, with a pore size of about 3 nm. These results were confirmed by small angle X-ray scattering (data not shown). Furthermore, BET measurements revealed specific surface areas below 35 m²/g for non-porous SNPs, while for mesoporous SNPs, the value was above 1200 m²/g. The ζ -potential of the SNPs varied between negative (approx. -25 mV) and positive (approx. +30 mV) values (10 mM HEPES buffer), which confirmed the success of the surface modification. For particles with sufficiently high absolute ζ -potential values, suspension stability is maintained chiefly by electrostatic repulsion. However, particles with a ζ -potential close to zero millivolts (neutral net surface charge) tend to agglomerate in buffer due to the absence of strong repulsive forces between the particles. However, even if the

electrostatic repulsion is low, particles can be suspended and stabilized with the aid of supplemented serum proteins, which are present in the cell medium to maintain cell viability. These proteins adsorb rapidly onto the nanoparticle's surface and create a so-called protein corona (Meißner et al., 2009). In our case, this corona prevented the agglomeration of SNPs with a net neutral charge. In addition, the successful APTES incorporation into the silica network was confirmed by TGA (Figure S1). As residual surfactant may cause cytotoxicity, we confirmed the removal of the template by FTIR (Figure S2).

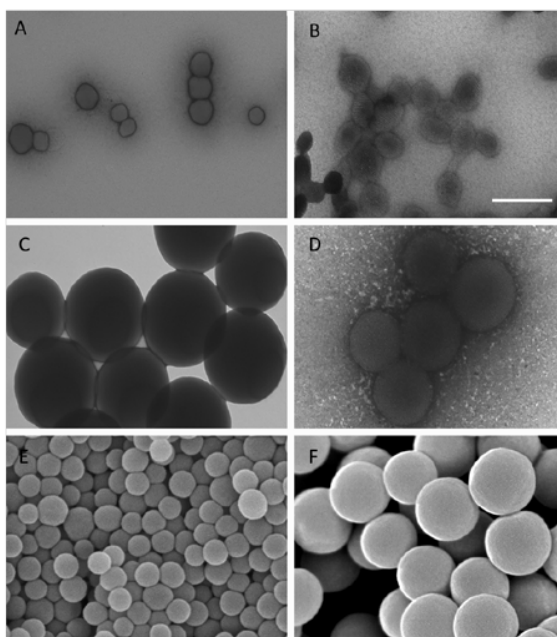


Figure 2: Representative TEM (A-D) and SEM (E, F) images of SNP: A: SS(-); B: MS(-); C: SB(-); D: MB(-); E: SEM of SS(-); F: SEM of SB(-). Scale bar: always 200 nm.

Cell viability

We evaluated the loss of cell viability upon exposure of HepG2 cells and THP-1 cells to SNPs for 24 h, 48 h, and 72 h. SNP concentrations ranged from 10 $\mu\text{g}/\text{mL}$ to 250 $\mu\text{g}/\text{mL}$. Figure 3 shows the viability of HepG2 cells and THP-1 cells after 24 h. The left diagram (HepG2) shows that most SNPs did not induce a severe viability decrease at any concentrations tested. The strongest effect was occurring for the big mesoporous series, regardless of their surface charge. A slight time-dependent effect was observed in both cell lines (data not shown). In addition, the higher SNP concentrations had a more pronounced impact, especially for

3.2. SAFETY OF SILICA NANOPARTICLES

bigger SNPs. Smaller SNPs also led to a cell viability decrease that was more marked after 72 h (data not shown).

Viability	80-100%	60-80%	40-60%	20-40%	0-20%
Rank	1	2	3	4	5

	µg/ml						
	0	10	50	100	250	sum	rank
SS(-)	1	1	1	1	1	5	3
SS(0)	1	1	1	1	1	5	3
SS(+)	1	1	1	1	1	5	3
SB(-)	1	1	1	1	1	5	3
SB(0)	1	1	1	1	1	5	3
SB(+)	1	2*	2*	2*	2*	9	2
MS(-)	1	1	1	1	1	5	3
MS(0)	1	1	1	1	1	5	3
MS(+)	1	1	1	1	1	5	3
MB(-)	1	1*	2*	3*	3*	10	1
MB(0)	1	2*	2*	3*	2*	10	1
MB(+)	1	2*	2*	2*	3*	10	1

	µg/ml						
	0	10	50	100	250	sum	rank
SS(-)	1	1	1	1	2*	6	4
SS(0)	1	1	1	1	1	5	5
SS(+)	1	1	2*	2*	2*	8	2
SB(-)	1	1	1	1	2*	6	4
SB(0)	1	1	1	1	2*	6	4
SB(+)	1	1	1	1	3*	7	3
MS(-)	1	1	1	1	1	5	5
MS(0)	1	1	1	1	1	5	5
MS(+)	1	1	1	1	1	5	5
MB(-)	1	1	2*	2*	5*	11	1
MB(0)	1	1	1	1	2*	6	4
MB(+)	1	1	1	2*	2*	7	3

Figure 3: Cell viability. Viability percentages are ranked and indicated by a corresponding color. The rank sum summarizes the level of cytotoxicity for each particle type. Bottom: Exemplary results from MTT assay over 24 h. Left side: HepG2 cells; right side: THP-1 cells. Data are means of three independent experiments with triplicate for each sample. Significance (*) was tested with one-way ANOVA and Tukey's post-hoc test ($p < 0.05$).

THP-1 cells seemed to be more sensitive towards SNPs, especially at higher concentrations. In both cell lines, MB(-) caused the highest viability decrease at 250 µg/mL. In THP-1 cells, this could be prevented when functionalizing the surface with primary amines. In contrary, HepG2 cells showed no change in the viability pattern when the surface charge was altered. In turn, a positive ζ -potential of solid big SNPs led to a more pronounced decrease of HepG2 cell viability. No viability decrease was shown for any MS samples. This may be attributed to the smaller size and prior dissolution of these SNPs (see below).

Oxidative stress and Hemolysis

We used the well-established DCFH-DA assay to determine oxidative stress induced by SNPs. After 1 h, 4 h, and 24 h, no elevated fluorescence signal was detected for any of the SNPs compared to the control (data not shown), indicating that there was no oxidative stress under the test conditions. However, the DCFH-DA assay only detects certain oxidative species and does not capture superoxide anion or hydrogen (Halliwell and Whiteman, 2004). We therefore aimed to confirm our results with a commercially available total ROS detection kit, with special emphasis placed on the superoxide anion. No oxidative stress was found (data not shown).

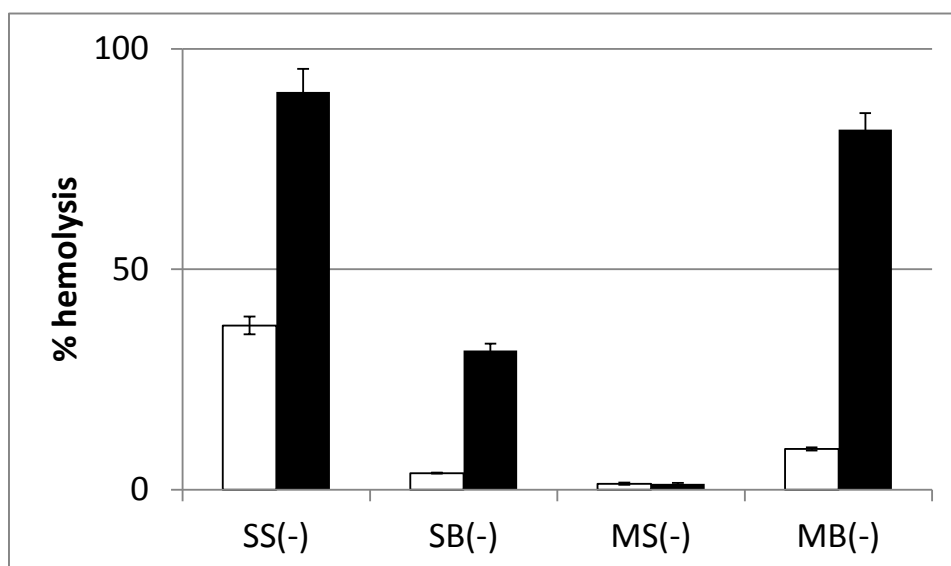


Figure 4: Concentration-dependent hemolysis of sheep erythrocytes in the presence of (-) SNPs. Data are mean \pm SD of three individual experiments with triplicates for each sample. Positively and neutrally charged SNPs did not cause any significant hemolysis (< 5%).

To further test if membrane interaction could lead to cytotoxicity, we performed the hemolysis assay. Indeed, all negatively charged SNPs showed hemolytic behavior in a concentration-dependent manner, except MS(-). The SS(-) showed hemolysis to a higher degree than their bigger counterparts (Figure 4).

Interference

For all assays, negligible adsorptive, catalytic, or optical interference was found. Previously, exocytosis of the water insoluble formazan crystals in the MTT assay lead to an overestimation of viability loss (Fischella

3.2. SAFETY OF SILICA NANOPARTICLES

et al., 2009). To confirm our MTT results, we also measured cellular viability with the MTS assay which uses a water-soluble indicator as opposed to the poorly water-soluble formazan. Our results showed no difference in cellular viability in the MTT and MTS assays.

Uptake into HepG2 and THP-1 cells

Both cell lines showed a time-dependent uptake of SNPs, whereas THP-1 cells internalized SNPs to a larger extent (Figure 5). These results were consistent with the confocal microscopy images. In Figure 5 C-F, the confocal images show a time-dependent uptake of SB(-) and MB(-) into THP-1 cells.

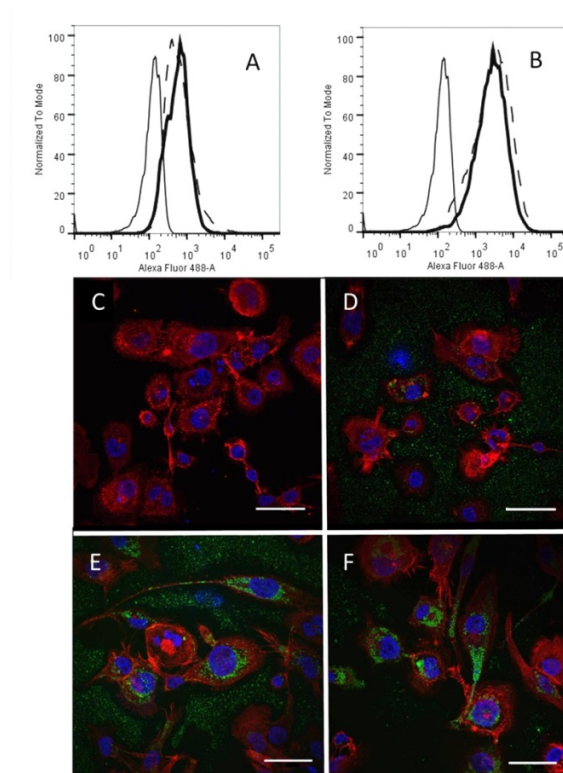


Figure 5: Quantitative and qualitative uptake of MB(-) and SB(-) into THP-1 cells. A, B: Flow cytometry results from time-dependent uptake in THP-1 cells. A: Uptake of MB(-) after 2 h (dashed) and 24 h (heavy line). Normal line = negative control. B: Uptake of SB(-) after 2 h (dashed) and 24 h (heavy line). Normal line = negative control. C-F: Representative confocal images of time-dependent uptake. Blue: nuclei, red: cytoskeleton, green: MB(-). C: 0 h; D: 2 h; E: 7 h, F: 24 h. Scale bar: 40 μm .

The uptake shift of the fluorescently labelled non-porous particles was stronger than the one of the mesoporous particles due to more rapid dissolution of porous silica particles, in this case MB(-). This dissolution was confirmed with live-cell imaging and the blue silicomolybdc assay (Figure 6A).

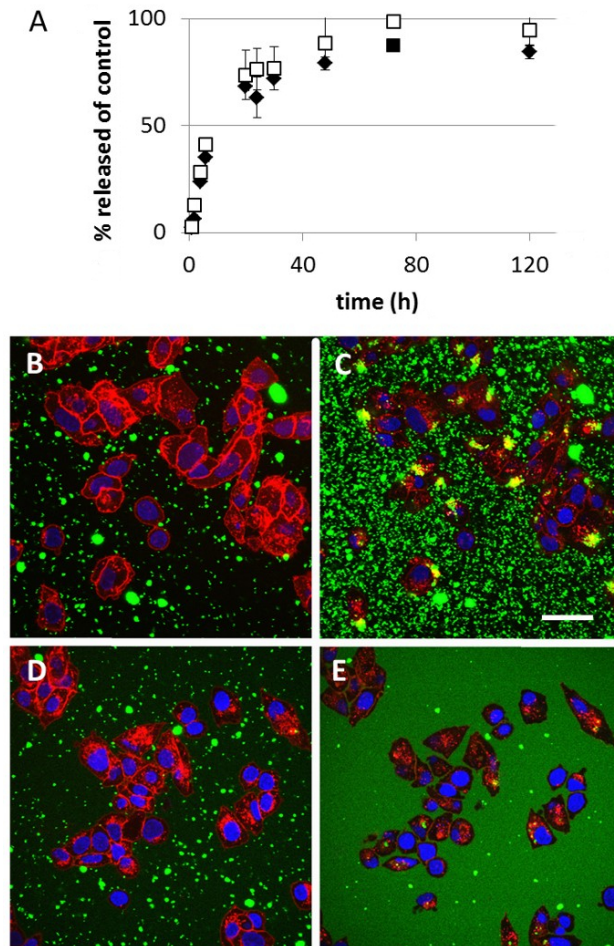


Figure 6: Degradation of mesoporous SNPs. A: Degradation data from blue silicomolybdc assay. Non-filled squares: MB(+); filled squares: MB(-). B-D: Representative qualitative live-cell experiments in HepG2. A: SB(-) in HepG2 after 15 min; B: SB(-) in HepG2 after 3 h; C: MB(-) in HepG2 after 15 min; D: MB(-) in HepG2 after 3 h. Scale bar is 40 μm (applies to all). Nuclei are shown in blue, cytoskeleton in red and SNPs in green.

Discussion

We assessed the physico-chemical properties of 12 SNPs with varying size, surface charge, and porosity and tested their cytotoxicity and oxidative stress in two cell lines. A phagocytic (THP-1) and non-phagocytic (HepG2) cell line allowed us to distinguish between different routes of cellular uptake of SNPs. Red blood cells, which are not capable of active uptake, were used to study SNP-membrane interaction. Nanoparticles are known to interfere with many test system and causing optical interference, catalytic interference, and adsorptive interference (Kroll et al., 2012). This can cause over- or underestimation of the readout of commonly applied toxicological assays. In the present study, appropriate measures were taken to avoid such artefacts.

Viability

Loss of cell viability occurred in a concentration-dependent manner and was dependent on the cell type and specific surface area of the SNPs. Almost all SNPs displayed a more marked loss of cell viability in THP-1 cells. Moreover, this effect was dependent on the incubation time, with longer incubation times showing a more marked loss of cell viability. The most extensive loss of cell viability occurred with MB(-) at 250 µg/mL.

Data in the literature show a tendency that smaller SNPs are more cytotoxic. However, this has been described for very small SNPs, e.g. those with a diameter of 16 nm (Napierska et al., 2012). This effect eventually plateaus for SNPs bigger than 100 nm (Lin and Haynes, 2010). However, it is difficult to compare results, since the route of synthesis of SNPs was not always specified. We found no viability decrease for the small mesoporous series due to prior dissolution. The dissolved species have shown to be essentially non-toxic (He et al., 2009).

The positive SNPs did not substantially affect cell viability, in line with reports on other nanoparticles with high positive charge (Zhang et al., 2011). Probably, the net surface charge density of the SNPs plays a crucial role in charge-mediated cytotoxicity as described above. There seems to be a ζ -potential threshold which was not reached with the highest amount of APTES used here, which might be due to the even distribution of APTES in the silica network as a result of the chosen co-condensation approach.

The non-porous nanoparticles induced little decrease in viability, and there appeared to be no influence of different surface groups. The viability decrease caused by MB(0) and MB(+) was not as marked, suggesting that the primary amines in this concentration prevented the loss of cell viability seen with the non-modified MB(-) in THP-1 cells.

Fischella et al. reported that there is an overestimation of viability decrease when using mesoporous SNPs in the MTT assay (Fischella et al., 2009). This is attributed to the exocytosed blue-violet formazan crystals. We therefore tested MB(-) with the MTS assay, which does not form crystals. For MB(-), we observed the same viability decrease in both assays. Moreover, we observed a strong morphological change in the cells exposed to MB(-). The observed difference to the literature may be due to another method to remove the template or in the cell lines used herein.

Oxidative stress

Since we used a sol-gel synthesis for all SNPs, oxidative stress induction was not expected because very few siloxanes are present on the surface of SNPs prepared with this method (Zhuravlev, 2000). This was confirmed by using two different assays, i.e. the commonly used DCFH-DA assay and a commercially available kit. None of our SNPs induced any oxidative stress in cell-free and cell-containing environments in either the DCFH-DA assay or the kit, which also captured superoxide anion. A recent study reported that annealing of the SNPs is predominantly responsible for oxidative stress in cells (Zhang et al., 2012). Our results are in agreement with those reported by Zhang et al. since our SNPs were synthesized by the sol-gel method. Oxidative stress associated with SNPs has mostly been described for very small particles (e.g. sized 16 nm), where the high surface curvature enhances the surface reactivity (Ahmad et al., 2012). Furthermore, Kim et al. showed that oxidative stress in macrophages was caused by small silica particles (15 nm) but not by solid SNPs of larger size (50 nm and 100 nm) (Kim et al., 2012). They concluded that the toxic mechanism shifts with particle size, with small-sized SNPs mediating ROS-induced toxicity.

Hemolysis

To study direct interaction of SNPs with a plasma membrane, we measured the hemolytic potential of the 12 SNPs. A clear dose-dependent relationship was observed for SS(-), SB(-), and MB(-). Non-porous SNPs with a "bare" silica surface are known to cause hemolysis (Slowing et al., 2009). This effect is abrogated

3.2. SAFETY OF SILICA NANOPARTICLES

when covering the surface with a polymer, i.e. poly ethylene glycol. In our case, we found no hemolysis when altering the surface with primary amines. In contrast, Yu et al. found enhanced RBC lysis for amine-modified SNPs (Yu et al., 2011). A reason for this discrepancy could be a certain threshold of positive charge/area unit. Since we synthesized our modified SNPs with the co-condensation method, we assume that the charge density on the surface was not sufficient to induce hemolysis, which is in line with published data (Yu et al., 2011; Yildirim et al., 2013).

The hypothesized hemolytic mechanism for solid SNPs is an electrostatic interaction between the silanol groups on the surface of the SNP and the choline headgroup in the phospholipids (Slowing et al., 2009).

In our study, MB(-) caused severe hemolysis in a dose-dependent manner, whereas MS(-) did not affect the RBC membrane. Assuming that smaller particles are more likely to cause hemolysis, it is puzzling that MS(-) did not induce RBC lysis. We attributed this to the prior dissolution of the SNPs. Dissolution experiments in live-cell incubations showed severe degradation after 3 h only, as shown in Figure 6 (B-D). In addition, the blue silicomolybdc assay showed dissolution of both MB(-) and MB(+). Since the SNPs of the MS series had a higher specific surface area, we assumed that dissolution was even faster than dissolution of SNPs of the MB series. Regarding hemolysis caused by mesoporous SNPs, there are contradictory results found in the literature. Slowing et al. found no hemolysis for mesoporous SNPs with a size and zeta potential comparable to the ones we synthesized (Slowing et al., 2009). However, Lin et al. described concentration- and size-dependent hemolytic properties of mesoporous SNPs, with a weaker hemolytic potential seen with larger SNPs (Lin and Haynes, 2010). Their results are in agreement with our finding that mesoporous silica particles can induce hemolysis, although we observed a much stronger hemolytic effect for particles of similar size and zeta potential.

Finally, residual surfactant (CTAB) may cause hemolysis, but TGA and FTIR confirmed the complete removal of the surfactant template in our study. Lin et al. investigated the effects of residual CTAB on hemolysis and found no correlation (Lin and Haynes, 2010). Thus, the mechanism of the effect of SNPs on RBCs remains insufficiently well understood and warrants further research.

Conclusions

We synthesized and analyzed 12 different SNPs systematically. Due to a step-by-step change of the physico-chemical parameters (size, surface charge and surface area) it was possible to investigate the influence of each parameter separately. However, cytotoxicity and also hemolysis do not seem to be restricted to only one specific physico-chemical parameter. Cell viability decrease was dependent on the concentration, surface charge, time, and cell line used. Cytotoxicity of SNPs was more pronounced at higher concentrations. We found no oxidative stress induction for any of the tested SNPs. Here, only negatively charged SNPs could induce hemolysis, whereas the introduction of primary amines into the SNPs reduced the hemolytic effect, irrespective of their size or specific surface area. SNPs which showed no effect were shown to degrade fast. We found no to negligible interference potential of all tested SNPs. Since all SNP types were synthesized and characterized in house, this study provides a comparable overview of one nanomaterial with different physico-chemical parameters and its biological interaction. The study can be a guideline for designing of safe drug delivery systems. Ongoing research is dedicated to elucidating the biophysical interaction with lipid membranes.

We propose that our standardized SNPs serve as a readily available reference material for nanotoxicological investigations.

Acknowledgments

We thank Marcel Düggelin (Zentrum für Mikroskopie, University of Basel) for his support with SEM and Dr. Silvia Rogers for editorial assistance. J.H. and H.K. obtained financial support from the Swiss Centre of Applied Human Toxicology (SCAHT). Financial support from the Centre of Functional Materials (provided to D.S.K.) and the Academy of Finland (provided to D.S.K. [project 260599] and J.M.R [project 278812]) is gratefully acknowledged.

Disclosure

The authors have no conflicts of interest.

References

- Ahmad J, Ahamed M, Akhtar MJ, Alrokayan SA, Siddiqui MA, Musarrat J, Al-Khedhairy AA. 2012. Apoptosis induction by silica nanoparticles mediated through reactive oxygen species in human liver cell line HepG2. *Toxicol Appl Pharmacol* 259:160–168.
- Bailey MM, Berkland CJ. 2009. Nanoparticle formulations in pulmonary drug delivery. *Med Res Rev* 29:196–212.
- Barandeh F, Nguyen P-L, Kumar R, Iacobucci GJ, Kuznicki ML, Kosterman A, Bergey EJ, Prasad PN, Gunawardena S. 2012. Organically Modified Silica Nanoparticles Are Biocompatible and Can Be Targeted to Neurons In Vivo. *PLoS ONE* 7:e29424.
- Byrne JD, Baugh JA. 2008. The significance of nanoparticles in particle-induced pulmonary fibrosis. *McGill J Med MJM* 11:43–50.
- Casey A, Herzog E, Lyng FM, Byrne HJ, Chambers G, Davoren M. 2008. Single walled carbon nanotubes induce indirect cytotoxicity by medium depletion in A549 lung cells. *Toxicol Lett* 179:78–84.
- Coradin T, Eglin D, Livage J. 2004. The silicomolybdic acid spectrophotometric method and its application to silicate/biopolymer interaction studies. *J Spectrosc* 18:567–576.
- Donaldson K, Murphy FA, Duffin R, Poland CA. 2010. Asbestos, carbon nanotubes and the pleural mesothelium: a review of the hypothesis regarding the role of long fibre retention in the parietal pleura, inflammation and mesothelioma. *Part Fibre Toxicol* 7:5.
- Ensign LM, Cone R, Hanes J. 2012. Oral drug delivery with polymeric nanoparticles: The gastrointestinal mucus barriers. *Adv Drug Deliv Rev* 64:557–570.
- Escobar-Chavez J, Diaz-Torres R, Rodriguez-Cruz IM, Dominguez-Delgado, Sampere-Morales, Angeles-Anguiano, Melgoza-Contreras. 2012. Nanocarriers for transdermal drug delivery. *Res Rep Transdermal Drug Deliv*:3.
- Fischella M, Dabboue H, Bhattacharyya S, Saboungi M-L, Salvétat J-P, Hevor T, Guerin M. 2009. Mesoporous silica nanoparticles enhance MTT formazan exocytosis in HeLa cells and astrocytes. *Toxicol. Vitro Int J Publ Assoc BIBRA* 23:697–703.
- Ge C, Du J, Zhao L, Wang L, Liu Y, Li D, Yang Y, Zhou R, Zhao Y, Chai Z, Chen C. 2011. Binding of blood proteins to carbon nanotubes reduces cytotoxicity. *Proc Natl Acad Sci* 108:16968–16973.
- Gu J, Fan W, Shimojima A, Okubo T. 2007. Organic–Inorganic Mesoporous Nanocarriers Integrated with Biogenic Ligands. *Small* 3:1740–1744.
- Halliwell B, Whiteman M. 2004. Measuring reactive species and oxidative damage in vivo and in cell culture: how should you do it and what do the results mean? *Br J Pharmacol* 142:231–255.
- Han L, Wei H, Tu B, Zhao D. 2011. A facile one-pot synthesis of uniform core–shell silver nanoparticle@mesoporous silica nanospheres. *Chem Commun* 47:8536–8538.
- He Q, Zhang Z, Gao Y, Shi J, Li Y. 2009. Intracellular localization and cytotoxicity of spherical mesoporous silica nano- and microparticles. *Small* 5:2722–2729.
- Karaman DS, Desai D, Senthilkumar R, Johansson EM, Rått N, Odén M, Eriksson JE, Sahlgren C, Toivola DM, Rosenholm JM. 2012. Shape engineering vs organic modification of inorganic nanoparticles as a tool for enhancing cellular internalization. *Nanoscale Res Lett* 7:358.

3.2. SAFETY OF SILICA NANOPARTICLES

- Kettiger H, Schipanski A, Wick P, Huwyler J. 2013. Engineered nanomaterial uptake and tissue distribution: from cell to organism. *Int J Nanomedicine* 8:3255–3269.
- Kim S, Jang J, Kim H, Choi H, Lee K, Choi I-H. 2012. The Effects of Silica Nanoparticles in Macrophage Cells. *Immune Netw* 12:296–300.
- Kroll A, Dierker C, Rommel C, Hahn D, Wohlleben W, Schulze-Isfort C, Göbber C, Voetz M, Hardinghaus F, Schnekenburger J. 2011. Cytotoxicity screening of 23 engineered nanomaterials using a test matrix of ten cell lines and three different assays. *Part Fibre Toxicol* 8:9.
- Kroll A, Pillukat MH, Hahn D, Schnekenburger J. 2012. Interference of engineered nanoparticles with in vitro toxicity assays. *Arch Toxicol* 86:1123–1136.
- Krug HF, Wick P. 2011. Nanotoxicology: An Interdisciplinary Challenge. *Angew Chem Int Ed* 50:1260–1278.
- Lin Y-S, Haynes CL. 2010. Impacts of Mesoporous Silica Nanoparticle Size, Pore Ordering, and Pore Integrity on Hemolytic Activity. *J Am Chem Soc* 132:4834–4842.
- Meißner T, Potthoff A, Richter V. 2009. Suspension characterization as important key for toxicological investigations. *J Phys Conf Ser* 170:012012.
- Napierska D, Rabolli V, Thomassen LCJ, Dinsdale D, Princen C, Gonzalez L, Poels KLC, Kirsch-Volders M, Lison D, Martens JA, Hoet PH. 2012. Oxidative Stress Induced by Pure and Iron-Doped Amorphous Silica Nanoparticles in Subtoxic Conditions. *Chem Res Toxicol* 25:828–837.
- Nel A, Xia T, Maedler L, Li N. 2006. Toxic potential of materials at the nanolevel. *Science* 311:622–627.
- Ow H, Larson DR, Srivastava M, Baird BA, Webb WW, Wiesner U. 2004. Bright and Stable Core–Shell Fluorescent Silica Nanoparticles. *Nano Lett* 5:113–117.
- Rosenholm JM, Peuhu E, Eriksson JE, Sahlgren C, Lindén M. 2009. Targeted intracellular delivery of hydrophobic agents using mesoporous hybrid silica nanoparticles as carrier systems. *Nano Lett* 9:3308–3311.
- Dos Santos T, Varela J, Lynch I, Salvati A, Dawson KA. 2011. Quantitative Assessment of the Comparative Nanoparticle-Uptake Efficiency of a Range of Cell Lines. *Small* 7:3341–3349.
- Sayes CM, Reed KL, Warheit DB. 2007. Assessing Toxicity of Fine and Nanoparticles: Comparing In Vitro Measurements to In Vivo Pulmonary Toxicity Profiles. *Toxicol Sci* 97:163–180.
- Seeland S, Toeroek M, Kettiger H, Treiber A, Hafner M, Huwyler J. 2013. A cell-based, multiparametric sensor approach characterises drug-induced cytotoxicity in human liver HepG2 cells. *Toxicol In Vitro* 27:1109–1120.
- Slowing II, Wu C-W, Vivero-Escoto JL, Lin VS-Y. 2009. Mesoporous Silica Nanoparticles for Reducing Hemolytic Activity Towards Mammalian Red Blood Cells. *Small* 5:57–62.
- Sohaebuddin SK, Thevenot PT, Baker D, Eaton JW, Tang L. 2010. Nanomaterial cytotoxicity is composition, size, and cell type dependent. *Part Fibre Toxicol* 7:22.
- Stoeber W, Fink A, Bohn E. 1968. Controlled growth of monodisperse silica spheres in the micron size range. *J. Colloid Interface Sci* 26:62–69.
- Tao Z, Toms BB, Goodisman J, Asefa T. 2009. Mesoporosity and functional group dependent endocytosis and cytotoxicity of silica nanomaterials. *Chem Res Toxicol* 22:1869–1880.

Vranic S, Boggetto N, Contremoulins V, Mornet S, Reinhardt N, Marano F, Baeza-Squiban A, Boland S. 2013. Deciphering the mechanisms of cellular uptake of engineered nanoparticles by accurate evaluation of internalization using imaging flow cytometry. *Part Fibre Toxicol* 10:2.

Wu S-H, Hung Y, Mou C-Y. 2011. Mesoporous silica nanoparticles as nanocarriers. *Chem Commun* 47:9972.

Yildirim A, Ozgur E, Bayindir M. 2013. Impact of mesoporous silica nanoparticle surface functionality on hemolytic activity, thrombogenicity and non-specific protein adsorption. *J Mater Chem B* 1:1909–1920.

Yu T, Malugin A, Ghandehari H. 2011. Impact of Silica Nanoparticle Design on Cellular Toxicity and Hemolytic Activity. *ACS Nano* 5:5717–5728.

Zhang H, Dunphy DR, Jiang X, Meng H, Sun B, Tarn D, Xue M, Wang X, Lin S, Ji Z, Li R, Garcia FL, Yang J, Kirk ML, Xia T, Zink JI, Nel A, Brinker CJ. 2012. Processing pathway dependence of amorphous silica nanoparticle toxicity: colloidal vs pyrolytic. *J Am Chem Soc* 134:15790–15804.

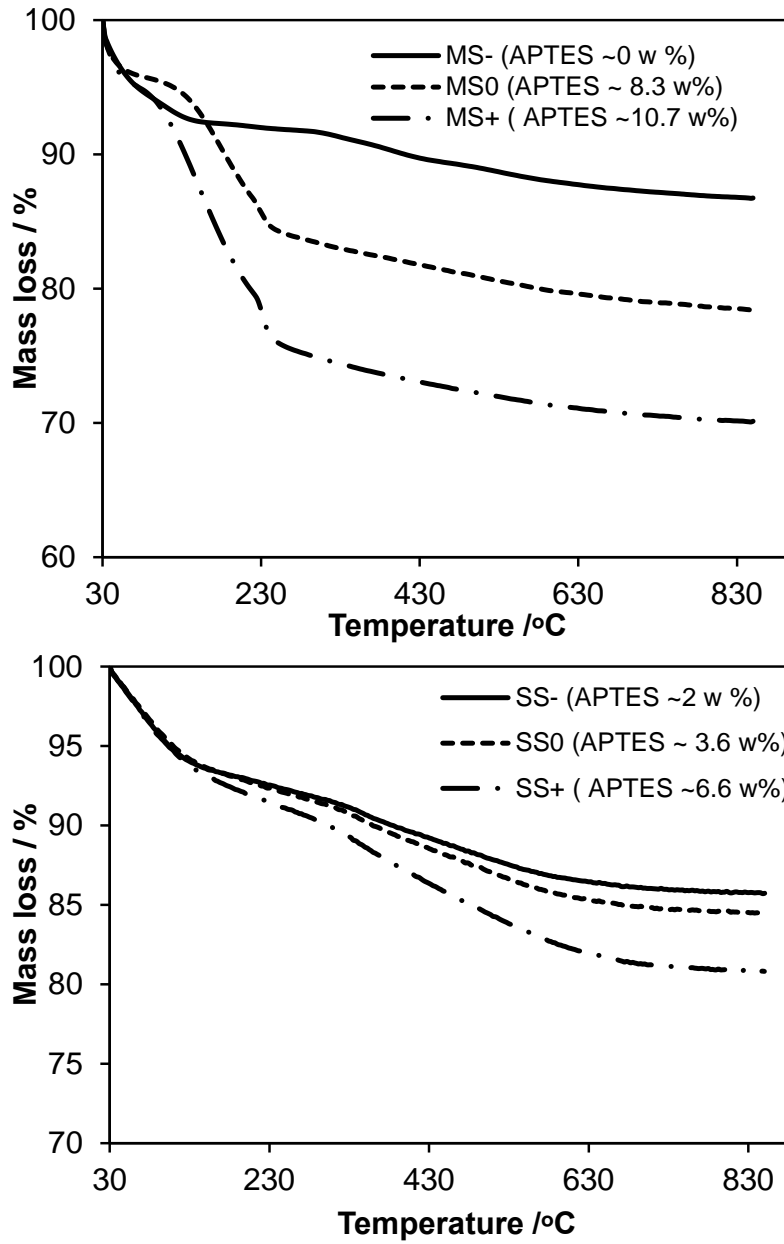
Zhang H, Xia T, Meng H, Xue M, George S, Ji Z, Wang X, Liu R, Wang M, France B, Rallo R, Damoiseaux R, Cohen Y, Bradley KA, Zink JI, Nel AE. 2011. Differential Expression of Syndecan-1 Mediates Cationic Nanoparticle Toxicity in Undifferentiated versus Differentiated Normal Human Bronchial Epithelial Cells. *ACS Nano* 5:2756–2769.

Zhuravlev LT. 2000. The surface chemistry of amorphous silica. Zhuravlev model. *Colloids Surf Physicochem Eng Asp* 173:1–38.

Supplementary information

Thermogravimetric analysis (TGA) was carried out to define the amount of APTES incorporated into the SNPs. Measurements (TGA-Netzsch STA 449F1 Jupiter) were carried with the resolution of is 0.025 µg under air atmosphere and in alumina crucibles, at the scanning rate of 10K/min. During the measurements, thermograms were recorded within the range of 30–900° C, and the results were analyzed with the software Proteus 5.1. Successful removal of CTAB template was confirmed with TGA (Figure S1) and FTIR measurements (Figure S2).

Figure S1: TGA results for all SNPs



3.2. SAFETY OF SILICA NANOPARTICLES

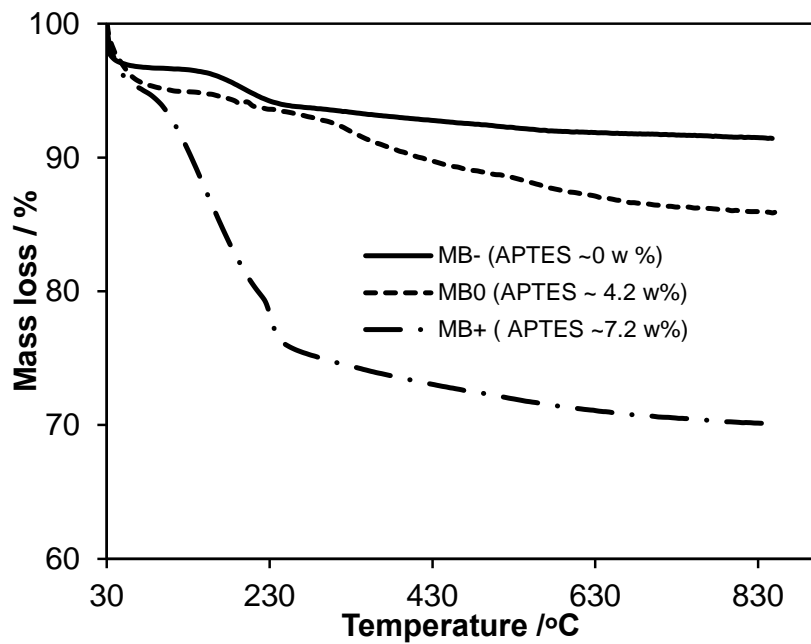
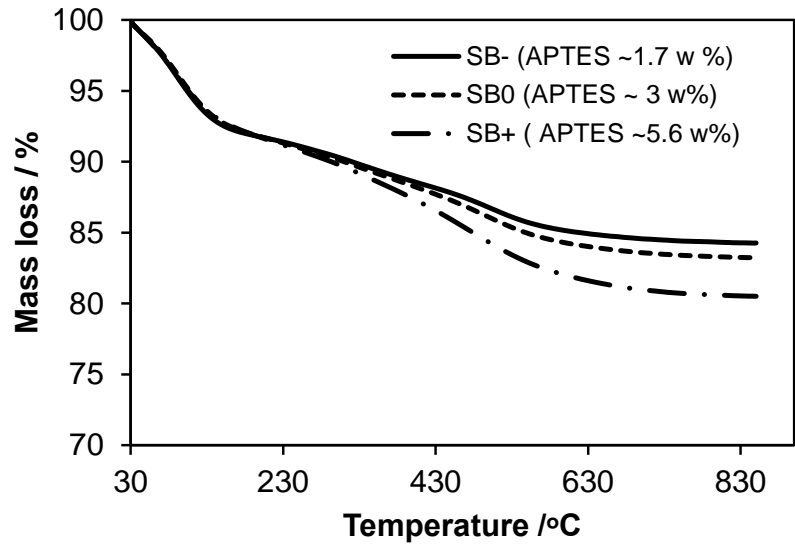
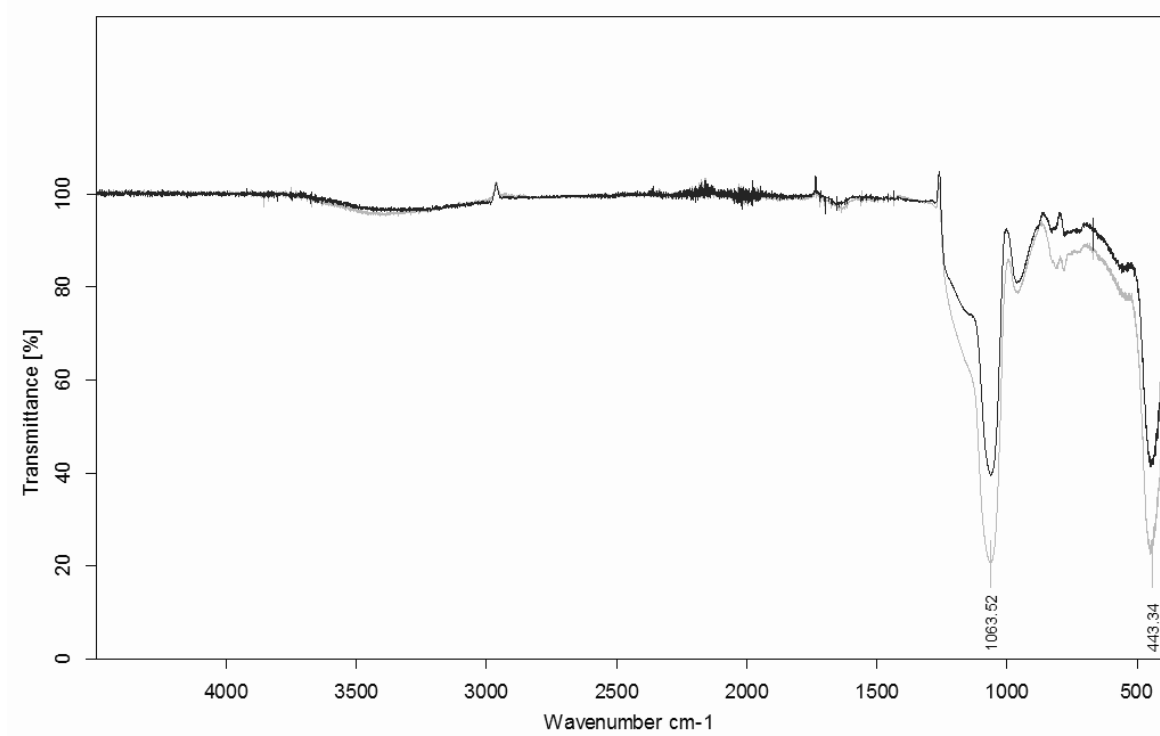


Figure S2: Template removal from MB(-) with FTIR. Black spectra: extracted MB(-). Grey: surfactant free control MB(-). No surfactant was left in the MB(-).



3.3 Hemolysis of silica nanoparticles: a mechanistic approach

Hemolytic effect of silica nanoparticles: a mechanistic approach

Helene Kettiger¹, Barbara Perrone², Jörg Huwyler¹, Gabriela Quebatte¹

¹ Department of Pharmaceutical Sciences, University of Basel, Switzerland

² Bruker BioSpin AG, Industriestrasse 26, 8117 Fällanden, Switzerland

Contribution H.Kettiger: concept, author, experimental part (synthesis, flow cytometry)

Drafted manuscript *Target journal: Particle and Fibre Toxicology*

Hemolysis by silica nanoparticles: a mechanistic approach

Helene Kettiger¹, Barbara Perrone², Jörg Huwyler¹, and Gabriela Québatte¹

¹Department of Pharmaceutical Sciences, Division of Pharmaceutical Technology, University of Basel, Basel, Switzerland

²Bruker BioSpin AG, Industriestrasse 26, 8117 Fällanden, Switzerland

ABSTRACT

Silica nanoparticles are proposed as drug delivery systems or imaging agents. However, bare silica nanoparticles are known to induce hemolysis. To date, two mechanisms are hypothesized in the literature, namely the electrostatic interaction between surface silanols and quaternary ammonia of the choline head groups in the plasma membrane. The other mechanism describes that hemolysis of silica nanoparticles is a consequence of reactive oxygen generation.

Here, we focused on the first approach and used biophysical techniques to investigate the interaction of hemolytic and non-hemolytic silica nanoparticles with a model membrane. We have studied this interaction with dye-leakage assay, dynamic light scattering, isothermal titration calorimetry, solid state nuclear magnetic resonance, and flow cytometry.

Our results showed that the electrostatic interaction between hemolytic silica nanoparticles and model membranes is negligible. We observed a rather strong adsorptive process and agglomeration upon mixing silica nanoparticles with model membrane vesicles. Furthermore, data from solid state nuclear magnetic resonance suggest that smaller lipid species were formed in presence of hemolytic silica nanoparticles. The presence of these species was assessed with flow cytometry.

The overall hemolytic effect mediated by a membrane interaction in the given set up is relatively low (10-20%). Other mechanisms such as osmotic pressure difference or interaction with membrane proteins may play a more important role in the hemolytic process.

Keywords: Hemolysis, silica nanoparticles, isothermal titration calorimetry, solid state nuclear magnetic resonance

INTRODUCTION

Silica nanoparticles (SNPs) have been long known in pharmaceutical technology. There, Aerosil[®] is used as flowing agent in solid dosage forms since almost 100 years. But only recently, SNPs were also proposed to use as drug delivery systems (DDS) or imaging agents (Rosenholm et al., 2009; Ow et al., 2005). As DDS, different routes of uptake are possible including skin penetration, oral absorption, upon inhalation or via intravenous (i.v.) injection.

3.3. HEMOLYSIS OF SILICA NANOPARTICLES: A MECHANISTIC APPROACH

The i.v. administration is the preferred route for nanoparticulate DDS since there is no need to cross an additional barrier like the gut wall or the blood-air interface (Bertrand and Leroux, 2012).

Upon i.v. injection, the nanoparticles come in direct contact with blood constituents as red blood cells (RBC) and plasma proteins. Depending on their physico-chemical properties, the nanoparticles interact after few seconds with these constituents (Kettiger et al., 2013). One of these interactions is the RBC-nanoparticles interaction. This interaction can cause hemolysis, i.e. severe damage to RBC. Abundant hemolysis *in vivo* causes different inherent diseases (Misztal and Tomasiak, 2011). This poses the question of the SNPs safety and their future use as DDS. Small nanoparticles have shown to passively diffuse through the lipid bilayer (Wang et al., 2012), while others undergo active uptake (Kettiger et al., 2013). In the case of RBC, no active uptake is involved and hence, the hemolytic effect is probably caused by an interaction with the lipid bilayer (Rothen-Rutishauser et al., 2006). Various studies showed the hemolytic effect of SNPs (Lin and Haynes, 2010; Zhao et al., 2011; Slowing et al., 2009). However, the underlying hemolytic mechanism of SNPs remains unknown.

So far, two different mechanisms of hemolysis are predominant in the literature. The first one is an electrostatic interaction with the silanol groups (Si-OH) of the silica surface with the quaternary ammonium on the lipid bilayer. (Slowing et al., 2009; Depasse and Warlus, 1976). The second one relies on the capacity to cause oxidative stress from siloxane bond distortion, where the reactive oxygen species (ROS) are responsible for the hemolysis via oxidation of the phospholipids in the cellular membrane (Zhang et al., 2012a).

Isothermal titration calorimetry can be used to study interactions of various kinds. These include protein-protein interactions, peptide-membrane interactions, and recently also protein-nanoparticles interactions (Cedervall et al., 2007). It is possible to determine the enthalpy of the interactions. When modifying the experimental setup, it is possible to determine the type of binding.

Solid state ^{31}P NMR spectroscopy is a technique which allows studying the structure and dynamics of both model and biological lipid membranes. Phospholipids are the major components of cell membranes and the natural abundance of the ^{31}P nucleus is 100%, therefore ^{31}P NMR allows studying phospholipid membranes and to distinguish between bilayer, hexagonal structure or micelles as each of the lipid phase is characterized by its typical ^{31}P NMR spectrum with defined the chemical shift anisotropy (Seelig, 1978; Sauder et al., 2011).

Solid state ^2H NMR reveals lipid order and packing of deuterium labeled phospholipids. The phospholipid molecule can be specifically labeled at the headgroup, the glycerol backbone or the fatty acyl chains. The natural abundance of deuterium is very low and deuterium magnetic resonance in the ^2H NMR signal can be easily assigned to the deuterium labeled site. In an unorientated sample the deuterium quadrupole interactions give characteristic powder-pattern

spectra with two distinct peaks separated by the deuterium quadrupole splitting and provide structural information about the lipid system.

We have shown previously, that amorphous SNPs with a primary size of 85 nm cause hemolysis. The same particles did not show any oxidative stress in cellular and in non-cellular environment. We were therefore exclusively interested in the electrostatic mechanism. To investigate this, we have used different approaches, namely the dye leakage assay, dynamic light scattering (DLS), isothermal titration calorimetry (ITC), solid state nuclear magnetic resonance (ssNMR), and flow cytometry. With these methods, we studied the interaction between SNP surface groups (silanols) with a choline-rich model membrane. As a non-hemolytic SNP control, we used surface modified SNPs, which have previously shown to be non-hemolytic. All experiments were conducted under physiological conditions.

MATERIALS AND METHODS

Materials

All chemicals for the nanoparticle synthesis were obtained from Sigma-Aldrich (Buchs, Switzerland). All lipids, including the fluorescent tail-labeled lipid (1-oleoyl-2-{6-(7-nitro-2-1,3-benzoxadiazol-4-yl)amino}hexanoyl)-sn-glycero-3-phosphocholine) and lipids for ssNMR (1-Palmitoyl-2-oleoyl-sn-glycero-3-phosphatidylcholine-1,1,2,2-d₄ (d₄-POPC) and 1-Palmitoyl-d₃₁-2-oleoyl-sn-glycero-3-phosphatidylcholine (d₃₁-POPC)) were obtained from Avanti Polar Lipids (Alabaster, USA). 8-Aminonaphthalene-1,3,6-Trisulfonic Acid, Disodium Salt (ANTS) and p-Xylene-Bis-Pyridinium Bromide (DPX) were obtained from Life Technologies, Switzerland.

Synthesis and characterization of silica nanoparticles

The SNPs were synthesized and characterized as follows. Briefly, the reaction solutions had the molar composition of 1 TEOS: 0.087 NH₃: 64.3 EtOH: 27.8 H₂O. Alteration of SNPs net surface charge was carried out by direct incorporation of amine groups through the co-condensation of aminosilanes (3-Aminopropyl)triethoxysilane during the synthesis (10 mol% of existing TEOS). The mixture was stirred under ambient conditions for 3h. The SNPs were collected by centrifugation and washed 3 times thoroughly with EtOH and dried overnight in a vacuum oven at ambient temperature. The resultant particles were analyzed with dynamic light scattering (DLS) to obtain their hydrodynamic diameters in DPBS and HEPES, their dry state diameter was measured by transmission electron microscopy (TEM). We also measured the specific surface area by the Brunnauer-Emmet-Teller (BET) method. The zeta potential was measured by electrophoretic light scattering from the Doppler shift of scattered light (Delsa Nano C, Beckman, Nyon, Switzerland).

Preparation of lipid vesicles

For our studies we used small unilamellar vesicles (SUVs, mean diameter 20 nm), large unilamellar vesicles (LUVs, mean diameter 100 nm), and multi lamellar vesicles (LMVs, mean diameter

3.3. HEMOLYSIS OF SILICA NANOPARTICLES: A MECHANISTIC APPROACH

1000 nm). For SUVs, LUVs, and non-labeled MLVs, a defined amount of 1-palmitoyl-2-oleoyl-sn-glycero-3-phosphocholine (POPC) was dried from a stock solution in chloroform with a gentle stream of nitrogen followed by vacuum overnight. For the preparation of the SUVs, we rehydrated the film with DPBS containing 150 mM NaCl. Then, the suspension was sonicated using a titanium tip ultrasonicator (Branson Sonifier, Danbury, CT) until an almost clear solution was obtained (45 min). Metal debris from the sonicator tip was removed by centrifugation for 4 min in an Eppendorf 5415 C benchtop centrifuge (Vaudaux-Eppendorf AG, Schönenbuch, Switzerland).

LUVs for the dye leakage assay were prepared as follows. The desired lipid films (POPC; POPC-sphingomyelin; POPC-cholesterol; POPC-sphingomyelin-cholesterol) were prepared as described for the SUVs. The lipid films were then rehydrated with a mixture of a fluorophore (ANTS, 12.5 mM) and a quencher (DPX, 45 mM) in DPBS with 150 mM NaCl. They were subjected to 5 freeze-thaw cycles and extruded through a 200 nm pore size filter. Non-incorporated dye was removed from the LUVs with size-exclusion chromatography on a Superose 6 prep column (GE Healthcare) eluting with 10 mM DPBS, pH 7.4.

MLVs were prepared as follows for flow cytometry experiments. Lipids (POPC and fluorescent tail lipid, 0.5%) were dried as above and MLVs were obtained by 5 freeze-thaw cycles and vortex in between. The film was rehydrated with the SNPs already in buffer. For ssNMR, MLVs were prepared as follows. Twenty to 25 mg of d4-POPC or d31-POPC were dried from a stock solution in chloroform with a gentle stream of nitrogen followed by a high vacuum for several hours. The lipid films were dispersed in 400 μ L of buffer (10 mM Hepes, 150 mM NaCl in deuterium depleted water, pH 7.4) containing different amount of SNPs. The samples were vortexed, freeze-thawed (5 times) and vortexed again.

Dye leakage assay and dynamic light scattering

The dye leakage assay has been performed as described earlier (Sauder et al., 2011). We mixed the LUVs with hemolytic and non-hemolytic SNPs in a weight ratio of 1:1 and 1:0.15. The fluorescent dye released from the LUVs was monitored over time at excitation wavelength of 360nm and emission of 518nm. The maximum release was obtained by adding 25 μ L of a 5% Triton X-100 solution and was set 100% leakage. The relative leakage was calculated as $RFU_{\text{sample}} - RFU_0 / RFU_{\text{max}} - RFU_0$, where RFU is the relative fluorescence unit.

We have measured the degree of agglomeration of POPC-SUVs with DLS to obtain insight into the SNPs:SUVs ratios, where agglomeration starts. We used the Beckman-Coulter Delsa Nano C (Beckman Coulter, Nyon, Switzerland). The data was plotted volume-weighted.

Isothermal titration calorimetry

A MicroCal VP-ITC (MicroCal, Northampton, MA) was used. Lipid-into-SNPs titrations were performed by injection of 4 – 10 μ L aliquots of lipid suspension at a concentration of 3.8 mg/mL – 7.6 mg/mL into the calorimeter cell ($V_{\text{Cell}} = 1.4105$ mL) containing SNPs at a concentration of

C_{SNPs} 0.5 – 1.0 mg/mL. The heats of dilution were determined in control titrations by injecting the lipid suspension into buffer. The heats of dilution were small and were included in the final analysis. Raw data were processed using the Origin software provided with the instrument.

Solid state NMR

Solid-state NMR experiments were performed on a Bruker Advance III 500 MHz spectrometer (Bruker BioSpin AG, Fällanden, Switzerland). Solid-state ^{31}P NMR spectra were recorded at 202 MHz using a Hahn-echo sequence with broadband proton decoupling (SPINAL64) and a recycle delay of 5 s. The excitation and refocusing pulse lengths were 4.25 μs and 8.50 μs respectively. 2048 free induction decays (FID) were accumulated and prior to Fourier transformation the FIDs were multiplied with an exponential window corresponding to a 100 Hz line broadening. Solid-state ^2H NMR experiments were recorded at 76.8 MHz using the quadrupole echo technique. The excitation pulse had a length of 3.5 μs . Four thousands (4096) FIDs were accumulated with a recycle delay of 1 s.

Flow cytometry

MLVs and SNPs (1:1 weight ratio) mixtures were prepared as described for ssNMR experiments. Then, the SNPs were subsequently removed by centrifugation (15'000g, 10min, 4° C). The supernatant was analyzed by flow cytometry (FACS Canto II). We first lowered the threshold and added previously prepared LUVs (100 nm by DLS, PDI about 0.1) to set an appropriate gate for our target vesicles. Between the samples, the flow chamber was cleaned with filtered DPBS to exclude sample-to-sample spill-over. Then, we set a gate where no particles were detected and counted the events in the 100 nm-frame for 120 s by forward scatter area and sideward scatter area.

RESULTS

Dye leakage assay

We have tested POPC alone, POPC with cholesterol, POPC with sphingomyelin, and POPC with sphingomyelin and cholesterol. Upon pore formation, distortion, the close proximity of quencher and fluorophore inside the vesicles is canceled resulting in a fluorescent signal in the probe. For hemolytic SNPs, we observed a total dye release up to 10% (data not shown) with POPC LUVs. For non-hemolytic SNPs we did not observe any dye-leakage from the LUVs. Moreover, the lipid composition of the LUVs did not alter the % leakage for hemolytic and non-hemolytic SNPs. It has been earlier reported that nanoparticles can interfere with dyes by non-specific adsorption (Kroll et al., 2009). We checked for adsorptive interference, i.e. if the free dye could bind to the nanoparticles and hence produce false negative data. This was not the case for hemolytic and non-hemolytic SNPs.

Dynamic light scattering

Instead of large unilamellar vesicles with the size of about 100 nm, we have chosen small unilamellar vesicles, with a size of about 30 nm. The reason for this choice was the discrimination

3.3. HEMOLYSIS OF SILICA NANOPARTICLES: A MECHANISTIC APPROACH

in size. DLS allows a size discrimination if the diameters are three times bigger or smaller, otherwise, it will simply display a polydisperse population. DLS results can be seen in 1 Figure 1

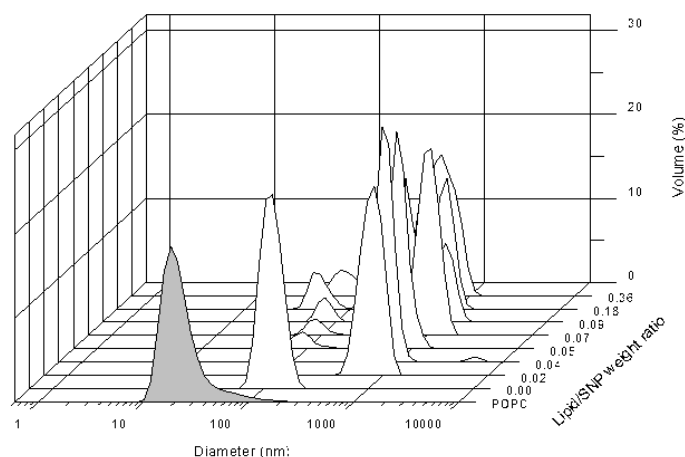


Figure 1. POPC SUVs into hemolytic SNP. This figure shows the size distribution of SUVs alone (grey) and hemolytic SNP alone (second peak on Y-axis) by volume distribution. Different weight ratios of lipid to HS are displayed along the Y-axis with an increasing ratio up to 0.36.

shows, that already upon a small hemolytic SNP to SUV ratio, heavy agglomeration is occurring. The DLS results indicated that upon mixing hemolytic SNPs with SUVs, an agglomeration process is starting at even low SUV concentration and there was no further size increase upon addition of more SUVs. With increasing lipid content, a second population starts to show at 100 nm. This population may either be single SNPs or lipid membrane wrapped SNPs. The data is volume-weighted in order not to overestimate the hemolytic SNP population.

Isothermal titration calorimetry (ITC)

Interaction of hemolytic and non-hemolytic SNPs with lipid membranes were monitored using ITC technique. Figure 2 shows a calorimetric heat flow trace (Figure 2A and 2C) and the corresponding titration curve (Figure 2B and 2D) obtained at 25 °C by titration of 0.5 mg/mL hemolytic SNPs with 4 μ L aliquots of POPC SUVs suspension (3.8 mg/mL). The integrated heats in Figure 2C and 2D represent the net heats of each injection after correcting for the heats of dilution of the POPC SUVs obtained in separate lipid-into-buffer titration. Figure 2 shows that the reaction at 25 °C is exothermic. The reaction comes to an end after three injections when all SNPs are bound to the injected lipid. The heat of reaction is given by $\sum h_i / (C_{\text{SNPs}} \times V_{\text{cell}})$ where C_{SNPs} is the SNPs concentration in the calorimeter cell. For the example given in Figure 2A the cumulative heat released is $\sum h_i = -22.8 \mu\text{cal}$ and the reaction enthalpy is $\delta H_{0\text{SNP}} = -0.026 \text{ cal/g}$. From calorimetric trace the calculated amount of lipid which binds 1 mg of particles is 0.043 mg (57.1 nmol). We have performed calorimetric titrations at different temperatures in the range of 15-45 °C and the reaction was exothermic at all temperature tested. However no temperature dependence on the enthalpy of hemolytic particles binding to POPC was observed.

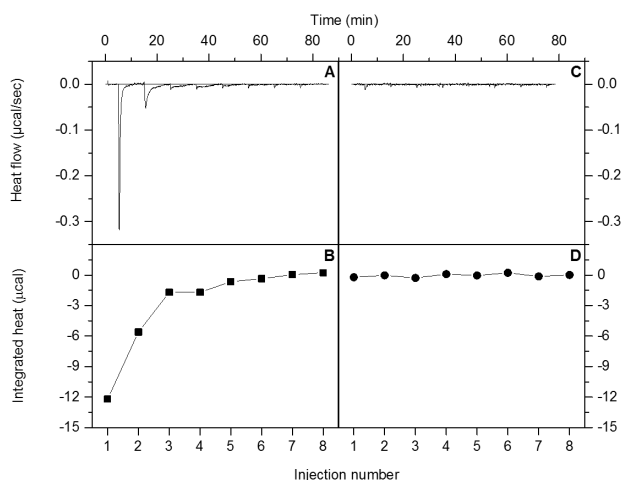


Figure 2. Titration of POPC SUVs into SNPs at 25 °C. (A) Titration of 3.8 mg/mL POPC SUVs into a suspension of hemolytic SNPs (0.5 mg/mL). Each peak corresponds to the injection of 4 μ L of lipid suspension into the cell. (B) Heats of reaction integrated from the calorimetric trace (A) as a function of injection number. (C) Calorimetric trace obtained by titration of 7.6 mg/mL POPC SUVs into a suspension of non-hemolytic SNPs (1.0 mg/mL). Each peak corresponds to the injection of 4 μ L of lipid suspension into the calorimeter cell. (D) Heats of reaction integrated from the calorimetric trace (C) as a function of injection number. Buffer: 10 mM phosphate, 150 mM NaCl, pH 7.4.

In contrast to hemolytic SNPs, very small heats in the range of control titration of lipids into buffer were recorded for non-hemolytic SNPs. The integrated heats shown in Figure 2D are $\sum h_i = -0.43 \mu\text{cal}$ and the enthalpy is almost hundredfold lower when compared to hemolytic SNPs (-0.003 cal/g vs. -0.026 cal/g) indicating no interaction between non-hemolytic SNPs and neutral lipid membrane. We have performed additional titration of POPC into non-hemolytic SNPs at higher temperature to our results. Similar to the result obtained at 25 °C, calorimetric titration at 40 °C did not reveal any binding of non-hemolytic SNPs to POPC SUVs.

To probe whether electrostatic interactions are involved in the binding between hemolytic SNPs and lipid membranes, we have performed titrations at lower salt concentration (50 mM NaCl). The ITC titration pattern was identical to the titration performed at 150 mM NaCl and cumulative heat released during the reaction was in the same range ($\sum h_i = -23.4 \mu\text{cal}$).

Solid state NMR

³¹P NMR studies on the silica nanoparticles-phospholipids interactions.

The phosphorus spectra of multilamellar lipid vesicles (MLVs) are characterized by a typical shape with the chemical shielding anisotropy of -50 ppm determined from the distance between low- and high-field shoulders of the spectrum. If molecules move rapidly in solution, isotropic motions will produce a complete averaging of the phosphorus chemical shift anisotropy and the spectrum consists of a single sharp line of about few Hz line width (Seelig, 1978). Figure

3.3. HEMOLYSIS OF SILICA NANOPARTICLES: A MECHANISTIC APPROACH

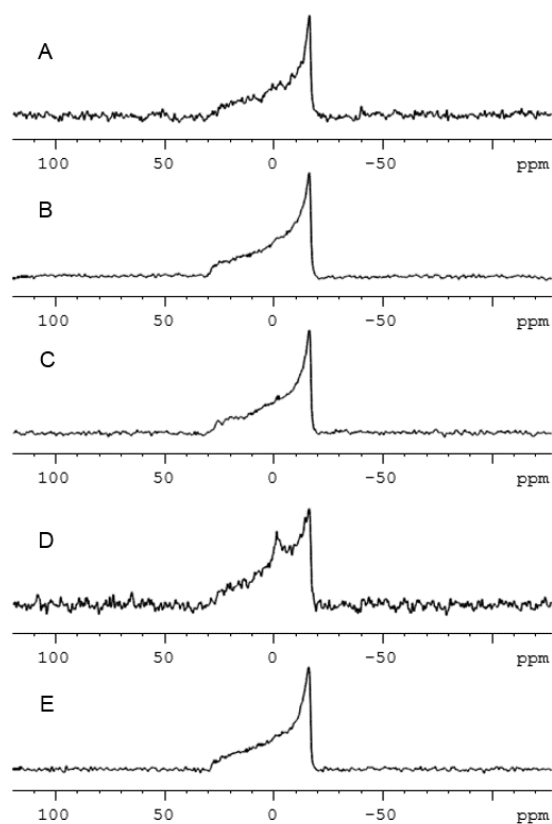


Figure 3. ^{31}P NMR of multilamellar phospholipid dispersions containing different amount of silica nanoparticles. Twenty to 25 mg of phospholipid alone (E) or with different amounts of SNPs (A, B, C, D) were suspended in 400 μL buffer. (A) non-hemolytic SNP/POPC weight ratio of 0.15; (B) non-hemolytic SNP/POPC weight ratio of 1.0; (C) hemolytic SNP/POPC weight ratio of 0.15; (D) hemolytic SNP/POPC weight ratio of 1.0; (E) POPC alone.

3 shows spectra obtained for multilamellar lipid dispersion composed of POPC in the absence (Figure 3E) or presence of hemolytic and non-hemolytic SNPs (Figure 3A, 3B, 3C, 3D).

The ^{31}P NMR spectrum of MLVs composed of POPC (Figure 3E) is a typical for a random distribution of bilayer domains (so called powder-type spectrum) with the chemical shielding anisotropy of -50 ppm. The addition of non-hemolytic SNPs to phospholipid dispersions did not have any influence on the bilayer structure. Phospholipid spectra with non-hemolytic SNPs, shown in Figure 3A and Figure 3B, exhibit the same pattern as the spectrum of phospholipid alone. No changes in spectral shape were also observed for hemolytic SNPs nanoparticles mixed with lipids at low weight ratios of hemolytic SNP/lipid weight ratio of 0.15 (Figure 3C). However an isotropic component at 0 ppm appears in the powder spectrum when the amount of hemolytic SNPs is increased to hemolytic SNP/POPC weight ratio of 1.0 (Figure 3E). Spectral simulation (not shown) indicates that the isotropic component comprises about 20% of the overall spectral

intensity. The presence of isotropic and bilayer component in the spectra indicates presence of lipids which exhibit different motion environments such as a formation of smaller vesicles or micelles.

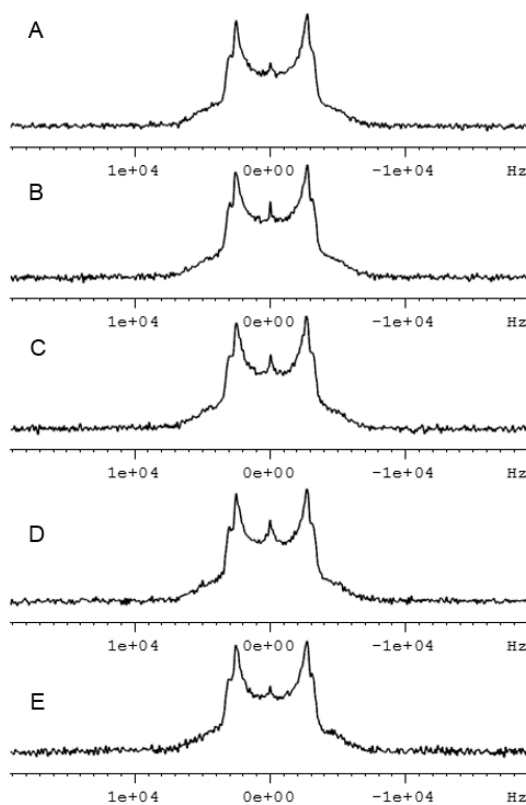


Figure 4. ^2H NMR spectra of multilamellar head group deuterium labeled phospholipid dispersions containing different amount of SNPs. 25 mg of phospholipid alone (E) or with different amounts of silica nanoparticles (A, B, C, D) were suspended in 400 μL buffer. (A) non-hemolytic SNPs/POPC weight ratio of 0.15. (B) non-hemolytic SNPs/POPC weight ratio of 1.0. (C) hemolytic SNPs/POPC weight ratio of 0.15. (D) hemolytic SNPs/POPC weight ratio of 1.0. (E) POPC alone.

^2H NMR measurements of the SNPs interactions with phospholipids.

To test whether there is direct interaction between the choline head group of the phospholipid and hydroxyl group of the SNPs we have employed ^2H NMR to monitor the head group region of POPC perdeuterated at choline moiety (d4-POPC). Figure 4 shows ^2H NMR spectra of d4-POPC in the absence and upon addition of different amounts of hemolytic and non-hemolytic silica nanoparticles. The measured quadrupole splitting of the head segment d4-POPC (in 10 mM Hepes and 150 mM NaCl) is 5.5 kHz. Addition of hemolytic or modified non-hemolytic SNPs did not change the quadrupole splitting of the head group segment. This result indicates that

there is no confirmation change of the phosphocholine polar group, as depicted in Figure 4.

The measurements of the deuterium quadrupole splitting using selectively deuterated lipids is a sensitive tool to directly monitor interaction of ions, small molecules and peptides with the choline group of the phosphatidylcholine (Altenbach and Seelig, 1984; Akutsu and Seelig, 1981). Even the weak binding of Na^+ could be detected and the changes in the quadrupole splitting up to 9 kHz were observed (Akutsu and Seelig, 1981). Our results with SNPs and d4-POPC showed that there are no direct electrostatic interactions between particles and choline headgroup. In addition we have also performed solid state ^2H NMR using lipids perdeuterated at the hydrocarbon chain (d31-POPC). Upon addition of SNPs no changes in the quadrupole splitting of the lipid chains were observed (data not shown).

Flow cytometry with MLVs

We first gated LUVs to find proper settings for the smaller species in the supernatant. Then we separated the supernatant with the 550 nm laser to only have lipid vesicles and no SNPs in the supernatant (although the samples was centrifuged prior to flow cytometry, the fluorescent signal served as a control). Then again, these fluorescent species were plotted as forward scatter area against sideward scatter area and a time dependent gating was set to count the lipid vesicles in the supernatant. For the hemolytic SNPs 14'000 vesicles were counted, whereas for the non-hemolytic non-hemolytic SNPs only 7000 were counted. This indicates that the faster tumbling species from ssNMR could result in smaller vesicles.

DISCUSSION

One of the hypotheses for hemolytic mechanism of SNPs is a direct electrostatic interaction of silanol groups with quaternary ammonium of phosphatidylcholine (Depasse and Warlus, 1976; Slowing et al., 2009). We were interested exclusively in the interaction of the surface silanols and the choline headgroups. Therefore, we have chosen POPC liposomes as model, since phosphatidylcholine lipid is the most abundant lipid in the outer leaflet of RBC membrane (Ziegler, 2008). This membrane model excludes other effects coming from membrane constituents or additional factors like osmotic pressure.

The dye leakage assay with LUVs showed a 10% leakage with hemolytic SNPs in a 1:1 weight ratio, whereas no leakage was observed for non-hemolytic SNPs. For strong hemolytic peptides like melittin, a high leakage is already observed at low peptide to lipid ratio (Klocek et al., 2009). However, a recent study has found similar % dye leakage for SNP of the same size (the primary size of 15 nm increased up to 100 nm upon salt addition, which is comparable with our size) (Mu et al., 2012). As different lipids might alter the interaction between SNPs and LUVs we have performed leakage with mixed membranes. The composition of the membrane did not alter the % of released dye. However, also for cell penetrating peptides like nona-arginine, no dye leakage was observed, although they form pores in the membrane (Liu et al., 2013). For other nanoparticles like gold nanoparticles (10 nm) or titanium dioxide (10 nm), it was shown that the

dye leakage is depending on the surface groups, where positively charged groups exhibited a time dependent release of carboxyfluorescein (Moghadam et al., 2012). However, comparison is hampered by the size difference and the surface charge density. The authors observed a time-dependent leakage, which was not the case for our particles (data not shown).

The DLS data showed a strong size increase when SUVs and hemolytic SNPs were mixed. This happened already at a very low SUV to SNP ratio. Hence a strong agglomeration process is present. A reason for this could be a locally high concentration which results in a stress of the membrane. With ITC we monitored the interaction between SNPs and SUVs. Our data support what was observed with DLS. Figure 2a shows a strong initial peak upon injection of SUVs into SNPs suspension, but already for the second injection, the heat effect is decreasing strongly. This initial peak suggests that all available binding partners are depleted after the first injection of SUVs. However, the heat effect is rather small compared to melittin, where the binding enthalpy to POPC SUVs is 2 cal/g (Québatte, unpublished data), whereas for hemolytic SNPs the binding enthalpy is -0.026 cal/g. However, the difference in binding enthalpy between hemolytic and non-hemolytic SNP is also by a factor of 100 (non-hemolytic SNPs: (-0.003 cal/g), as stated in the results. Even if the effect is not comparable with cell penetrating peptides, this difference is striking. However, we did not observe a temperature dependency in binding enthalpy. Furthermore, no change was observed upon salt addition or abduction, which does not support the evidence of an electrostatic interaction, as postulated in the literature (Slowing et al., 2009).

Our adsorption data are in agreement with the literature, where adsorption of SNPs to a monolayer was shown. The adsorption interaction there was mainly driven by Van-der-Waals forces (Vakurov et al., 2012). For the hemolytic SNPs to be attracted to DOPC monolayer, the surface potential must be positive. This surface potential can arise only from fixed charges within the phospholipid polar groups, namely, the N^+ terminus of the $P^- - N^+$ dipole. The observation that voltammetric peak suppression is independent of the solution pH and ionic strength clearly negates any suggestion that the interaction is dominated by electrostatic forces. The ionic strength and the pH change did not alter the results. This is indicative for van der Waals forces.

We further explored where the interaction between SNPs and lipid vesicles are located (head region of the phospholipid or at its tail). Deuterium ssNMR of headgroup perdeuterated phosphatidylcholine showed no change in the quadrupole splitting indicating no direct interaction with the phospholipid head group. This observation is in contrary to results obtained by Depasse and Warlus who showed high affinity of SNPs to quaternary ammonium ions. However their study has used tetraalkylammonium bromide and tetralkylammonium hydroxide as positively charged constituents of the outer layer of the membrane (Depasse and Warlus, 1976). Phosphatidylcholine, the main lipid of the outer membrane of RBC (Ziegler, 2008) is a zwitter ion due to presence of the negatively charged phosphate group. The phosphorous and the nitrogen atom of the phosphatidylcholine headgroup are lying in the plane parallel to the surface of the

membrane and the flexibility of the headgroup is limited (Seelig et al., 1977).

Using ^{31}P NMR, we observed an isotropic peak in the presence of hemolytic SNPs. This isotropic peak suggest that smaller lipid vesicles are formed. Brisebois et al. studied interaction of fulleranol with DPPC/cholesterol membranes using ^{31}P ssNMR (Brisebois et al., 2012). The effect of fulleranol nanoparticles on the ^{31}P was minor. ^2H NMR with deuterated acyl chain lipids also showed no change in signal after addition of fulleranol. These results were in agreement with molecular dynamic simulations on fulleranol in DPPC bilayers, which suggest that the polar nanoparticles would preferentially remain at the bilayer/water interface (D'Rozario et al., 2009). From our data, we conclude that the direct interaction in the choline headgroup and the SNPs is not very likely, since we would have observed a shift in the deuterium spectrum.

With flow cytometry, we gained insight into the smaller species that were formed upon addition of hemolytic SNPs. For hemolytic SNPs we observed that 100% more smaller vesicles than for the non-hemolytic SNPs. What remains also to be elucidated is whether a membrane wrapping of SNPs was present. This means that the MLVs could spontaneously form a lipid bilayer around the silica nanoparticles. This process is called supported lipid bilayer (SLB). It has been reported that also neutrally charged or zwitter ionic phospholipids would be able to wrap around SNPs (Mornet et al., 2005). Monet et al. found for liposomes with positive, neutral, and low negative charge formed SLB around SNPs. The SNPs used in the study have the same diameter. However, the liposomes used there were SUVs, where in our case they were present as MLVs. The curvature of the surface may play a role in this case. Zhang et al. showed that silica nanoparticles bigger than 78 nm caused membrane wrapping, followed by increase in lipid lateral mobility and the eventual collapse of giant unilamellar vesicles (GUVs) composed of DOPC Zhang et al. (2012b). However it should be noted that GUVs are very fragile structures when compared to SUVs or LUVs Schwille (2011). Even though we centrifuged the SNP-MLV mixture prior to flow cytometry experiments, membrane wrapping could still be present for the centrifuged SNPs. Further experiments using cryo-TEM could give insight into membrane wrapping process.

CONCLUSION

In this study we investigated the hemolytic effect by SNPs with biophysical methods. Our findings suggest that the interaction of surface silanols and a model membrane composed of phosphatidyl choline is rather low. ITC data showed no significant heat change at different temperatures and salt concentrations, which would be present, if there is an electrostatic interaction. Also ssNMR data indicated that an interaction with the choline headgroup is not prevalent, but the phosphorus spectrum pointed towards formation of faster (i.e. smaller) tumbling species. The presence of these species could be confirmed by flow cytometry. Even though the effects measured were rather small, there was a clear difference between hemolytic and non-hemolytic SNPs. Hemolysis may be partly explained by our data, however, more research needs to be conducted, also involving membrane proteins and osmotic pressure.

ACKNOWLEDGMENTS

J.H. and H.K. obtained financial support from the Swiss Centre of Applied Human Toxicology (SCAHT).

REFERENCES

- Akutsu, H. and Seelig, J. (1981). Interaction of metal ions with phosphatidylcholine bilayer membranes. *Biochemistry*, 20(26):7366–7373.
- Altenbach, C. and Seelig, J. (1984). Ca²⁺ binding to phosphatidylcholine bilayers as studied by deuterium magnetic resonance. evidence for the formation of a ca²⁺ complex with two phospholipid molecules. *Biochemistry*, 23(17):3913–3920.
- Bertrand, N. and Leroux, J.-C. (2012). The journey of a drug-carrier in the body: An anatomophysiological perspective. *Journal of Controlled Release*, 161(2):152–163.
- Brisebois, P. P., Arnold, A. A., Chabre, Y. M., Roy, R., and Marcotte, I. (2012). Comparative study of the interaction of fullerene nanoparticles with eukaryotic and bacterial model membranes using solid-state NMR and FTIR spectroscopy. *European biophysics journal: EBJ*, 41(6):535–544.
- Cedervall, T., Lynch, I., Lindman, S., Berggård, T., Thulin, E., Nilsson, H., Dawson, K. A., and Linse, S. (2007). Understanding the nanoparticle–protein corona using methods to quantify exchange rates and affinities of proteins for nanoparticles. *Proceedings of the National Academy of Sciences*, 104(7):2050–2055.
- Depasse, J. and Warlus, J. (1976). Relation between the toxicity of silica and its affinity for tetraalkylammonium groups. comparison between siO₂ and tiO₂. *Journal of Colloid and Interface Science*, 56(3):618–621.
- D’Rozario, R., Wee, C., Wallace, E., and Sansom, M. (2009). The interaction of c60 and its derivatives with a lipid bilayer via molecular dynamics simulations. *Nanotechnology*, 20(11):115102.
- Kettiger, H., Schipanski, A., Wick, P., and Huwyler, J. (2013). Engineered nanomaterial uptake and tissue distribution: from cell to organism. *International journal of nanomedicine*, 8:3255–3269.
- Klocek, G., Schulthess, T., Shai, Y., and Seelig, J. (2009). Thermodynamics of melittin binding to lipid bilayers. aggregation and pore formation. *Biochemistry*, 48(12):2586–2596.
- Kroll, A., Pillukat, M. H., Hahn, D., and Schnekenburger, J. (2009). Current in vitro methods in nanoparticle risk assessment: Limitations and challenges. *European Journal of Pharmaceutics and Biopharmaceutics*, 72(2):370–377.
- Lin, Y.-S. and Haynes, C. L. (2010). Impacts of mesoporous silica nanoparticle size, pore ordering, and pore integrity on hemolytic activity. *J. Am. Chem. Soc.*, 132(13):4834–4842.
- Liu, B. R., Huang, Y.-W., and Lee, H.-J. (2013). Mechanistic studies of intracellular delivery of proteins by cell-penetrating peptides in cyanobacteria. *BMC Microbiology*, 13(1):57.
- Misztal, T. and Tomasiak, M. (2011). [pathophysiological consequences of hemolysis. role of cell-free hemoglobin]. *Postepy Higieny I Medycyny Doswiadczalnej (Online)*, 65:627–639.

3.3. HEMOLYSIS OF SILICA NANOPARTICLES: A MECHANISTIC APPROACH

- Moghadam, B. Y., Hou, W.-C., Corredor, C., Westerhoff, P., and Posner, J. D. (2012). Role of nanoparticle surface functionality in the disruption of model cell membranes. *Langmuir: the ACS journal of surfaces and colloids*, 28(47):16318–16326.
- Mornet, S., Lambert, O., Duguet, E., and Brisson, A. (2005). The formation of supported lipid bilayers on silica nanoparticles revealed by cryoelectron microscopy. *Nano Letters*, 5(2):281–285.
- Mu, Q., Hondow, N. S., Krzeminski, L., Brown, A. P., Jeuken, L. J., and Routledge, M. N. (2012). Mechanism of cellular uptake of genotoxic silica nanoparticles. *Particle and Fibre Toxicology*, 9(1):29.
- Ow, H., Larson, D. R., Srivastava, M., Baird, B. A., Webb, W. W., and Wiesner, U. (2005). Bright and stable core-shell fluorescent silica nanoparticles. *Nano Letters*, 5(1):113–117.
- Rosenholm, J. M., Peuhu, E., Eriksson, J. E., Sahlgren, C., and Lindén, M. (2009). Targeted intracellular delivery of hydrophobic agents using mesoporous hybrid silica nanoparticles as carrier systems. *Nano letters*, 9(9):3308–3311.
- Rothen-Rutishauser, B. M., Schürch, S., Haenni, B., Kapp, N., and Gehr, P. (2006). Interaction of fine particles and nanoparticles with red blood cells visualized with advanced microscopic techniques. *Environmental Science & Technology*, 40(14):4353–4359.
- Sauder, R., Seelig, J., and Ziegler, A. (2011). Thermodynamics of lipid interactions with cell-penetrating peptides. *Methods in Molecular Biology (Clifton, N.J.)*, 683:129–155.
- Schwille, P. (2011). Giant unilamellar vesicles: From minimal membrane systems to minimal cells? In Luisi, P. L. and Stano, P., editors, *The Minimal Cell*, pages 231–253. Springer Netherlands.
- Seelig, J. (1978). ³¹P nuclear magnetic resonance and the head group structure of phospholipids in membranes. *Biochimica Et Biophysica Acta*, 515(2):105–140.
- Seelig, J., Gally, G. U., and Wohlgemuth, R. (1977). Orientation and flexibility of the choline head group in phosphatidylcholine bilayers. *Biochimica Et Biophysica Acta*, 467(2):109–119.
- Slowing, I. I., Wu, C.-W., Vivero-Escoto, J. L., and Lin, V. S.-Y. (2009). Mesoporous silica nanoparticles for reducing hemolytic activity towards mammalian red blood cells. *Small*, 5(1):57–62.
- Vakurov, A., Brydson, R., and Nelson, A. (2012). Electrochemical modeling of the silica nanoparticle–biomembrane interaction. *Langmuir*, 28(2):1246–1255.
- Wang, T., Bai, J., Jiang, X., and Nienhaus, G. U. (2012). Cellular uptake of nanoparticles by membrane penetration: A study combining confocal microscopy with FTIR spectroelectrochemistry. *ACS Nano*, 6(2):1251–1259.
- Zhang, H., Dunphy, D. R., Jiang, X., Meng, H., Sun, B., Tarn, D., Xue, M., Wang, X., Lin, S., Ji, Z., Li, R., Garcia, F. L., Yang, J., Kirk, M. L., Xia, T., Zink, J. I., Nel, A., and Brinker, C. J. (2012a). Processing pathway dependence of amorphous silica nanoparticle toxicity: colloidal vs pyrolytic. *Journal of the American Chemical Society*, 134(38):15790–15804.
- Zhang, S., Nelson, A., and Beales, P. A. (2012b). Freezing or wrapping: The role of particle size in the mechanism of nanoparticle–biomembrane interaction. *Langmuir*, 28(35):12831–12837.

- Zhao, Y., Sun, X., Zhang, G., Trewyn, B. G., Slowing, I. I., and Lin, V. S.-Y. (2011). Interaction of mesoporous silica nanoparticles with human red blood cell membranes: size and surface effects. *ACS nano*, 5(2):1366–1375.
- Ziegler, A. (2008). Thermodynamic studies and binding mechanisms of cell-penetrating peptides with lipids and glycosaminoglycans. *Advanced Drug Delivery Reviews*, 60(4–5):580–597.

3.4 Polymersomes containing quantum dots

Polymersomes containing quantum dots for cellular imaging

Marine Camblin¹, Pascal Detampel¹, Helene Kettiger¹, Dalin Wu², Vimalkumar Balasubramanian¹
Jörg Huwyl¹

¹ Department of Pharmaceutical Sciences, University of Basel, Switzerland

² Department of Chemistry, University of Basel, Switzerland

Contribution H.Kettiger: author, experiments (MTT assay)

International Journal of Nanomedicine 2014;9(1):2287-2298.

Polymersomes containing quantum dots for cellular imaging

Marine Camblin¹
 Pascal Detampel¹
 Helene Kettiger¹
 Dalin Wu²
 Vimalkumar
 Balasubramanian^{1,*}
 Jörg Huwyler^{1,*}

¹Division of Pharmaceutical Technology, ²Department of Chemistry, University of Basel, Basel, Switzerland

*These authors contributed equally to this work

Abstract: Quantum dots (QDs) are highly fluorescent and stable probes for cellular and molecular imaging. However, poor intracellular delivery, stability, and toxicity of QDs in biological compartments hamper their use in cellular imaging. To overcome these limitations, we developed a simple and effective method to load QDs into polymersomes (Ps) made of poly(dimethylsiloxane)-poly(2-methylloxazoline) (PDMS-PMOXA) diblock copolymers without compromising the characteristics of the QDs. These Ps showed no cellular toxicity and QDs were successfully incorporated into the aqueous compartment of the Ps as confirmed by transmission electron microscopy, fluorescence spectroscopy, and fluorescence correlation spectroscopy. Ps containing QDs showed colloidal stability over a period of 6 weeks if stored in phosphate-buffered saline (PBS) at physiological pH (7.4). Efficient intracellular delivery of Ps containing QDs was achieved in human liver carcinoma cells (HepG2) and was visualized by confocal laser scanning microscopy (CLSM). Ps containing QDs showed a time- and concentration-dependent uptake in HepG2 cells and exhibited better intracellular stability than liposomes. Our results suggest that Ps containing QDs can be used as nanoprobe for cellular imaging.

Keywords: quantum dots, polymersomes, cellular imaging, cellular uptake

Introduction

Development of highly sensitive and stable imaging probes is of considerable interest in many areas of biomedical research, ranging from cellular biology to molecular imaging and diagnostics. Fluorescent semiconductor quantum dots (QDs) are promising fluorescent nanoprobe offering an alternative to conventional organic fluorophores due to their unique properties.^{1,2} QDs show superior optical and chemical properties, ie, broad spectral absorption with a narrow emission band, higher brightness of fluorescence despite a low quantum yield, high photostability, and resistance to photobleaching.^{3,4} However, poor chemical stability, particle aggregation, and toxicity mediated by the cadmium semiconductor core limit the use of QDs in imaging.⁵⁻⁷ These limitations are of major concern in applications where cellular uptake of QDs is required to visualize intracellular compartments.

In cell culture media, QDs have low stability due to particle aggregation and surface degradation, which leads to minimal cellular uptake and difficulties with respect to the interpretation of cellular images.⁸ Therefore, attempts have been made to improve the stability and promote cellular uptake of QDs using surface chemistry modifications. This includes the functionalization of QDs with biomolecules such as antibodies,⁹ proteins,¹⁰ or peptides,¹¹ as well as their coating with polymers or amphiphilic copolymers.^{12,13} However, modification of the QD surface may significantly

Correspondence: Jörg Huwyler
 University of Basel, Department of
 Pharmaceutical Sciences, Division
 of Pharmaceutical Technology,
 Klingelbergstrasse 50, Basel,
 Switzerland
 Tel +41 61 267 1513
 Fax +41 61 267 1516
 Email joerg.huwyler@unibas.ch

submit your manuscript | www.dovepress.com

Dovepress

<http://dx.doi.org/10.2147/IJN.S59189>

International Journal of Nanomedicine 2014:9 2287–2298

2287



© 2014 Camblin et al. This work is published by Dove Medical Press Limited, and licensed under Creative Commons Attribution – Non Commercial (unported, v3.0) License. The full terms of the License are available at <http://creativecommons.org/licenses/by-nc/3.0/>. Non-commercial uses of the work are permitted without any further permission from Dove Medical Press Limited, provided the work is properly attributed. Permissions beyond the scope of the License are administered by Dove Medical Press Limited. Information on how to request permission may be found at: <http://www.dovepress.com/permissions.php>

alter their fluorescence properties.¹⁴ Once taken up by target cells, QDs often end up in the endolysosomal compartment or aggregate in intracellular regions.¹⁵ Earlier studies showed that QDs may disintegrate under acidic conditions in these compartments, leading to intracellular release of toxic heavy metals. This leads to oxidative stress, induction of apoptosis, and eventually, cell death.¹⁶ Recently, it was shown that polymer-coated QDs could be stabilized during cellular uptake. However, their coating dissociated in intracellular compartments such as lysosomes.¹⁷ Thus, new strategies are needed to improve both the uptake and the intracellular stability of QDs.

Amphiphilic block copolymers are known to self-assemble into various supramolecular aggregates such as micelles, tubes, sheets, or vesicles in aqueous solutions.¹⁸ In particular, polymersomes (Ps; so-called polymeric vesicles) have gained increasing interest in recent years for various biomedical applications, including their use as drug and gene delivery nanocarriers, nanoreactors, and even artificial organelles.¹⁹ Ps are nanometer-sized hollow spheres with an aqueous cavity surrounded by a hydrophobic membrane and hydrophilic inner and outer surfaces. They are promising candidates for nanocarriers because many hydrophilic and hydrophobic molecules can be incorporated into their aqueous cavity or their membrane, respectively.^{20,21} Additionally, chemical surface modifications can be used to tailor their physicochemical and biological properties to improve the delivery of a wide range of therapeutics.^{22,23} Numerous types of Ps have been proposed as nanocarriers for encapsulating small drug molecules, larger therapeutic proteins, and other types of nanoparticles.^{24–26} Reports on the use of Ps as carriers of water-soluble nanoparticles such as QDs are scarce.²⁷ Recently, Ps prepared from amphiphilic poly(D,L-lactide)-poly(2-methacryloyl-oxy-ethylphosphorylcholine) (PLA-PMPC) diblock copolymers have been used to encapsulate phosphorylcholine-coated QDs. This coating confers hydrophilic properties to the QDs and also creates ion-pair interactions with PMPC, binding QDs to the inner and outer surfaces of Ps.²⁷ However, this approach has limitations, since the presence of physiological buffer can destabilize the QDs and release them from the surface of the Ps.

The present study aimed to use a recent type of diblock copolymers composed of poly(dimethylsiloxane)-poly(2-methyloxazoline) (PDMS-PMOXA)²⁸ to prepare Ps and to load them with QDs. The hydrophilic fraction and molecular weight of the PDMS-PMOXA were chosen to meet the prerequisites for diblock amphiphilic copolymers to form vesicles.²⁹ The neutral hydrophilic PMOXA

outside the Ps thereby acts as a protein repellent, similar to conventional polyethylene glycol (PEG), to minimize interactions with phagocytic cells such as macrophages and monocytes.^{30,31} In this way, colloidal stability, cellular delivery, and intracellular stability needed for cellular imaging were improved. QDs were loaded into the aqueous cavity of Ps made of PDMS-PMOXA without altering the surface properties of Ps. Loading efficiency and colloidal stability in suspension were characterized by transmission electron microscopy (TEM), fluorescence spectroscopy (FS), zeta potential, and fluorescence correlation spectroscopy (FCS). The cellular toxicity of PDMS-PMOXA Ps was excluded by the 3-(4,5-dimethylthiazol-2-yl)-2,5-diphenyltetrazolium bromide (MTT) assay. Intracellular delivery of Ps containing QDs was investigated in human liver carcinoma (HepG2) cells. Concentration- and time-dependent cellular uptake of Ps containing QDs in HepG2 cells was analyzed using confocal laser scanning microscopy (CLSM). Results were compared to those obtained for liposomes containing QDs.

Materials and methods

Amphiphilic block copolymers

Poly(dimethylsiloxane)-poly(2-methyloxazoline) (PDMS₆₅-PMOXA₁₄) was kindly provided by Prof Wolfgang Meier (Department of Chemistry, University of Basel, Basel, Switzerland). This amphiphilic diblock copolymer was synthesized as described elsewhere.^{28,31} An excess of pre-activated PDMS was used to induce the polymerization of the hydrophilic PMOXA blocks. Unreacted PDMS was removed from the diblock copolymer by centrifugation.

Preparation of Ps

Ps were prepared using a film rehydration method.³² PDMS-PMOXA diblock copolymer (5 mg) was first dissolved in pure ethanol (1 mL). The polymeric solution was evaporated to dryness using a rotary evaporator (Rotavapor; BÜCHI Labortechnik AG, Flawil, Switzerland; 174 mbar, 40°C, 80 rpm) to obtain a thin film. Residual humidity was removed in a vacuum oven (Vacutherm; Thermo Scientific, Wohlen, Switzerland) in high vacuum (0.3 mbar, 40°C, 4 hours). Phosphate buffer solution (PBS; 1 mL, 0.1 mM) was added to the film for rehydration under vigorous stirring at room temperature for 6 hours. The resulting suspension was extruded (Mini extruder; Avanti Polar Lipids, Alabaster, AL, USA) eleven times through a polycarbonate filter with an average pore diameter of 0.4 µm, followed by eleven extrusions through a filter with an average pore diameter of

0.2 μm (Nucleopores; Whatman, VWR International AG, Dietikon, Switzerland).

Loading of QDs

An aliquot (100 μL) of QDs solution (8 μM solution in 50 mM borate, pH 9) with a maximum red fluorescence emission of 625 nm (Qdot[®] ITK[™] carboxyl quantum dots, cadmium–selenium core; Invitrogen, Life technologies, Lucerne, Switzerland) was mixed with PBS (900 μL , 1 mM) to obtain a final QDs concentration of 200 nM. The photoluminescence yield of CdSe QDs was previously reported to be negligible for emission wavelengths in the red spectral range.³³ This suspension was added to a dry polymer film and stirred for 6 hours at room temperature and protected from light. QDs were encapsulated in Ps during the self-assembly process. After extrusion (as described in paragraph Preparation of PS), non-encapsulated QDs were removed by size-exclusion chromatography using a Sepharose 2B column (Sigma Aldrich, Buchs, Switzerland) eluted with PBS (0.1 mM). The first fraction corresponding to the Ps-containing QDs was detected by UV absorption at 280 nm. It should be noted that free QDs cannot be separated from the suspension by dialysis due to their big molecular size.

Dynamic light scattering

Suspensions of empty Ps and Ps-containing QDs were measured for average size and size distribution using dynamic light scattering (DLS) with a Delsa[™] Nano C (Beckman Coulter, Inc., Nyon, Switzerland) equipped with Dual 30 mW laser diodes (wavelength λ : 632.8 nm). Data were analyzed using the CONTIN program³⁴ (DelsaNano UI software version 3.73/2.30, Beckman Coulter, Inc.).

Surface charge – zeta potential

Suspensions of free QDs, empty Ps, and Ps-containing QDs were measured for zeta potential determination using electrophoretic light scattering in a Delsa[™] Nano C. Suspensions were measured in a flow cell using PBS as buffer. Data were converted with the Smoluchowski equation (DelsaNano UI software, Beckman Coulter, Inc.).

Transmission electron microscopy

Samples for transmission electron microscopy (TEM) were prepared using an aliquot (5 μL) of suspension of empty Ps and Ps-containing QDs on a carbon-coated grid. Samples were negatively stained with freshly prepared 2% uranyl acetate. The grids were air-dried overnight before TEM analysis (CM-100; Philips, Eindhoven, the Netherlands).

Fluorescence spectroscopy

A microplate fluorescence spectrometer (SpectraMax M2e, Molecular Device, Biberach an der Riss, Germany) was used to analyze the efficiency of loading QDs into Ps. All samples (free QDs, empty Ps, and Ps-containing QDs) were excited at 405 nm, and continuous emission spectra were recorded from 500 to 700 nm. All measurements were performed in a polystyrene 96-well microplate (Greiner-bio one, Frickenhausen, Germany). Fluorescence intensity of QDs changes over time. Therefore, fluorescence signals are represented in relative fluorescent units.

FCS

FCS measurements were performed on the surface of a cover glass using a Zeiss 510-META/Confocor2 laser-scanning microscope (Carl Zeiss AG, Feldbach, Switzerland) equipped with an argon laser (477 nm) in the FCS mode. Fluctuations of fluorescence intensity were processed by means of an autocorrelation function. FCS was used to analyze the loading of QDs into Ps and to determine quantitatively the number of QDs in each polymersome.³⁵ Diffusion times of free QDs determined independently were included in the fitting procedure. All results represent the average of ten measurements. For stability determinations, Ps-containing QDs were analyzed regularly over a period of 6 weeks.

Cell culture

HepG2 cells (ATCC HB-8065) were kindly provided by Prof Dietrich von Schweinitz (University Hospital Basel, Basel, Switzerland). Cells were cultured in Dulbecco's Modified Eagle Medium (DMEM) supplemented with low glucose (1 g/L), 10% fetal bovine serum (FBS), 0.1 mM non-essential amino acids (NEAA), 2 mM GlutaMAX[™], and 10 mM HEPES (all obtained from Gibco, Life Technologies, Lucerne, Switzerland) at 37°C under 5% CO₂ and saturated humidity. Cells were confirmed to be free of mycoplasma (MycAlert[™]; Lonza, Visp, Switzerland).

MTT cellular toxicity assay

The 3-(4,5-dimethylthiazol-2-yl)-2,5-diphenyltetrazolium bromide (MTT) assay was used with some modifications as described elsewhere.³⁶ The MTT stock solution (Roth AG, Arlesheim, Switzerland) was prepared by dissolving 5 mg MTT/mL PBS, sterile-filtered, and stored at 4°C. Briefly, HepG2 cells were seeded at a density of 2.5×10^4 cells/well in a 96-well plate. After 24 hours, the medium was removed and 100 μL aliquots containing the corresponding concentration of Ps were added. A blank medium served as a negative

control. After 24 hours, the medium was replaced by blank medium containing 10% MTT solution. The plates were incubated for 2 hours at 37°C, and the resultant formazan crystals were dissolved by adding 3% sodium dodecyl sulfate (20 μ L) and 40 mM HCl (100 μ L) in isopropanol. Optical density was measured at 550 nm using a spectrophotometer (SpectraMax M2e; Molecular Device). Test substances showed no absorbance overlapping with the signal of MTT. Unspecific background signal was determined at 680 nm and subtracted to reduce artifacts.

Cellular uptake of Ps-containing QDs

We analyzed the cellular uptake of Ps-containing QDs in HepG2 liver cancer cells using CLSM. HepG2 cells were cultured on poly-D-lysine-coated cover slips (#1.5; Menzel Glasbearbeitungswerk GmbH & Co, KG, Braunschweig, Germany). Cells were incubated at 37°C with Ps (100–500 μ g/mL) or liposomes (0.14 mM of phospholipids) loaded with QDs. Nucleus counterstaining was performed by adding Hoechst 33342 dye (1 μ g/mL) to the cells 5 minutes before the completion of the uptake assay. Cells were washed three times with cold D-PBS (Dulbecco's PBS) and fixed for 15 minutes with 2% paraformaldehyde at 4°C. After an additional wash, slides were embedded in Prolong Gold antifade reagent (Gibco) and sealed with nail polish after drying. Samples were analyzed with an Olympus FV-1000 inverted confocal laser scanning microscope (Olympus, Le Mont-sur-Lausanne, Switzerland), using a 60 \times Plan Apo N oil-immersion objective (numerical aperture 1.40), and images were processed using either the Olympus FluoView software (v3.1, Olympus) or Gimp software (v2.8; GNU image manipulation program, <http://www.gimp.org>). Intracellular QDs were activated by light-emitting diodes (LEDs) with a wavelength of 400 nm (210 mW/cm²) or 490 nm (190 mW/cm²),³⁷ using a pE-2 LED (CoolLED Limited, Andover, UK) excitation system. For activation, samples were exposed to a wavelength of 490 nm for 1 minute prior to analysis.

Results and discussion

Characterization of Ps

These last years, the development of Ps for technical or pharmaceutical applications is increasing. In this study, we have formulated Ps with a PDMS-PMOXA diblock copolymer, composed of 65 siloxane and 14 2-methyloxazoline units (Figure 1B),^{28,31} as nanosized carriers for QDs.

Size and morphology of extruded PDMS-PMOXA Ps were determined by DLS and TEM (Figure 1). The mean

hydrodynamic diameter was approximately 205 nm for empty Ps and 223 nm for Ps-containing QDs (Figure 1A). Table 1 shows the polydispersity index (PDI) of free QDs, empty Ps, and Ps-containing QDs. The very low PDI values for both Ps preparations indicated a homogeneous population with a very narrow size distribution range.

However, the absence of a significant difference in average diameters of the two Ps preparations suggests that encapsulation of high-molecular weight QD nanoparticles did not affect the molecular self-assembly of PDMS-PMOXA copolymers into Ps. In TEM investigations, we observed spherical vesicles with a diameter of approximately 200 nm, confirming the formation of Ps. Collapsed Ps revealed a hollow vesicular structure (Figure 1C). A recent report on self-assembly of a similar molecular composition of PDMS-PMOXA into vesicular structures supports our findings.²⁸

Loading of QDs into Ps

TEM investigations showed the presence of monodispersed QDs inside the Ps. QDs incorporated into Ps had the same appearance as free QDs in suspension, confirming that QDs were located in the aqueous compartment of the Ps without any aggregations. The morphology of empty Ps and Ps loaded with QDs remained the same (Figure 1D), confirming that encapsulation of QDs did not affect the formation of Ps. The number of QDs per Ps ranged from a single QD to tens of QDs, according to the statistical probability of available QDs in close proximity (for loading) during Ps formation. The stabilizing effect of the Ps provides indirect evidence

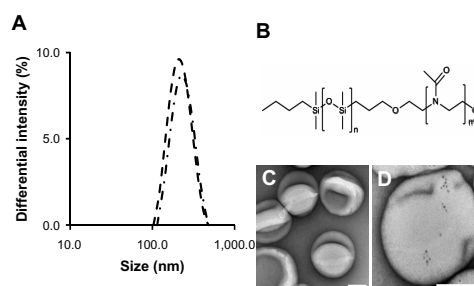


Figure 1 Chemical composition, size, and morphology of PDMS-PMOXA Ps-containing QDs. (A) Size distribution of Ps determined by DLS. Average diameter of Ps was 200 nm (dashed line: empty Ps, dot-dashed line: Ps-containing QDs); (B) chemical structure of PDMS-PMOXA amphiphilic block copolymers; (C) TEM analysis of Ps; (D) TEM analysis of Ps-containing QDs.

Note: The scale bars represent 100 nm.

Abbreviations: DLS, dynamic light scattering; PDMS-PMOXA, poly(dimethylsiloxane)-poly(2-methyloxazoline); Ps, polymersomes; QDs, quantum dots; TEM, transmission electron microscopy.

Table 1 Size, PDI, and surface charge of QDs and Ps

Sample	Diameter (nm)	PDI	Zeta potential (mV)
Free QDs	7–10 ^a	nd	-24.18
Empty Ps	205±7	0.075	5.62
Ps-containing QDs	223.9±9	0.053	9.69

Note: ^aSize according to data provided by the manufacturer for ITK™ carboxyl quantum dots (Invitrogen, Life Technologies, Lucerne, Switzerland).

Abbreviations: nd, no data; PDI, polydispersity index; Ps, polymersomes; QDs, quantum dots.

that the QDs are contained inside the Ps, and are not just loosely attached to the outer surface of the Ps membrane. Figure 2A shows characteristic emission spectra of free QDs, empty Ps, and Ps-containing QDs at the excitation wavelength of 405 nm. The appearance of the characteristic emission of QDs without any shift in the Em_{max} (625 nm) in Ps-containing QDs and the absence of this emission peak in empty Ps demonstrated the loading of QDs in Ps without alteration of the fluorescent properties of QDs. Thus, QDs can be incorporated into Ps without aggregation and without affecting the fluorescence properties of QDs. The main advantage of QDs is not their high quantum yield, which is often lower than that of many organic dyes. However, their high absorption rate and increased photostability finally result in a brighter fluorescence signal. Moreover, the Stokes shift leads to a very low background signal. In Figure 2A, fluorescence signals obtained from Ps-containing QDs are lower than from free QDs. This can be explained by the fact that QDs are encapsulated within Ps, which absorbs some of the excitation light. In addition, not all QDs were entrapped within the Ps during their preparation and were thus lost during the consecutive purification steps. However, this reduced fluorescence intensity of encapsulated QDs can be

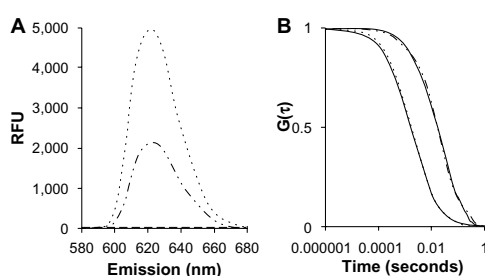


Figure 2 Analysis of QDs loading efficacy by fluorescence spectroscopy and FCS. (A) Emission fluorescence spectra of free QDs (dotted-lines), Ps-containing QDs (dot-dashed lines), and empty Ps (dashed lines), excitation wavelength 405 nm; (B) FCS auto-correlation curves, experimental (solid lines) and fitted (dashed-lines) of free QDs (dotted-lines) and Ps-containing QDs (dot-dashed lines).

Abbreviations: FCS, fluorescence correlation spectroscopy; Ps, polymersomes; QDs, quantum dots; RFU, relative fluorescent units.

easily compensated by an increased excitation light intensity since there is no risk of photobleaching.

Free QDs are characterized by a negative surface charge (zeta potential: -25 mV; Table 1). After loading into Ps, the zeta potential increases to 9 mV. This positive value is very similar to the zeta potential of empty Ps. Thus, masking of the surface charge of QDs after loading into Ps is an indication of their presence within the Ps as opposed to a mere binding to the outer surface of the Ps.

FCS analyzes the intensity fluctuations of molecules in a defined confocal volume. These signals can be correlated to the diffusion time of molecules (τ_D). We determined that $\tau_D=4,000 \mu s$ for freely diffusing QDs and $\tau_D=15,000-17,000 \mu s$ for QDs loaded into Ps (Figure 2B). This is in agreement with the reported diffusion time of Ps of a similar size based on the PDMS-PMOXA block copolymer.²⁸

Molecular brightness measurements have been used to calculate the number of fluorescent molecules encapsulated inside each polymersome.^{25,38} We estimated the average number of QDs per polymersome based on brightness obtained from the count rate per molecule (cpm, kHz). We calculated an average of four QDs/polymersome based on the brightness of free QDs and QDs encapsulated in Ps. The loading efficiency of Ps in our study was comparable with the reported loading efficiency of liposomes (ie, three QDs/liposome on average).^{39,40} However, we aimed to improve the loading efficiency by introducing 5% amine-functionalized PDMS-PMOXA copolymers in hydroxyl-functionalized PDMS-PMOXA copolymers to generate charges in the copolymer system (Figures S1–S4 in supplementary material). We calculated an average of eight QDs/Ps based on brightness measurements. This was clearly superior to the loading of purely hydroxyl-functionalized copolymers (neutral charge). Our results suggest that introducing a small amount of amine-functionalized monomers to the copolymer system causes favorable electrostatic interactions leading to improved loading efficiency. Geometric considerations and analysis of TEM images suggest that much higher loading efficiency can be achieved up to a theoretical maximal up-loading content of 4,900 QDs per polymersome. However, the achieved accumulation of QDs at picomolar concentrations within individual Ps is sufficient to induce a bright fluorescence signal suitable for cellular imaging (see below).

Stability of Ps-containing QDs

The stability of Ps-containing QDs was investigated using size measurements by DLS, morphology analysis by TEM,

3.4. POLYMERSOMES CONTAINING QUANTUM DOTS

and FCS analysis yielding release profiles of QDs from Ps. These tests were carried out over a period of 6 weeks at regular intervals (Figure 3). We did not observe any significant changes in size (~200 nm) or size distribution, suggesting that Ps were highly stable and remained intact (Figure 3D). In addition, TEM showed the presence of QDs inside the Ps (~200 nm), with no free QDs outside the Ps between day 1 and week 6 (Figure 3B and C).

For stability analysis, auto-correlation curves obtained with FCS were fitted with a two components model. Diffusion times of free QDs were determined independently and were included in the fitting procedure. The majority of the particle population (99.9%) represented QDs encapsulated in Ps, as confirmed by corresponding diffusion times ($\tau_D=15,000-17,000 \mu s$), that were similar to those of freshly prepared Ps loaded with QDs (Figure 3A). This finding confirms that QDs were not released from the Ps even after 6 weeks, due to the robust impermeable membrane of the Ps (~15 nm).²⁸ In addition, passive transmembrane diffusion is

unlikely due to the high molecular weight of the QDs. Thus, DLS, TEM, and FCS experiments clearly indicated that Ps were highly stable. They retained their size and shape and entrapped the QDs for a long period of time.

Cellular viability (MTT) assay

Various types of PMOXA-PDMS-PMOXA tri-block copolymers were previously suggested to be non-toxic and non-immunogenic.^{30,31} The PDMS-PMOXA diblock copolymer used in the present study showed no cellular toxicity in a HepG2 human liver carcinoma cell line (Figure 4). There was no loss of viability in HepG2 cells after 24 hours of incubation with PDMS-PMOXA Ps at concentrations up to 300 $\mu g/mL$.

Cellular uptake of Ps-containing QDs

Time- and dose-dependent uptake kinetics of Ps-containing QDs were studied using incubation times of 1, 7, and 24 hours and different polymer concentrations

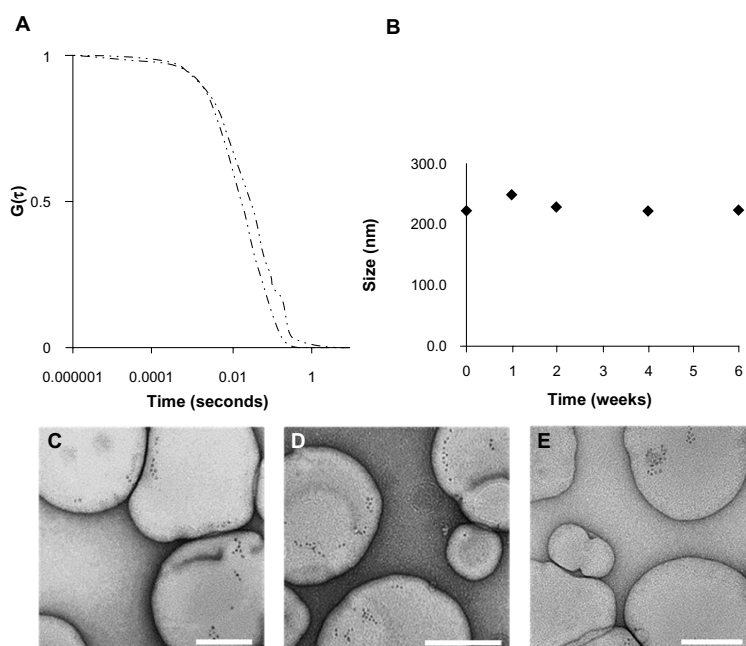


Figure 3 Long-term stability of Ps-containing QDs.

Notes: (A) FCS auto-correlation curve of Ps-containing QDs at day 1 (dot-dashed lines) and Ps-containing QDs at week 6 (double-dot-long dashed lines); (B) average particle size determined by DLS over 6 weeks (C) TEM analysis of Ps-containing QDs at day 1 (week 0); (D) TEM micrograph analysis of Ps-containing QDs at week 6; (E) TEM micrograph analysis of Ps-containing QDs after 1 year of storage at 4°C. Average size determined by DLS for the Ps-containing QDs after of 1 year storage was 221.1 nm (PDI =0.068). Scale bar represents 100 nm.

Abbreviations: DLS, dynamic light scattering; FCS, fluorescence correlation spectroscopy; PDI, polydispersity index; Ps, polymersomes; QDs, quantum dots; TEM, transmission electron microscopy.

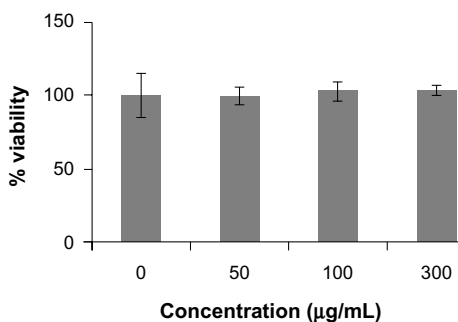


Figure 4 Viability of HepG2 cells incubated with Ps (MTT assay). HepG2 cells showed no loss of viability after 24 hours of incubation with different concentrations of Ps (50–300 µg/mL).

Note: Data are means \pm SD, n=3.

Abbreviations: Ps, polymersomes; HepG2, human liver carcinoma cells.

(100 µg/mL, 300 µg/mL, 500 µg/mL). While no uptake was observed for any concentrations after 1 hour of incubation, the uptake rate increased linearly from 7 hours to 24 hours, indicating the time-dependent uptake of Ps-containing QDs. Simultaneously, we observed a gradual increase in the uptake rate between the low concentration (100 µg/mL) to higher concentration (300 µg/mL), suggesting dose-dependent uptake (Figure 5). The appearance of red fluorescent signals, mainly in the perinuclear regions, was indicative of the

intracellular accumulation of Ps-containing QDs in HepG2 cells. Concentrations of Ps used for imaging purposes rarely exceed 100 µg/mL. Under these conditions, cellular uptake is minimal. Free QDs are rapidly taken up by living cells. However, this process is not specific, and therefore QDs cannot be used to label defined tissues or sub-populations of cells within tissues. In addition, free Cd/Se QDs are cytotoxic because of their heavy metal core. In contrast, Ps-containing QDs were demonstrated in our work to be non-cytotoxic. Their cellular uptake is negligible. This absence of unspecific cellular interactions is a mandatory prerequisite for their use to implement specific targeting strategies. For this latter purpose (ie, to promote cellular targeting and uptake), Ps can be modified by covalent modification of their surfaces using, for example, receptor-specific targeting ligands. Thus, surface-modified, polymer-based nanoparticles can be conveniently labeled with stabilized QDs to study and visualize their cellular interactions.⁴¹ The low uptake between 1 hour and 7 hours suggests that the PMOXA block acts as a protein repellent, reducing cellular interactions of Ps. This property has previously been described for other types of nanoparticles such as PEGylated liposomes,⁴¹ and is a prerequisite for in vivo implementation of targeting strategies. Thus, prolonged incubation (24 hours) was needed to induce forced uptake by HepG2 cells. We presume that cellular

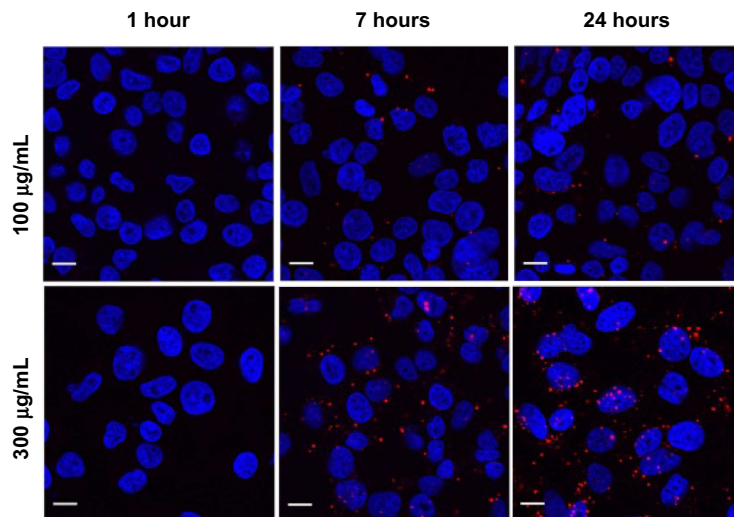


Figure 5 Dose- and time-dependent uptake of Ps-containing QDs in HepG2 cells. Ps concentrations incubated with HepG2 cells were 100 µg/mL (upper row, recommended concentration) to 300 µg/mL (lower row). Incubation times were 1 hour (left column), 7 hours (center column), and 24 hours (right column, condition of forced uptake). QDs were photo-activated at a wavelength of 490 nm for 1 minute. Red fluorescence: Ps-containing QDs, blue fluorescence: nuclei stained with Hoechst 33342.

Note: Scale bars represent 10 µm.

Abbreviations: Ps, polymersomes; QDs, quantum dots; HepG2, human liver carcinoma cells.

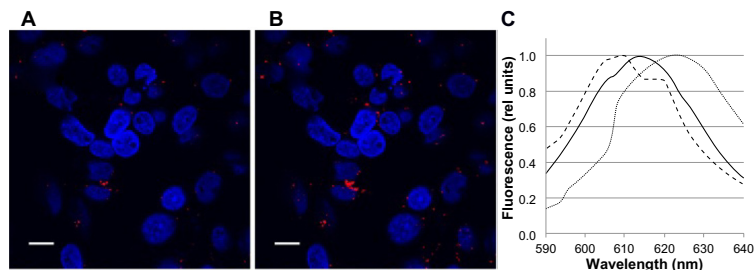


Figure 6 Fluorescence activities of QDs loaded into Ps under intracellular conditions.

Notes: HepG2 cells were incubated with Ps-containing QDs (red signal) and were analyzed before (A) and after (B) photo-activation at a wavelength of 400 nm for 15 seconds. (C) Emission peak of a lambda scan of intracellular QDs in Ps (solid lines) and in liposomes (dashed-lines) compared with free QDs (dotted-lines). Nuclei were stained with Hoechst 33342 (blue signal).

Abbreviations: Ps, polymersomes; QDs, quantum dots; HepG2, human liver carcinoma cells.

uptake can be further increased by surface modifications of the Ps, such as, for example, cationization or coupling of specific receptor ligands.⁴¹ Previous publications suggest that cellular uptake of nanoparticles is a prerequisite to induce cellular toxicity.⁴² In order to explore the potential toxic effect of the Ps, the concentration in medium was increased to 300 $\mu\text{g}/\text{mL}$. A long incubation time (24 hours) under these conditions led to cellular uptake. However, the MTT assay demonstrated an absence of toxicity under these conditions of forced uptake. Therefore, we recommend to limit incubation times with Ps-containing QDs to 24 hours and not to exceed a polymer concentration of 100 $\mu\text{g}/\text{mL}$.

Intracellular stability of Ps-containing QDs

QDs encapsulated in Ps or liposomes can be photoactivated by UV irradiation at 405 nm. This is a widely used technique to enhanced fluorescence signals of QDs in suspension or cells.⁴³ Photoactivation was made evident by a blue-shift of cellular emission fluorescence signals by 10 nm (Ps) or 15 nm (liposomes), as compared to free QDs (Figure 6C). This is indicative of the slow degradation of the QD core under these conditions. In liposomes, photoactivation of encapsulated QDs resulted in a blurred and unspecific staining of the whole cell cytoplasm (data not shown, preparation of liposomes containing QDs can be found in supplementary material). However, photoactivation of QDs in Ps resulted in a sharp and punctuated intracellular staining pattern (Figure 6A and B). These results suggest that QDs encapsulated in Ps were retained in the intact polymer vesicles, whereas QDs encapsulated in liposomes were released into the cytoplasm due to degradation of the liposomal carrier.

In living cells, photoactivation of QDs is caused by the generation of reactive oxygen species (ROS) within the target cell.⁴³ In view of the pronounced intracellular stability of Ps,

the question arises how oxidation of QDs within Ps can be induced by cellular ROS. It was recently proposed that the membranes of Ps are permeable to ROS, such as superoxide or singlet oxygen, which are major contributors to the degradation of the QD surface.^{43,44}

For a similar type of Ps made of PMOXA-PDMS-PMOXA, ROS were reported to permeate the polymer membrane. Ps remained stable inside cells after having escaped from endosomes without releasing the encapsulated compounds.^{24,25,45} Therefore, it is possible that in our experiments, QDs were partially degraded inside the Ps without being released. Due to the stability of Ps in cellular conditions, degradation of QDs and background signals were dramatically lower in Ps than in liposomes. Similarly, increased photo-enhancement of QDs embedded in silica colloids have been reported in living cells, due to partial degradation mediated by oxidation with minimal aggregation.⁴⁶ Results suggested that Ps protect QDs from biological interactions in cell compartments, thus improving the quality of cellular imaging.

Conclusion

QDs are a promising tool for a variety of bio-imaging applications. However, their use in biological systems is limited by their chemical instability and toxicity. We demonstrated that loading of QDs into Ps made of the diblock copolymer PDMS-PMOXA may overcome these problems. In particular, Ps-containing QDs were stable for a prolonged time upon storage and had improved optical properties after cellular uptake.

The implications of these findings are two-fold. First, stabilization of QDs by a protective shell of diblock copolymers may facilitate their preparation, storage, and use in biological systems. Second, chemical modification of the

Ps surface may improve their recognition and uptake by target cells. Therefore, design of such targeted Ps offers the possibility to deliver QDs to specific cellular targets within the organism for diagnostic purposes or imaging applications.

Acknowledgments

We would like to thank Professor Dr Wolfgang Meier for providing the PDMS-PMOXA diblock copolymers. We thank Dr Silvia Rogers for editorial assistance.

Disclosure

The authors report no conflicts of interest in this work.

References

- Bruchez M, Moronne M, Gin P, Weiss S, Alivisatos AP. Semiconductor nanocrystals as fluorescent biological labels. *Science*. 1998;281(5385):2013–2016.
- Chan WC. Quantum dot bioconjugates for ultrasensitive nonisotopic detection. *Science*. 1998;281(5385):2016–2018.
- Resch-Genger U, Grabolle M, Cavaliere-Jaricot S, Nitschke R, Nann T. Quantum dots versus organic dyes as fluorescent labels. *Nat Methods*. 2008;5(9):763–775.
- Alivisatos AP, Gu W, Larabell C. Quantum dots as cellular probes. *Annu Rev Biomed Eng*. 2005;7:55–76.
- Derfus AM, Chan WCW, Bhatia SN. Probing the cytotoxicity of semiconductor quantum dots. *Nano Lett*. 2004;4(1):11–18.
- Michalet X, Pinaud FF, Bentolila LA, et al. Quantum dots for live cells, in vivo imaging, and diagnostics. *Science*. 2005;307(5709):538–544.
- Hardman R. A toxicologic review of quantum dots: toxicity depends on physicochemical and environmental factors. *Environ Health Perspect*. 2006;114(2):165–172.
- Hu X, Gao X. Silica-polymer dual layer-encapsulated quantum dots with remarkable stability. *ACS Nano*. 2010;4(10):6080–6086.
- Zhang H, Zeng X, Li Q, Gaillard-Kelly M, Wagner CR, Yee D. Fluorescent tumour imaging of type IIGF receptor in vivo: comparison of antibody-conjugated quantum dots and small-molecule fluorophore. *Br J Cancer*. 2009;101(1):71–79.
- Selvan ST, Tan TTY, Yi DK, Jana NR. Functional and multifunctional nanoparticles for bioimaging and biosensing. *Langmuir*. 2010;26(14):11631–11641.
- Derfus AM, Chan WCW, Bhatia SN. Intracellular delivery of quantum dots for live cell labeling and organelle tracking. *Adv Mater*. 2004;16(12):961–966.
- Jańczewski D, Tomczak N, Han MY, Vancso GJ. Synthesis of functionalized amphiphilic polymers for coating quantum dots. *Nat Protoc*. 2011;6(10):1546–1553.
- Gao X, Cui Y, Levenson RM, Chung LWK, Nie S. In vivo cancer targeting and imaging with semiconductor quantum dots. *Nat Biotechnol*. 2004;22(8):969–976.
- Gerion D, Pinaud F, Williams SC, et al. Synthesis and properties of biocompatible water-soluble silica-coated CdSe/ZnS semiconductor quantum dots. *J Phys Chem B*. 2001;105(37):8861–8871.
- Bayles AR, Chahal HS, Chahal DS, Goldbeck CP, Cohen BE, Helms BA. Rapid cytosolic delivery of luminescent nanocrystals in live cells with endosome-disrupting polymer colloids. *Nano Lett*. 2010;10(10):4086–4092.
- Kong L, Zhang T, Tang M, Pu Y. Apoptosis induced by cadmium selenide quantum dots in JB6 cells. *J Nanosci Nanotechnol*. 2012;12(11):8258–8265.
- Chen H, Zou P, Connarn J, Paholak H, Sun D. Intracellular dissociation of a polymer coating from nanoparticles. *Nano Res*. 2012;5(11):815–825.v
- Balasubramanian V, Onaca O, Enea R, Hughes DW, Palivan CG. Protein delivery: from conventional drug delivery carriers to polymeric nanoreactors. *Expert Opin Drug Deliv*. 2010;7(1):63–78.
- Battaglia G. Polymersomes and Their Biomedical Applications. In: *Nanotechnologies for the Life Sciences*. Weinheim, Germany: Wiley-VCH Verlag; 2007. Available at: <http://onlinelibrary.wiley.com/doi/10.1002/9783527610419.ntls0250/abstract>. Accessed June 3, 2013.
- Lee JS, Feijen J. Polymersomes for drug delivery: design, formation and characterization. *J Controlled Release*. 2012;161(2):473–483.
- Ahmed F, Pakunlu RI, Brannan A, Bates F, Minko T, Discher DE. Biodegradable polymersomes loaded with both paclitaxel and doxorubicin permeate and shrink tumors, inducing apoptosis in proportion to accumulated drug. *J Controlled Release*. 2006;116(2):150–158.
- Sanson C, Schatz C, Le Meins J-F, et al. A simple method to achieve high doxorubicin loading in biodegradable polymersomes. *J Controlled Release*. 2010;147(3):428–435.
- Lomas H, Canton I, MacNeil S, et al. Biomimetic pH sensitive polymersomes for efficient DNA encapsulation and delivery. *Adv Mater*. 2007;19(23):4238–4243.
- Balasubramanian V, Onaca O, Ezhevskaya M, Doorslaer SV, Sivasankaran B, Palivan CG. A surprising system: polymeric nanoreactors containing a mimic with dual-enzyme activity. *Soft Matter*. 2011;7(12):5595–5603.
- Tanner P, Onaca O, Balasubramanian V, Meier W, Palivan CG. Enzymatic cascade reactions inside polymeric nanocontainers: a means to combat oxidative stress. *Chemistry*. 2011;17(16):4552–4560.
- Jaskiewicz K, Larsen A, Schaeffel D, et al. Incorporation of nanoparticles into polymersomes: size and concentration effects. *ACS Nano*. 2012;6(8):7254–7262.
- Liu GY, Liu XS, Wang SS, Chen CJ, Ji J. Biomimetic polymersomes as carriers for hydrophilic quantum dots. *Langmuir*. 2012;28(1):557–562.
- Egli S, Nussbaumer MG, Balasubramanian V, et al. Biocompatible functionalization of polymersome surfaces: a new approach to surface immobilization and cell targeting using polymersomes. *J Am Chem Soc*. 2011;133(12):4476–4483.
- Mai Y, Eisenberg A. Self-assembly of block copolymers. *Chem Soc Rev*. 2012;41(18):5969.
- De Vocht C, Ranquin A, Van Ginderachter J, et al. Polymeric nanoreactors for enzyme replacement therapy of MNGIE. *J Control Release*. 2010;148(1):e19–e20.
- Nardin C, Hirt T, Leukel J, Meier W. Polymerized ABA triblock copolymer vesicles. *Langmuir*. 2000;16(3):1035–1041.
- Lee JC-M, Bermudez H, Discher BM, et al. Preparation, stability, and in vitro performance of vesicles made with diblock copolymers. *Biotechnol Bioeng*. 2001;73(2):135–145.
- Qu L, Peng X. Control of photoluminescence properties of CdSe nanocrystals in growth. *J Am Chem Soc*. 2002;124(9):2049–2055.
- Williams G, Watts DC, Dev SB, North AM. Further considerations of non symmetrical dielectric relaxation behaviour arising from a simple empirical decay function. *Trans Faraday Soc*. 1971;67(0):1323–1335.
- Rigler P, Meier W. Encapsulation of fluorescent molecules by functionalized polymeric nanocontainers: investigation by confocal fluorescence imaging and fluorescence correlation spectroscopy. *J Am Chem Soc*. 2006;128(1):367–373.
- Seeland S, Török M, Kettiger H, Treiber A, Hafner M, Huwyler J. A cell-based, multiparametric sensor approach characterises drug-induced cytotoxicity in human liver HepG2 cells. *Toxicol In Vitro*. 2013;27(3):1109–1120.
- CoolLED. LED Intensity – CoolLED. 2012. Available at: <http://www.coolled.com/Life-Sciences-Analytical/Products/pE-2/>. Accessed October 17, 2012.
- Onaca O, Hughes DW, Balasubramanian V, Grzelakowski M, Meier W, Palivan CG. SOD antioxidant nanoreactors: influence of block copolymer composition on the nanoreactor efficiency. *Macromol Biosci*. 2010;10(5):531–538.

3.4. POLYMERSOMES CONTAINING QUANTUM DOTS

39. Sigot V, Arndt-Jovin DJ, Jovin TM. Targeted cellular delivery of quantum dots loaded on and in biotinylated liposomes. *Bioconjug Chem.* 2010;21(8):1465–1472.
40. Chen C-S, Yao J, Durst R. Liposome encapsulation of fluorescent nanoparticles: quantum dots and silica nanoparticles. *J Nanoparticle Res.* 2006;8(6):1033–1038.
41. Huwyler J, Drewe J, Krähenbuhl S. Tumor targeting using liposomal antineoplastic drugs. *Int J Nanomedicine.* 2008;3(1):21–29.
42. Kettiger H, Schipanski A, Wick P, Huwyler J. Engineered nanomaterial uptake and tissue distribution: from cell to organism. *Int J Nanomedicine.* 2013;8:3255–3269.
43. Zhang Y, He J, Wang P-N, et al. Time-dependent photoluminescence blue shift of the quantum dots in living cells: effect of oxidation by singlet oxygen. *J Am Chem Soc.* 2006;128(41):13396–13401.
44. Carrillo-Carrión C, Cárdenas S, Simonet BM, Valcárcel M. Quantum dots luminescence enhancement due to illumination with UV/Vis light. *Chem Commun (Camb).* 2009;(35):5214–5226.
45. Baumann P, Balasubramanian V, Onaca-Fischer O, Sienkiewicz A, Palivan CG. Light-responsive polymer nanoreactors: a source of reactive oxygen species on demand. *Nanoscale.* 2013;5(1):217–224.
46. Dembski S, Graf C, Krüger T, et al. Photoactivation of CdSe/ZnS quantum dots embedded in silica colloids. *Small.* 2008;4(9):1516–1526.

Supplementary material

Materials and methods

Preparation of liposomes containing QDs

A mixture of lipids of disuccinatocisplatin (DSPC; 5.5 μmol), cholesterol (4.5 μmol), and 1,2-distearoyl-sn-glycero-3-phosphoethanolamine-N-poly(ethylene glycol) (DSPE-PEG; 0.27 μmol), were dissolved in chloroform/methanol (2:1, volume/volume). The solution was evaporated by vacuum in a water bath at 60°C for 1 hour to form a homogenous lipid film using a rotary evaporator (Rotavapor, BÜCHI Labortechnik AG, Flawil, Switzerland). The lipid film was hydrated for 10 minutes in 1 mL in a 100 nM solution of QDs (Qdot® ITK™ carboxyl quantum dots; Invitrogen, Life Technologies, Lucerne, Switzerland) in 0.1 M phosphate buffer solution (PBS) containing 1 mM EDTA, pH 7.2; extrusion was performed five times through a polycarbonate filter with an average pore diameter of 0.2 μm , followed by nine extrusions through a filter with an average pore diameter of 0.08 μm (Nucleopores, Whatman, VWR International AG, Dietikon, Switzerland).

Liposomes containing QDs were purified by size exclusion chromatography using a Superose 6 prep column (1.6 \times 20 cm), (GE Healthcare, Cleveland, OH, USA) eluting with 0.01 M PBS, pH 7.2.

Results

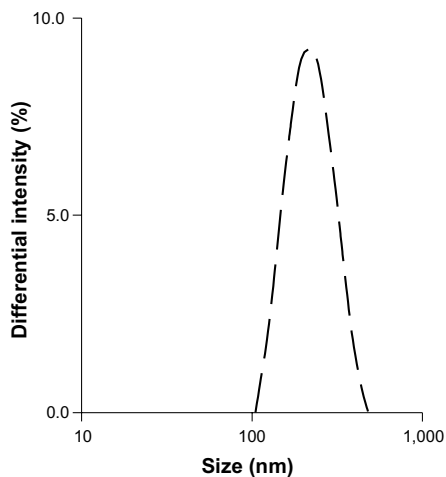


Figure S1 Size of Ps made of PDMS-PMOXA with 5% amine function (long-dashed lines), loaded with QDs. Average diameter of Ps was 210 nm.

Abbreviations: PDMS-PMOXA, poly(dimethylsiloxane)-poly(2-methyloxazoline); Ps, polymersomes; QDs, quantum dots.

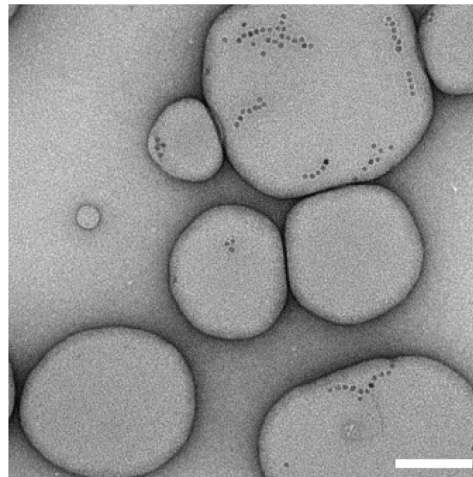


Figure S2 TEM morphology analysis of Ps made of PDMS-PMOXA with 5% amine function, loaded with QDs.

Note: Scale bar represents 100 nm.

Abbreviations: PDMS-PMOXA, poly(dimethylsiloxane)-poly(2-methyloxazoline); Ps, polymersomes; QDs, quantum dots; TEM, transmission electron microscopy.

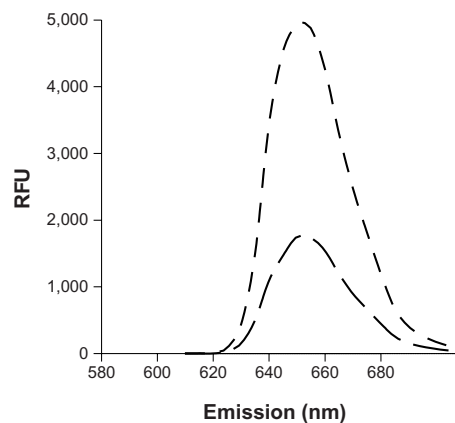


Figure S3 Analysis of QDs loading efficacy by fluorescence spectroscopy. Emission fluorescence spectra of free QDs (dotted-lines), Ps with 5% amine function containing QDs (long-dashed lines), and empty Ps (dashed lines), excitation wavelength 405 nm.

Abbreviations: Ps, polymersomes; QDs, quantum dots; RFU, relative fluorescent units.

3.4. POLYMERSOMES CONTAINING QUANTUM DOTS

Camblin et al

Dovepress

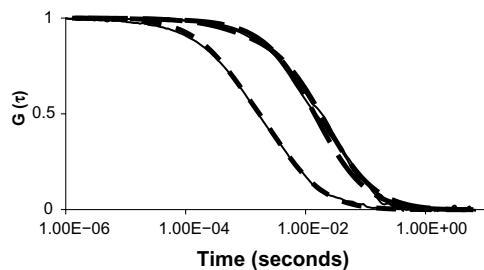


Figure S4 Analysis of QDs loading efficacy by FCS. FCS auto-correlation curves, experimental (solid lines) and fitted (dashed-lines) of free QDs (dotted-lines), Ps-containing QDs (dot-dashed lines), and Ps with 5% amine function containing QDs (long-dashed lines).

Abbreviations: FCS, fluorescence correlation spectroscopy; Ps, polymersomes; QDs, quantum dots.

International Journal of Nanomedicine

Publish your work in this journal

The International Journal of Nanomedicine is an international, peer-reviewed journal focusing on the application of nanotechnology in diagnostics, therapeutics, and drug delivery systems throughout the biomedical field. This journal is indexed on PubMed Central, MedLine, CAS, SciSearch®, Current Contents®/Clinical Medicine,

Submit your manuscript here: <http://www.dovepress.com/international-journal-of-nanomedicine-journal>

Dovepress

Journal Citation Reports/Science Edition, EMBase, Scopus and the Elsevier Bibliographic databases. The manuscript management system is completely online and includes a very quick and fair peer-review system, which is all easy to use. Visit <http://www.dovepress.com/testimonials.php> to read real quotes from published authors.

2298 submit your manuscript | www.dovepress.com
Dovepress

International Journal of Nanomedicine 2014:9

3.5 Multiparametric sensor approach for drug-induced toxicity

A cell-based, multiparametric sensor approach characterises drug-induced cytotoxicity in human liver HepG2 cells.

Seeland Swen^{1,2,3}, Török Michael¹, Helene Kettiger², Treiber Alexander¹, Hafner Matthias^{2,3} Jörg Huwyler²

¹ Actelion Pharmaceuticals Ltd., Gewerbestrasse 16, 4123 Allschwil, Switzerland

² Institute for Molecular and Cell Biology, University of Applied Sciences, Paul-Wittsack Strasse 10, 68163 Mannheim, Germany

³ Medical Faculty Mannheim, University of Heidelberg, Theodor-Kutzer-Ufer 1-3, 68167 Mannheim, Germany

⁴ Department of Pharmaceutical Sciences, University of Basel, Switzerland

Contribution H.Kettiger: author, experiments (MTT assay)

Toxicology in vitro 2013 Apr;27(3):1109-20.



Contents lists available at SciVerse ScienceDirect

Toxicology in Vitro

journal homepage: www.elsevier.com/locate/toxinvit

A cell-based, multiparametric sensor approach characterises drug-induced cytotoxicity in human liver HepG2 cells

Swen Seeland^{a,b,c}, Michael Török^a, Helene Kettiger^d, Alexander Treiber^a, Mathias Hafner^{b,c}, Jörg Huwyler^{d,*}

^a Actelion Pharmaceuticals Ltd., Gewerbestrasse 16, 4123 Allschwil, Switzerland

^b Institute for Molecular and Cell Biology, University of Applied Sciences, Paul-Wittsack Strasse 10, 68163 Mannheim, Germany

^c Medical Faculty Mannheim, University of Heidelberg, Theodor-Kutzer-Ufer 1-3, 68167 Mannheim, Germany

^d Department of Pharmaceutical Sciences, Division of Pharmaceutical Technology, University of Basel, Klingelbergstrasse 50, 4056 Basel, Switzerland

ARTICLE INFO

Article history:
Received 15 October 2012
Accepted 6 February 2013
Available online 14 February 2013

Keywords:
HepG2
Cytotoxicity
Metabolic stress
Cytosensor
Mitochondrial respiration
Respiratory stress
Drug-induced liver injury (DILI)

ABSTRACT

Drug-induced toxicity is of considerable concern in drug discovery and development, placing emphasis on the need for predictive *in vitro* technologies that identify potential cytotoxic side effects of drugs.

A label-free, real-time, multiparametric cytosensor system has therefore been established for *in vitro* assessment of drug-induced toxicity. The system is based on monitoring cellular oxygen consumption, acidification and impedance of human hepatocarcinoma-derived HepG2 cells. The read-out derived from the multiparametric cytosensor system has been optimised and permits sensitive, reliable, and simultaneous recording of cell physiological signals, such as metabolic activity, cellular respiration and morphological changes and cell adhesion upon exposure to a drug.

Analysis of eight prototypic reference drugs revealed distinct patterns of drug-induced physiological signals. Effects proved to be rigidly concentration-dependent. Based on signal patterns and reversibility of the observed effects, compounds could be classified based as triggering mechanisms of respiratory or metabolic stress or conditions leading to cell death (necrosis-like and apoptosis-like). A test-flag-risk mitigation strategy is proposed to address potential risks for drug-induced cytotoxicity.

© 2013 Elsevier Ltd. All rights reserved.

1. Introduction

The prediction of chemically induced toxicity in animals or humans remains a challenge. Biochemical or cell based *in vitro* test systems often fall short in predicting toxicities involving multiple organs, such as inflammation or immune-mediated adverse reactions, or events associated with adaptation to chronic chemical exposure. However, such models have nevertheless been proven to provide valuable insight into molecular mechanisms of toxicity on a cellular level. This is in particular true for organotypic liver cell culture models, which may be applied in situations where biotransformation and bioactivation of chemicals contribute to their toxicity (LeCluyse et al., 2012). In the field of clinical toxicology, drug-induced liver injury (DILI) is a prime example of a chemically induced liver injury, which in 80% of all cases is caused by direct concentration-dependent toxicity of an administered drug or its metabolites

(Smith and Schmid, 2006). Drugs that exhibit such chemical (direct) hepatotoxicity have predictable dose–response curves and well characterised mechanisms of toxicity. Examples include promotion of dysfunction of physiological pathways and finally cell death by direct insult by chemically reactive compounds, induction of an apoptotic process or infliction of cellular stress (David and Hamilton, 2010). The latter phenomenon is often observed in the context of oxidative or metabolic stress, where inhibition of the mitochondrial respiratory chain results in a release of reactive oxygen species (ROS) to an excessive level and depletion of adenosine triphosphate (ATP) (Berson et al., 1996; Fromenty and Pessayre, 1995; Jaeschke et al., 2002). Furthermore, certain drugs influence mitochondrial activity by inhibiting fatty acid β -oxidation (Fromenty and Pessayre, 1995), impairing mitochondrial DNA replication (Setzer et al., 2008) or opening the mitochondrial permeability transition pore, which is implacably associated with cell death (Lee and Farrell, 2001). All of the physiological dysfunctions mentioned above ultimately lead to hepatic tissue damage. If energy is available in the form of ATP, injured cells enter programmed cell death (apoptosis). If ATP sources are exhausted, cells follow the necrosis pathway, enhancing hepatic inflammation (Leist et al., 1997).

Abbreviations: ATP, adenosine triphosphate; DMSO, dimethyl sulfoxide; GSH, glutathione; IU, international unit; NAPQI, N-acetyl-p-benzoquinone imine; ROS, reactive oxygen species.

* Corresponding author. Tel.: +41 61 267 15 13; fax: +41 61 267 15 16.

E-mail address: joerg.huwyler@unibas.ch (J. Huwyler).

0887-2333/\$ - see front matter © 2013 Elsevier Ltd. All rights reserved.
<http://dx.doi.org/10.1016/j.tiv.2013.02.001>

Drug-induced toxicities leading to organ dysfunction are generally paralleled by a rise in biochemical markers such as liver-specific alanine aminotransferase or alkaline phosphatase (Liss and Lewis, 2009). These initial indicators of cell damage, when observed during the drug discovery and development process, call for alert and necessitate mechanistic follow-up studies. Such studies are ideally based on the use of additional biomarkers as predictors and are time consuming and costly if performed in experimental animals (Liss et al., 2010). However, in view of the poor correlation between clinical findings of toxicity and standard preclinical animal studies, such efforts remain a challenge and are in some cases a source of concern for investigators and regulatory authorities. Ongoing efforts are therefore directed towards the development of predictive *in silico* or *in vitro* models to gain better insight into mechanisms leading to cytotoxicity. One strategy is the use of cytosensor systems, where a silica-based sensor system allows online-monitoring of metabolic activity in target cells in the presence of potentially toxic chemicals (Twiner et al., 1998). Recently, we used a multiparametric, chip-based sensor system to determine extracellular acidification, and cell respiration and adhesion in a cell line overexpressing the drug efflux transporter P-glycoprotein (P-gp) (Seeland et al., 2011). In light of the sensitivity of such cytosensor systems to deviations in the metabolic balance between glycolysis and mitochondrial respiration, the question arises as to whether this approach might be adapted to monitor the early onset of drug-induced cellular damage *in vitro*.

The aim of the present study was therefore to implement and validate a cell-based multiparametric sensor system to characterise drug induced cytotoxicity. For this approach, eight prototypic drugs known to be hepatotoxic in therapeutic use were investigated with respect to their toxicological potential on human hepatocarcinoma-derived HepG2 cells. The distinct difference in the mechanisms of toxicity and liver pathology were considered during the selection of these eight drugs. The HepG2 cell line is frequently used as a model system because these cells are adherent, well established and characterised by a limited potential to metabolise drugs in terms of cytochrome P450 monooxygenase metabolism. Emphasis was placed on the assessment of mitochondrial respiration, glycolytic (catabolic) activity and/or morphological changes and cell adhesion as major cellular markers for toxicity. Based on the nature of cellular response, different types of effects, including necrosis-like, apoptosis-like and metabolic or respiratory stress, were discriminated.

2. Material and methods

2.1. Compounds

All chemicals were purchased from Sigma (Buchs, Switzerland) if not otherwise indicated. Amiodarone, cyclosporine A, doxorubicin, isoniazide, and methotrexate were used as stock solutions dissolved in either water or dimethyl sulfoxide (DMSO). DMSO concentrations in none of the experiments exceeded 1% (v/v). Acetaminophen, D-sorbitol and valproic acid were directly dissolved in assay medium. The pH of solutions was adjusted to pH 7.4 prior to the experiment. The MTT (3-(4, 5-dimethylthiazol-2-yl)-2, 5-diphenyltetrazolium bromide) stock solution was prepared in phosphate buffered saline at a concentration of 5 mg/mL, then was sterile-filtered and stored at 4 °C in the dark.

2.2. Cell culture

The human epithelial hepatocarcinoma-derived cell line HepG2 was obtained from the American Type Culture Collection (ATCC, Rockville, MD, US) and was maintained under standard cell culture

conditions as described previously (Van Summeren et al., 2011). In brief, cells were cultivated at passage numbers 3–15 in modified Eagle medium (MEM) with 1 g/L glucose and 2 mM GlutaMAX™ (Life Technologies, Carlsbad, CA, US) supplemented with 1 mM sodium pyruvate, 1% (v/v) non-essential amino acids, 50 IU/mL penicillin, 50 µg/mL streptomycin and 10% (v/v) heat-inactivated foetal bovine serum (PAA Laboratories, Pasching, Austria) in a humidified atmosphere containing 5% carbon dioxide. Prior to the experiment, HepG2 cells were detached by trypsinisation, viability determined by a Vi-cell XR analyser (Beckman Coulter, Krefeld, Germany) and seeded onto pre-warmed, non-coated metabolic sensor chips at a density of 2×10^5 cells/chip. Seeded cells were incubated for at least 20 h prior to use. Integrity of the cell monolayer covering the surface of the cytosensor chip was verified using a Motic DM-39C reflected-light microscope (Motic Group Ltd., Hong Kong, China). Cell monolayers with a cellular confluence below 80% were rejected for use. It should be noted that expression of drug transporters such as P-glycoprotein by HepG2 cells (Hilgen-dorf et al., 2007) may influence drug uptake by this cell line and thereby modulate its response towards toxic insults. The mRNA expression level of MDR1 in primary human hepatocytes is in the range of the one of HepG2 cells (Le Vee et al., 2006) and below the level of human liver tissue (Hilgen-dorf et al., 2007).

2.3. Cytosensor experiments

A Bionas®2500 cytosensor system (Bionas, Rostock, Germany) was used to record cell physiological parameters continuously. The system consists of six metabolic sensor chips SC1000 working in parallel and containing ion-sensitive field effect transistor- (IS-FET) and Clark-type sensors for the measurement of changes of acidification and oxygen consumption. Cell adhesion, morphological changes, and membrane functionality were monitored by means of impedance measurements. The cytosensor system was used as described previously (Seeland et al., 2011) with the following modifications: a flow head with 200 µm spacers (as determined by the distance between the flow head and the sensor chip surface) was used (Fig. 1) leading to an effective chamber volume of 5.7 µL. The assay medium was prepared from a 10-fold concentrated, modified Eagle medium (Life Technologies, Basel, Switzerland) supplemented with 2 mM GlutaMAX, 1 mM sodium pyruvate, 1% (v/v) non-essential amino acids, 25 IU/mL penicillin, 25 µg/mL streptomycin, and 0.1% (v/v) heat-inactivated foetal bovine serum. The assay medium contained neither Hepes nor sodium bicarbonate and was adjusted to pH 7.4 using sodium hydroxide. During analysis, the assay medium was delivered to the cells at a constant flow rate of 56 µL/min and interrupted periodically (stop phases and pump phase lasted 3 min each) as described previously (Seeland et al., 2011). Raw data were recorded by all sensors at intervals of 10 s to obtain 18 raw data points per cycle. A linear regression analysis was performed to determine initial rates of extracellular acidification and respiration. Rates were calculated based on datapoints recorded during the stop phases of the experiment. The Bionas data analyser software (version 1.66) was used for data evaluation. Impedance measurements were carried out continuously to monitor cell adhesion and thus cell morphology and membrane functionality (Ehret et al., 1998). Signals were normalised to a reference value, which represented the baseline signal of a cell-coated chip prior to treatment with the compound. At the end of each experiment, 0.2% (v/v) Triton X-100 was added to the cells to detach cells from the surface of the sensor chip. The signal that was generated under these conditions was used to provide a reference signal from the cell-free sensor surface (0% baseline value). Data from the metabolic sensor chip were recorded after a stabilisation phase of 3 h, which resulted in a constant baseline signal from the different sensors. Cells

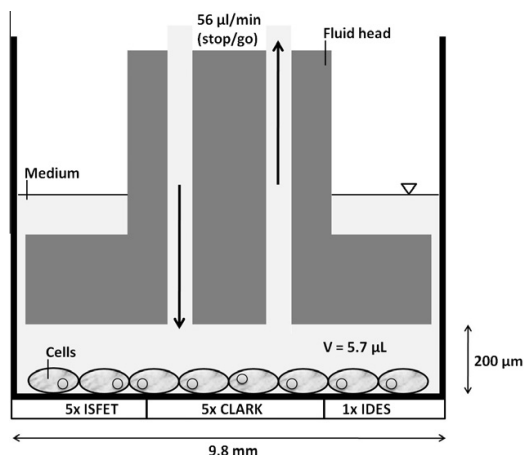


Fig. 1. Schematic diagram of the experimental setup of the multiparametric cytosensor system. Incubation volumes, flow rates, and dimensions of the perfusion chamber are shown. The direction of the flow of incubation medium is indicated by arrows. The core of the system consists of a sensor chip with a surface area of 75 mm².

were incubated for 19 h with the test compounds (Table 1). For those compounds whose stock solutions were prepared in other media, an equivalent amount of DMSO was added to the incubation medium. DMSO concentrations were below 1% (v/v) in all experiments. The drug treatment phase was followed by a 2 h wash-out period to detect cell recovery processes if occur.

2.4. MTT cell viability assay

HepG2 cells were seeded in 96-well plates at a density of 5×10^4 cells/well and were cultured as described above. Twenty-four hours after seeding, medium was removed and 100 μ L aliquots of cell culture medium containing the test compounds were added to each well in triplicate. Control cells were incubated in the presence of 1% (v/v) DMSO (100% viability control). After 24 h, cell culture medium was replaced by 100 μ L cell culture medium containing 10% (v/v) MTT stock solution. Cells were incubated for additional 2 h at 37 °C. In a final step, the cell culture medium was discarded and reduced MTT, which is present as water-insoluble formazan dye crystals, was dissolved by adding 20 μ L of 3% (v/v) sodium dodecylsulphate solution in water, and 100 μ L of a 40 mM hydrochloric acid in isopropanol. Optical density was measured at 550 nm using a Spectramax M2 plate reader (Molecular Devices, Sunnyvale, CA, US). The 24 h incubation in the MTT assay is comparable to the 24 h total duration of the cytosensor assay considering a 19 h incubation time with test compound and a 5 h pre- and post-conditioning phase.

2.5. Data analysis and statistics

The calculation of the standard rates was done with the Bionas[®] 2500 Data Analyzer software (Version 1.66, Bionas[®], Rostock, Germany). The control (running medium without drug) was normalised to 100% and was used for better visualisation. The evaluation and interpretation of the multiparametric cytosensor system data was performed using GraphPad Prism software (Version 5.04, GraphPad Software Inc., La Jolla, CA, USA). Each experiment was performed at least in triplicates. MTT test was performed two times in quadruplicate samples. The calculations for the MTT were performed using Microsoft Excel and the results

are expressed as the mean \pm SD, where SD is the standard deviation.

3. Results

3.1. Experimental setup using a multiparametric cytosensor system

Changes in three cellular parameters (i.e. extracellular acidification, oxygen consumption and impedance) were monitored in real-time using a multiparametric cytosensor system. The experimental set-up was optimised to achieve maximal sensitivity to physiological alterations (Fig. 1). Important assay parameters included the use of an assay medium (see section cytosensor experiments) with a low buffer capacity which was additionally supplemented with 0.1% (v/v) heat-inactivated foetal bovine serum albumin. Optimal cell density was determined as 2×10^5 viable HepG2 cells per chip. Minimal required cell viability, estimated by a trypan blue dye exclusion test, was 90%. The effective volume of the incubation chamber, i.e. the volume of the space between the surface of the sensor chip and the chamber lid, was 5.7 μ L and was determined by the distance (200 μ m) between the flow head and the sensor chip surface (Fig. 1). This minimal volume enhances the responsiveness of the system with respect to alterations in pH and oxygen partial pressure. Signals from cell respiration, acidification, and impedance were recorded after an initial stabilisation phase of 3 h. Subsequently, cells were exposed to test compounds for 19 h followed by a drug wash-out period of 2 h to detect cell recovery. After the experiment, baseline signals of the cell-free cytosensor chips (i.e. 0% reference signal) were recorded after solubilisation of cells using a non-ionic detergent (Triton X-100). Cellular adhesion was monitored continuously by measurements of cellular impedance. Thus, signals from the three sensor types were recorded relative to initial conditions (100% reference signal) and 0% background signal. Eight marketed drugs were used at, above, and below their clinically relevant plasma concentrations to study hepatotoxic effects *in vitro* (Table 1). In control experiments, the metabolic activity of HepG2 cells was assessed by 19 h incubations of acetaminophen and amiodarone (20 μ M each, data not shown). Metabolites were detected using high-resolution liquid chromatography coupled with mass spectrometry in positive ion mode. Acetaminophen incubations with HepG2 cells resulted in formation of an oxidised metabolite (m/z 168, 0.1 μ M), N-acetyl-p-benzoquinone imine (NAPQI) (m/z 150, 0.6 μ M), and two phase II metabolites (a cysteine adduct at m/z 271, 5.0 μ M and a glucuronic acid conjugate at m/z 328, 4.4 μ M). In incubations with amiodarone, the major metabolite was desethylamiodarone (m/z 618, 1.0 μ M) accompanied by a hydrated- (m/z 648, 0.1 μ M), a dehydrated- (m/z 644, 0.1 μ M) and an oxidised metabolite (m/z 662, 0.1 μ M). These results are in line with previous reports suggesting residual metabolic phase I activity and intact phase II metabolism in HepG2 cells (Roe et al., 1993; Westerink and Schoonen, 2007a,b).

3.2. Effect of D-sorbitol on HepG2 cells

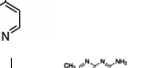
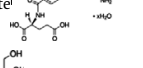
D-sorbitol, known to be well tolerated even at high concentrations and non-toxic, was used as a negative control (Lederle, 1995). D-sorbitol (Fig. 2) showed no relevant effects in the multiparametric cytosensor system at concentrations from 0.001 mM to 5.0 mM. A small but continuous increase in cellular oxygen consumption, reaching 110–120% of the control values, was detected at all concentrations.

3.5. MULTIPARAMETRIC SENSOR APPROACH FOR DRUG-INDUCED TOXICITY

1112

S. Seeland et al./Toxicology in Vitro 27 (2013) 1109–1120

Table 1
Characteristics and toxicological profiles of reference drugs used in the present study.

Drug	Indication (C_{max} , range of therapeutic plasma concentration)	Mechanism of toxicity	Reactive metabolites	Liver pathology
 Acetaminophen	NSAID ^a 0.13 mM (el-Azab et al., 1996; Stocker and Montgomery, 2001)	GSH depletion, mitochondrial toxicity (Zhou et al., 2005; Leung et al., 2011; Kumari and Kakkar, 2012b)	N-acetyl-p-benzoquinone imine (NAPQI), other quinones	Hepatocellular degeneration
 Amiodarone	Antiarrhythmic 2.1 μ M (Meng et al., 2001)	ROS formation, mitochondrial toxicity (Fromenty et al., 1990a,b; Kim et al., 2011)	Desethyl-amiodarone	Steatosis, hepatocellular death
 Cyclosporine A	Immunosuppressant 1.5 μ M (Grant et al., 1999)	Covalent binding to microsomal proteins, ROS formation, oxidative stress (Zhou et al., 2005)	Reactive metabolites	Cholestasis
 Doxorubicin	Anticancer 1.9 μ M (Speth et al., 1988)	DNA intercalation, ROS formation, oxidative stress, mitochondrial toxicity (King and Perry, 2001; Ye et al., 2007)	Semiquinone radical	Hepatocellular death
 Isoniazide	Antibacterial 0.11 mM (McIlleron et al., 2006)	Oxidative stress, GSH depletion (Woo et al., 1992; Zhou et al., 2005; Chowdhury et al., 2006; Bhadauria et al., 2007, 2010)	Hydrazine, reactive acetyl species	Steatosis, necrosis, hepatocyte and vasculature damage
 Methotrexate	Anticancer up to 1200 μ M Immunosuppressant 0.4 μ M (Comandone et al., 2005; Shiozawa et al., 2005)	Inhibition of biosynthetic pathways, metabolic stress (Kaminskas and Nussey, 1978; Kevat et al., 1988; West, 1997; Cetin et al., 2008)	Polyglutamated methotrexate	Fatty infiltration, fibrosis, cirrhosis
 D-Sorbitol	Laxative 70 μ M (Hubinont et al., 1981)	None	None	None
 Valproic acid	Anticonvulsant 0.62 mM (Fisher and Broderick, 2003)	Oxidative stress, altered mitochondrial β -oxidation and oxidative phosphorylation, GSH/NAC ^b depletion (Fromenty and Pessayre, 1995; Tong et al., 2005b; Zhou et al., 2005; Ji et al., 2010)	Acyl glucuronides, 2-N-propyl-4-pentenoic acid	Necrosis, steatosis, cholestasis

^a Non-steroidal anti-inflammatory drug.

^b N-acetylcysteine.

3.3. Effect of acetaminophen on HepG2 cells

Acetaminophen was used in a concentration range of 0.01–10 mM (Fig. 2) and induced concentration-dependent effects in the multiparametric cytosensor system at all considered parameters over a 19 hour incubation period. The change in impedance was indicative of shrinking and retraction of cells reflected by a maximal drop to 80% from baseline values at 10 mM acetaminophen within the first 70 min after addition of the compound. It then remained at around 80–90% for the remaining incubation time. Impedance was reversible in the recovery phase, reaching baseline levels similar to the initial values prior to acetaminophen treatment. The osmolality of control assay medium and assay medium containing 10 mM acetaminophen were 272 mmol/kg and 280 mmol/kg, respectively, as determined by the freeze point depression method. This is within the physiological range of osmolalities of human plasma (i.e. 276–295 mmol/kg) (Glasser et al., 1973). Reduction of cellular oxygen consumption was detected immediately after acetaminophen application. Maximal reduction was observed at 20 min after drug application reaching 40% of baseline values and was constant until the end of drug treatment. Conversely, at the same time, extracellular acidity increased in a concentration-dependent manner up to 130% (10 mM) and remained constant at this level over six hours before it returned to initial baseline levels. These effects were partially reversible during the recovery phase, reaching values equal to those prior to drug treatment. In the MTT test, cell viability was significantly decreased (Table 2) showing a reduction to 80% and 62% in cell viability at 1 mM and 10 mM acetaminophen, respectively.

3.4. Effect of amiodarone on HepG2 cells

Amiodarone caused intense changes in the multiparametric cytosensor system experiments (Fig. 2). These changes were proportional to the concentrations used, which covered a range of 1.0–30 μ M. Concentrations below 10 μ M amiodarone did not influence cellular physiology. However, pronounced effects were observed at concentrations equal to and above 10 μ M. Three hours after amiodarone application, dying cells were released from the sensor chip resulting in a persistent decrease in cell impedance. At the end of the drug treatment period, only 16% (approx. 32,000 cells) of the initial cell number remained. At concentrations of 10 μ M and above, amiodarone affected mitochondrial respiration and metabolic activity non-reversibly. The oxygen consumption at 30 μ M amiodarone described a steep drop until 280 min post-treatment with 30% residual cell respiration, followed by a levelling-off to 15% at the end of the incubation period. The extracellular acidification at 15 μ M and 30 μ M amiodarone increased with a maximal amplitude of 150% at 400 min post-treatment. At 30 μ M amiodarone, this boost in metabolic activity changed into a sustained reduction until the end of the drug-treatment with only 7% metabolic activity left. In the MTT assay, amiodarone had no statistical significant effect on HepG2 cell viability at all concentrations of the MTT assay (Table 2).

3.5. Effect of cyclosporine A on HepG2 cells

Cyclosporine A was analysed at concentrations up to 60 μ M and showed no obvious effects with respect to cell impedance (Fig. 2). In cell respiration, concentrations below 30 μ M showed no obvious

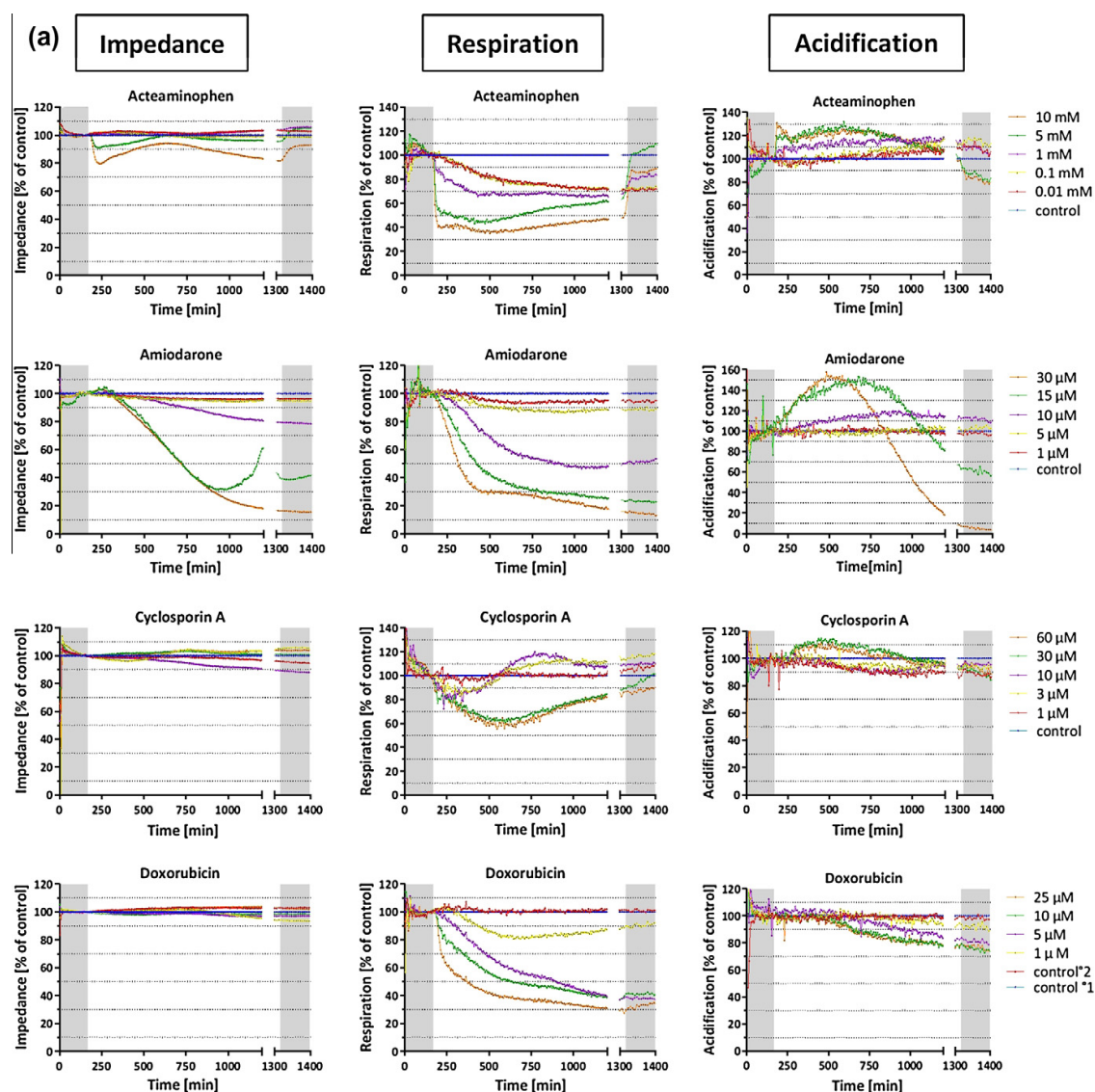


Fig. 2. (a) and (b) Representative patterns of cytosensor signals upon stimulation of HepG2 cells with selected drugs. Cells were incubated with the indicated concentrations of reference drugs. Using the multiparametric sensor system, three physiological parameters were monitored on-line: cell impedance being an indicator for cell morphology/adhesion, cellular respiration based on oxygen consumption and metabolic activity resulting in extracellular acidification. The grey areas indicate the initial stabilisation and final recovery periods, which are carried out in the absence of a test compound. Depict are the mean patterns of $n \geq 3$ experiments.

effects in the first 400 min of treatment, followed by a small increase in oxygen consumption to 110% of baseline values. A decrease to 60% was monitored within the first 400 min after application of 30 μM and 60 μM cyclosporine A, followed by a nearly complete recovery of respiratory activity (90%) at the end of the treatment period. The decrease in respiration at 30 μM and 60 μM was paralleled by an increase in extracellular acidification up to 110%. Along the time course, this metabolic activity was continually reduced to 90% at the end of the cyclosporine A incubation. The MTT assay showed a statistically significant reduction of 18% in cell viability at the highest concentration of 60 μM (Table 2). No effects were observed in the MTT assay at concentrations below 60 μM .

3.6. Effect of doxorubicin on HepG2 cells

Cells treated with up to 25 μM doxorubicin were found to have stable impedance during the experiments (Fig. 2). In contrast, oxygen consumption was directly affected and reacted with a sudden, concentration-dependent drop after drug application. At 25 μM doxorubicin, cell respiration diminished to 46% within 230 min, followed by a constant and non-reversible reduction to 30% during the remaining incubation period. Simultaneously, extracellular acidification was reduced in a concentration-dependent and non-reversible manner. Doxorubicin initiated a sustained decrease of this metabolic activity at 390 min post-application. At the end of the incubation period, the extracellular acidification was in the

3.5. MULTIPARAMETRIC SENSOR APPROACH FOR DRUG-INDUCED TOXICITY

1114

S. Seeland et al./Toxicology in Vitro 27 (2013) 1109–1120

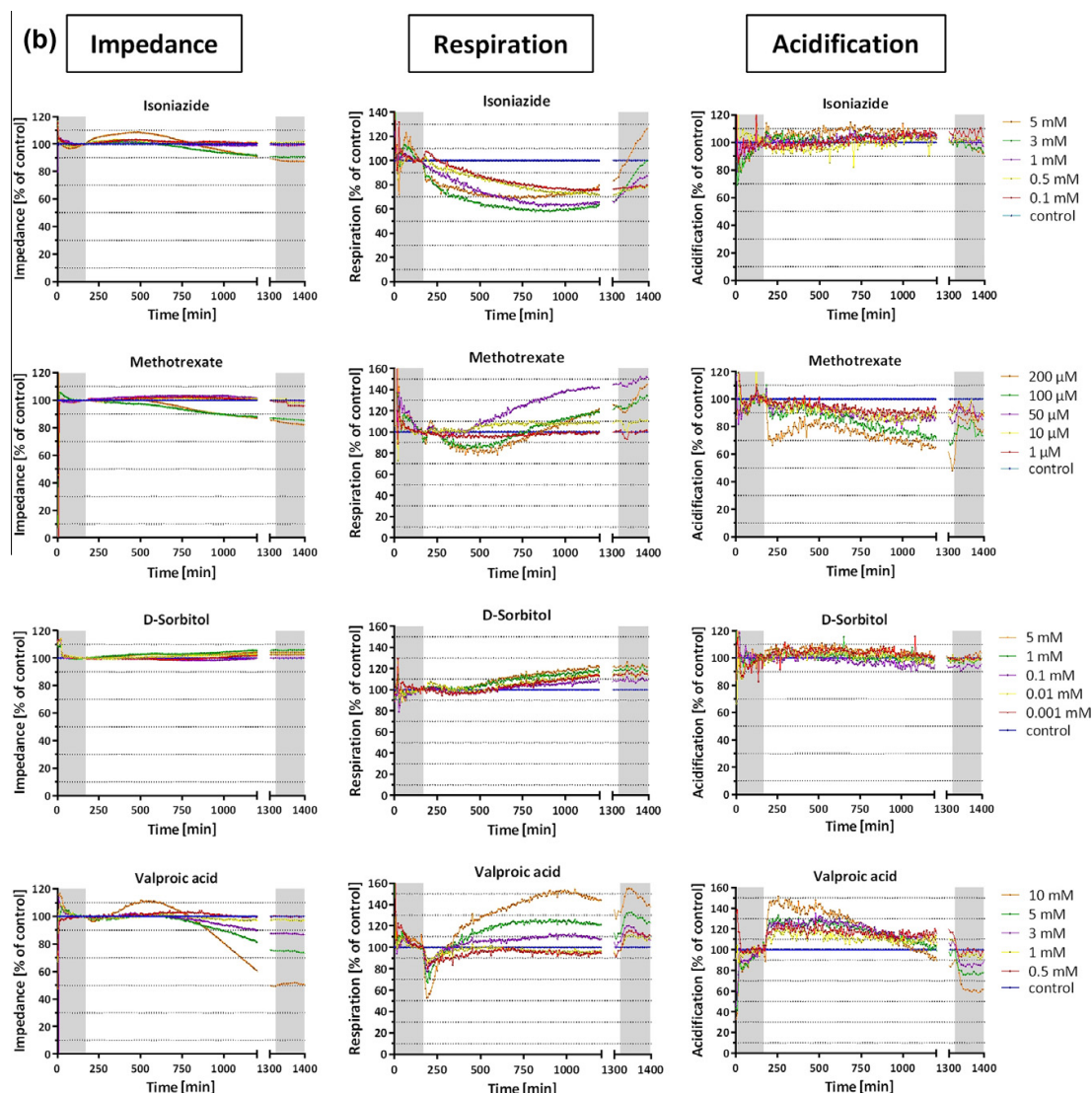


Fig. 2. (continued)

range of 75% and 90% for doxorubicin concentrations equal to and above 5 μM and 1 μM , respectively. The 24 h incubations of doxorubicin in the MTT assay indicate an impairment of cell viability (Table 2) showing a 61% and 54% reduction in viability for 10 μM and 25 μM doxorubicin, respectively.

3.7. Effect of isoniazide on HepG2 cells

Isoniazide was used in a concentration from 0.1 mM to 5.0 mM. After applying isoniazide to HepG2 cells, a non-reversible and sustained reduction to 90% in impedance was observed until the end of the incubation period. An initial increase in cell impedance was detected at the highest concentration (5.0 mM), reaching a maximum of 110% at 400 min post-application (Fig. 2). Immediately after drug application, oxygen consumption decreased con-

tinually during the entire incubation period and remained at levels of 60–80% for all concentrations used. Extracellular acidification was not affected and remained stable during all experiments. There was also no impact on cell viability as determined by the MTT assay (Table 2), with a viability of 103% at 5.0 mM isoniazide.

3.8. Effect of methotrexate on HepG2 cells

Methotrexate was investigated at concentrations from 1.0 μM to 200 μM . The two highest concentrations of methotrexate (100 μM and 200 μM) initiated a reduction of impedance at 80 min post-application, described by a sustained decrease to 86% of baseline values at the end of the incubation (Fig. 2). This reduction was not reversible during the recovery phase, which

Table 2
Cellular viability of HepG2 cells determined after a 24 h incubation by the MTT assay.

Compound	% Viability	Concentration
Acetaminophen	80.3 ± 0.5 ^{***}	1.0 mM
	61.8 ± 0.5 ^{***}	10 mM
Amiodarone	95.7 ± 1.1	10 μM
	108 ± 10.2	30 μM
	101 ± 1.4	10 μM
Cyclosporine A	81.8 ± 4.5 ^{**}	60 μM
	61.3 ± 2.1 ^{***}	10 μM
Doxorubicin	53.5 ± 3.2 ^{***}	25 μM
	99.5 ± 3.1	1.0 mM
Isoniazide	103 ± 1.4	5.0 mM
	70.3 ± 4.3 ^{***}	50 μM
Methotrexate	79.3 ± 1.3 ^{***}	200 μM
	89.0 ± 2.4 ^{**}	3.0 mM
Valproic acid	85.2 ± 3.1 ^{**}	10 mM
	98.9 ± 10.9	5.0 μM
Terfenadine (control)	1.4 ± 0.4 ^{***}	25 μM

Values are means ± SD ($n = 3$ independent sets of experiments) as compared to untreated control cells (100% viability). The two highest concentrations are shown. Level of significance (Student's *t*-test as compared to 100% control).

^{**} $p \leq 0.01$.

^{***} $p \leq 0.001$.

indicates cell death and was corroborated by observations in the MTT assay, where cellular viability was reduced to 79% at 200 μM (Table 2). The oxygen consumption curves at the two highest concentrations described an initial decrease to 78% during the first 320 min after application, followed by a persistent increase, reaching 125% at the end of the incubation. With the exception of the initial decrease, treatment with 50 μM methotrexate showed similar curves, reaching 145% of this cell respiration signal at the end of the incubation. Extracellular acidification was inhibited in a concentration-dependent manner 30 min after drug treatment, with a maximal reduction to 70% at 200 μM and was subsequent maintained at levels between 60% and 80%. In contrast to oxygen consumption, extracellular acidification was restored after the removal of the drug, reaching levels of around 90%.

3.9. Effect of valproic acid on HepG2 cells

Valproic acid was used in the concentration range of 0.5–10 mM. An increase to 112% in cellular impedance was observed during the first six hours of treatment with 10 mM valproic acid (Fig. 2). After 640 min of treatment with 3–10 mM valproic acid, dying cells detached from the sensor chip, indicated by a constant decrease in cell impedance. Half of the initial cell amount (1×10^5 cells) remained on the sensor chip at the end of the incubation period with 10 mM valproic acid. Signals reflecting oxygen consumption were concentration-dependent. The respiration curve described a sudden steep drop to 52% at 10 mM valproic acid, followed by a bell-shaped curve with maximal amplitude of 153% at 820 min post-application. At the end of drug incubation period, the cell respiration was 130% at 10 mM valproic acid. Extracellular acidification and cell respiration were reciprocally related. Simultaneous to the reduction of cell respiration, the acidification increased to equal extents, reaching levels up to 145%. This amplification levelled off until the end of treatment, with residual extracellular acidification rate of 82% at 10 mM valproic acid. Neither cell respiration nor extracellular acidification was reversible in the recovery phase. The MTT assay indicated a statistically significant trend towards decreased HepG2 cell viability at 10 mM and 1 mM, showing 85% and 89% remaining viability, respectively (Table 2).

4. Discussion

Identifying cytotoxic effects of potential drug candidates remains a challenge. Standard preclinical animal models do not reliably predict human toxicity (animal concordance of 55%) (Olson et al., 2000). To improve predictability, specialised animal models can be combined with, for example, *in silico*, *in vitro* (endpoint assays) or toxicogenomic approaches (Liu et al., 2011). In this context, it was proposed that cytosensor systems be used to monitor reduction in metabolic rates as an indicator of cell death (Cao et al., 1997). Due to technical limitations, measurements were limited to measuring cellular acidification rates. Only recently have novel, multiparametric sensor chips become available that can be used for the simultaneous determination of three parameters, namely cellular impedance as a measure of cell morphology and adherence, oxygen consumption as a measure of mitochondrial respiration, and extracellular acidification as a measure of cellular metabolism. Changes in extracellular pH are thereby caused by release of metabolic breakdown products such as lactate and carbonate (Seeland et al., 2011). It should be noted that a reduction of impedance is an indication for cellular detachment from the surface of the cytosensor chip. This process is not necessarily associated with cellular viability. Consequently, changes in impedance are not always associated with cell viability as determined in the MTT assay. Furthermore, the reduction of MTT to the assessed water-insoluble formazan dye is rather related to the mitochondrial succinate dehydrogenase activity than to the pyridine containing reduction equivalent NADH and NADPH. As the succinate dehydrogenase only partly contributes, the MTT assay reflects a mixed pattern of glycolytic activity and mitochondrial respiration (Berridge et al., 1996). In the present study, high sensitivity and responsiveness of the multiparametric cytosensor system was achieved by combining an assay medium with low buffer capacity and a minimal inner volume of the perfusion chamber (Fig. 1). The system therefore permitted real-time monitoring of physiological changes resulting from toxicological insult over a 24-h period in human hepatocarcinoma-derived HepG2 cells.

To validate the cytosensor approach, eight well characterised reference drugs known to be cytotoxic at certain concentrations (Table 1) were selected. They exhibit different hepatotoxic mechanism and liver pathological patterns. The drugs are structurally diverse, are used for different clinical indications, and the selection included the intrinsically cytotoxic drugs doxorubicin and methotrexate used to treat cancer. D-sorbitol, known to be non-toxic and well tolerated even at high concentrations, was used as a negative control (Lederle, 1995). Assay concentrations were comparable to clinically relevant plasma concentrations, covering a nanomolar to millimolar range.

The test compounds have been reported to have different mechanisms of toxicity (Table 1). Cellular viability was measured by the MTT assay, which responded in statistically significant way to the antineoplastic drugs, acetaminophen, cyclosporine A and valproic acid (Table 2). Methotrexate and doxorubicin thereby used at clinical plasma concentrations observed in human cancer treatment. Clinical plasma concentrations of methotrexate and doxorubicin are in the range of 1150 μM (Comandone et al., 2005) and 1.9 μM (Speth et al., 1988), respectively. All other drugs investigated in the MTT viability assay reduced cell viability only at concentrations clearly above the clinical relevant human plasma concentrations. Interestingly, all analysed compounds known to cause DILI in humans also responded with very distinct and characteristic signal patterns in the multiparametric cytosensor assay (Fig. 2). All observed effects were rigidly concentration-dependent. This result was unexpected, because reactive metabolites (and not the parent compound alone) are often suspected sources of adverse

3.5. MULTIPARAMETRIC SENSOR APPROACH FOR DRUG-INDUCED TOXICITY

1116

S. Seeland et al./Toxicology in Vitro 27 (2013) 1109–1120

Table 3
Classification of toxic effects based on multiparametric cytosensor signal patterns.

Type	Classification	Endpoint	Impedance	Acidification	Respiration	Example
1	No toxicity	No effect	○	○	○/+	D-sorbitol
2	Necrosis-like	Cell death	–	○/+	+	Valproic acid
3	Apoptosis-like	Cell death	–	○/+	–	Amiodarone
4	Respiratory stress	Cell stress	○	○/+	–	Acetaminophen
5	Metabolic stress	Cell stress	○	–	+	Methotrexate
6	Respiratory and metabolic stress	Cell stress	○	–	–	Doxorubicin

Physiological parameters were monitored online in HepG2 cells and included metabolic activity (acidification), respiration (oxygen consumption) and cell morphology and adhesion (increased by swelling of cells or decreased by cell detachment or shrinking). Signals were stable over time (○), increasing in intensity (+) or decreasing (–). Typical signal patterns of representative drugs are shown in Fig. 3.

effects (Table 1). Thus, in liver tissue, hepatotoxicity is frequently linked to accumulation of the parent drug in combination with its metabolites, initiating pathological effects, and/or an altered cellular defence mechanism, such as the depletion of glutathione (GSH), formation of ROS or the inhibition of metabolising enzymes. In the present study, the human hepatocarcinoma-derived HepG2 cell line was used. As opposed to primary human hepatocytes, HepG2 cells are characterised by a defined but low expression level of cytochrome P450 monooxygenases (Roe et al., 1993). In contrast expression levels of most phase II enzymes seem to be normal (Westerink and Schoonen, 2007a,b). Our results suggest that phase II metabolic enzymes in combination with residual phase I metabolic enzymes (e.g. cytochrome P450) activity may generate adequate levels of intracellular metabolites to trigger cytotoxic reactions. HepG2 cells therefore seem to be a convenient, stable, economic, and relatively easy to handle alternative to hepatocytes for cytosensor-based toxicological investigations. This view was supported by control experiments where amiodarone and acetaminophen were used to assess the phase I and phase II metabolising enzymes (see above).

Analysis of the reference drugs in the multiparametric cytosensor system revealed distinct signal patterns that allowed for classification according to six distinct cytotoxic reaction types (Table 3, Fig. 3). Type 1 is represented by D-sorbitol, a well tolerated and safe compound (Lederle, 1995), as confirmed in the present study (Fig. 3). The slight increase in cell respiration of 20% at 5 mM during the 24 h of the experiment was attributed to active compensation of the osmotic effect of D-sorbitol to cells.

Type 2 signal patterns are represented by valproic acid (Fig. 3). This compound is one of the most widely used antiepileptic drugs, with a black box warning for hepatotoxicity. Oxidative stress, GSH depletion, as well as mitochondrial dysfunction and necrosis have been associated with valproic acid treatment (Tong et al., 2005a,b,c; Kiang et al., 2010). Recently, Ji et al. reported toxicological effects due to valproic acid and its reactive metabolites, suggesting an ability to damage liver cell plasma membranes and resulting in leakage of intracellular enzymes and finally cell death via necrotic or apoptotic pathways (Ji et al., 2010). These findings were confirmed in the cytosensor assay: an irreversible decrease of 50%, at 10 mM, of the impedance value over time, which indicated cell death. This effect was preceded by a short and transient period of water influx resulting in transient cell swelling (i.e. increased impedance), as described recently (Noch and Khalili, 2009). A sudden drop in respiration was observed after the addition of valproic acid in the first 20 min of incubation, apparently indicating reduced oxidative phosphorylation and hence reduced ATP generation. The reduced cell respiration was compensated by an increase in metabolic activity for a similar time range. The observed reduction of intracellular concentration of ATP led to strong respiratory and metabolic stress and caused an initiation of energy-independent necrotic-like pathways, which was detected in a previous study (Bown et al., 2000). Consequently, metabolic activity levelled off to 82% over the entire experiment. The changes

in pH, observed in the experimental system, are transient and limited to the 3 min stop phases during the assay. In addition, pH changes are very small and cover a range of 0.4 pH units only over 24 h. Under these conditions, induction of toxic effects by pH changes is unlikely. This assumption is corroborated by the lack of correlation between changes of pH and changes in respiration or impedance (Table 3).

Amiodarone was used as a second drug with a black box warning for hepatotoxicity and it is known to generate liver steatosis and hepatocellular death (Van Summeren et al., 2011). In the multiparameter cytosensor system, the strong tendency of amiodarone to damage cells was confirmed (i.e. irreversible decrease in impedance) and was classified by us as type 3 (Fig. 3), representing drugs causing apoptotic-like cell death. Amiodarone showed the most distinct concentration-dependent cytotoxic behaviour of all drugs analysed in this study. After 9 h of amiodarone treatment (15 μM and 30 μM), only 50% of the initial cells remained on the sensor chip. Higher concentrations of amiodarone showed almost complete inhibition of cellular respiration (15% of control), correlating with a continuous release of dying cells from the sensor chip. It is interesting to note that these concentrations of amiodarone can also be reached in human plasma (Table 1). Mitochondrial toxicity induced an amplification of metabolic activity as a compensatory but transient means of ATP regeneration. This compensatory mechanism failed after approx. 6–8 h and amplified metabolic stress, as previously described (Kim et al., 2011) and demonstrated by the steep drop of the acidification curve down to 7%. Amiodarone showed no recovery of signals, thus identifying amiodarone as a potent hazard to liver cells at elevated levels in tissue, without the possibility of regeneration. Furthermore, the observed effects support the previous findings of the production of reactive oxygen species, induced mitochondrial damage, and promoted apoptosis in HepG2 cells (Zahno et al., 2011). It is still unclear whether amiodarone, its postulated reactive metabolite (desethylamiodarone) or both cause toxicity (Zhou et al., 2005). However, the findings showed the significant potential of amiodarone to damage the liver, which was in good agreement with the black box warning for hepatotoxicity on this drug.

In contrast to drugs that induce cell death (i.e. type 2 and type 3 cytotoxicity), several drugs were identified that caused cellular stress only but no changes in cellular impedance. Three out of eight compounds in this study were identified as inducing respiratory stress in HepG2 cells (type 4, acetaminophen, cyclosporine A, and isonidazide). Acetaminophen induces mitochondrial stress upon formation of its reactive metabolites as a consequence of depletion of GSH. Acetaminophen is widely used as an analgesic and antipyretic compound, and is classified as a non-steroidal anti-inflammatory drug. The first hours of the treatment phase showed slight and reversible shrinking of the cells, reflected by reduced impedance values of 70–80%, followed by an apparent recovery period (Fig. 3) during which the impedance was maintained at around 80%. This apparent recovery is most likely linked to the disturbance of mitochondrial Ca²⁺ homeostasis (Moore et al., 1985), character-

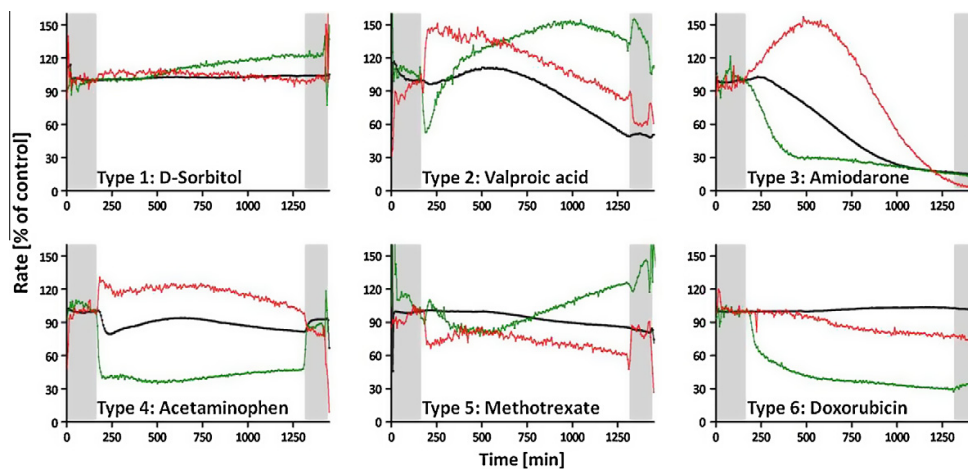


Fig. 3. Classification of cytotoxic effects based on cytosensor signal patterns. Incubation of HepG2 cells with elevated concentrations of hepatotoxic drugs has an impact on cell morphology/adhesion (impedance, black line), metabolic activity (acidification, red line), and cellular respiration (oxygen consumption, green line). Cellular responses and cytotoxic effects can be classified according to six typical signal patterns (Table 3). Representative examples of experiments are shown where treatment of HepG2 cells resulted in cytotoxicity and cell death (toxicological effects type 2 and 3) or cellular stress (effects of type 4–6). D-sorbitol served as a negative control (no cytotoxicity type 1). Effects are considered reversible if baseline levels of signals are re-established after wash-out of drug (grey areas, absence of test compound). Depict are the mean patterns of $n \geq 3$ experiments.

ised by a phenotypic blebbing of the cell surface. The osmolality of 10 mM acetaminophen was determined to be comparable to the osmolality of human plasma (Glasser et al., 1973). Induction of shrinking effects due to hyper-osmotic medium is therefore unlikely. Cellular respiration was intensely affected in a concentration-dependent manner and inhibited the respiration to 40% at 10 mM, indicating severe respiratory stress on the cell respiratory system, the formation of toxic benzoquinone metabolites, and the linked depletion of GSH, as previously described (Kumari and Kakkar, 2012a,b). The intense impairment of respiration and the consequent deficit of oxidative phosphorylation results in an apparent lack of ATP generation. In such events, the cells typically compensate the lack of energy generation by enhancing ATP generation via glycolysis, which is confirmed by the increase in metabolic activity to 130% at 10 mM. During the drug wash-out period, the signals of impedance and cell respiration almost recovered to initial baseline values prior to acetaminophen treatment. Wash-out of the drug reactivated the formation of ATP via oxidative respiration leading to a decrease in metabolic activity, as the generation of ATP via glycolysis was no longer in demand. A study by Roe et al. (1993) confirmed the formation of the reactive metabolite (NAPQI) and phase 2 conjugation products in HepG2 cells, among others (e.g. benzoquinone) that were also responsible for adverse effects (Roe et al., 1993). Cyclosporine A showed similar effects (Fig. 2) in all three physiological parameters. This potent immunosuppressive agent prolongs survival of allergenic transplants by suppressing humoral immunity and, to a greater extent, cell-mediated immune reactions such as allograft rejection and delayed hypersensitivity. Unfortunately, cyclosporine A is associated with toxic effects to several organs, mainly the kidney but also the liver, which is confirmed in our experiments. Respiratory stress was induced in HepG2 cells particular at concentrations equal to and above 30 μM followed by a recovery phase and a slight compensatory amplification of the metabolic activity. It should be noted that the observed effects were apparent at concentrations that were 40 times higher than clinically relevant plasma concentrations of cyclosporine A and therefore of no direct clinical relevance. Additional cyclosporine A exemplified the limitations of the HepG2

cells, because the hepatotoxicity of cyclosporine A is accompanied by the ability to inhibit hepatic bile-salt export transporters (e.g. ABCB11) (Kullak-Ublick et al., 2000). These pumps are responsible for the secretion of bile components into the bile canaliculi. A block of these bile-salt export pumps results in an intracellular accumulation of bile salts and thus cholestasis (Bohme et al., 1994; Van Summeren et al., 2011). HepG2 cells are a common *in vitro* model to analyse toxic effects to the liver (Lin and Will, 2012). However, in previous studies, HepG2 cells showed impaired bile-salt transporter levels (Cooper et al., 1994) and therefore HepG2 seems not to be the most appropriate model for studying such specific effects. An alternative to indicate toxicological effects linked with these efflux transporters would be the use of primary hepatocytes.

Isoniazide, another example of a drug that induces respiratory stress, is associated with mild to severe liver toxicity in 2% of patients (Sarich et al., 1999). Its metabolism is characterised by the formation of hydrazine (H_2NNH_2) and an additional toxic intermediate, isonicotinic acid. Hydrazine is a well-characterised hepatotoxin (Patrick and Back, 1965; Gent et al., 1992). Hydrazine can be formed directly by amidohydrolase or indirectly via the isonicotinic acid pathway (N-acetyltransferase) to form acetylhydrazine and then hydrazine. Histopathological observations of isoniazide-induced liver toxicity reveal inflammatory processes and cell death (Sarich et al., 1999). In our experiments (Fig. 2), cellular respiration was affected in a concentration-dependent manner and was maximally reduced to 60%, indicative of previously described observations of respiratory stress to cells after isoniazide treatment (Bhadoria et al., 2007, 2010).

Methotrexate is a compound that induces metabolic stress to cells (type 5, Fig. 3). This drug is a folic acid antagonist used at high doses in cancer therapy. The intrinsic toxicity of methotrexate was evident in the MTT assay, showing reductions to 70% and 79% of cell viability at 50 μM and 200 μM , respectively. The mechanism of liver injury is poorly understood (West, 1997). The pathological pattern of methotrexate-induced liver injury varies from mild liver enzyme elevations to severe fibrosis and cirrhosis. Methotrexate enters the cell via a folate transporter and is retained within the

3.5. MULTIPARAMETRIC SENSOR APPROACH FOR DRUG-INDUCED TOXICITY

1118

S. Seeland et al./Toxicology in Vitro 27 (2013) 1109–1120

cell as a polyglutamate (Kevat et al., 1988). The drug inhibits the enzymes required for the synthesis of purines and pyrimidines (Aithal, 2011). It additionally blocks the conversion of homocysteine to methionine. High levels of homocysteine cause metabolic stress, with the above-described consequences, i.e. impaired metabolic activity (Mato and Lu, 2005; Basseri and Austin, 2008). Metabolic stress was clearly observed using the multiparametric sensor system, by a metabolic inhibition to a maximum of 60% of baseline values at 200 μM . The highest concentration (200 μM) investigated was 6-fold below the detected clinical plasma concentrations in humans receiving methotrexate at high doses for anti-cancer therapy ($\geq 1150 \mu\text{M}$, see above). Therefore methotrexate was a prime example of a drug that is intrinsically toxic, intensely inhibits metabolic activity and induces metabolic stress in HepG2 cells, which was previously described (Kaminskas and Nussey, 1978). The amplified cellular respiration agreed well with the apparent impaired glycolytic activity, which represents a compensatory mechanism to generate ATP.

Doxorubicin indicates a combined pattern of respiratory and metabolic stress (type 6, Fig. 3). Doxorubicin is an anthracycline derivative, commonly used in the treatment of a wide range of cancers, including hematological malignancies, many types of carcinomas, and soft tissue sarcomas. The MTT assay reflects the intrinsic cytotoxicity of the drug (54% viability at 25 μM), even at concentrations below the human plasma concentrations, which is 1.9 μM (see above). The MTT assay at 1.0 μM doxorubicin showed a statistical significant decrease in cell viability of 30% (data not shown) on HepG2 cells after 24 h treatment. During its metabolism, doxorubicin undergoes a one-electron reduction by different oxidoreductases to form a doxorubicin-semiquinone radical (Minotti, 1989). The re-oxidation of the radical back to the parent drug leads to the formation of ROS and hydrogen peroxide

(Minotti, 1989). The reactive species might then cause oxidative stress, lipid peroxidation, damage to proteins and the mitochondrial membrane, oxidation of mitochondrial DNA, as well as the activation of the redox-sensitive mitochondrial permeability transition pore (Sardao et al., 2008). Consequently, the bioenergetics of the cells alters radically (Zhou et al., 2001). We were able to monitor these effects in the cytosensor assay, in that cellular respiration was significantly inhibited (IC_{50} of $<5 \mu\text{M}$) as a consequence of mitochondrial damage that inhibits cellular respiration. In addition, an inhibition of cellular metabolic activity was observed. These findings are in agreement with previous studies (Sardao et al., 2008). Neither metabolic nor respiratory activities recovered during the drug wash-out period, indicating irreversible impairment of cellular adhesion, even at clinical relevant concentrations (Table 1).

Using the multiparametric cytosensor system, we were able to monitor alterations in cellular metabolism, respiration and impedance in real-time. These changes were linked to chemical-induced toxicological effects of the drug or its reactive metabolites. An assessment of reversibility of the effects was used to acquire additional insight into the underlying mechanisms of toxicity. In contrast to the well-established cellular viability (MTT) endpoint assay, the onset of toxic effects was monitored on-line, as opposed to the determination of a physiological endpoint. Based on these results, a Test-Flag-Risk Mitigation strategy (Fig. 4) is being introduced; it can be used to extrapolate from an *in vitro* to an *in vivo* situation and to determine risk of cytotoxicity of a given test compound. We propose that signals from the cytosensor system should trigger an alert (flag) that will determine a further course of action and a follow-up strategy. Depending on concentrations used and reversibility of effects, animal experiments will be needed. Such studies can be combined with additional *in vitro* and/or *in vivo* experiments (e.g. enzyme induction or inhibition, drug transporter studies, etc.) to elucidate the mechanism of any adverse effect. Such a Test-Flag-Risk Mitigation strategy helps reduce the risk of cytotoxicity and therefore leads to better management of risks associated with drug-induced injury. It remains to be elucidated whether this approach can be extended to organ-specific cell lines that are used to evaluate organ specific toxicity (Lin and Will, 2012).

5. Conclusions

A panel of eight marketed drugs was used to develop a novel cytosensor-based *in vitro* toxicological assay. Reference drugs in our study were classified as either non-toxic (D-sorbitol), as intrinsically toxic (antineoplastic drugs) or as potentially toxic under conditions of exaggerated exposure observed as a consequence of, for example, intentional intoxication, drug-drug interactions or disease-induced physiological alterations. Drugs were tested using concentrations equal to, above, and below the clinically relevant plasma concentrations. Real-time monitoring of drug-induced physiological effects in HepG2 cells revealed characteristic signal patterns. Mechanistic insight into the action of these compounds was used to predict detrimental events such as cell stress, cell death or cytotoxicity in humans. In addition, information was obtained on reversibility of the observed effects. All identified alterations were rigidly concentration-dependent. Our findings suggest that cytosensor-based toxicological investigations may provide early indications of potential mechanisms of cytotoxicity, which might be followed up by studies in experimental animal models. The early indications of potential mechanisms of toxicity, together with the Test-Flag-Risk Mitigation strategy (Fig. 4), may therefore guide the design of specific follow-up studies in experimental animals.

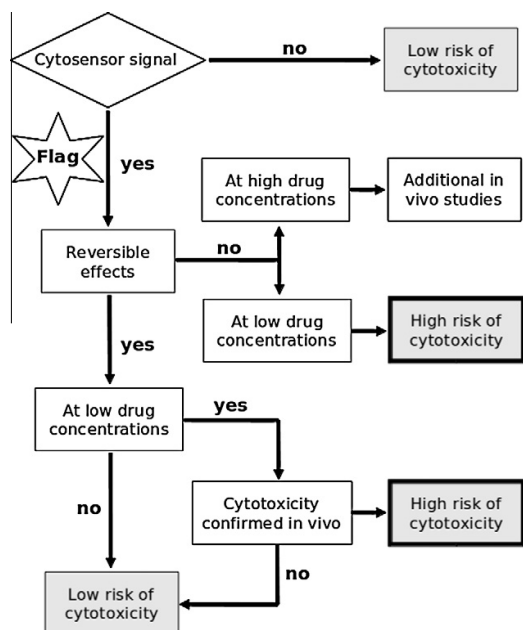


Fig. 4. Test-flag-risk-mitigation strategy based on findings in the cytosensor *in vitro* assay. Decisions to be taken during the drug discovery and development process will depend on the mechanism and extent of observed cytotoxicity relative to the predicted therapeutic drug concentrations (i.e. classification as “low” or “high” drug concentrations). Potential risks uncovered in the multiparametric cytosensor test system will raise a flag and have to be addressed by confirmatory *in vivo* studies.

Conflicts of interest

The authors state no conflict of interest.

Acknowledgments

We thank Mark Inglin for editorial assistance. The generous support of the PhD thesis Project of S. Seeland by Actelion Ltd. (Allschwil, Switzerland) is acknowledged. The PhD thesis Project of H. Kettiger is supported by the “Freiwillige Akademische Gesellschaft Basel” and the Swiss Centre of Applied Human Toxicology (SCAHT).

References

- Aithal, G.P., 2011. Hepatotoxicity related to antirheumatic drugs. *Nat. Rev. Rheumatol.* 7, 139–150.
- Basseri, S., Austin, R.C., 2008. ER stress and lipogenesis: a slippery slope toward hepatic steatosis. *Dev. Cell* 15, 795–796.
- Berridge, M.V., Tan, A.S., McCoy, K.D., Wang, R., 1996. The biochemical and cellular basis of cell proliferation assays that use tetrazolium salts. *Roche Appl. Sci.*, 14–19.
- Berson, A., Renault, S., Letteron, P., Robin, M.A., Fromenty, B., Fau, D., Le Bot, M.A., Riche, C., Durand-Schneider, A.M., Feldmann, G., Pessayre, D., 1996. Uncoupling of rat and human mitochondria: a possible explanation for taurine-induced liver dysfunction. *Gastroenterology* 110, 1878–1890.
- Bhadoria, S., Mishra, R., Kanchan, R., Tripathi, C., Srivastava, A., Tiwari, A., Sharma, S., 2010. Isoniazid-induced apoptosis in HepG2 cells: generation of oxidative stress and Bcl-2 down-regulation. *Toxicol. Mech. Methods* 20, 242–251.
- Bhadoria, S., Singh, G., Sinha, N., Srivastava, S., 2007. Isoniazid induces oxidative stress, mitochondrial dysfunction and apoptosis in Hep G2 cells. *Cell. Mol. Biol. (Noisy-le-grand)* 53, 102–114.
- Bohme, M., Muller, M., Leier, I., Jedlitschky, G., Keppler, D., 1994. Cholestasis caused by inhibition of the adenosine triphosphate-dependent bile salt transport in rat liver. *Gastroenterology* 107, 255–265.
- Bown, C.D., Wang, J.F., Young, L.T., 2000. Increased expression of endoplasmic reticulum stress proteins following chronic valproate treatment of rat C6 glioma cells. *Neuropharmacology* 39, 2162–2169.
- Cao, C.J., Mioduszewski, R.J., Menking, D.E., Valdes, J.J., Cortes, V.I., Eldefrawi, M.E., Eldefrawi, A.T., 1997. Validation of the cytosensor for in vitro cytotoxicity studies. *Toxicol. In Vitro* 11, 285–293.
- Cetin, A., Kaynar, L., Kocuyigit, I., Hacıoglu, S.K., Saraymen, R., Ozturk, A., Sari, I., Sagdic, O., 2008. Role of grape seed extract on methotrexate induced oxidative stress in rat liver. *Am. J. Chin. Med.* 36, 861–872.
- Chowdhury, A., Santra, A., Bhattacharjee, K., Ghatak, S., Saha, D.R., Dhali, G.K., 2006. Mitochondrial oxidative stress and permeability transition in isoniazid and rifampicin induced liver injury in mice. *J. Hepatol.* 45, 117–126.
- Comandone, A., Passera, R., Boglione, A., Tagini, V., Ferrari, S., Cattel, L., 2005. High dose methotrexate in adult patients with osteosarcoma: clinical and pharmacokinetic results. *Acta Oncol.* 44, 406–411.
- Cooper, A.D., Craig, W.Y., Taniguchi, T., Everson, G.T., 1994. Characteristics and regulation of bile salt synthesis and secretion by human hepatoma HepG2 cells. *Hepatology* 20, 1522–1531.
- David, S., Hamilton, J.P., 2010. Drug-induced liver injury. *US Gastroenterol. Hepatol. Rev.* 6, 73–80.
- Ehret, R., Baumann, W., Brischwein, M., Schwinde, A., Wolf, B., 1998. On-line control of cellular adhesion with impedance measurements using interdigitated electrode structures. *Med. Biol. Eng. Comput.* 36, 365–370.
- el-Azab, G., Youssef, M.K., Higashi, Y., Murakami, T., Yata, N., 1996. Acetaminophen plasma level after oral administration in liver cirrhotic patients suffering from schistosomiasis. *Int. J. Clin. Pharmacol. Ther.* 34, 299–303.
- Fisher, C., Broderick, W., 2003. Sodium valproate or valproate semisodium: is there a difference in the treatment of bipolar disorder? *Psychiatr. Bull.* 27, 446–448.
- Fromenty, B., Fisch, C., Berson, A., Letteron, P., Larrey, D., Pessayre, D., 1990a. Dual effect of amiodarone on mitochondrial respiration. Initial protonophoric uncoupling effect followed by inhibition of the respiratory chain at the levels of complex I and complex II. *J. Pharmacol. Exp. Ther.* 255, 1377–1384.
- Fromenty, B., Fisch, C., Labbe, G., Degott, C., Deschamps, D., Berson, A., Letteron, P., Pessayre, D., 1990b. Amiodarone inhibits the mitochondrial beta-oxidation of fatty acids and produces microvesicular steatosis of the liver in mice. *J. Pharmacol. Exp. Ther.* 255, 1371–1376.
- Fromenty, B., Pessayre, D., 1995. Inhibition of mitochondrial beta-oxidation as a mechanism of hepatotoxicity. *Pharmacol. Ther.* 67, 101–154.
- Gent, W.L., Seifart, H.L., Parkin, D.P., Donald, P.R., Lamprecht, J.H., 1992. Factors in hydrazine formation from isoniazid by paediatric and adult tuberculosis patients. *Eur. J. Clin. Pharmacol.* 43, 131–136.
- Glasser, L., Sternglanz, P.D., Combie, J., Robinson, A., 1973. Serum osmolality and its applicability to drug overdose. *Am. J. Clin. Pathol.* 60, 695–699.
- Grant, D., Kneteman, N., Tchervenkov, J., Roy, A., Murphy, G., Tan, A., Hendricks, L., Guilbault, N., Levy, G., 1999. Peak cyclosporine levels (C_{max}) correlate with freedom from liver graft rejection: results of a prospective, randomized comparison of neoral and sandimmune for liver transplantation (NOF-8). *Transplantation* 67, 1133–1137.
- Hilgendorf, C., Ahlin, G., Seithel, A., Artursson, P., Ungell, A.-L., Karlsson, J., 2007. Expression of thirty-six drug transporter genes in human intestine, liver, kidney, and organotypic cell lines. *Drug Metab. Dispos.* 35, 1333–1340.
- Hubinont, C., Sener, A., Malaisse, W.J., 1981. Sorbitol content of plasma and erythrocytes during induced short-term hyperglycemia. *Clin. Biochem.* 14, 19–20.
- Jaeschke, H., Gores, G.J., Cederbaum, A.I., Hinson, J.A., Pessayre, D., Lemasters, J.J., 2002. Mechanisms of hepatotoxicity. *Toxicol. Sci.* 65, 166–176.
- Ji, Q., Shi, X., Lin, R., Mao, Y., Zhai, X., Lin, Q., Zhang, J., 2010. Participation of lipid transport and fatty acid metabolism in valproate sodium-induced hepatotoxicity in HepG2 cells. *Toxicol. In Vitro* 24, 1086–1091.
- Kaminskas, E., Nussey, A.C., 1978. Effects of methotrexate and of environmental factors on glycolysis and metabolic energy state in cultured ehrlich ascites carcinoma cells. *Cancer Res.* 38, 2989–2996.
- Kevat, S., Ahern, M., Hall, P., 1988. Hepatotoxicity of methotrexate in rheumatic diseases. *Med. Toxicol. Adv. Drug Exp.* 3, 197–208.
- Kiang, T.K.L., Teng, X.W., Karagiozov, S., Surendrass, J., Chang, T.K.H., Abbott, F.S., 2010. Role of oxidative metabolism in the effect of valproic acid on markers of cell viability, necrosis, and oxidative stress in sandwich-cultured rat hepatocytes. *Toxicol. Sci.* 118, 501–509.
- Kim, I.Y., Kang, Y.J., Yoon, M.J., Kim, E.H., Kim, S.U., Kwon, T.K., Kim, I.A., Choi, K.S., 2011. Amiodarone sensitizes human glioma cells but not astrocytes to TRAIL-induced apoptosis via CHOP-mediated DR5 upregulation. *Neuro Oncol.* 13, 267–279.
- King, P.D., Perry, M.C., 2001. Hepatotoxicity of chemotherapy. *Oncologist* 6, 162–176.
- Kullak-Ublick, G.A., Stieger, B., Hagenbuch, B., Meier, P.J., 2000. Hepatic transport of bile salts. *Semin. Liver Dis.* 20, 273–292.
- Kumari, A., Kakkar, P., 2012a. Lupeol prevents acetaminophen-induced in vivo hepatotoxicity by altering the Bax/Bcl-2- and oxidative stress-mediated mitochondrial signaling cascade. *Life Sci.*
- Kumari, A., Kakkar, P., 2012b. Lupeol protects against acetaminophen-induced oxidative stress and cell death in rat primary hepatocytes. *Food Chem. Toxicol.*
- Le Vee, M., Jigorel, E., Glaize, D., Gripon, P., Guguen-Guillouzo, C., Fardel, O., 2006. Functional expression of sinusoidal and canalicular hepatic drug transporters in the differentiated human hepatoma HepaRG cell line. *Eur. J. Pharm. Sci.* 28, 109–117.
- LeCluyse, E.L., Witke, R.P., Andersen, M.E., Powers, M.J., 2012. Organotypic liver culture models: meeting current challenges in toxicity testing. *Crit. Rev. Toxicol.* 42, 501–548.
- Lederle, F.A., 1995. Epidemiology of constipation in elderly patients. *Drug utilisation and cost-containment strategies. Drugs Aging* 6, 465–469.
- Lee, A.U., Farrell, G.C., 2001. Mechanism of azathioprine-induced injury to hepatocytes: roles of glutathione depletion and mitochondrial injury. *J. Hepatol.* 35, 756–764.
- Leist, M., Single, B., Castoldi, A.F., Kuhnle, S., Nicotera, P., 1997. Intracellular adenosine triphosphate (ATP) concentration: a switch in the decision between apoptosis and necrosis. *J. Exp. Med.* 185, 1481–1486.
- Leung, L., Kalgutkar, A.S., Obach, R.S., 2011. Metabolic activation in drug-induced liver injury. *Drug Metab. Rev.*
- Lin, Z., Will, Y., 2012. Evaluation of drugs with specific organ toxicities in organ-specific cell lines. *Toxicol. Sci.* 126, 114–127.
- Liss, G., Lewis, J.H., 2009. Drug-induced liver injury: what was new in 2008? *Expert Opin. Drug Metab. Toxicol.* 5, 843–860.
- Liss, G., Rattan, S., Lewis, J.H., 2010. Predicting and preventing acute drug-induced liver injury: what's new in 2010? *Expert Opin. Drug Metab. Toxicol.* 6, 1047–1061.
- Liu, Z., Shi, Q., Ding, D., Kelly, R., Fang, H., Tong, W., 2011. Translating clinical findings into knowledge in drug safety evaluation – drug induced liver injury prediction system (DILIPS). *PLoS Comput. Biol.* 7, e1002310.
- Mato, J.M., Lu, S.C., 2005. Homocysteine, the bad thiol. *Hepatology* 41, 976–979.
- McClerron, H., Wash, P., Burger, A., Norman, J., Folb, P.J., Smith, P., 2006. Determinants of rifampin, isoniazid, pyrazinamide, and ethambutol pharmacokinetics in a cohort of tuberculosis patients. *Antimicrob. Agents Chemother.* 50, 1170–1177.
- Meng, X., Mojaverian, P., Doedee, M., Lin, E., Weinryb, I., Chiang, S.T., Kowey, P.R., 2001. Bioavailability of amiodarone tablets administered with and without food in healthy subjects. *Am. J. Cardiol.* 87, 432–435.
- Minotti, G., 1989. Reactions of adriamycin with microsomal iron and lipids. *Free Radic. Res. Commun.* 7, 143–148.
- Moore, M., Thor, H., Moore, G., Nelson, S., Moldeus, P., Orrenius, S., 1985. The toxicity of acetaminophen and N-acetyl-p-benzoquinone imine in isolated hepatocytes is associated with thiol depletion and increased cytosolic Ca²⁺. *J. Biol. Chem.* 260, 13035–13040.
- Noch, E., Khalili, K., 2009. Molecular mechanisms of necrosis in glioblastoma: the role of glutamate excitotoxicity. *Cancer Biol. Ther.* 8, 1791–1797.
- Olson, H., Betton, G., Robinson, D., Thomas, K., Monro, A., Kolaja, G., Lilly, P., Sanders, J., Sipes, G., Bracken, W., Dorato, M., Van Deun, K., Smith, P., Berger, B., Heller, A., 2000. Concordance of the toxicity of pharmaceuticals in humans and in animals. *Regul. Toxicol. Pharmacol.* 32, 56–67.
- Patrick, R.L., Back, K.C., 1965. Pathology and toxicology of repeated doses of hydrazine and 1,1-dimethyl hydrazine in monkeys and rats. *Ind. Med. Surg.* 34, 430–435.

3.5. MULTIPARAMETRIC SENSOR APPROACH FOR DRUG-INDUCED TOXICITY

1120

S. Seeland et al./Toxicology in Vitro 27 (2013) 1109–1120

- Roe, A.L., Snawder, J.E., Benson, R.W., Roberts, D.W., Casciano, D.A., 1993. HepG2 cells: an in vitro model for P450-dependent metabolism of acetaminophen. *Biochem. Biophys. Res. Commun.* 190, 15–19.
- Sardao, V.A., Pereira, S.L., Oliveira, P.J., 2008. Drug-induced mitochondrial dysfunction in cardiac and skeletal muscle injury. *Expert Opin. Drug Saf.* 7, 129–146.
- Sarich, T.C., Adams, S.P., Petricca, G., Wright, J.M., 1999. Inhibition of isoniazid-induced hepatotoxicity in rabbits by pretreatment with an amidase inhibitor. *J. Pharmacol. Exp. Ther.* 289, 695–702.
- Seeland, S., Treiber, A., Hafner, M., Huwyler, J., 2011. On-line identification of P-glycoprotein substrates by monitoring of extracellular acidification and respiration rates in living cells. *Biochim. Biophys. Acta* 1808, 1827–1831.
- Setzer, B., Lebrecht, D., Walker, U.A., 2008. Pyrimidine nucleoside depletion sensitizes to the mitochondrial hepatotoxicity of the reverse transcriptase inhibitor stavudine. *Am. J. Pathol.* 172, 681–690.
- Shiozawa, K., Tanaka, Y., Yoshihara, R., Imura, S., Murata, M., Yamane, T., Miura, Y., Hashiramoto, A., Shiozawa, S., 2005. Serum levels and pharmacodynamics of methotrexate and its metabolite 7-hydroxy methotrexate in Japanese patients with rheumatoid arthritis treated with 2-mg capsule of methotrexate three times per week. *Mod. Rheumatol.* 15, 405–409.
- Smith, D.A., Schmid, E.F., 2006. Drug withdrawals and the lessons within. *Curr. Opin. Drug Discov. Devel.* 9, 38–46.
- Speth, P.A., van Hoesel, Q.G., Haanen, C., 1988. Clinical pharmacokinetics of doxorubicin. *Clin. Pharmacokinet.* 15, 15–31.
- Stocker, M.E., Montgomery, J.E., 2001. Serum paracetamol concentrations in adult volunteers following rectal administration. *Brit. J. Anaesth.* 87, 638–640.
- Tong, V., Teng, X.W., Chang, T.K., Abbott, F.S., 2005a. Valproic acid I: time course of lipid peroxidation biomarkers, liver toxicity, and valproic acid metabolite levels in rats. *Toxicol. Sci.* 86, 427–435.
- Tong, V., Teng, X.W., Chang, T.K., Abbott, F.S., 2005b. Valproic acid II: effects on oxidative stress, mitochondrial membrane potential, and cytotoxicity in glutathione-depleted rat hepatocytes. *Toxicol. Sci.* 86, 436–443.
- Tong, V., Teng, X.W., Karagiozov, S., Chang, T.K., Abbott, F.S., 2005c. Valproic acid glucuronidation is associated with increases in 15-F2t-isoprostane in rats. *Free Radic. Biol. Med.* 38, 1471–1483.
- Twiner, M.J., Hirst, M., Valenciano, A., Zacharewski, T.R., Dixon, S.J., 1998. N,N-Dimethylformamide modulates acid extrusion from murine hepatoma cells. *Toxicol. Appl. Pharmacol.* 153, 143–151.
- Van Summeren, A., Renes, J., Bouwman, F.G., Noben, J.-P., van Delft, J.H.M., Kleinjans, J.C.S., Mariman, E.C.M., 2011. Proteomics investigations of drug-induced hepatotoxicity in HepG2 cells. *Toxicol. Sci.* 120, 109–122.
- West, S.G., 1997. Methotrexate hepatotoxicity. *Rheum. Dis. Clin. North Am.* 23, 883–915.
- Westerink, W.M., Schoonen, W.G., 2007a. Cytochrome P450 enzyme levels in HepG2 cells and cryopreserved primary human hepatocytes and their induction in HepG2 cells. *Toxicol. In Vitro* 21, 1581–1591.
- Westerink, W.M., Schoonen, W.G., 2007b. Phase II enzyme levels in HepG2 cells and cryopreserved primary human hepatocytes and their induction in HepG2 cells. *Toxicol. In Vitro* 21, 1592–1602.
- Woo, J., Chan, C.H., Walubo, A., Chan, K.K., 1992. Hydrazine – a possible cause of isoniazid – induced hepatic necrosis. *J. Med.* 23, 51–59.
- Ye, N., Qin, J., Liu, X., Shi, W., Lin, B., 2007. Characterizing doxorubicin-induced apoptosis in HepG2 cells using an integrated microfluidic device. *Electrophoresis* 28, 1146–1153.
- Zahno, A., Brecht, K., Morand, R., Maseneni, S., Torok, M., Lindinger, P.W., Krahenbuhl, S., 2011. The role of CYP3A4 in amiodarone-associated toxicity on HepG2 cells. *Biochem. Pharmacol.* 81, 432–441.
- Zhou, S., Chan, E., Duan, W., Huang, M., Chen, Y.Z., 2005. Drug bioactivation, covalent binding to target proteins and toxicity relevance. *Drug Metab. Rev.* 37, 41–213.
- Zhou, S., Starkov, A., Froberg, M.K., Leino, R.L., Wallace, K.B., 2001. Cumulative and irreversible cardiac mitochondrial dysfunction induced by doxorubicin. *Cancer Res.* 61, 771–777.

3.6 P2X7 receptors and cellular stress

ATP-induced cellular stress and mitochondrial toxicity in cells expressing purinergic P2X7 receptor

Swen Seeland^{1,2,4}, Helene Kettiger⁴, Mark Murphy², Alexander Treiber¹, Jasmin Giller¹, Andreas Kiss¹, Romain Sube¹, Stephan Krähenbühl³, Mathias Hafner² Jörg Huwyler⁴

¹ Actelion Pharmaceuticals Ltd., Gewerbestrasse 16, 4123 Allschwil, Switzerland

² Institute for Molecular and Cell Biology, University of Applied Sciences, Paul-Wittsack Strasse 10, 68163 Mannheim, Germany

³ Division of Clinical Pharmacology and Toxicology, University Hospital Basel, 4056 Basel, Switzerland

⁴ Department of Pharmaceutical Sciences, University of Basel, Switzerland

Contributions H.Kettiger: author, experiments (mitochondrial membrane potential)

Submitted to Journal of Pharmacology and Experimental Therapeutics *reformatted for thesis layout*

Abstract

Under pathological conditions, the purinergic P2X7 receptor is activated by elevated concentrations of extracellular ATP. Thereby, the receptor forms a slowly dilating pore, allowing cations and, upon prolonged stimulation, large molecules to enter the cell. This process has a strong impact on cell signalling, metabolism, and viability. The present study aimed to establish a link between gradual P2X7 activation and pharmacological endpoints including oxidative stress, hydrogen peroxide generation, and cytotoxicity. We investigated the stimulatory effects of exogenously applied ATP or a more specific P2X7-receptor agonist (BzATP) on the P2X7 receptor, in combination with the selective P2X7-receptor antagonist AZD9056. Mechanisms of cellular stress and cytotoxicity were studied in P2X7-transfected HEK293 cells. P2X7-receptor activation was studied by patch-clamp experiments using a primary mouse microglia cell line. Oxidative stress induced by ATP or BzATP in target cells was monitored by hydrogen peroxide release in human mononuclear blood cells. We performed real-time monitoring of metabolic and respiratory activity of cells expressing the P2X7-receptor protein using a cytosensor system. Stimulation of the P2X7 receptor leads to cytotoxicity. Conversion of the P2X7 receptor from a small cation channel to a large pore occurring under prolonged stimulation could be monitored in real time. Our findings established a direct link between P2X7-receptor activation by extracellular ATP or BzATP and cellular events culminating in cytotoxicity. Mechanisms of toxicity include metabolic and oxidative stress, increase in intracellular calcium concentration, disturbance of mitochondrial membrane potential, and mitochondrial toxicity.

Introduction

Adenosine triphosphate (ATP) plays a central role in cell metabolism. Intracellular concentrations of ATP range from 1 to 10 mM (Beis and Newsholme, 1975). Extracellular ATP concentrations are regulated by ATPases (Burnstock, 2006), and are typically very low under physiological conditions. There are, however, conditions in which local extracellular ATP concentrations reach high levels (Volonte et al., 2003; Burnstock, 2006). For example, ATP is released at the synapses of neurons, where it acts as a neurotransmitter (Bardoni et al., 1997; Pankratov et al., 2006). In addition, intracellular ATP is released into the extracellular space in conditions of cell necrosis or hypoxia (Billingsley et al., 2004; Rousseau et al., 2004; Sharnez et al., 2004; Schroder and Tschopp, 2010). Moreover, prolonged stimulation with ATP induces cell death in leukocytes and endothelial cells (Dawicki et al., 1997; Yoon et al., 2006; Cosentino et al., 2011). These extreme effects occurring at extracellular ATP concentrations above 500 μ M are thought to be induced, in part, by the purinergic receptor P2X7 (Chessell et al., 1998; Arbeloa et al., 2012). Such ATP concentrations are more than ten times higher than those required for activation of other P2X or P2Y receptors. Sustained exposure (> 1 min) to ATP levels above 500 μ M enables the P2X7 receptor to form a large, non-selective pore, which allows molecules of up to 900 Dalton to enter the cell (Surprenant, 1996). Prolonged opening of the P2X7 pore initiates several events with serious consequences for the cells, including cell death (Buisman et al., 1988; Ferrari et al., 1997; Labasi et al., 2002).

Mechanistic studies indicated that activation of the P2X7 receptor leads to a distinct sequence of events (North, 2002). Electrophysiological studies have shown that opening of an ion channel selective for small cations (Na^+ , K^+ , and Ca^{2+}) occurs within the first milliseconds of stimulation. After several seconds, permeability for larger organic cations increases progressively, with maximum dilatation of the ion channel reached after several minutes. However, the underlying molecular mechanisms of this process are still unclear (North, 2002).

Activation of the P2X7 receptor initiates a series of cellular responses that include depolarization, activation of phospholipase C, and a rise in intracellular Ca^{2+} concentrations, which stimulates caspase-1 activity, cytokine release, and activation of p38 mitogen-activated protein kinase [MAPK] (Armstrong et al., 2002; Ferrari et al., 2006). Such events, in turn,

have a plethora of effects. For example, cytokine signalling provokes an inflammatory stimulus in cells of the immune system (Volonte et al., 2012). Some of these events are pathologically important, for example in neurodegeneration (Takenouchi et al., 2010), tumour growth (Ryu et al., 2011) and kidney disease (Birch et al., 2013). In transgenic mice, disruption of P2X7-receptor function has a detrimental impact on adipogenesis and lipid metabolism, pointing to an important physiological role of P2X7 in energy metabolism (Beaucage et al., 2013). Consequently, several P2X7 antagonists have been developed in recent years (Chrovian et al., 2014). One of these compounds is the selective P2X7-receptor antagonist AZD9056 (Bhattacharya et al., 2011) whose efficacy in rheumatoid arthritis was evaluated in a phase II clinical trials (Keystone et al., 2012).

While many of the above-mentioned phenomena have been extensively characterized, their link to P2X7 activity has not been conclusively shown. In particular, it is difficult to monitor gradual activation of the P2X7 receptor on a time scale ranging from a few milliseconds up to minutes or hours. Thus, the present project aimed to study the dynamics of P2X7-receptor activation, using a P2X7-expressing mouse microglia cell line (BV2) and a recombinant human HEK293 cell line overexpressing P2X7 (HEK-hP2X7). To this end, we linked pharmacological endpoints, such as cytotoxicity or hydrogen peroxide (H₂O₂) release as an indicator of oxidative stress, to P2X7-receptor activation, altered ion flow, disturbance of membrane potential, cellular metabolism, and respiration. Real-time monitoring of metabolic and respiratory activity of P2X7-expressing cells was achieved using a novel cytosensor system (Seeland et al., 2013). This cell-based cytosensor system allows real-time monitoring of metabolic activity (pH changes), respiration (oxygen consumption), as well as cellular morphology and adhesion of cells (Thedinga et al., 2007).

Materials and Methods

Chemicals. ATP and BzATP were purchased from Sigma (Buchs, Switzerland), dissolved in water, and adjusted to pH 7.4 using sodium hydroxide. Fluo-4 acetoxymethyl ester (Fluo-4-AM) was obtained from Life Technologies (Basel, Switzerland). The cyanine dye JC-1 (5,5',6,6'-tetrachloro-1,1',3,3'-tetraethylbenzimidazolylcarbocyanine iodide) was obtained from Enzo Life Sciences (Lausen, Switzerland). Valinomycin was obtained from Sigma-Aldrich (St. Louis, MO). All other chemicals were of analytical quality. The P2X7-receptor antagonist AZD9056 (Bhattacharya et al., 2011) was used as a stock solution in

dimethyl sulfoxide (DMSO). Final DMSO concentrations in experiments did not exceed 1.0% (v/v). As demonstrated by control incubations, these DMSO concentrations were not cytotoxic and did not interfere with the assays. The CellTiter-Blue cell viability assay was obtained from Promega (Dübendorf, Switzerland).

Preparation of mononuclear blood cells (lymphocytes, monocytes, and macrophages). For the preparation of fresh mononuclear cells, 30 mL of male human blood containing 10% (v/v) sodium citrate as anticoagulant was collected, and mononuclear cells were isolated by Polymorphprep™ (Axis-Shield, Oslo, Norway) density centrifugation according to the manufacturer's protocol. Briefly, 15 mL of human blood was layered on 17 mL of Polymorphprep buffer (Axis-Shield) in a 50 mL reaction tube and centrifuged at 500 g for 30 min at 22°C. The resulting mononuclear cell band was transferred to a new 50 mL reaction tube and diluted with one equivalent of aqueous sodium chloride solution (0.45%, v/v) to restore physiological osmolarity. The solution was centrifuged at 450 g for 18 min at 20°C and the supernatant removed. Subsequently, the cell pellet was reconstituted in 0.9% (w/v) aqueous sodium chloride solution and again centrifuged at 400 g for 10 min at 20°C. The supernatant was removed, and remaining red blood cells were hypertonicity lysed by adding 9 mL of demineralized water for 17 s, and then centrifuged at 300 g for 10 min at 20°C. The cell pellet obtained in the last centrifugation step was reconstituted in 20 mL of phosphate-buffered saline (PBS), and cell viability and concentration were analysed using a Vi-cell XR cell viability analyser (Beckman Coulter, Krefeld, Germany). Cell concentration was adjusted to 2×10^6 cells/mL, and a 250 µL aliquot of this cell suspension was dispensed into a 96-well plate and immediately used for experiments.

Primary Wistar rat cortical cells. Freshly prepared cortical cultures originated from Wistar rat embryos 18 days after gestation. After enzymatic cell dissociation with papain (Worthington, Lakewood, NJ), the cells were resuspended and diluted to 3×10^5 cells/mL in neurobasal medium supplemented with 0.5 mM L-glutamine, 2% B27, 50 IU/mL penicillin, and 50 µg/mL streptomycin. Aliquots (50 µL) of this suspension were dispensed into poly-D-lysine-coated BioCoat 384-well microplates (Becton Dickinson, Basel, Switzerland) and incubated at 37°C for about eight days in a humidified atmosphere containing 5% CO₂. Primary cortical cells represented a mixed neuronal and astroglial culture system from which probably only the astroglial component contains P2X7 receptors. Animal experiments were carried out in accordance with local legislation on animal welfare and protection.

HEK-hP2X7 cell line overexpressing P2X7. HEK293 cells (HEK-hP2X7) were generated according to established molecular cloning protocols. Specifically, RNA was extracted from human whole blood using the Qiagen RNeasy kit (Qiagen, Hombrechtikon, Switzerland) according to the manufacturer's instructions. Subsequently, cDNA was generated (Superscript II, Life Technologies), and the human P2X7 gene (gene bank ref. BC011913) was amplified and ligated into a pcDNA3.1 (+) vector. HEK293 cells (CRL 1573, ATCC American type culture collection, Manassas, VA) were transfected with the pcDNA3.1 (+) hP2X7 plasmid using lipofectamine transfection reagent (Life Technologies) according to the manufacturer's instructions. After exposure to DNA for 24 h, cells were trypsinised and re-seeded at low density in the presence of 0.25 mg/mL geneticin. Geneticin-resistant cells were then selected in two consecutive rounds of cloning by serial limiting dilution with visual inspection. Individual clones were screened for P2X7 expression by applying ATP and recording the resulting uptake of YoPro1. A specific cell clone was chosen based on RNA and protein expression. Parental HEK293 cells and HEK-hP2X7 cells were cultured under standard cell culture conditions in Dulbecco's modified Eagle medium (DMEM) with 2.0 mM L-glutamine (Life Technologies) supplemented with 50 IU/mL penicillin, 50 µg/mL streptomycin, and 10% (v/v) foetal calf serum (BioConcept, Allschwil, Switzerland). Subcultures were obtained twice a week from confluent cell monolayers using a split ratio of 1:5. HEK-hP2X7 cells were cultured in the presence of 0.25 mg/mL geneticin to maintain P2X7-expression levels. Under these conditions, cells expressed constant levels of P2X7 for at least 30 passages.

Human umbilical vein endothelial cells (HUVEC). HUVEC were obtained from Lonza (CC-2517, Walkersville, MD) and maintained under standard cell culture conditions in EBM® medium with Clonetics® EGM® SingleQuots (Lonza) supplemented with 2% (v/v) foetal bovine serum (PAA Laboratories, Pasching, Austria), 1.0 µg/mL hydrocortisone (Lonza), 36 µg/mL bovine brain extract (Lonza), 3.0 ng/mL human embryonic growth factor (Lonza), 30 µg/mL gentamicin, 15 ng/mL amphotericin-B (Lonza), 50 IU/mL penicillin, and 50 µg/mL streptomycin (Life Technologies).

Mouse microglia BV2 cells. The mouse microglia BV2 cell line used for patch-clamp experiments was cultured under standard cell culture conditions. The cells were maintained in DMEM with 2 mM GlutaMAX (Life Technologies) supplemented with 50 IU/mL penicillin, 50 µg/mL streptomycin, and 10% (v/v) foetal calf serum (BioConcept).

3.6. P2X7 RECEPTORS AND CELLULAR STRESS

Electrophysiology. For patch-clamp experiments, mouse microglia BV2 cells were analysed in the whole-cell patch-clamp configuration (Hamill et al., 1981). Patch electrodes were filled with intracellular buffer containing 120 mM KF, 20 mM KCl, 1.0 mM ethylene glycol-bis(aminoethyl ether)-tetraacetic acid (EGTA), and 10 mM 4-(2-hydroxyethyl)-1-piperazineethanesulfonic acid (Hepes) adjusted to pH 7.2 with potassium hydroxide. Recordings were done at room temperature in external buffer containing 147 mM NaCl, 2.0 mM KCl, 0.3 mM CaCl₂, 10 mM Hepes, and 12 mM D-glucose adjusted to pH 7.4 with sodium hydroxide. At a constant holding potential of -70 mV, BzATP (100 μM) was added in the presence or absence of different concentrations of the P2X7-receptor antagonist by a computer-controlled application system. Agonist-induced steady-state currents were corrected for leak, and concentration-response curves were fitted to averaged current amplitudes derived from 3 to 4 cells.

Fluo-4-AM calcium measurements. Intracellular calcium concentrations were determined using rat primary cortical cells at day 8 in culture. Cells were loaded with 1.0 μM Fluo-4-AM in Hank's balanced salt solution (HBSS; Life Technologies) containing 20 mM Hepes, pH 7.4. Cells were washed once at 10 min before recording. After pre-incubation with 0.01 μM to 10 μM of AZD9056 for 15 min, BzATP was added at a final concentration of 250 μM. Fluorescence signals were measured using a fluorescent imaging plate reader.

YoPro1 uptake analysis. The membrane-impermeable fluorescent dye YoPro1 was used to determine P2X7-receptor permeability for larger ions (Rassendren et al., 1997; Michel et al., 1998). HEK-hP2X7 cells were diluted in cell culture medium without geneticin to a final concentration of 2×10^5 cells/mL, and an aliquot (50 μL) of this cell suspension was transferred to a poly-L-lysine pre-coated black-wall, clear-bottom plate and incubated at 37°C in a humidified atmosphere containing 5% CO₂ for 48 h. The medium was then removed from cells, and assay buffer containing 0.5 μM YoPro1 was added to the wells. Cells were incubated with the indicated concentrations of AZD9056 and ATP at a final concentration of 250 μM for 45 min. Fluorescence signals were measured using a fluorescent imaging plate reader (tetra, Molecular Device, Sunnyvale, CA). Excitation wavelength and emission wavelength were 485 nm and 530 nm, respectively.

Hydrogen peroxide generation by mononuclear cells. Production of cellular H₂O₂ by mononuclear blood cells after stimulation with P2X7 agonists (ATP or BzATP) was determined by the Amplex Red assay (Life Technologies). Briefly, 5×10^5 mononuclear

blood cells were incubated with 50 μM Amplex Red and 0.1 U/mL horseradish peroxidase for 0.5 h at 37°C in Krebs Ringer phosphate solution (145 mM NaCl, 5.7 mM sodium phosphate, 4.9 mM KCl, 0.5 mM CaCl_2 , 1.2 mM MgSO_4 , and 5.5 mM glucose) protected from light. After adding ATP (1 mM) or BzATP (0 - 400 μM) to the cells, the fluorescence was quantified by means of a microplate reader (Synergy MX, BioTek®, Luzern, Switzerland) at an excitation wavelength of 550 nm and absorbance wavelength of 600 nm. Background fluorescence was determined in a reaction without mononuclear blood cells.

Dynamic mass redistribution assay. Dynamic mass distribution was determined using the Corning Epic system (Corning Inc., Tewksbury, MA), consisting of a temperature-controlled unit, optical detection unit, and on-board robotic liquid handling device. The Epic system measures changes in the index of refraction upon mass redistribution which can be ligand-induced within the cell monolayer. HUVEC were detached by trypsination, and viability was analysed. Cells were then diluted in culture medium to reach a final concentration of 4×10^5 cells/mL. An aliquot (30 μL) of this cell suspension was transferred to a fibronectin-coated Epic 384-well microplate containing 10 μL HUVEC medium (see section ‘HUVEC cells’) and incubated at 37°C for 20 h in a humidified atmosphere containing 5% CO_2 to reach a confluent monolayer. Each well bottom of the microplate contained a resonant waveguide-grating biosensor. Prior to starting the experiment, the medium was replaced by 30 μL HBSS supplemented with 20 mM Hepes and 0.06% (w/v) bovine serum albumin. Subsequently, microplates were kept in the Epic reader for 2 h to equilibrate at a constant temperature (26°C). An initial baseline curve was recorded. Then, the ATP solution in assay buffer was dispensed into the microplate at concentrations ranging from 0 to 5.0 mM, and dynamic mass redistribution was monitored for 4000 s. Control experiments without ATP were performed under otherwise identical conditions.

Cytosensor experiments. HEK-hP2X7 cells and parental HEK293 cells were detached by trypsination (Life Technologies), and cell viability was analysed. Cells were then diluted in culture medium to a final concentration of 5.7×10^5 cells/mL. An aliquot (0.35 mL) of this cell suspension was transferred to the pre-warmed fibronectin-coated sensor chip (SC1000) and incubated for at least 20 h prior to use. A cytosensor system (Bionas 1500 system, Bionas, Rostock, Germany) was used to continuously record cellular physiology parameters as described previously (Seeland et al., 2011). Briefly, a flow head with 50 μm spacers (as determined by the distance between the flow head and sensor chip surface) was used, leading

to an effective chamber volume of 1.4 μL . The assay medium used was DMEM supplemented with 2.0 mM L-glutamine, 0.1% (v/v) foetal bovine serum, 25 IU/mL penicillin, and 25 $\mu\text{g/mL}$ streptomycin. The assay medium contained neither Hepes nor NaHCO_3 and was adjusted to pH 7.4 using sodium hydroxide. During analysis, the assay medium was delivered to the cells at a constant flow rate (63 $\mu\text{L/min}$) and interrupted periodically (stop phases of 4 min and pump phases of 3 min). Signals from the microsensor chip were recorded after a stabilization phase of at least 3 h. During three stop/go cycles (21 min in total), cells were exposed to increasing concentrations of the agonist BzATP (0 - 100 μM) in assay medium and adjusted to pH 7.4 using sodium hydroxide. In experiments with BzATP, cells were exposed to AZD9056 (10 μM) prior to treatment with 50 μM BzATP. Stimulation and/or inhibition phases with BzATP and/or AZD9056 were followed by a wash-out phase of at least 4 h before a new stimulation phase was initiated.

Cellular viability assay. The effect of agonists on cell viability was assessed in parental HEK293 cells and HEK-hP2X7 cells using the CellTiter-Blue assay according to the manufacturer's instructions. In brief, an aliquot (60 μL) of cell suspension with a nominal cell density of 8×10^6 cells/mL was dispensed into a 96-well plate. The cells were incubated for 24 h in a humidified atmosphere containing 5% CO_2 to allow cell attachment. At the end of the pre-incubation period, ATP or BzATP was added to the cells at concentration ranges up to 5 mM and 0.5 mM, respectively. For inhibition experiments, AZD9056 was added to the cells at concentrations up to 10 μM 5 min prior to the addition of ATP (2.5 mM) or BzATP (0.25 mM). After incubation for 30 min at 37°C, an aliquot (20 μL) of the pre-warmed CellTiter-Blue reagent was added. Samples were incubated for 1 h at 37°C. Fluorescence signals were measured using a fluorescent imaging plate reader (tetra, Molecular Device, Sunnyvale, CA). Excitation and emission wavelengths were 560 nm and 590 nm, respectively.

Mitochondrial membrane potential. To determine mitochondrial membrane potential ($\Delta\psi\text{m}$), JC-1 cyanine dye was used as a marker for mitochondrial integrity. In cells with intact membrane potential, JC-1 dye forms orange aggregates within the mitochondria. Depolarization of the mitochondrial membrane leads to JC-1 disaggregation and a shift of the fluorescence emission wavelength. Parental HEK293 cells and HEK-hP2X7 cells were seeded on a poly-D-lysine-coated Ibidi μ -Slide (Vitaris AG, Baar, Switzerland) to reach a final cell density of 5×10^4 cells per well. Cells were allowed to adhere overnight. Then, JC-1

dye was added to the medium at a final concentration of 10 $\mu\text{g}/\text{mL}$. Cells were incubated for 15 min at 37°C allowing the dye to accumulate within the mitochondria. Subsequently, the medium was removed, and cells were carefully rinsed with pre-warmed PBS and incubated for 1 h at 37°C with medium containing BzATP at concentrations of 31.3 μM or 250 μM . The K^+ ionophore valinomycin (1 mM) served as a positive control, while untreated cells were used as a negative control. Fluorescence emission was monitored with an IX81 Olympus confocal microscope at 37 C in an atmosphere containing 5% CO_2 . JC-1 aggregates were excited with a laser at 559 nm, and emission was recorded with a wavelength filter in the range of 574 nm to 627 nm. JC-1 monomers were excited at 488 nm, and emission was recorded with a wavelength filter in the range of 500 nm to 535 nm as described earlier (Perelman et al., 2012).

Data analysis and statistics. Concentration-response curves were obtained from experiments with the cell-based microsensor system in the presence or absence of the antagonist. Evaluation as well as kinetic and statistic calculations were performed using GraphPad Prism software (Version 5.04, GraphPad Software Inc., La Jolla, CA). Each experiment was performed at least in triplicate. Results were expressed as means \pm SD or means with 95% confidence intervals (CI).

Results

Electrophysiology of P2X7-receptor activation and effects on calcium and YoPro1 dye influx. Fig. 1A shows the activation of the P2X7 receptor by BzATP as studied in patch-clamp experiments using the P2X7 receptor-expressing mouse microglia BV2 cell line. Effects were characterized by an EC_{50} of $197 \pm 5.1 \mu\text{M}$ (mean \pm SD, $n = 5$). The P2X7-receptor antagonist AZD9056 inhibited BzATP-induced currents in these cells (Fig. 1B). BzATP induced stable, inward currents at a holding potential of -70 mV that were blocked by AZD9056 with an IC_{50} of 2.1 μM (95% CI, 1.8 – 2.5 μM , $n \geq 5$; Fig. 1C).

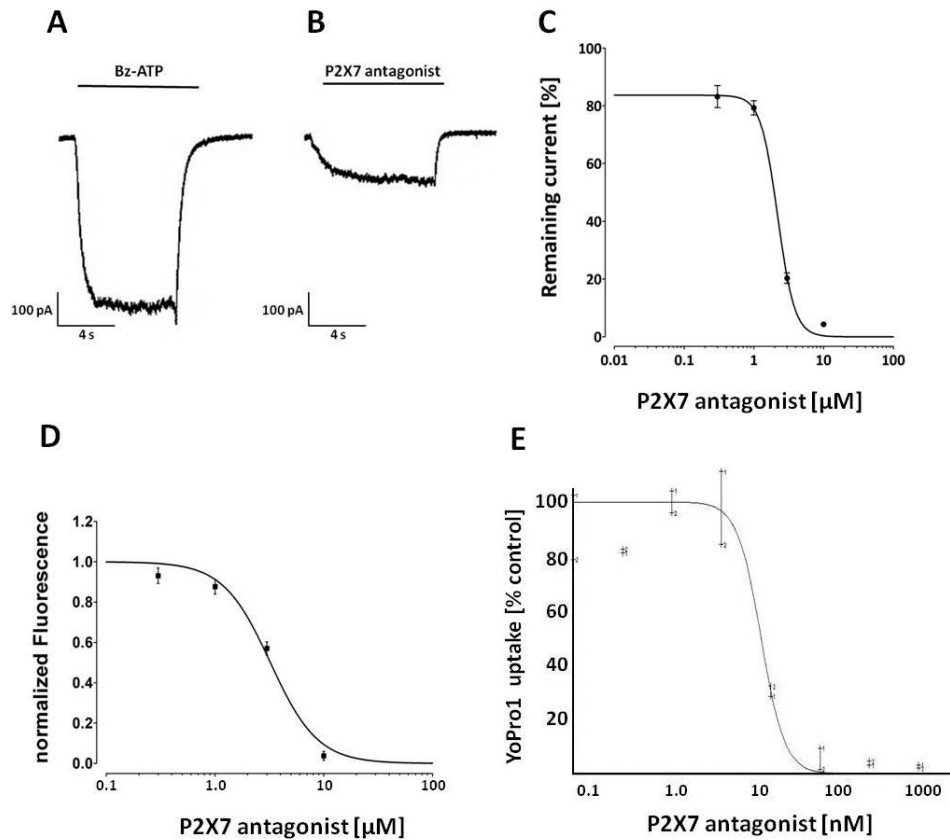


Figure 1: Patch-clamp experiments using P2X7-receptor-expressing mouse microglia BV2 cells. (A) Raw current signal pattern after stimulation of BV2 cells using 100 μM BzATP. (B) Raw current signal pattern after stimulation of BV2 cells using 100 μM BzATP in the presence of 10 μM of AZD9056. (C) Dose-dependent inhibition of membrane currents in mouse microglia BV2 cells using AZD9056. Cells were stimulated using 100 μM BzATP. (D) Intracellular Ca^{2+} increase after 100 μM BzATP stimulation of rat cortical cells in the presence of increasing concentrations of AZD9056. (E) YoPro1 dye membrane permeability measurements using P2X7-overexpressing HEK-hP2X7 cells stimulated by 250 μM ATP in the presence of increasing concentrations of AZD9056. (C, D, E). Values are means \pm SD, $n \geq 4$.

When measuring Ca^{2+} influx via P2X7 receptors using a calcium-sensitive fluorescent dye in primary cortical cultures from rat embryonic brains, AZD9056 inhibited BzATP-induced Ca^{2+} influx with an IC_{50} of 3.2 μM (95% CI, 2.8 – 3.7 μM , $n \geq 4$; Fig. 1D). YoPro1 influx was determined upon stimulation of HEK-hP2X7 cells with BzATP for 45 min. Observed effects were antagonised with an IC_{50} of 11.2 nM (95% CI, 9.6 – 13.2 nM; Fig. 1E).

ATP-induced hydrogen peroxide release by mononuclear blood cells and dynamic mass redistribution in HUVEC cells. Mononuclear cells were freshly prepared from human donor blood. Within 20 min, exogenously applied ATP induced a marked, concentration-dependent

increase in H_2O_2 release with an EC_{50} of $558 \pm 8.7 \mu\text{M}$ (mean \pm SD, $n = 3$), as depicted in Fig. 2A. The P2X7-specific receptor antagonist AZD9056 elicited moderate inhibition of H_2O_2 formation with an IC_{50} of $3.0 \pm 0.9 \mu\text{M}$ (mean \pm SD, $n = 3$) at 1 mM ATP, indicating involvement of the P2X7 receptor (Fig. 2B). When we tested the effect of extracellular ATP on dynamic mass redistribution in HUVEC cells, we observed a concentration-response correlation with an EC_{50} of $933 \pm 156 \mu\text{M}$ (mean \pm SD, $n = 3$ independent experiments; Fig. 2C).

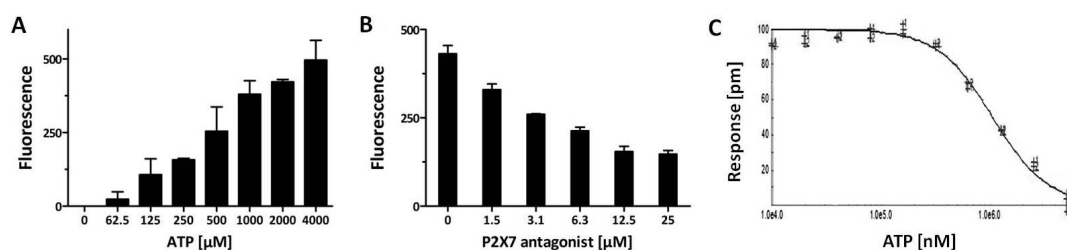


Figure 2: P2X7-mediated cellular formation of hydrogen peroxide and mass redistribution. (A) Rate of H_2O_2 formation in mononuclear blood cells after stimulation with extracellular ATP. (B) Effect of AZD9056 on H_2O_2 levels in mononuclear blood cells stimulated with 1 mM ATP. (C) Morphological changes as determined by mass redistribution of human umbilical-vein endothelial cells (HUVEC) upon treatment with exogenously applied ATP.

BzATP-induced metabolic activation of HEK239 cells and HEK-hP2X7 cells overexpressing P2X7. We used a cytosensor system for real-time monitoring of metabolic activation of HEK-hP2X7 cells. Measured parameters were oxygen concentration, pH, and cell impedance. The sensor system was optimized with respect to maximum stimulation amplitudes, as described previously (Seeland et al., 2011). Optimal cell density was 2×10^5 attached cells per sensor chip and an effective incubation chamber volume of $1.4 \mu\text{L}$. Viability of cells was monitored continuously by measuring cellular impedance. Continuous deviations from initial values in the order of approx. $\pm 1.2\%$ per hour were considered acceptable and were attributed to cell proliferation or cell release from the chip. HEK-hP2X7 cells responded immediately to BzATP in a concentration-dependent manner (Fig. 3). In HEK-hP2X7 cells but not in HEK293 control cells, metabolic activity (i.e., acidification) and cellular respiration increased in a concentration-dependent manner upon BzATP treatment (Fig. 3A). At high BzATP concentrations ($100 \mu\text{M}$), a sharp decrease in cellular respiration was observed, which was in strict contrast to cellular acidification (Fig. 3A). Maximum changes in cell morphology (i.e., impedance) were reached at $100 \mu\text{M}$ BzATP (Fig. 3B). Compared to

3.6. P2X7 RECEPTORS AND CELLULAR STRESS

HEK-hP2X7 cells, parental HEK293 cells showed only negligible effects on the impedance sensor (Fig. 3B).

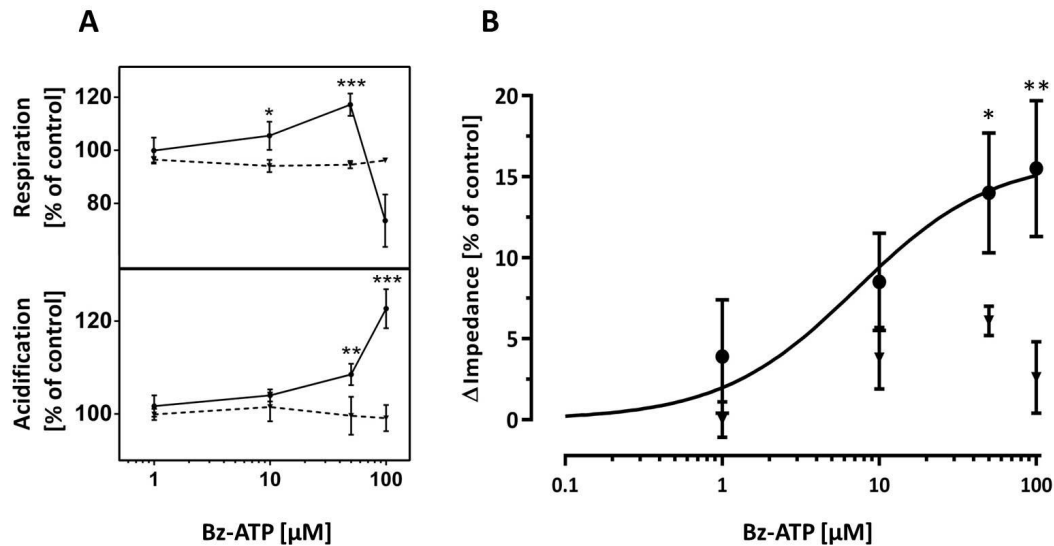


Figure 3: Cytosensor measurements in HEK-hP2X7 cells overexpressing P2X7 and parental HEK293 cells. (A) Concentration-dependent stimulation of HEK-hP2X7 cells (solid lines, black circles) and parental HEK293 cells (dotted lines, inverted triangles) by BzATP as analysed using a cytosensor system. Parental HEK293 cells and human HEK-hP2X7 cells were compared with respect to respiration and metabolic activity (acidification). Respiratory inhibition in HEK-hP2X7 cells at 100 μM BzATP was indicative of cellular toxicity. Level of significance: *p < 0.05, **p < 0.01, ***p < 0.001, n = 4. (B) Cell impedance as a function of stimulation of P2X7 using BzATP. Curve was fitted to HEK-hP2X7 signals (solid line, black circles) using an enzyme kinetic model. Parental HEK293 cells were used as a control (inverted triangles). Level of significance: *p < 0.05, **p < 0.01, n = 4.

Activation of the P2X7 receptor by BzATP was saturated at high concentrations and was characterized by an EC_{50} of $9.6 \pm 1.8 \mu\text{M}$ (mean \pm SD, n = 5; Fig. 3B). These effects were inhibited by AZD9056 (Fig. 4). Inhibitory effects of AZD9056 were reversible since responsiveness of the cells towards BzATP was partially restored by washing out the antagonist (Fig. 4). Inhibition of the BzATP-induced effects observed in HEK-hP2X7 cells overexpressing P2X7 did not take place in the parental HEK293 cells (Fig. 4).

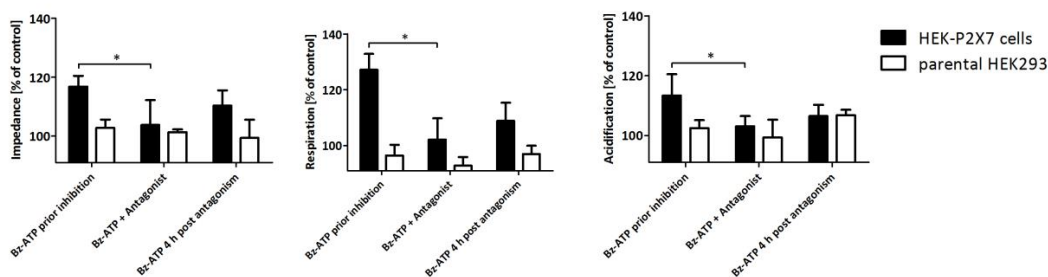


Figure 4: Reversible inhibition of BzATP-induced effects by AZD9056. Cytosensor measurements using HEK-hP2X7 cells and parental HEK293 cells in the presence and absence of 10 μM AZD9056. After a wash-out period of 4 h, the cells were again stimulated with 50 μM BzATP to assess regeneration and reactivation. Level of significance in the presence and absence of antagonist: $*p < 0.05$, $n = 4$.

ATP- and BzATP-induced cytotoxicity. Stimulation of P2X7-expressing HEK-hP2X7 cells with ATP (Fig. 5A) or BzATP (Fig. 5B) resulted in concentration-dependent cytotoxic effects. These effects were absent in parental HEK293 cells. LD_{50} values for HEK-hP2X7 cells were $1017 \pm 81 \mu\text{M}$ (mean \pm SD, $n = 3$) for ATP and $119.7 \pm 4.4 \mu\text{M}$ (mean \pm SD, $n = 3$) for BzATP. These effects were antagonised by AZD9056 with an IC_{50} of $11.4 \pm 1.8 \text{ nM}$ (mean \pm SD, $n = 3$) at 2.5 mM ATP (Fig. 5C) and $5.62 \pm 0.75 \text{ nM}$ (mean \pm SD, $n = 3$) at 0.25 mM BzATP (Fig. 5D). Again, parental HEK293 cells were not responsive to ATP, BzATP, or AZD9056 (Fig. 5C and Fig. 5D).

3.6. P2X7 RECEPTORS AND CELLULAR STRESS

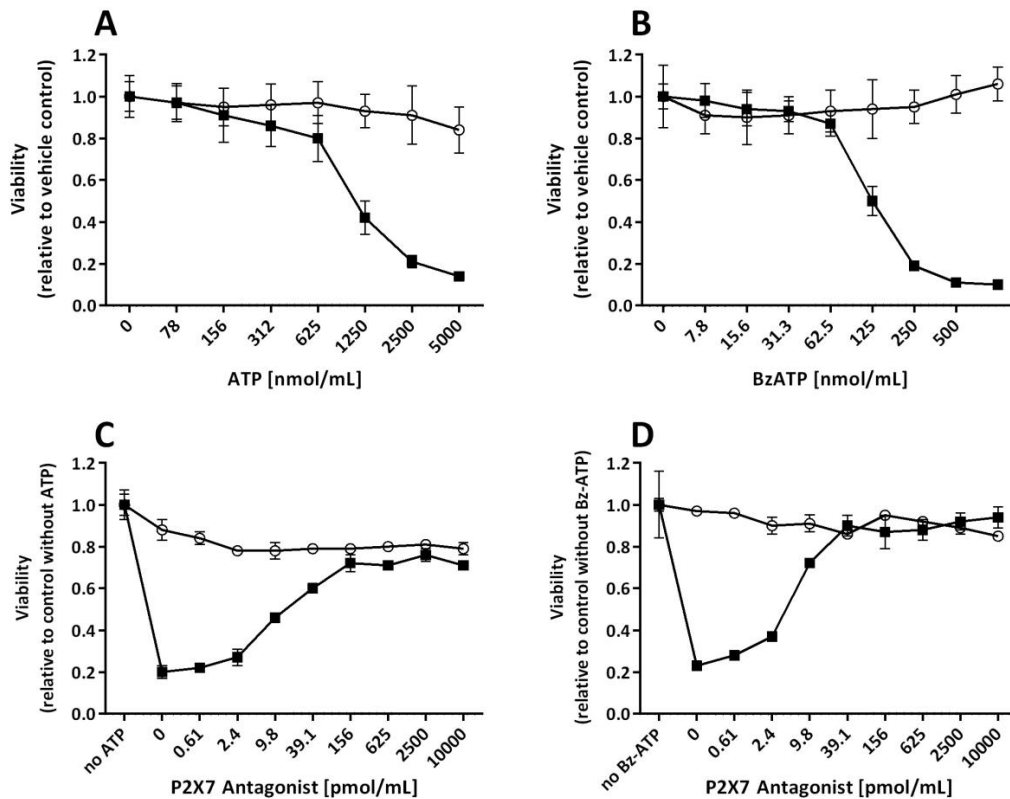


Figure 5: Cellular viability of parental HEK293 cells (empty circles) and HEK-hP2X7 cells (filled squares). Cellular viability was analysed in the presence of increasing concentrations of the two P2X7 agonists (A: ATP; B: BzATP). A cell-protective function of the P2X7-specific antagonist AZD9056 was demonstrated in inhibition experiments where cells were pre-incubated with increasing concentrations of a P2X7-specific antagonist (AZD9056) prior to addition of the agonists ATP (C: 2.5 mM) or BzATP (D: 0.25 mM). Values are means \pm SD, n = 3.

BzATP-induced mitochondrial toxicity. Figure 6 shows a decrease of mitochondrial membrane potential ($\Delta\psi_m$) in BzATP-treated HEK-hP2X7 cells (but not in P2X7-deficient control cells) as visualized by a change from red to green fluorescent signals in the target cells. The shift in the emission spectrum of the cyanine dye JC-1 was monitored upon stimulation of HEK-hP2X7 cells for 1 h with elevated concentrations of BzATP (30 - 250 μ M). Valinomycin, a K^+ ionophore, served as a positive control.

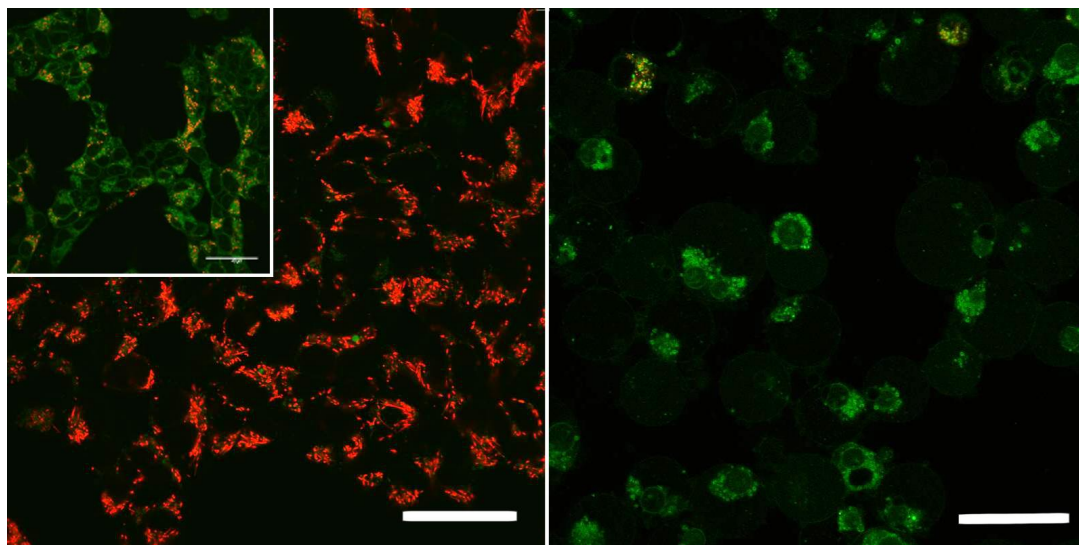


Figure 6: Induction of mitochondrial toxicity in HEK-hP2X7 cells. Parental HEK293 (left panel) and HEK-hP2X7 (right panel) cells were stimulated using 250 μ M BzATP. A decrease in mitochondrial membrane potential is indicated by a shift from red fluorescent signals to green fluorescent signals. Insert, left panel: 1 mM valinomycin was used as a positive control. Size of bars: 40 μ m.

Discussion

The present study investigated the effect of the P2X7-receptor agonists ATP and the metabolically stable analogue BzATP (Le Feuvre et al., 2003) on different P2X7-expressing cell lines. Real-time monitoring of the effects for the timescale of seconds was achieved electrophysiologically and for the timescales up to minutes and hours by using a novel cytosensor system. The effects were highly specific for P2X7 as demonstrated by the use of P2X7-deficient control cells and the selective P2X7-receptor antagonist AZD9056 (Bhattacharya et al., 2011; Elsby et al., 2011). Activation of P2X7 had a direct impact on membrane permeability for ions, intracellular calcium release, cell morphology (i.e. swelling), and cellular respiration and metabolism (Table 1). This induced oxidative and metabolic stress in target cells, ultimately leading to cellular toxicity and cell death.

In order to characterize the human P2X7 receptor, a recombinant HEK-hP2X7 cell line was prepared. Functionality of the recombinant human P2X7 receptor was confirmed using the YoPro1 uptake assay upon stimulation of the target cells with ATP. The antagonist AZD9056 blocked P2X7 receptors with an IC_{50} of 11.2 nM, indicating a high selectivity of the antagonist for the P2X7 receptor. This IC_{50} value is comparable to values determined

3.6. P2X7 RECEPTORS AND CELLULAR STRESS

previously for mouse and rat P2X7 receptors (in the order of 1 - 2 nM, data not shown). Thus, the YoPro1 uptake experiment allowed comparing and confirming the pharmacological properties of the P2X7 receptor in our study with those determined with methods traditionally used for studying the P2X7 receptor.

Table 1: Summary of agonist-induced and antagonist-induced effects mediated by the P2X7 receptor

Assay	Cells	Agonist ¹ [μ M]	P2X7-receptor antagonist ² [μ M]	IC ₅₀ or % inhibition
Peroxide release	Mononuclear blood cells	1000	0 - 25	3.0 μ M
YoPro1 uptake	HEK-hP2X7	3000	3.8×10^{-5} - 10	11.2 nM
Fluo-4-AM	Rat cortex	250	0.01 - 10	3.2 μ M
Patch-clamp	Mouse microglia	100	0.3 - 10	2.1 μ M 96% ³
Sensor system respiration	HEK-hP2X7	50	10	92%
Sensor system acidification	HEK-hP2X7	50	10	77%
Sensor system impedance	HEK-hP2X7	50	10	77%

¹ Assays for H₂O₂ release and YoPro1 uptake were performed with ATP, all other assays with BzATP;

² P2X7-receptor antagonist AZD9056; ³ at 10 μ M AZD9056.

Furthermore, the characteristics of human P2X7 receptor in this cell line were similar to those of rodent P2X7 receptor expressed by mouse microglia BV2 cells and rat cortical cells, as

demonstrated electrophysiologically. In these experiments, patch-clamp techniques were used to measure directly the flux of small, inorganic ions across the P2X7 channels.

Mouse microglia BV2 cells express both P2X7 and P2X4 receptors (Bernier et al., 2012). BzATP showed distinct effects on receptor activity, and the P2X7-receptor antagonist AZD9056 had a clear inhibitory effect ($IC_{50} = 2.1 \mu\text{M}$), which allows to attribute the effects to the P2X7 receptor.

Activation of the P2X7 receptor triggers Ca^{2+} influx and thus cell depolarization. We used primary rat cortical cells for these experiments because P2X-mediated Ca^{2+} influx cannot be determined in HEK293 cells due to co-activation of endogenously expressed purinergic P2Y receptors (He et al., 2003). As shown previously (Takenouchi et al., 2005; Donnelly-Roberts et al., 2009), exogenously triggered P2X7 activation led to an increased Ca^{2+} signal in the cells and was blocked by the P2X7 receptor antagonist AZD9056 ($IC_{50} = 3.2 \mu\text{M}$) with inhibitory affinity similar to that observed in patch-clamp experiments.

It is not possible to deduce a clear pathway from ATP-gated channel opening to the activation of cellular metabolism. However, small cations (e.g., Ca^{2+}) as well as larger molecules entering the cell upon P2X7-receptor pore opening are known to trigger further downstream effects such as interleukin-1 β release, MAPK activation, apoptosis, etc., and are therefore linked to cell signalling and cell death (Kukley et al., 2005; Ferrari et al., 2006). Hydrogen peroxide (H_2O_2), a metabolic side product of cell respiration, can be used as a marker for cellular toxicity (Giorgio et al., 2007). We measured H_2O_2 released in human mononuclear blood cells upon ATP treatment and found that ATP induced a concentration-dependent increase in H_2O_2 release, confirming previous reports (Skaper et al., 2006). It should be noted that the concentration-response curve for ATP induction of H_2O_2 release with an EC_{50} above 0.5 mM did not fit with the ATP sensitivity of the 12 known metabotropic P2Y receptors. Only the P2X7 receptor exhibits such low sensitivity to extracellular ATP (Coddou et al., 2011). In addition, assessment of the mass redistribution of HUVEC cells as a second, independent variable resulted in EC_{50} values above 900 μM . Morphological changes upon ATP treatment are an indication of ligand binding to the human P2X7 receptor (Pfeiffer et al., 2004) and can therefore be used to calculate EC_{50} values of activation. Based on the similarity of EC_{50} values, we hypothesized that the P2X7 receptor was involved in mediating the concentration-dependent increase in metabolic activity and morphological changes. Our hypothesis was supported by experiments with the antagonist AZD9056 that achieved

3.6. P2X7 RECEPTORS AND CELLULAR STRESS

concentration-dependent inhibition of ATP-induced H₂O₂ release in human mononuclear blood cells. Furthermore, AZD9056 (10 μM) showed no inhibition of signalling on P2 receptors in recombinant 1321N1 cells overexpressing P2X1, P2X2, P2X3, and P2X4 when measuring Ca²⁺ flux after ATP stimulation (data not shown). AZD9056 can therefore be considered to be selective for the P2X7 receptor, in contrast to other known antagonists of P2 receptors such as suramin and pyridoxal-phosphate-6-azophenyl-2',4'-disulphonic acid (PPADS) (Chessell et al., 1998; Ralevic and Burnstock, 1998). The concentration of BzATP used was one tenth (400 μM) of the concentration of ATP (4000 μM) and induced equal H₂O₂ release from human mononuclear blood cells at these concentrations. BzATP was chosen for these experiments since it is a specific agonist for both P2X4 and P2X7 receptors with only partial activity towards P2X1, P2X2, and P2X3 receptors (Coddou et al., 2011).

We subsequently used the HEK-hP2X7 cells overexpressing P2X7 to study changes in metabolic activity in real time by means of a cell-based cytosensor system. We were able to record simultaneously extracellular acidification as a marker for metabolic activity, oxygen consumption as a measure for cellular respiration, and impedance as a means to assess changes in cell morphology and adhesion. P2X7 receptors are co-localized with α-actin, β-actin, and the β2-integrin subunit, i.e., factors that determine changes in the cytoskeleton (Kim et al., 2001). Pfeiffer *et al.* previously described morphological changes in cells expressing P2X7 receptors when P2X7 agonists were present (Pfeiffer et al., 2004). We confirmed these morphological changes by measuring cellular impedance. In addition, HEK-hP2X7 cells exhibited concentration-dependent swelling upon treatment with BzATP, possibly reflecting the osmotic influx of water into the cells due to pore dilatation. We estimated the potency of BzATP to induced morphological changes using an enzyme kinetic model (EC₅₀ = 9.6 μM). Cellular respiration was maximally increased at 50 μM BzATP when compared with parental cells. Treatment with 100 μM BzATP, however, led to a sharp drop in respiration, which indicates mitochondrial toxicity (Gandelman et al., 2010). Strong amplification of metabolic activity under these conditions (monitored by an increase in extracellular acidification) clearly indicates a compensatory cellular response in terms of enhanced glycolysis. Reduction in cellular respiration was probably linked to both the formation of reactive oxygen species (Skaper et al., 2006) and activation of the apoptosis cascade (Hillman et al., 2003). The distinctness of stimulatory effects observed in the cytosensor system confirms that the effects mostly derived from the highly expressed P2X7 receptors rather than from other endogenously expressed P2 receptors in HEK293 cells.

These results are in line with our findings for H₂O₂ formation by mononuclear cells. Using the cytosensor system, we were able to determine simultaneously multiple variables of cellular metabolism, thus providing a more complete picture of how ATP affects cellular metabolism via the P2X7 receptor. All effects on cell morphology, mitochondrial respiration, and metabolic activity were induced at 50 μ M BzATP and were inhibited with 10 μ M AZD9056 at potencies between 77% and 92%. Because parental HEK293 cells did not respond to activation or inhibition, all effects observed in HEK-hP2X7 cells appear to be mediated by the human P2X7 receptor.

Prolonged stimulation of HEK-hP2X7 cells with ATP or BzATP led to cytotoxicity. This effect was also dose-dependent, was antagonised by AZD9056, and was not observed in P2X7-deficient HEK293 control cells. Our mechanistic studies revealed a collapse of mitochondrial membrane potential and mitochondrial integrity under these conditions. These findings are in line with our results from cytosensor studies and confirm that mitochondrial toxicity is indeed a trigger for P2X7-mediated cytotoxicity.

We conclude that an increase in membrane leakiness led to disturbance of mitochondrial membrane potential, mitochondrial toxicity, and oxidative stress. Metabolic activity by glycolysis increased as a compensatory mechanism due to the lack of energy generated by oxidative phosphorylation. Prolonged stimulation led to morphological changes and cytotoxicity. Further experiments are necessary to investigate the specificity of these effects and to clarify their role under normal or pathological conditions. Extracellular ATP has been shown to be a key player in triggering inflammatory processes, cellular stress, and apoptosis. Our investigations demonstrate that these processes are tightly linked to oxidative and metabolic activity, which we were able to monitor in real-time simultaneously with an additional confirmation of agonist-induced changes in cell morphology.

List of references

- Arbeloa J, Perez-Samartin A, Gottlieb M and Matute C (2012) P2X7 receptor blockade prevents ATP excitotoxicity in neurons and reduces brain damage after ischemia. *Neurobiol Dis* **45**:954-961.
- Armstrong JN, Brust TB, Lewis RG and MacVicar BA (2002) Activation of presynaptic P2X7-like receptors depresses mossy fiber-CA3 synaptic transmission through p38 mitogen-activated protein kinase. *J Neurosci* **22**:5938-5945.

- Bardoni R, Goldstein PA, Lee CJ, Gu JG and MacDermott AB (1997) ATP P2X receptors mediate fast synaptic transmission in the dorsal horn of the rat spinal cord. *J Neurosci* **17**:5297-5304.
- Beaucage KL, Xiao A, Pollmann SI, Grol MW, Beach RJ, Holdsworth DW, Sims SM, Darling MR and Dixon SJ (2013) Loss of P2X7 nucleotide receptor function leads to abnormal fat distribution in mice. *Purinergic Signal*.
- Beis I and Newsholme EA (1975) The contents of adenine nucleotides, phosphagens and some glycolytic intermediates in resting muscles from vertebrates and invertebrates. *Biochem J* **152**:23-32.
- Bernier LP, Ase AR, Boue-Grabot E and Seguela P (2012) P2X4 receptor channels form large noncytolytic pores in resting and activated microglia. *Glia* **60**:728-737.
- Bhattacharya A, Neff RA and Wickenden AD (2011) The physiology, pharmacology and future of P2X7 as an analgesic drug target: hype or promise? *Curr Pharm Biotechnol* **12**:1698-1706.
- Billingsley KG, Stern LE, Lowy AM, Kahlenberg MS and Thomas CR, Jr. (2004) Uncommon anal neoplasms. *Surg Oncol Clin N Am* **13**:375-388.
- Birch RE, Schwiebert EM, Peppiatt-Wildman CM and Wildman SS (2013) Emerging key roles for P2X receptors in the kidney. *Front Physiol* **4**:262.
- Buisman HP, Steinberg TH, Fischbarg J, Silverstein SC, Vogelzang SA, Ince C, Ypey DL and Leijh PC (1988) Extracellular ATP induces a large nonselective conductance in macrophage plasma membranes. *Proc Natl Acad Sci U S A* **85**:7988-7992.
- Burnstock G (2006) Historical review: ATP as a neurotransmitter. *Trends Pharmacol Sci* **27**:166-176.
- Chessell IP, Michel AD and Humphrey PP (1998) Effects of antagonists at the human recombinant P2X7 receptor. *Br J Pharmacol* **124**:1314-1320.
- Chrovian CC, Rech JC, Bhattacharya A and Letavic MA (2014) P2X7 Antagonists as Potential Therapeutic Agents for the Treatment of CNS Disorders. *Prog Med Chem* **53**:65-100.
- Coddou C, Yan Z, Obsil T, Huidobro-Toro JP and Stojilkovic SS (2011) Activation and regulation of purinergic P2X receptor channels. *Pharmacol Rev* **63**:641-683.
- Cosentino S, Banfi C, Burbiel JC, Luo H, Tremoli E and Abbracchio MP (2011) Cardiomyocyte death induced by ischemic/hypoxic stress is differentially affected by distinct purinergic P2 receptors. *J Cell Mol Med* **16**:1074-1084.

- Dawicki DD, Chatterjee D, Wyche J and Rounds S (1997) Extracellular ATP and adenosine cause apoptosis of pulmonary artery endothelial cells. *Am J Physiol* **273**:L485-494.
- Donnelly-Roberts DL, Namovic MT, Han P and Jarvis MF (2009) Mammalian P2X7 receptor pharmacology: comparison of recombinant mouse, rat and human P2X7 receptors. *Br J Pharmacol* **157**:1203-1214.
- Elsby R, Fox L, Stresser D, Layton M, Butters C, Sharma P, Smith V and Surry D (2011) In vitro risk assessment of AZD9056 perpetrating a transporter-mediated drug-drug interaction with methotrexate. *Eur J Pharm Sci* **43**:41-49.
- Ferrari D, Chiozzi P, Falzoni S, Dal Susino M, Collo G, Buell G and Di Virgilio F (1997) ATP-mediated cytotoxicity in microglial cells. *Neuropharmacology* **36**:1295-1301.
- Ferrari D, Pizzirani C, Adinolfi E, Lemoli RM, Curti A, Idzko M, Panther E and Di Virgilio F (2006) The P2X7 receptor: a key player in IL-1 processing and release. *J Immunol* **176**:3877-3883.
- Gandelman M, Peluffo H, Beckman JS, Cassina P and Barbeito L (2010) Extracellular ATP and the P2X7 receptor in astrocyte-mediated motor neuron death: implications for amyotrophic lateral sclerosis. *J Neuroinflammation* **7**:33.
- Giorgio M, Trinei M, Migliaccio E and Pelicci PG (2007) Hydrogen peroxide: a metabolic by-product or a common mediator of ageing signals? *Nat Rev Mol Cell Biol* **8**:722-728.
- Hamill OP, Marty A, Neher E, Sakmann B and Sigworth FJ (1981) Improved patch-clamp techniques for high-resolution current recording from cells and cell-free membrane patches. *Pflugers Arch* **391**:85-100.
- He M-L, Zemkova H, Koshimizu T-a, Tomic M and Stojilkovic SS (2003) Intracellular calcium measurements as a method in studies on activity of purinergic P2X receptor channels. *American Journal of Physiology - Cell Physiology* **285**:C467-C479.
- Hillman KA, Harada H, Chan CM, Townsend-Nicholson A, Moss SE, Miyamoto K, Suketa Y, Burnstock G, Unwin RJ and Dunn PM (2003) Chicken DT40 cells stably transfected with the rat P2X7 receptor ion channel: a system suitable for the study of purine receptor-mediated cell death. *Biochem Pharmacol* **66**:415-424.
- Keystone EC, Wang MM, Layton M, Hollis S and McInnes IB (2012) Clinical evaluation of the efficacy of the P2X7 purinergic receptor antagonist AZD9056 on the signs and symptoms of rheumatoid arthritis in patients with active disease despite treatment with methotrexate or sulphasalazine. *Ann Rheum Dis* **71**:1630-1635.

3.6. P2X7 RECEPTORS AND CELLULAR STRESS

- Kim M, Jiang LH, Wilson HL, North RA and Surprenant A (2001) Proteomic and functional evidence for a P2X7 receptor signalling complex. *EMBO J* **20**:6347-6358.
- Kukley M, Schwan M, Fredholm BB and Dietrich D (2005) The role of extracellular adenosine in regulating mossy fiber synaptic plasticity. *J Neurosci* **25**:2832-2837.
- Labasi JM, Petrushova N, Donovan C, McCurdy S, Lira P, Payette MM, Brissette W, Wicks JR, Audoly L and Gabel CA (2002) Absence of the P2X7 receptor alters leukocyte function and attenuates an inflammatory response. *J Immunol* **168**:6436-6445.
- Le Feuvre RA, Brough D, Touzani O and Rothwell NJ (2003) Role of P2X7 receptors in ischemic and excitotoxic brain injury in vivo. *J Cereb Blood Flow Metab* **23**:381-384.
- Michel AD, Chessell IP, Hibell AD, Simon J and Humphrey PP (1998) Identification and characterization of an endogenous P2X7 (P2Z) receptor in CHO-K1 cells. *Br J Pharmacol* **125**:1194-1201.
- North RA (2002) Molecular Physiology of P2X Receptors. *Physiological Reviews* **82**:1013-1067.
- Pankratov Y, Lalo U, Verkhratsky A and North RA (2006) Vesicular release of ATP at central synapses. *Pflugers Arch* **452**:589-597.
- Perelman A, Wachtel C, Cohen M, Haupt S, Shapiro H and Tzur A (2012) JC-1: alternative excitation wavelengths facilitate mitochondrial membrane potential cytometry. *Cell Death Dis* **3**:e430.
- Pfeiffer ZA, Aga M, Prabhu U, Watters JJ, Hall DJ and Bertics PJ (2004) The nucleotide receptor P2X7 mediates actin reorganization and membrane blebbing in RAW 264.7 macrophages via p38 MAP kinase and Rho. *J Leukoc Biol* **75**:1173-1182.
- Ralevic V and Burnstock G (1998) Receptors for purines and pyrimidines. *Pharmacol Rev* **50**:413-492.
- Rassendren F, Buell GN, Virginio C, Collo G, North RA and Surprenant A (1997) The permeabilizing ATP receptor, P2X7. Cloning and expression of a human cDNA. *J Biol Chem* **272**:5482-5486.
- Rousseau DL, Jr., Petrelli NJ and Kahlenberg MS (2004) Overview of anal cancer for the surgeon. *Surg Oncol Clin N Am* **13**:249-262.
- Ryu JK, Jantarotnai N, Serrano-Perez MC, McGeer PL and McLarnon JG (2011) Block of purinergic P2X7R inhibits tumor growth in a C6 glioma brain tumor animal model. *J Neuropathol Exp Neurol* **70**:13-22.
- Schroder K and Tschopp J (2010) The inflammasomes. *Cell* **140**:821-832.

- Seeland S, Torok M, Kettiger H, Treiber A, Hafner M and Huwyler J (2013) A cell-based, multiparametric sensor approach characterises drug-induced cytotoxicity in human liver HepG2 cells. *Toxicol In Vitro* **27**:1109-1120.
- Seeland S, Treiber A, Hafner M and Huwyler J (2011) On-line identification of P-glycoprotein substrates by monitoring of extracellular acidification and respiration rates in living cells. *Biochim Biophys Acta* **1808**:1827-1831.
- Sharnez R, Lathia J, Kahlenberg D, Prabhu S and Dekleva M (2004) In situ monitoring of soil dissolution dynamics: a rapid and simple method for determining worst-case soils for cleaning validation. *PDA J Pharm Sci Technol* **58**:203-214.
- Skaper SD, Facci L, Culbert AA, Evans NA, Chessell I, Davis JB and Richardson JC (2006) P2X(7) receptors on microglial cells mediate injury to cortical neurons in vitro. *Glia* **54**:234-242.
- Surprenant A (1996) Functional properties of native and cloned P2X receptors. *Ciba Found Symp* **198**:208-219; discussion 219-222.
- Takenouchi T, Ogihara K, Sato M and Kitani H (2005) Inhibitory effects of U73122 and U73343 on Ca²⁺ influx and pore formation induced by the activation of P2X7 nucleotide receptors in mouse microglial cell line. *Biochim Biophys Acta* **1726**:177-186.
- Takenouchi T, Sekiyama K, Sekigawa A, Fujita M, Waragai M, Sugama S, Iwamaru Y, Kitani H and Hashimoto M (2010) P2X7 receptor signaling pathway as a therapeutic target for neurodegenerative diseases. *Arch Immunol Ther Exp (Warsz)* **58**:91-96.
- Thedinga E, Kob A, Holst H, Keuer A, Drechsler S, Niendorf R, Baumann W, Freund I, Lehmann M and Ehret R (2007) Online monitoring of cell metabolism for studying pharmacodynamic effects. *Toxicol Appl Pharmacol* **220**:33-44.
- Volonte C, Amadio S, Cavaliere F, D'Ambrosi N, Vacca F and Bernardi G (2003) Extracellular ATP and neurodegeneration. *Curr Drug Targets CNS Neurol Disord* **2**:403-412.
- Volonte C, Apolloni S, Skaper SD and Burnstock G (2012) P2X7 receptors: channels, pores and more. *CNS Neurol Disord Drug Targets* **11**:705-721.
- Yoon MJ, Lee HJ, Kim JH and Kim DK (2006) Extracellular ATP induces apoptotic signaling in human monocyte leukemic cells, HL-60 and F-36P. *Arch Pharm Res* **29**:1032-1041.

Chapter 4

Discussion

The aim of this thesis was to investigate different aspects in nanotoxicology. Firstly, a suitable reference particle was chosen, synthesized, and characterized. An in-depth understanding of the synthesis allowed modifying the particles with regard to size, specific surface area, and surface groups. Hence, a library consisting of different SNPs was synthesized. The cytotoxic effect of each SNP was tested in three cell lines. The most interesting SNP was studied in depth regarding its hemolytic potential.

4.1 The importance of characterized material

The literature described a size-dependent toxicity for SNPs [81]. Hence, the first parameter of interest was the size. Could a size dependent toxicity be observed in the size range of DDS? The second parameter was the specific surface area. By keeping the size constant, mesopores were introduced into the SNPs to enhance their specific surface area. It has been reported that the specific surface area can influence toxicity in an indirect manner, namely by depleting nutrients from the medium [56]. The third parameter was the surface charge. It was reported that a high, especially positive charge density results in cytotoxicity [27]. This is related to the electrostatic interaction with the cell membrane, which carries an overall negative charge [82].

As described earlier, different synthesis methods exist to obtain SNPs. For the SNPs explored in this thesis, the basic growth approach ("Stöber" method) has shown to be the most reproducible one. Apart from the reproducibility, particles synthesized in-house have a known thermal history. This knowledge is important since it could be the reason for contradictory outcome of SNP toxicity in the literature [37]. Of course, there are other factors influencing outcomes, such as the choice of the cell line and the inclusion or abduction of serum proteins in an *in vitro* assay.

Appropriate protocols to observe critical steps in the synthesis (eg. drying or removal of surfactant) with critical steps which could alter the physico-chemical properties of a nanoparticle [48]. This applies not only to SNPs, but for any nanoparticles (synthesized in house or obtained from a commercial supplier): trace metals from the synthesis, additives to maintain colloidal stability, and the synthesis history of a nanoparticle can influence the toxicity profile. Trace metals as yttrium caused toxicity of carbon nanotubes [83]. Surfactants added to maintain colloidal stability may exert three distinct pitfalls. The first one is that adsorbed surfactants change the appearance

of the particle (own experience and [18]). The second one is the toxicity of the surfactant itself and the third is that upon dilution of the stock suspension, the surfactant also gets diluted. This then results in agglomeration of nanoparticles. Dispersion protocols can also influence cytotoxicity. This has been shown by Wick, where the dispersion protocol lead to totally different outcomes for carbon nanotube cytotoxicity [84]. The third one is the cytotoxicity of the dispersant. With the SNPs in house synthesis and characterization, several of these pitfalls were minimized.

As mentioned in the introduction, degradation of nanoparticles and release of metal ions or trace metals could lead to cytotoxicity. Mesoporous SNPs also degrade [85], so the effect of the degradation products was tested (data not shown). The degradation products showed no cytotoxicity. This is in agreement with previous published data [86]. The degradation kinetic was explored in cell-free environment and with in cells using live-cell imaging. This fast degradation process of mesoporous SNPs was responsible for the absence of hemolysis. Overall, several pitfalls can be excluded when synthesizing own nanoparticles, while others (degradation and toxicity of degraded products for instance) always need to be tested.

4.2 Experimental considerations

4.2.1 Choice of assay

As described in the introduction, numerous assays are available, starting from live-dead assays like trypan blue staining to highly sophisticated assays to localize the site of production of ROS [87]. This high amount of assays leaves numerous of choices in what we want to observe. Before choosing an assay, it is important to consider (a) the endpoints, (b) the time frame of the investigated endpoint, (c) appropriate controls. As mentioned in the introduction, common nanotoxicity studies mainly address viability, genotoxicity, inflammation, and oxidative stress.

Here, we have chosen three assays to screen our SNPs due to the following reasons: The MTT was chosen for viability, since it is measuring an important endpoint. For oxidative stress we have chosen the DCFH-DA since its results show if oxidative stress is present or not. The generation of ROS has been described to be a main contributor for nanotoxicity [4]. With minor modifications, this assay also allows measuring the oxidative stress in cell-free environment. The hemolysis assay was chosen to study the interaction between negatively charged SNPs and the cellular membrane exclusively, since RBC lack of the endocytic machinery.

4.2.2 Cell lines and cell density

The literature has described that not all cell-lines are equally sensitive towards nano-mediated toxicity. Moreover there is no reliable evidence that phagocytic cells are more sensitive. A recent

4.2. EXPERIMENTAL CONSIDERATIONS

study has compared 23 nanoparticles in 10 cell lines and found that the same nanoparticle exerted various responses. This was dependent on the cell line and the endpoint chosen [61].

In this thesis, three cell lines were used. They differed in their mechanisms of uptake, where the leukemic monocytes (human) (THP-1) is able to take up bigger nanoparticles (see review in section 3.1). Liver hepatocellular cells (human) (HepG2) are not able of phagocytosis, but still able of incorporating nanoparticles up to a certain size. The third cell line is fresh sheep RBC, which totally lack an endocytic machinery. Another difference is their origin. HepG2 cells are resident cells in the liver and not involved in the first line defense. THP-1 cells were chosen because they play a main role in the first line defense mechanism in our body. Sheep RBC are constituents of the blood and come into contact with nanoparticles immediately upon i.v. injection.

Cell density for nanotoxicological studies play a key role, as depicted in Figure 4.1. Here, different

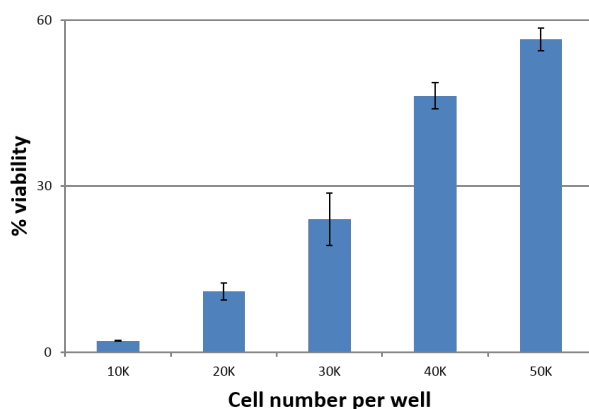


Figure 4.1: Viability decrease is cell-number dependent. HepG2 cells were seeded at various cell densities (expressed as numbers per well) and incubated for 24h with positively charged polystyrene beads at 60 $\mu\text{g}/\text{ml}$.

cells per well were seeded and treated with the same concentration of highly positively charged polystyrene beads at 60 $\mu\text{g}/\text{mL}$. The viability is plotted against the cells seeded per well. The plot shows the vast difference in cell viability, based solely on the amounts of seeded cells. Ideally, toxicity assays should be performed, when the cells are growing in the log-phase. A confluence of 70% is normally recommended. The percentage implies that for each cell line the amount of cells needs to be adjusted to reach this value. Throughout this thesis, experiments were conducted at 70% confluence.

4.2.3 Plasma proteins

The interaction of nanoparticles with the soft surfaces of biological systems (i.e. plasma membrane) plays a key role in their beneficial (medical) and adverse (toxicological) functions. The first

encounter of a nanoparticle with a biological constituent is most probably the preparation of the dispersion for cell-based experiments. Here, serum proteins adsorb to the particle, dependent of size, surface charge, wettability, and other factors [15, 80, 88, 89]. Hence, a biological identity, a so-called protein corona is formed. It has been shown that upon serum addition some nanoparticles start to agglomerate, whereas other nanoparticles de-agglomerate [90]. It is therefore important to study the suspension stability (or simply the behavior of the suspension) prior to cell-based assays, where proteins are added. Some researchers refrained from using serum in assays and thus retaining the native surface of the nanoparticle. It was shown that the protein corona adds a "protection" to the nanoparticles, rendering them less cytotoxic [91, 92]. Furthermore, the protein corona can modulate the uptake pathway into a specific cell and the subsequent intracellular distribution [93, 94]. In this work, we have decided to use serum for the MTT assay and the DCFH-DA assay, since it is closer to the *in vivo* situation (for details see section 3.1). For hemolysis, we refrained to use serum, since the interaction of SNPs surface groups was the main interest.

4.2.4 Interference

In the case of nanoparticles, not only a positive control and a negative control need to be considered in each assay. It has been described in the literature that numerous particles, especially carbonaceous materials interfere with the assay readout and therefore causing either false-positive or false-negative results [95]. Essentially, three interferences can be caused by nanoparticles when using a colorimetric or fluorimetric assay, as depicted in Figure 4.2. The first interference is of op-

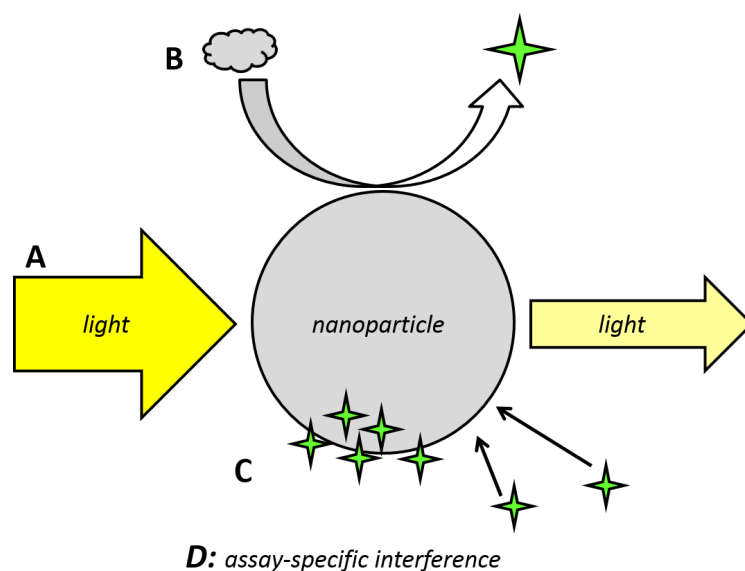


Figure 4.2: Interferences of nanoparticles with reporters. A: optical interference, B: catalytic interference, C: adsorptive interference, D: assay-specific interference.

4.2. EXPERIMENTAL CONSIDERATIONS

tical nature (denoted as A): if the particles are interfering with the measured wavelength (may be the case for some gold- or iron nanoparticles), this amplifies the measured outcome. Even without an optical property at the respective wavelength, the suspension can increase the absorbance by reducing the transmittance non-specifically. This interference is mostly present for black material or for any material at higher concentrations [61, 95]. In contrary, if there is a quenching of fluorescence, the result is underestimated. Optical interference can be easily controlled by subtracting a background from the measured values ("blank control"). However, if the particles interfere strongly, additional washing steps prior to the optical measurement may reduce this interference. Some researchers propose to centrifuge their samples, however toxicity assays are performed in a 96-well plate. The centrifugation speed for 96-well plates is very limited and it is unlikely to bring forth a particle-free supernatant.

Interference B is a catalytic interference, where the high specific surface area (and therefore the high surface reactivity) can convert a substrate in the absence of cells. Hence, an overestimation of the measured outcome is the consequence. This means that the outcome (oxidative stress for example) generated by the cells is overestimated, since some signal is coming from the dye solely converted by the catalytic surface of a nanoparticle. This effect has been described for multi-walled carbon nanotubes and the DCFH-DA assay, where in absence of cells, a highly fluorescent signal was detected. Estimating this interference in a cell-free environment, the dye can be first deacetylated and then the conversion from non-fluorescent to fluorescent dye is measured in presence and absence of the nanoparticles [96]. Interference C is explained by the surface characteristics of the nanoparticle. Numerous substances can adsorb to the surface of particles and therefore not contributing to a final readout [97]. Adsorptive interference can be tested by incubating the nanoparticles with the reporter, subsequent centrifugation and readout of the supernatant. Each nanoparticle needs to be tested for these interferences separately. Already size or surface group change can alter the behavior in adsorptive, optical, and catalytic interferences. Besides these three interferences, specific interferences for each assay still need to be kept in mind, which is denoted as D in Figure 4.2. One of them is the exocytosis of formazan crystals (see publication in section 3.2).

4.2.5 Mechanistic studies

In this thesis, the underlying mechanism of hemolysis caused by SNPs was studied in depth with the aid of biophysical methods. The interactions investigated were those with bare nanoparticles (i.e. not coated with proteins) and RBC.

The proposed mechanism of hemolysis in literature suggests that an electrostatic interaction of the silanols (deprotonated at pH 7.4 and hence negatively charged) with the quaternary ammonia of the choline head group is responsible for hemolysis [36]. Therefore, a hemolytic SNP was chosen

to elucidate its mechanism of toxicity towards RBC using a biophysical approach. This involved methods such as dye leakage assay with variant model membranes (according to the natural composition of RBC) to study the influence of the membrane lipid components [98]. Furthermore, ITC was used to measure the enthalpy of the interaction of model membranes and hemolytic and non-hemolytic SNPs. In a last step, solid state nuclear magnetic resonance (ssNMR) experiments were conducted to see where the interaction of the phospholipid and the surface silanols are located (tail, phosphorus region, headgroup).

The biophysical investigation suggests, that the interaction between surface silanols and phospholipids plays a minor role in the hemolytic effect. ITC results showed no electrostatic interaction between nanoparticles and lipid membrane and additional data obtained from DLS and ssNMR suggest a rather adsorptive process. This adsorptive process may result in membrane wrapping or forming of smaller lipid vesicles of 100 nm size (see chapter 3.4 for detailed discussion). It is important to point out, that the composition of the RBC membrane differs from other cells [82], so a translation from hemolysis to results obtained from the MTT with other cells is not possible. Furthermore, the viability decrease may be due to either internalized SNPs or adsorption to the surface. This remains to be further elucidated. Overall, further research, especially in the field of membrane-protein unfolding may shed light to this underlying mechanism. More research on the membrane protein-SNP interaction would complete the picture how and to which extents the particle-bilayer and particle-protein interaction lead to hemolysis.

4.3 Translation of knowledge to small molecule toxicity

Table 1.1. from the introduction displays the main differences for small molecules and nanoparticles, i.e. size, motion forces, physico-chemical characteristics, and interaction with cells. This table further strengthens the need of considering an own nanoparticle-related toxicological science.

Chemical properties matter, physical properties matter, and the biological system interaction matters. These three key factors have been explored in this thesis, as depicted in Figure 1.5.

Chapter 5

Conclusion and Outlook

In this thesis, silica nanoparticles were tested in three different assays. A concentration-, time-, surface group-dependent, and specific surface area-dependent cytotoxicity was observed. It was shown that not one exclusive physico-chemical parameter was responsible for viability decrease. No oxidative stress was detected in the given setup. Introduction of primary amines into the SNPs reduced the hemolytic effect of the SNPs, irrespective of their size or specific surface area. All negatively charged SNPs caused hemolysis, except the small mesoporous SNPs, because of their fast degradation in aqueous solutions.

For a hemolytic SNP, biophysical approaches were chosen to obtain insight into the mechanism of hemolysis. Our findings suggest that the interaction of surface silanols and a model membrane composed of phosphatidyl choline is rather low. ITC data showed no significant change in enthalpy at different temperatures and salt concentrations, which would be present for electrostatic interactions. Also ssNMR data indicated that an interaction with the choline headgroup is not prevalent, but the phosphorus spectrum pointed towards formation of faster (i.e. smaller) tumbling species. The presence of these species could be confirmed by flow cytometry. Even though the effects measured were rather small, there was a clear difference between hemolytic and non-hemolytic SNPs. Hemolysis may be partly explained by our data, however, more research needs to be conducted, also involving membrane proteins and osmotic pressure.

Combining the gained knowledge from the nanotoxicological studies, the mechanistic studies on hemolysis and the cytotoxicity studies for small molecules, it is of utmost importance to distinguish between these two domains in toxicology. Small molecule toxicity has to address other concerns than nanotoxicology prior to a cell experiment. Other parameters mitigate toxicity: small molecules may interact very specifically with a receptor or transporter, whereas nanoparticles may exert their toxicity by unfolding a protein or disturbing the membrane. Mechanistic studies for nanoparticles are challenging, because the effect on a certain receptor may be delayed and not readily detectable. Furthermore, particle for positive controls in mechanistic pathways only exist partially. Hence, these two classes cannot be compared. The bulk material (microparticles) does not exert the quantum effects as observed for nanoparticles. This transitional nano-zone remains a challenge for safety assessment.

Particle modification

- For toxicological studies, more SNPs with different shapes could be included. The density of the surface groups can be varied with the post-grafting synthesis approach. With a step-wise change in surface density of various groups, a cytotoxicity threshold may be established.
- For drug delivery, more complex silane precursors can be introduced to the SNPs to render them biocompatible. Advanced SNPs, *release-on-demand* systems, could be explored to reduce cytotoxicity (side effects) of their cargo.

Advanced *in vitro* models

- Co-cultures, where two or even more different cell types are cultivated in close proximity, might give insight in how the communication between cell types is influenced by nanoparticles. This approach has already been shown to work for lung co-cultures, and the idea should be translated to other organs as well.
- If SNPs are used as DDS, their uptake, distribution, and degradation should be studied under flow conditions, where shear forces influence strongly the exposure of the particles to the cells. With this flow approach, a more realistic scenario of both, therapeutic efficacy and toxicology (degradation or exocytosis) can be studied. Taken together, these data and the data from co-culture, display a better prediction as with 2D cell culture models.
- Expand the array of *in vitro* assays to assure biocompatibility. This may include testing of hemocompatibility, the ability of SNPs to cross barriers like the blood brain barrier or the gut wall.

Upcoming mechanistic approaches

- The interactions of SNPs with model membranes are rather weak as shown in this thesis. One reason could be that the model does not take the osmotic influences in account, or that intra- and extracellular ions play a pivotal role. Another important aspect is to study the mechanistic approach of interaction with SNPs with membrane proteins. Here, mass spectrometry and labeling of certain amino acids could give insight into this process in more detail.

In vivo strategies for nanosafety

- Not many *in vivo* studies involving nanoparticles are available. Most of the studies investigate the effect of a high single dose in *in vivo* studies, with the aim to show the efficiency

of accumulation in a tumor. However, biodistribution studies upon multiple injections in subtoxic dosages are of strong interest for drug delivery systems, since patients may need multiple injections over longer time periods up to several years. Additionally, chronic inflammation in the vasculature strongly influences the tolerance of such a carrier.

- *In vivo* studies that investigate the biodistribution by varying the route of entry. Oral vs. inhalation or oral vs. i.v injection give information about the organs, where most of the SNPs are distributed to. Hence, safety should address the degradation of the SNPs in these organs.

Chapter 6

Appendix

6.1 Bibliography

Bibliography

- [1] Andrea Haase, Jutta Tentschert, and Andreas Luch. Nanomaterials: a challenge for toxicological risk assessment? *EXS*, 101:219–250, 2012.
- [2] Richard Feynman. There's plenty of room at the bottom. *Caltech Eng Sci*, pages 22–26, 1960.
- [3] Harald F Krug and Peter Wick. Nanotoxicology: An interdisciplinary challenge. *Angewandte Chemie International Edition*, 50(6):1260–1278, February 2011.
- [4] Andre Nel, Tian Xia, Lutz Maedler, and Ning Li. Toxic potential of materials at the nanolevel. *Science*, 311(5761):622–627, February 2006.
- [5] Zhengyong Zhang, Lingjia Xu, Huixiang Li, and Jilie Kong. Wavelength-tunable luminescent gold nanoparticles generated by cooperation ligand exchange and their potential application in cellular imaging. *RSC Advances*, 3(1):59–63, November 2012.
- [6] Simon P. Boilard, Paul R. Amyotte, Faisal I. Khan, Ashok G. Dastidar, and Rolf K. Eckhoff. Explosibility of micron- and nano-size titanium powders. *Journal of Loss Prevention in the Process Industries*, 26(6):1646–1654, November 2013.
- [7] Melanie Auffan, Jerome Rose, Jean-Yves Bottero, Gregory V. Lowry, Jean-Pierre Jolivet, and Mark R. Wiesner. Towards a definition of inorganic nanoparticles from an environmental, health and safety perspective. *Nature Nanotechnology*, 4(10):634–641, October 2009.
- [8] Chia-Hao M. Chuang, Patrick R. Brown, Vladimir Bulovic, and Mounqi G. Bawendi. Improved performance and stability in quantum dot solar cells through band alignment engineering. *Nature Materials*, 13(4):796–801, August 2014.
- [9] Susana Patricia Egusquiaguirre, Manuela Igartua, Rosa Maria Hernandez, and Jose Luis Pedraz. Nanoparticle delivery systems for cancer therapy: advances in clinical and preclinical research. *Clinical & Translational Oncology: Official Publication of the Federation of Spanish Oncology Societies and of the National Cancer Institute of Mexico*, 14(2):83–93, February 2012.
- [10] Jessica M. Rosenholm, Emilia Peuhu, John E. Eriksson, Cecilia Sahlgren, and Mika Lindén. Targeted intracellular delivery of hydrophobic agents using mesoporous hybrid silica nanoparticles as carrier systems. *Nano Letters*, 9(9):3308–3311, September 2009.
- [11] Hooisweng Ow, Daniel R. Larson, Mamta Srivastava, Barbara A. Baird, Watt W. Webb, and Ulrich Wiesner. Bright and stable core-shell fluorescent silica nanoparticles. *Nano Letters*, 5(1):113–117, January 2005.

- [12] Novel cancer-targeting investigational nanoparticle receives FDA IND approval for first-in-human trial, <http://www.mskcc.org/pressroom/press/novel-targeting-investigational-nanoparticle-receives-fda-ind-approval-first-human-trial>, accessed 14.10.2014.
- [13] Christopher A Lipinski, Franco Lombardo, Beryl W Dominy, and Paul J Feeney. Experimental and computational approaches to estimate solubility and permeability in drug discovery and development settings. *Advanced Drug Delivery Reviews*, 46(1-3):3–26, March 2001.
- [14] Wim H De Jong, Werner I Hagens, Petra Krystek, Marina C Burger, Adrienne J A M Sips, and Robert E Geertsma. Particle size-dependent organ distribution of gold nanoparticles after intravenous administration. *Biomaterials*, 29(12):1912–1919, April 2008.
- [15] Helene Kettiger, Angela Schipanski, Peter Wick, and Joerg Huwyler. Engineered nanomaterial uptake and tissue distribution: from cell to organism. *International journal of nanomedicine*, 8:3255–3269, 2013.
- [16] Susana Patricia Egusquiaguirre, Manuela Igartua, Rosa Maria Hernandez, and Jose Luis Pedraz. Nanoparticle delivery systems for cancer therapy: advances in clinical and preclinical research. *Clinical & Translational Oncology: Official Publication of the Federation of Spanish Oncology Societies and of the National Cancer Institute of Mexico*, 14(2):83–93, February 2012.
- [17] Ernest Hodgson. *A Textbook of Modern Toxicology*. John Wiley & Sons, April 2004.
- [18] Francoise Schrurs and Dominique Lison. Focusing the research efforts. *Nature Nanotechnology*, 7(9):546–548, September 2012.
- [19] Hidenori Matsuzaki, Megumi Maeda, Suni Lee, Yasumitsu Nishimura, Naoko Kumagai-Takei, Hiroaki Hayashi, Shoko Yamamoto, Tamayo Hatayama, Yoko Kojima, Rika Tabata, Takumi Kishimoto, Junichi Hiratsuka, and Takemi Otsuki. Asbestos-induced cellular and molecular alteration of immunocompetent cells and their relationship with chronic inflammation and carcinogenesis. *BioMed Research International*, 2012:e492608, February 2012.
- [20] Ken Donaldson and Craig A. Poland. Nanotoxicity: challenging the myth of nano-specific toxicity. *Current Opinion in Biotechnology*, 24(4):724–734, August 2013.
- [21] Yu Pan, Sabine Neuss, Annika Leifert, Monika Fischler, Fei Wen, Ulrich Simon, Guenter Schmid, Wolfgang Brandau, and Willi Jahnen-Dechent. Size-dependent cytotoxicity of gold nanoparticles. *Small*, 3(11):1941–1949, November 2007.
- [22] Anda R. Gliga, Sara Skoglund, Inger Odnevall Wallinder, Bengt Fadeel, and Hanna L. Karlsson. Size-dependent cytotoxicity of silver nanoparticles in human lung cells: the role of cellular uptake, agglomeration and ag release. *Particle and Fibre Toxicology*, 11(1):11, February 2014.

- [23] Li Shang, Karin Nienhaus, and Gerd U. Nienhaus. Engineered nanoparticles interacting with cells: size matters. *Journal of Nanobiotechnology*, 12(1):5, February 2014.
- [24] Andreas M. Studer, Ludwig K. Limbach, Luu Van Duc, Frank Krumeich, Evangelos K. Athanassiou, Lukas C. Gerber, Holger Moch, and Wendelin J. Stark. Nanoparticle cytotoxicity depends on intracellular solubility: Comparison of stabilized copper metal and degradable copper oxide nanoparticles. *Toxicology Letters*, 197(3):169–174, September 2010.
- [25] Renata Behra, Laura Sigg, Martin J. D. Clift, Fabian Herzog, Matteo Minghetti, Blair Johnston, Alke Petri-Fink, and Barbara Rothen-Rutishauser. Bioavailability of silver nanoparticles and ions: from a chemical and biochemical perspective. *Journal of the Royal Society, Interface / the Royal Society*, 10(87):20130396, October 2013.
- [26] Tiantian Wang, Jing Bai, Xiue Jiang, and G Ulrich Nienhaus. Cellular uptake of nanoparticles by membrane penetration: a study combining confocal microscopy with FTIR spectroelectrochemistry. *ACS nano*, 6(2):1251–1259, February 2012.
- [27] Bogdan I. Florea, Clare Meaney, Hans E. Junginger, and Gerrit Borchard. Transfection efficiency and toxicity of polyethylenimine in differentiated calu-3 and nondifferentiated COS-1 cell cultures. *AAPS pharmSci*, 4(3):E12, 2002.
- [28] Ying Liu, Yuliang Zhao, Baoyun Sun, and Chunying Chen. Understanding the toxicity of carbon nanotubes. *Accounts of Chemical Research*, 46(3):702–713, March 2013.
- [29] Dorota Napierska, Leen CJ Thomassen, Dominique Lison, Johan A Martens, and Peter H Hoet. The nanosilica hazard: another variable entity. *Particle and Fibre Toxicology*, 7:39, December 2010.
- [30] Chan Jin, Ying Tang, F. Guang Yang, X. Lin Li, Shan Xu, X. Yan Fan, Y. Ying Huang, and Y. Ji Yang. Cellular toxicity of TiO₂ nanoparticles in anatase and rutile crystal phase. *Biological Trace Element Research*, 141(1-3):3–15, June 2011.
- [31] Francois Huaux. New developments in the understanding of immunology in silicosis. *Current Opinion in Allergy and Clinical Immunology*, 7(2):168–173, April 2007.
- [32] Bice Fubini and Andrea Hubbard. Reactive oxygen species (ROS) and reactive nitrogen species (RNS) generation by silica in inflammation and fibrosis. *Free Radical Biology & Medicine*, 34(12):1507–1516, June 2003.
- [33] Tian Yu, Alexander Malugin, and Hamidreza Ghandehari. Impact of silica nanoparticle design on cellular toxicity and hemolytic activity. *ACS Nano*, 5(7):5717–5728, 2011.

- [34] Syed K. Sohaebuddin, Paul T. Thevenot, David Baker, John W. Eaton, and Liping Tang. Nano-material cytotoxicity is composition, size, and cell type dependent. *Particle and Fibre Toxicology*, 7(1):22, August 2010.
- [35] Margriet V.D.Z. Park, Wijtske Annema, Anna Salvati, Anna Lesniak, Andreas Elsaesser, Clifford Barnes, George McKerr, C. Vyvyan Howard, Iseult Lynch, Kenneth A. Dawson, Aldert H. Piersma, and Wim H. de Jong. In vitro developmental toxicity test detects inhibition of stem cell differentiation by silica nanoparticles. *Toxicology and Applied Pharmacology*, 240(1):108–116, October 2009.
- [36] Igor I. Slowing, Chia-Wen Wu, Juan L. Vivero-Escoto, and Victor S.-Y. Lin. Mesoporous silica nanoparticles for reducing hemolytic activity towards mammalian red blood cells. *Small*, 5(1):57–62, 2009.
- [37] Haiyuan Zhang, Darren R Dunphy, Xingmao Jiang, Huan Meng, Bingbing Sun, Derrick Tarn, Min Xue, Xiang Wang, Sijie Lin, Zhaoxia Ji, Ruibin Li, Fred L Garcia, Jing Yang, Martin L Kirk, Tian Xia, Jeffrey I Zink, Andre Nel, and C Jeffrey Brinker. Processing pathway dependence of amorphous silica nanoparticle toxicity: colloidal vs pyrolytic. *Journal of the American Chemical Society*, 134(38):15790–15804, September 2012.
- [38] Hooisweng Ow, Daniel R. Larson, Mamta Srivastava, Barbara A. Baird, Watt W. Webb, and Ulrich Wiesner. Bright and stable core-shell fluorescent silica nanoparticles. *Nano Letters*, 5(1):113–117, January 2005.
- [39] Qianjun He, Zhiwen Zhang, Yu Gao, Jianlin Shi, and Yaping Li. Intracellular localization and cytotoxicity of spherical mesoporous silica nano- and microparticles. *Small*, 5(23):2722–2729, December 2009.
- [40] Ralph K. Iler. *The Chemistry of Silica: Solubility, Polymerization, Colloid and Surface Properties and Biochemistry of Silica*. Wiley, 1979.
- [41] Werner Stoeber, Arthur Fink, and Ernst Bohn. Controlled growth of monodisperse silica spheres in the micron size range. *Journal of Colloid and Interface Science*, 26(1):62–69, January 1968.
- [42] Zeid A. Allothman. A review: Fundamental aspects of silicate mesoporous. *Materials*, 5(12):2874–2902, December 2012.
- [43] Didem Sen Karaman, Diti Desai, Rajendran Senthilkumar, Emma M. Johansson, Natalie Ratts, Magnus Oden, John E. Eriksson, Cecilia Sahlgren, Diana M. Toivola, and Jessica M. Rosenholm. Shape engineering vs organic modification of inorganic nanoparticles as a tool for enhancing cellular internalization. *Nanoscale Research Letters*, 7(1):358, 2012.

- [44] Feng Zhao, Ying Zhao, Ying Liu, Xueling Chang, Chunying Chen, and Yuliang Zhao. Cellular uptake, intracellular trafficking, and cytotoxicity of nanomaterials. *Small*, 7(10):1322–1337, May 2011.
- [45] Fangqiong Tang, Linlin Li, and Dong Chen. Mesoporous silica nanoparticles: synthesis, biocompatibility and drug delivery. *Advanced materials*, 24(12):1504–1534, March 2012.
- [46] null Schacht, null Huo, null Voigt-Martin, null Stucky, and null Schuth. Oil-water interface templating of mesoporous macroscale structures. *Science*, 273(5276):768–771, August 1996.
- [47] Lu Han, Hao Wei, Bo Tu, and Dongyuan Zhao. A facile one-pot synthesis of uniform core-shell silver nanoparticle@mesoporous silica nanospheres. *Chemical Communications*, 47(30):8536–8538, July 2011.
- [48] L.T. Zhuravlev. The surface chemistry of amorphous silica. zhuravlev model. *Colloids and Surfaces A: Physicochemical and Engineering Aspects*, 173(1-3):1–38, November 2000.
- [49] Alok Dhawan, Vyom Sharma, and Devendra Parmar. Nanomaterials: A challenge for toxicologists. *Nanotoxicology*, 3(1):1–9, January 2009.
- [50] Emilia Izak-Nau, Matthias Voetz, Stefanie Eiden, Albert Duschl, and Victor F. Puntes. Altered characteristics of silica nanoparticles in bovine and human serum: the importance of nanomaterial characterization prior to its toxicological evaluation. *Particle and Fibre Toxicology*, 10(1):1–12, December 2013.
- [51] Leen C. J. Thomassen, Alexander Aerts, Virginie Rabolli, Dominique Lison, Laetitia Gonzalez, Micheline Kirsch-Volders, Dorota Napierska, Peter H. Hoet, Christine E. A. Kirschhock, and Johan A. Martens. Synthesis and characterization of stable monodisperse silica nanoparticle sols for in vitro cytotoxicity testing. *Langmuir*, 26(1):328–335, 2009.
- [52] Christie M. Sayes, Kenneth L. Reed, and David B. Warheit. Assessing toxicity of fine and nanoparticles: Comparing in vitro measurements to in vivo pulmonary toxicity profiles. *Toxicological Sciences*, 97(1):163–180, May 2007.
- [53] Nicole Hondow, Rik Brydson, Peiyi Wang, Mark D. Holton, M. Rowan Brown, Paul Rees, Huw D. Summers, and Andy Brown. Quantitative characterization of nanoparticle agglomeration within biological media. *Journal of Nanoparticle Research*, 14(7):1–15, July 2012.
- [54] Christina Brandenberger, Martin JD Clift, Dimitri Vanhecke, Christian Muehlfeld, Vicki Stone, Peter Gehr, and Barbara Rothen-Rutishauser. Intracellular imaging of nanoparticles: Is it an elemental mistake to believe what you see? *Particle and Fibre Toxicology*, 7(1):15, June 2010.

- [55] Alok Dhawan and Vyom Sharma. Toxicity assessment of nanomaterials: methods and challenges. *Analytical and Bioanalytical Chemistry*, 398(2):589–605, September 2010.
- [56] Lin Guo, Annette Von Dem Bussche, Michelle Buechner, Aihui Yan, Agnes B. Kane, and Robert H. Hurt. Adsorption of essential micronutrients by carbon nanotubes and the implications for nanotoxicity testing. *Small*, 4(6):721–727, June 2008.
- [57] Kaihua Chen, Jixi Zhang, and Hongchen Gu. Dissolution from inside: a unique degradation behaviour of core-shell magnetic mesoporous silica nanoparticles and the effect of polyethyleneimine coating. *Journal of Materials Chemistry*, 22(41):22005–22012, October 2012.
- [58] Cristiane X Galhardo and Jorge C Masini. Spectrophotometric determination of phosphate and silicate by sequential injection using molybdenum blue chemistry. *Analytica Chimica Acta*, 417(2):191–200, July 2000.
- [59] Justin G. Teeguarden, Paul M. Hinderliter, Galya Orr, Brian D. Thrall, and Joel G. Pounds. Particokinetics in vitro: Dosimetry considerations for in vitro nanoparticle toxicity assessments. *Toxicological Sciences*, 95(2):300–312, February 2007.
- [60] Paul M. Hinderliter, Kevin R. Minard, Galya Orr, William B. Chrisler, Brian D. Thrall, Joel G. Pounds, and Justin G. Teeguarden. ISDD: A computational model of particle sedimentation, diffusion and target cell dosimetry for in vitro toxicity studies. *Particle and Fibre Toxicology*, 7(1):36, 2010.
- [61] Alexandra Kroll, Christian Dierker, Christina Rommel, Daniela Hahn, Wendel Wohlleben, Christian Schulze-Isfort, Christian Goebbert, Matthias Voetz, Ferdinand Hardinghaus, and Juergen Schnekenburger. Cytotoxicity screening of 23 engineered nanomaterials using a test matrix of ten cell lines and three different assays. *Particle and Fibre Toxicology*, 8:9, 2011.
- [62] Tim Mosmann. Rapid colorimetric assay for cellular growth and survival: application to proliferation and cytotoxicity assays. *Journal of Immunological Methods*, 65(1-2):55–63, December 1983.
- [63] Michael Berridge, A.S. Tan, Kathy McCoy, and Rui Wang. The biochemical and cellular basis of cell proliferation assays that use tetrazolium salts. *Biochemica*, 4:14–19, 1996.
- [64] Francis Ka-Ming Chan, Kenta Moriwaki, and Maria Jose De Rosa. Detection of necrosis by release of lactate dehydrogenase (LDH) activity. *Methods in molecular biology*, 979:65–70, 2013.
- [65] Aja M. Rieger, Kimberly L. Nelson, Jeffrey D. Konowalchuk, and Daniel R. Barreda. Modified annexin v/propidium iodide apoptosis assay for accurate assessment of cell death. *Journal of Visualized Experiments : JoVE*, (50), April 2011.

- [66] V. A. Fadok, D. R. Voelker, P. A. Campbell, J. J. Cohen, D. L. Bratton, and P. M. Henson. Exposure of phosphatidylserine on the surface of apoptotic lymphocytes triggers specific recognition and removal by macrophages. *Journal of Immunology*, 148(7):2207–2216, April 1992.
- [67] Barry Halliwell. Reactive species and antioxidants. redox biology is a fundamental theme of aerobic life. *Plant Physiology*, 141(2):312–322, 2006.
- [68] Barry Halliwell and Matthew Whiteman. Measuring reactive species and oxidative damage in vivo and in cell culture: how should you do it and what do the results mean? *British Journal of Pharmacology*, 142(2):231–255, 2004.
- [69] L. J. Marnett. Oxyradicals and DNA damage. *Carcinogenesis*, 21(3):361–370, March 2000.
- [70] Vicki Stone, Helinor Johnston, and Roel P. F. Schins. Development of in vitro systems for nanotoxicology: methodological considerations, August 2009.
- [71] Claudia Fruijtier-Poelloth. The toxicological mode of action and the safety of synthetic amorphous silica-a nanostructured material. *Toxicology*, 294(2-3):61–79, April 2012.
- [72] Catrin Albrecht, Ad M. Knaapen, Andrea Becker, Doris Hoehr, Petra Haberzettl, Frederik J. van Schooten, Paul J. A. Borm, and Roel P. F. Schins. The crucial role of particle surface reactivity in respirable quartz-induced reactive oxygen/nitrogen species formation and APE/ref-1 induction in rat lung. *Respiratory Research*, 6:129, 2005.
- [73] Alexandra Kroll, Mike H. Pillukat, Daniela Hahn, and Juegen Schnekenburger. Current in vitro methods in nanoparticle risk assessment: limitations and challenges. *European Journal of Pharmaceutics and Biopharmaceutics: Official Journal of Arbeitsgemeinschaft Fuer Pharmazeutische Verfahrenstechnik e.V.*, 72(2):370–377, June 2009.
- [74] Zuzana Magdolenova, Andrew Collins, Ashutosh Kumar, Alok Dhawan, Vicki Stone, and Maria Dusinska. Mechanisms of genotoxicity. a review of in vitro and in vivo studies with engineered nanoparticles. *Nanotoxicology*, 8(3):233–278, May 2014.
- [75] Yang Li, Paola Italiani, Eudald Casals, Ngoc Tran, Victor F. Puentes, and Diana Boraschi. Optimising the use of commercial lal assays for the analysis of endotoxin contamination in metal colloids and metal oxide nanoparticles. *Nanotoxicology*, (4):1–12, August 2014.
- [76] Marina A Dobrovolskaia, Barry W. Neun, Jeffrey D. Clogson, Jennifer H. Grossman, and Scott E. McNeil. Choice of method for endotoxin detection depends on nanoformulation. *Nanomedicine*, 9(4):1847–1856, August 2014.

- [77] Tao Chen, Jian Yan, and Yan Li. Genotoxicity of titanium dioxide nanoparticles. *Journal of Food and Drug Analysis*, 22(4):95–104, August 2014.
- [78] Yanping Liu, Qiyue Xia, Shuyang Zhang, Feng Cheng, Zhong Zhihui, Li Wang, Li Hongxia, and Kai Xiao. Genotoxicity assessment of magnetic iron oxide nanoparticles with different particle sizes and surface coatings. *Nanotechnology*, 25(4):425101, October 2014.
- [79] Antonella De Palma, Antonella Roveri, Mattia Zaccarin, Louise Benazzi, Simone Daminelli, Giorgia Pantano, Mauro Buttarello, Fulvio Ursini, Massimo Gion, and Pier Luigi Mauri. Extraction methods of red blood cell membrane proteins for multidimensional protein identification technology (MudPIT) analysis. *Journal of Chromatography. A*, 1217(33):5328–5336, August 2010.
- [80] Marina A. Dobrovolskaia, Anil K. Patri, Jiwen Zheng, Jeffrey D. Clogston, Nader Ayub, Parag Aggarwal, Barry W. Neun, Jennifer B. Hall, and Scott E. McNeil. Interaction of colloidal gold nanoparticles with human blood: effects on particle size and analysis of plasma protein binding profiles. *Nanomedicine: Nanotechnology, Biology and Medicine*, 5(2):106–117, June 2009.
- [81] Dorota Napierska, Virginie Rabolli, Leen C J Thomassen, David Dinsdale, Catherine Princen, Laetitia Gonzalez, Katrien L C Poels, Micheline Kirsch-Volders, Dominique Lison, Johan A Martens, and Peter H Hoet. Oxidative stress induced by pure and iron-doped amorphous silica nanoparticles in subtoxic conditions. *Chemical research in toxicology*, 25(4):828–837, April 2012.
- [82] Andre Ziegler. Thermodynamic studies and binding mechanisms of cell-penetrating peptides with lipids and glycosaminoglycans. *Advanced Drug Delivery Reviews*, 60(4-5):580–597, March 2008.
- [83] Lorin Jakubek, Spiro Marangoudakis, Jessica Raingo, Xinyuan Liu, Diane Lipscombe, and Robert Hurt. The inhibition of neuronal calcium ion channels by trace levels of yttrium released from carbon nanotubes. *Biomaterials*, 30(31):6351–6357, October 2009.
- [84] Peter Wick, Pius Manser, Ludwig K. Limbach, Ursula Dettlaff-Weglikowska, Frank Krumeich, Siegmund Roth, Wendelin J. Stark, and Arie Bruinink. The degree and kind of agglomeration affect carbon nanotube cytotoxicity. *Toxicology Letters*, 168(2):121–131, January 2007.
- [85] Kaihua Chen, Jixi Zhang, and Hongchen Gu. Dissolution from inside: a unique degradation behaviour of core-shell magnetic mesoporous silica nanoparticles and the effect of polyethyleneimine coating. *Journal of Materials Chemistry*, 22(41):22005–22012, October 2012.
- [86] Qianjun He, Zhiwen Zhang, Yu Gao, Jianlin Shi, and Yaping Li. Intracellular localization and cytotoxicity of spherical mesoporous silica nano- and microparticles. *Small*, 5(23):2722–2729, December 2009.

- [87] Colette T. Dooley, Timothy M. Dore, George T. Hanson, W. Coyt Jackson, S. James Remington, and Roger Y. Tsien. Imaging dynamic redox changes in mammalian cells with green fluorescent protein indicators. *Journal of Biological Chemistry*, 279(21):22284–22293, May 2004.
- [88] Parag Aggarwal, Jennifer B Hall, Christopher B McLeland, Marina A Dobrovolskaia, and Scott E McNeil. Nanoparticle interaction with plasma proteins as it relates to particle biodistribution, biocompatibility and therapeutic efficacy. *Advanced drug delivery reviews*, 61(6):428–437, June 2009.
- [89] Shruti R. Saptarshi, Albert Duschl, and Andreas L. Lopata. Interaction of nanoparticles with proteins: relation to bio-reactivity of the nanoparticle. *Journal of Nanobiotechnology*, 11(1):26, July 2013.
- [90] Tobias Meissner, Annegret Potthoff, and Volkmar Richter. Suspension characterization as important key for toxicological investigations. *Journal of Physics: Conference Series*, 170:012012, May 2009.
- [91] Laetitia Gonzalez, Magdalena Lukamowicz-Rajska, Leen C. J. Thomassen, Christine E. A. Kirschhock, Luc Leyns, Dominique Lison, Johan A. Martens, Azeddine Elhajouji, and Micheline Kirsch-Volders. Co-assessment of cell cycle and micronucleus frequencies demonstrates the influence of serum on the in vitro genotoxic response to amorphous monodisperse silica nanoparticles of varying sizes. *Nanotoxicology*, 8(8):876–884, September 2013.
- [92] Kimberly J. Ong, Tyson J. MacCormack, Rhett J. Clark, James D. Ede, Van A. Ortega, Lindsey C. Felix, Michael K. M. Dang, Guibin Ma, Hicham Fenniri, Jonathan G. C. Veinot, and Greg G. Goss. Widespread nanoparticle-assay interference: Implications for nanotoxicity testing. *PLoS ONE*, 9(3):e90650, March 2014.
- [93] Ying Zhu, Wenxin Li, Qingnuan Li, Yuguo Li, Yufeng Li, Xiaoyong Zhang, and Qing Huang. Effects of serum proteins on intracellular uptake and cytotoxicity of carbon nanoparticles. *Carbon*, 47(5):1351–1358, April 2009.
- [94] Fengjuan Wang, Mariana G. Bexiga, Sergio Anguissola, Patricia Boya, Jeremy C. Simpson, Anna Salvati, and Kenneth A. Dawson. Time resolved study of cell death mechanisms induced by amine-modified polystyrene nanoparticles. *Nanoscale*, 5(22):10868–10876, October 2013.
- [95] Alexandra Kroll, Mike Hendrik Pillukat, Daniela Hahn, and Juergen Schnekenburger. Interference of engineered nanoparticles with in vitro toxicity assays. *Archives of toxicology*, 86(7):1123–1136, July 2012.

- [96] T. Takanashi, Y. Ogura, H. Taguchi, M. Hashizoe, and Y. Honda. Fluorophotometric quantitation of oxidative stress in the retina in vivo. *Investigative Ophthalmology & Visual Science*, 38(13):2721–2728, December 1997.
- [97] J. M. Woerle-Knirsch, K. Pulskamp, and H. F. Krug. Oops they did it again! carbon nanotubes hoax scientists in viability assays. *Nano Letters*, 6(6):1261–1268, June 2006.
- [98] Reto Sauder, Joachim Seelig, and Andre Ziegler. Thermodynamics of lipid interactions with cell-penetrating peptides. *Methods in Molecular Biology*, 683:129–155, 2011.

6.2 Curriculum vitae

CV Helene Kettiger, Dec. 2013

Helene Kettiger

Blochmonterstrasse 19

4054 Basel, Switzerland

Mail: h.kettiger-at-unibas.ch

Phone: +41 61 481 19 75

Current activity

09.2011 - 12.2014
(expected end)

PhD candidate Division of Pharmaceutical Technology (Prof. Dr. Jörg Huwyler), University of Basel, Switzerland

- Investigation of nanoparticle mediated cytotoxic effects (establishing nanoparticle synthesis, physico-chemical characterization, cell-based assays)
- Supervision of master thesis, set-up and supervision of semi-solid practical for bachelor students
- Presentations (oral and poster) in front of national and international committees
- **Further education:** CAS Regulatory Sciences, University of Basel (Successful grant application: 7000.- CHF)

Working experience

09.2009 - 09.2011

Pharmacist in community pharmacy (100%), Amavita Apotheke Stücki, Basel (Galenica Group)

- Co-working with insurance companies, medical doctors, customers
- Supervision and guidance of apprentice (Cantonal approved supervision of apprentices)
- Implementing and maintaining a GMP laboratory

05.2005 - 05.2007

Logistician at PharmaFocus (10%), Swiss drug distributor

Experience abroad

11.2012 - 12.2012

Intern (100%) as **chosen candidate** at physical chemistry department, Abo Akademi, Turku, Finland

02.2007 - 03.2007

Intern (100%) at R&D Bosnalijek (pharmaceutical company, generics), Sarajevo, Bosnia

Education

08.2007 - 08.2009

MSc Pharmacy and Swiss federal diploma of pharmacy, University of Basel. Score: 5.3 (very good)

01.2008 - 06.2008

Master thesis at Novartis Basel, MAP, *in vitro* ADME (Caroline Rynn): Validation of a higher throughput method to determine plasma protein binding by rapid equilibrium dialysis (RED). Score: 5.5 (very good)

08.2004 - 08.2007

BSc Pharmacy, University of Basel

08.2000 - 12.2003

Matura, profile: Latin and philosophy, Gymnasium Oberwil, Baselland

CV Helene Kettiger, Dec. 2013

Language skills

German	Native speaker
English	Fluent (team language, publications, presentations (oral/poster) 2013)
French	Intermediate knowledge
Spanish	Basic knowledge

IT knowledge

Microsoft Office	<ul style="list-style-type: none">• Word• Excel• PowerPoint
Image editing	<ul style="list-style-type: none">• GIMP
Sales program	<ul style="list-style-type: none">• Arizona

Commitments

11.2013	Founder of webpage femalescientists.unibas.ch
08.2004 - 08.2009	Student representative in education committee, University of Basel
1994 - 2002	Scouts, from 1999 to 2002 team leader

Interests

Geocaching with friends, hiking, restoring of bikes
